

**STUDY ON ELECTRODEPOSITION OF LIGHT RARE
EARTH METALS AND ALLOYS FROM MOLTEN
CHLORIDE ELECTROLYTES**

By

Deepak Kumar Sahoo
CHEM01200904002

Bhabha Atomic Research Centre, Mumbai

*A thesis submitted to the
Board of Studies in Chemical Sciences
In partial fulfillment of requirements
For the Degree of*

DOCTOR OF PHILOSOPHY

of

HOMI BHABHA NATIONAL INSTITUTE

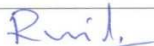
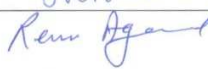


September, 2015

Homi Bhabha National Institute¹

Recommendations of the Viva Voce Committee

As members of the Viva Voce Committee, we certify that we have read the dissertation prepared by Sri Deepak Kumar Sahoo entitled "Study on electrodeposition of light rare earth metal and alloys from molten chloride electrolytes" and recommend that it may be accepted as fulfilling the thesis requirement for the award of Degree of Doctor of Philosophy.

Chairman - Dr. D. Das		Date: 07/6/2016
Guide / Convener - Dr. R. Mishra		Date: 7/6/2016
Co-guide - NA		Date:
Examiner - Prof. Rajiv Shekhar		Date: 7/6/2016
Member 1- Dr.(Mrs.) S.R. Bharadwaj		Date: 7/6/2016
Member 2- Dr. (Mrs.) Renu Agarwal		Date: 7/6/2016

Final approval and acceptance of this thesis is contingent upon the candidate's submission of the final copies of the thesis to HBNI.

I/We hereby certify that I/we have read this thesis prepared under my/our direction and recommend that it may be accepted as fulfilling the thesis requirement.

Date: 7/6/2016

Place: Trombay

<Signature>

Co-guide (if applicable)


<Signature>

Guide

¹ This page is to be included only for final submission after successful completion of viva voce.

STATEMENT BY AUTHOR

This dissertation has been submitted in partial fulfillment of requirements for an advanced degree at Homi Bhabha National Institute (HBNI) and is deposited in the Library to be made available to borrowers under rules of the HBNI.

Brief quotations from this dissertation are allowable without special permission, provided that accurate acknowledgement of source is made. Requests for permission for extended quotation from or reproduction of this manuscript in whole or in part may be granted by the Competent Authority of HBNI when in his or her judgment the proposed use of the material is in the interests of scholarship. In all other instances, however, permission must be obtained from the author.



Deepak Kumar Sahoo

DECLARATION

I, hereby declare that the investigation presented in the thesis has been carried out by me. The work is original and has not been submitted earlier as a whole or in part for a degree/diploma at this or any other Institution/University.

Deepak Kumar Sahoo.

Deepak Kumar Sahoo

List of publications arising from the thesis

Journal publications

- 1- Current efficiency in electro-winning of lanthanum and cerium metals from molten chloride electrolytes **D.K.Sahoo**, H.Singh, Krishnamurthy, *Rare Metals* 32-3 (2013) 305-311.
- 2- Determination of thermodynamic stability of lanthanum chloride hydrates ($\text{LaCl}_3 \cdot x\text{H}_2\text{O}$) by dynamic transpiration method by **D.K. Sahoo**, R. Mishra, H. Singh, N. Krishnamurthy, *Journal of Alloys and Compounds* 588 (2014) 578-584.
- 3- Electrochemical deposition of La-Mg alloys in LaCl_3 - MgCl_2 -KCl system with molten salt electrolysis process by **D.K.Sahoo**, H.Singh, N.Krishnamurthy, *J. Min. Metall. Sect. B-Metall.* 50 (2) B (2014) 109 – 114.
- 4- Electrochemical properties of Ce (III) in equimolar mixture of LiCl-KCl and NaCl-KCl molten salts by **D.K.Sahoo**, A.K.Satpati, N.Krishnamurthy. *RSC Adv.*, 5 (2015) 33163-33170.

Conference publications

- 1- Electrodeposition of light rare earth metals in fused chloride bath “**D.K.Sahoo**, Sanjay Kumar, A Mukherjee, N.Krishnamurthy” Proceedings of international symposium on environmental management of mining and minerals based industries, August 18-20 (2010) , Bhubaneswar, pp-51-58.
- 2- Determination of vapor pressure of H_2O over $\text{LaCl}_3 \cdot 7\text{H}_2\text{O}$ and intermediate compounds by dynamic transpiration method; **D.K.Sahoo**, R.Mishra, D Das and N Krishnamurthy; 18th International symposium on thermal analysis, Feb.2-4 (2012), Anushaktinagar, Mumbai pp 67-69.
- 3- Study on electrodeposition of La-Mg alloys in chloride system with molten salt electrolysis process, **D.K.Sahoo**, H.Singh, N.Krishnamurthy, National conference on Rare earths and uranium processing & utilizations (REPUT-2014).May 2-4 (2014), Anushaktinagar, Mumbai-400094.p-45.

4- Electrochemical behavior of Pr (III) In NaCl-KCl molten salt,
D.K.Sahoo,R.Mishra,EUCHEM Conference on Molten Salts AND Ionic Liquids,3rd -8th
July 2016,Austria,Vienna.

Deepak Kumar Sahoo.

Deepak Kumar Sahoo

DEDICATED TO MY

PARENTS.....

ACKNOWLEDGEMENT

I wish to express my deep sense of gratitude and sincere thanks to my research guide Dr. R. Mishra for his unstinted inspiration, invaluable guidance, encouragement, keen interest, good wishes and valuable suggestions throughout my entire research tenure. This work would not have been completed without his guidance and support.

I also would like to thank Dr. N. Krishnamurthy and H. Singh for their unconditional support to carry out my research work. It is my great privilege to acknowledge Dr. D. Das, Dr (Mrs.) Shyamla Bharadwaj and Dr. (Mrs.) Renu Agarwall for critically evaluating my research activities time to time as members of HBNI doctoral committee and provide valuable suggestions for the completion of this work. I would also like to express my thanks to Dr. A. Satapati, Analytical Chemistry Division, BARC for his valuable technical support in carrying out electrochemical studies.

It's a great pleasure to acknowledge my two colleagues Mr. Y. R. Tiwari and Mr. S. J. Dulgachh for their help in carrying out my research activities. I am thankful to all my REDS colleagues and staff members for their support at different times. I would like to thank my colleagues Jyoti Prakash, Sanjay Kumar, Abhishek Mukherjee, Bhaskar Paul, Jitendra Sonebar, and TSRCh Murthy for their diversified help throughout the course of my research work.

Content

Synopsis	i
List of Figures	iv
List of Tables	xvii
Chapter I	
Introduction	
1.1 Background	1
1.2 Importance of rare earths to India	3
1.3 General processing of RE minerals	4
1.4 Reduction of REEs	5
1.4.1 Metallolthermic reduction process	5
1.4.2 Molten salt electrolysis	6
1.4.3 Comparison between metallolthermic and molten salt electrolysis	6
1.5 Research objective	7
1.6 Contribution from thesis	8
Chapter II	
Literature review	
2.1 Introduction	9
2.2 Methods available for extraction of RE metals	10
2.2.1 Metallolthermic reduction process	10
2.2.1.1 Reduction of rare earth oxide	13

2.2.1.2 Reduction of rare earth fluoride	13
2.2.1.3 Reduction of rare earth chloride	14
2.2.2 Electrolytic production of RE metal	14
2.2.2.1 Chloride electrolysis	15
2.2.2.2 Oxide-fluoride electrolysis	18
2.2.2.3 Current efficiency	20
2.3 Reason for using chloride electrolysis	21
2.4 Electrolyte properties for chloride electrolysis	21
2.5 Methods for production of anhydrous rare earth chlorides	27
2.6 Kinetic parameters in the electrodeposition of RE (III) in molten alkali chloride melts	29
2.7 Bulk preparation of rare earth metals	31
2.8 Recovery of rare earth alloys	32
2.8.1 Electrochemical co-deposition technique	32
2.8.2 Consumable cathode technique	33
2.9 Scope of the present thesis	33
Chapter III	
Instrumentations	
3.1 Introduction	35
3.2 X-ray fluorescence spectrometry	35
3.2.1 Energy dispersive X-ray fluorescence (EDXRF)	37
3.3 X-ray diffraction (XRD)	38
3.4 Electron microscopy	42

3.4.1 Scanning electron microscopy	43
3.5 Thermal analysis	45
3.5.1 Thermogravimmetric Analysis (TGA)	45
3.5.2 Differential Thermal Analysis (DTA)	45
3.5.3 Differential Scanning Calorimetry (DSC)	45
3.5.4 Evolved Gas Analysis (EGA)	47
3.6 Inductively coupled plasma atomic emission spectroscopy (ICP-AES)	47
3.7 Back ground of voltammetric studies	50
3.7.1 Potentiostat	50
3.7.2 Cyclic Voltammetry (CV)	52
3.7.3 Electron transfer co-efficient	53
3.7.4 Square wave Voltammetry (SWV)	54
3.7.5 Exchange current density	56

Chapter IV

Dehydration study of rare earth chloride hydrates:

4.1 Introduction	57
4.2 Vapor pressure measurement	59
4.3 Results and discussion	62
4.3.1 Determination of thermodynamic stability of $\text{LaCl}_3 \cdot \text{XH}_2\text{O}$	62
4.3.1.1 Dehydration mechanism	62
4.3.1.2 Characterization of LaCl_3 hydrates	66
4.3.1.3 Establishment of equilibrium condition	68
4.3.1.4 Vapor pressure analysis	69

4.3.1.5 Estimation of thermodynamic parameters	73
4.3.2 Determination of thermodynamic stability of $\text{CeCl}_3 \cdot \text{XH}_2\text{O}$	76
4.3.2.1 Dehydration mechanism	76
4.3.2.2 Establishment of equilibrium condition	79
4.3.2.3 Vapor pressure analysis	80
4.3.2.4 Estimation of thermodynamic parameters	84
4.3.3 Determination of thermodynamic stability of $\text{PrCl}_3 \cdot \text{XH}_2\text{O}$	86
4.3.3.1 Dehydration mechanism	86
4.3.3.2 Establishment of equilibrium condition	89
4.3.3.3 Vapor pressure analysis	90
4.3.3.4 Estimation of thermodynamic parameters	95
4.3.4 Determination of thermodynamic stability of $\text{NdCl}_3 \cdot \text{XH}_2\text{O}$	96
4.3.4.1 Dehydration mechanism	96
4.3.4.2 Characterization of NdCl_3 hydrates	99
4.3.4.3 Establishment of equilibrium condition	102
4.3.4.4 Vapor pressure analysis	103
4.3.4.5 Estimation of thermodynamic parameters	107
4.4 Summary	109

Chapter V

Electrochemical behavior of RE (III) in alkali chloride melts:

5.1 Introduction	113
5.1.1 Preparation and purification of electrolyte	114

5.1.2 Electrolytic Cell	115
5.1.3 Electrochemical apparatus and electrodes	115
5.2 Results and discussion	118
5.2.1 Electrochemical investigation of LaCl_3 in alkali chloride melts	118
5.2.1.1 Reduction behavior of La (III) in LiCl-KCl and NaCl-KCl	118
5.2.1.2 Reversibility of the electrode Process	122
5.2.1.3 Diffusion coefficient of La (III) in molten mixture	126
5.2.1.4 Determination of standard rate constant	131
5.2.1.5 Exchange current density	133
5.2.2 Electrochemical investigation of CeCl_3 in alkali chloride melts	135
5.2.2.1 Reduction behavior of Ce (III) in alkali chloride melts	135
5.2.2.2 Kinetics of the electrode Process	138
5.2.2.3 Calculation of standard rate constant	141
5.2.2.4 Square Wave Voltammetry	143
5.2.2.5 Diffusion coefficient of Ce (III) in molten mixture	144
5.2.2.6 Estimation of activation energy	146
5.2.2.7 Exchange current density	147
5.2.3 Electrochemical investigation of PrCl_3 in alkali chloride melts	151
5.2.3.1 Reduction behavior of Pr (III) in alkali chloride melts	151
5.2.3.2 Reversibility of the electrode Process	154
5.2.3.3 Diffusion coefficient of Pr (III) in molten mixture	158
5.2.3.4 Determination of standard rate constant	160
5.2.3.5 Exchange current density	161

5.2.4 Electrochemical investigation of NdCl ₃ in alkali chloride melts	163
5.2.4.1 Reduction behavior of Nd (III) in alkali chloride melts	163
5.2.4.2 Reversibility of the electrode Process	165
5.2.4.3 Diffusion coefficient of Nd ions in molten mixture	169
5.2.4.4 Determination of standard rate constant	170
5.2.4.5 Exchange current density	171
5.3 Summary	173

Chapter VI

Electrodeposition of RE metals in alkali chloride melts

6.1 Introduction	175
6.2 Experimental	175
6.2.1 Preparation of electrolyte	175
6.2.2 Electrolytic cell	176
6.2.3 Instrumentation	180
6.3 Results and Discussion	180
6.3.1 Analysis of the electrodeposited metals	180
6.3.2 Electrolytic reaction	184
6.3.3 Relation between electrolytic temperature and current efficiency	185
6.3.4 Effect of concentration of functional electrolyte on current efficiency	187
6.3.5 Effect of cathode current density on current efficiency	189
6.3.6 Effect of electrolysis duration on yield and current efficiency	190
6.3.7 Effect of single carrier electrolyte	192
6.4 Conclusion	193

6.5 Verification of optimized parameters by Taguchi method	194
6.5.1 Selection of parameters for Taguchi optimization	196
6.5.2 Conclusion	197
6.6 Summary	200
Chapter VII	
Electrodeposition of alloys	
7.1 Introduction	203
7.2 Electrochemical co-deposition technique	204
7.2.1 Basic electrochemical study	205
7.2.1.1 Cyclic Voltammetry	205
7.2.1.2 Open Circuit Potentiometry	206
7.2.1.3 Potentiostatic electrolysis and characterization of La-Mg alloys	207
7.2.1.4 Conclusion	208
7.2.2 Bulk deposition of alloy	209
7.2.2.1 Results and discussion	210
7.2.2.1.1 Effect of electrolyte composition	210
7.2.2.1.2 Formation of alloys	211
7.2.2.1.3 Microstructure evolution	214
7.2.2.1.4 Current efficiency	215
7.2.2.1.5 Effect of electrolysis temperature on current efficiency	215
7.2.2.1.6 Effect of cathode current density on current efficiency	216
7.2.2.2 Conclusion	217
7.3 Consumable cathode technique	218

7.3.1 Analysis of Voltammogram	218
7.3.2 Bulk deposition of Nd-Fe alloy	221
7.3.2.1 Results and discussion	223
7.3.2.1.1 Effect of concentration of electrolyte on current efficiency	223
7.3.2.1.2 Effect of cathode current density on current efficiency	224
7.3.2.2 Conclusion	225
7.4 Summary	226
Chapter-VIII	
Conclusion	227
References	230



Homi Bhabha National Institute
SYNOPSIS of Ph.D. THESIS

1. **Name of the Student:** Deepak Kumar Sahoo
2. **Name of the Constituent Institution:** Bhabha Atomic Research Centre
3. **Enrolment No.:** CHEM01200904002
4. **Title of the Thesis:** Study on electrodeposition of light rare earth metals and alloys from molten chloride electrolytes.
5. **Board of Studies:** Chemical Science

SYNOPSIS

The present thesis describes the molten salt electrolysis process for the extraction of four light rare earth metals i.e. lanthanum (La), cerium (Ce), Praseodymium (Pr) and neodymium (Nd) with emphasis on basic fundamentals, cell design and optimization of process parameters for maximum current efficiency and yield. Several aspects of electrolysis process like dehydration of starting material, electrode kinetics, cell design, and operational parameters in the extraction of metals from their corresponding chlorides have been investigated in details. In this work, the equilibrium vapor pressure of water over various RE chloride hydrates was measured employing dynamic transpiration technique. The standard molar Gibbs energy of formation of RE chloride hydrates have been derived using the measured equilibrium vapor pressure data. Based on this information a simple and economic way of dehydration process was established. Extensive research has been carried out to know the mechanism and kinetics of the electrodeposition of rare earth metal in LiCl-KCl and NaCl-KCl electrolytes. Studies related to electro-kinetic parameters such as electron transfer co-efficient, electron transfer rate constant, diffusion coefficient have been carried out to draw more insight into the process. One of the major objectives of this current investigation was to determine the optimum operating conditions for the electrowinning of light rare earth metals from their corresponding chlorides in alkali chloride melts i.e. (i) LiCl-KCl and (ii) NaCl-KCl melts. Process parameters like temperature of operation, electrolytic composition and cathode current densities have been standardized to get maximum current efficiency and yield. Taguchi method has been adopted to optimize the electrolysis parameters and also to find out the most dominant parameter in the electrowinning process.

This thesis also includes the results of investigations on the preparation of two alloys i.e. La-Mg and Nd-Fe alloy using molten chloride as media. The electrochemistry and the mechanism of the deposition process were studied by cyclic voltammetry and open circuit potentiometry. The effects of various process parameters such as composition of electrolyte in the bath, temperature of electrolysis and cathode current density on current efficiency have been investigated to get maximum current efficiency in both the cases.

List of figures

Figure No.	Figure captions	page no.
1.1	<i>Steps of extractive metallurgy</i>	5
2.1	<i>Standard free energy of formation of selected oxides of rare earths and certain common metals as a function of temperature</i>	11
2.2	<i>Standard free energy of formation of selected chlorides of rare earths and certain common metals as a function of temperature</i>	12
2.3	<i>Standard free energy of formation of selected fluorides of rare earths and certain common metals as a function of temperature.</i>	12
2.4	<i>Phase diagram of LiCl-KCl</i>	24
2.5	<i>Phase diagram of NaCl-KCl</i>	24
3.1	<i>Schematic of EDXRF equipment</i>	38
3.2	<i>Typical X-ray of Cu target</i>	40
3.3	<i>Schematic of XRD equipment</i>	41
3.4	<i>Schematic of SEM equipment</i>	44
3.5	<i>Schematic of DTA/DSC equipment</i>	46
3.6	<i>Schematic of ICP-AES equipment</i>	49

3.7	<i>Schematic of potentiostat connected to three electrode system</i>	51
3.8	<i>Potential simulation (a) and resulting current response (b) in a cyclic voltammetry experiment.</i>	52
3.9	<i>Excitation waveform and current sampling points for Osteryoung square wave.</i>	55
4.1	<i>Sketch diagram of the micro thermo-balance assembly used for dynamic transpiration vapor measurements.</i>	61
4.2	<i>TG plot of $\text{LaCl}_3 \cdot 7\text{H}_2\text{O}$ recorded at the heating rate of 0.5, 2, 5 and 10 K/min under 2 l/h flowing argon atmosphere.</i>	64
4.3	<i>Plot of decomposition temperature versus heating rate for step-1, step-2 and step-3 of $\text{LaCl}_3 \cdot 7\text{H}_2\text{O}$ decomposition.</i>	64
4.4	<i>DTA plot of $\text{LaCl}_3 \cdot 7\text{H}_2\text{O}$ recorded at a heating rate of 0.5K/min under 2l/h flowing argon atmosphere</i>	65
4.5	<i>TGA-EGA plot of $\text{LaCl}_3 \cdot 7\text{H}_2\text{O}$ recorded at the heating rate of 5K/min under 2l/h flowing argon atmosphere.</i>	65
4.6	<i>a-HTXRD patterns of $\text{LaCl}_3 \cdot x\text{H}_2\text{O}(s)$ sample recorded at 30, 75 and 105 °C</i> <i>b-HTXRD patterns of $\text{LaCl}_3(s)$ sample recorded at 140 and 180 °C</i>	67
4.7	<i>The apparent pressure versus flow rate of the carrier gas for $\text{LaCl}_3 \cdot 7\text{H}_2\text{O}(s) \rightarrow \text{LaCl}_3 \cdot 3\text{H}_2\text{O}(s) + 4\text{H}_2\text{O}(g)$ reaction measured at 330 K</i>	69
4.8	<i>Plots of $\ln p$ versus $1/T$ for the vaporization reaction $\text{LaCl}_3 \cdot 7\text{H}_2\text{O}(s) \rightarrow \text{LaCl}_3 \cdot 3\text{H}_2\text{O}(s) + 4\text{H}_2\text{O}(g)$ (Step-I).</i>	71

4.9	<i>Plots of $\ln p$ versus $1/T$ for the vaporization reaction $\text{LaCl}_3 \cdot 3\text{H}_2\text{O}(s) \rightarrow \text{LaCl}_3 \cdot \text{H}_2\text{O}(s) + 2\text{H}_2\text{O}(g)$ (Step-II)</i>	71
4.10	<i>Plots of $\ln p$ versus $1/T$ for the vaporization reaction $\text{LaCl}_3 \cdot \text{H}_2\text{O}(s) \rightarrow \text{LaCl}_3(s) + \text{H}_2\text{O}(g)$ (Step-III).</i>	72
4.11	<i>TG plot of $\text{CeCl}_3 \cdot 7\text{H}_2\text{O}(s)$ recorded at the heating rates of 0.5 K/min under 2.5 l/h flowing argon atmosphere.</i>	76
4.12	<i>DTA plot of $\text{CeCl}_3 \cdot 7\text{H}_2\text{O}$ recorded at a heating rate of 5K/min under 2.5l/h flowing argon atmosphere</i>	78
4.13	<i>EGA plot of $\text{CeCl}_3 \cdot 7\text{H}_2\text{O}$ recorded at the heating rate of 5K/min under 2.5l/h flowing argon atmosphere.</i>	78
4.14	<i>The apparent pressure versus flow rate of the carrier gas for $\text{CeCl}_3 \cdot 7\text{H}_2\text{O}(s) \rightarrow \text{CeCl}_3 \cdot 3\text{H}_2\text{O}(s) + 4\text{H}_2\text{O}(g)$ reaction measured at 330 K.</i>	80
4.15	<i>Plots of $\ln p$ versus $1/T$ for the vaporization reaction $\text{CeCl}_3 \cdot 7\text{H}_2\text{O}(s) \rightarrow \text{CeCl}_3 \cdot 3\text{H}_2\text{O}(s) + 4\text{H}_2\text{O}(g)$ (Step-I)</i>	82
4.16	<i>Plots of $\ln p$ versus $1/T$ for the vaporization reaction $\text{CeCl}_3 \cdot 3\text{H}_2\text{O}(s) \rightarrow \text{CeCl}_3 \cdot 2\text{H}_2\text{O}(s) + \text{H}_2\text{O}(g)$ (Step-II)</i>	82
4.17	<i>Plots of $\ln p$ versus $1/T$ for the vaporization reaction $\text{CeCl}_3 \cdot 2\text{H}_2\text{O}(s) \rightarrow \text{CeCl}_3 \cdot \text{H}_2\text{O}(s) + \text{H}_2\text{O}(g)$ (Step-III).</i>	83
4.18	<i>Plots of $\ln p$ versus $1/T$ for the vaporization reaction $\text{CeCl}_3 \cdot \text{H}_2\text{O}(s) \rightarrow \text{CeCl}_3(s) + \text{H}_2\text{O}(g)$ (Step-IV).</i>	83

4.19	<i>TG plot of $\text{PrCl}_3 \cdot 7\text{H}_2\text{O}$ recorded at the heating rate of 0.5, 2, 5 and 10 K/min under 2.5 l/h flowing argon atmosphere.</i>	86
4.20	<i>Plot of decomposition temperature versus heating rate for step-1, step-2, step-3 and step-IV of $\text{PrCl}_3 \cdot 7\text{H}_2\text{O}$ decomposition.</i>	87
4.21	<i>DTA plot of $\text{PrCl}_3 \cdot 7\text{H}_2\text{O}$ recorded at a heating rate of 5K/min under 2.5l/h flowing argon atmosphere</i>	88
4.22	<i>EGA plot of $\text{PrCl}_3 \cdot 7\text{H}_2\text{O}$ recorded at the heating rate of 5K/min under 2.5l/h flowing argon atmosphere.</i>	88
4.23	<i>The apparent pressure versus flow rate of the carrier gas for $\text{PrCl}_3 \cdot 7\text{H}_2\text{O}(s) \rightarrow \text{PrCl}_3 \cdot 3\text{H}_2\text{O}(s) + 4\text{H}_2\text{O}(g)$ reaction measured at 335 K.</i>	90
4.24	<i>Plots of $\ln p$ versus $1/T$ for the vaporization reaction $\text{PrCl}_3 \cdot 7\text{H}_2\text{O}(s) \rightarrow \text{PrCl}_3 \cdot 3\text{H}_2\text{O}(s) + 4\text{H}_2\text{O}(g)$ (Step-I).</i>	92
4.25	<i>Plots of $\ln p$ versus $1/T$ for the vaporization reaction $\text{PrCl}_3 \cdot 3\text{H}_2\text{O}(s) \rightarrow \text{PrCl}_3 \cdot 2\text{H}_2\text{O}(s) + \text{H}_2\text{O}(g)$ (Step-II)</i>	92
4.26	<i>Plots of $\ln p$ versus $1/T$ for the vaporization reaction $\text{PrCl}_3 \cdot 2\text{H}_2\text{O}(s) \rightarrow \text{PrCl}_3 \cdot \text{H}_2\text{O}(s) + \text{H}_2\text{O}(g)$ (Step-III)</i>	93
4.27	<i>Plots of $\ln p$ versus $1/T$ for the vaporization reaction $\text{PrCl}_3 \cdot \text{H}_2\text{O}(s) \rightarrow \text{PrCl}_3(s) + \text{H}_2\text{O}(g)$ (Step-IV)</i>	93
4.28	<i>TG plot of $\text{NdCl}_3 \cdot 6\text{H}_2\text{O}$ recorded at the heating rate of 0.5, 2, 5 and 10 K/min under 2.5 l/h flowing argon atmosphere.</i>	97

4.29	<i>Plot of decomposition temperature versus heating rate for step-1, step-2, step-3 and step-4 of $\text{NdCl}_3 \cdot 6\text{H}_2\text{O}$ decomposition.</i>	98
4.30	<i>DTA plot of $\text{NdCl}_3 \cdot 6\text{H}_2\text{O}$ recorded at a heating rate of 5K/min under 2.5l/h flowing argon atmosphere</i>	98
4.31	<i>a- HTXRD patterns of $\text{NdCl}_3 \cdot x\text{H}_2\text{O}(s)$ sample recorded at 50, 80 and 95 °C</i>	100
	<i>b- HTXRD patterns of $\text{NdCl}_3(s)$ sample recorded at 120 and 180 °C</i>	101
4.32	<i>EGA plot of $\text{NdCl}_3 \cdot 6\text{H}_2\text{O}$ recorded at the heating rate of 5K/min under 2.5l/h flowing argon atmosphere.</i>	101
4.33	<i>The apparent pressure versus flow rate of the carrier gas for $\text{NdCl}_3 \cdot 6\text{H}_2\text{O}(s) \rightarrow \text{NdCl}_3 \cdot 3\text{H}_2\text{O}(s) + 3\text{H}_2\text{O}(g)$ reaction measured at 340 K.</i>	102
4.34	<i>Plots of $\ln p$ versus $1/T$ for the vaporization reaction $\text{NdCl}_3 \cdot 6\text{H}_2\text{O}(s) \rightarrow \text{NdCl}_3 \cdot 3\text{H}_2\text{O}(s) + 3\text{H}_2\text{O}(g)$ (Step-I).</i>	104
4.35	<i>Plots of $\ln p$ versus $1/T$ for the vaporization reaction $\text{NdCl}_3 \cdot 3\text{H}_2\text{O}(s) \rightarrow \text{NdCl}_3 \cdot 2\text{H}_2\text{O}(s) + \text{H}_2\text{O}(g)$ (Step-II) ,</i>	104
4.36	<i>Plots of $\ln p$ versus $1/T$ for the vaporization reaction $\text{NdCl}_3 \cdot 2\text{H}_2\text{O}(s) \rightarrow \text{NdCl}_3 \cdot \text{H}_2\text{O}(s) + \text{H}_2\text{O}(g)$ (Step-III) ,</i>	105
4.37	<i>Plots of $\ln p$ versus $1/T$ for the vaporization reaction $\text{NdCl}_3 \cdot \text{H}_2\text{O}(s) \rightarrow \text{NdCl}_3(s) + \text{H}_2\text{O}(g)$ (Step-IV) ,</i>	105
4.38	<i>Schematic of the dehydration set-up used in the present investigation</i>	111

5.1	<i>The schematic view of the electrochemical set-up used in the cyclic voltammetry measurement.</i>	117
5.2	<i>Variations of cathodic peak current vs. immersion depth of working electrode in LaCl₃-LiCl-KCl melt.</i>	117
5.3	<i>Comparison of the cyclic voltammogram for pure LiCl-KCl melt and LaCl₃-LiCl-KCl melt in the potential range of 1 to -2.5V.</i>	119
5.4	<i>EDS spectra of the deposit (metallic lanthanum) obtained under potentiostatic condition in equimolar LiCl-KCl mixture at 973K).</i>	119
5.5	<i>SEM micrograph of the deposit product (metallic lanthanum) obtained under potentiostatic condition in equimolar LiCl-KCl mixture at 973K</i>	120
5.6	<i>Comparison of the cyclic voltammogram for pure NaCl-KCl melt and LaCl₃-NaCl-KCl melt in the potential range of 0 to -2.75V.</i>	121
5.7	<i>Cyclic voltammogram of LaCl₃-LiCl-KCl melt on molybdenum electrode at various scan rates of 0.025 to 0.5Vs⁻¹.</i>	123
5.8	<i>Cyclic voltammogram of LiCl-KCl melt on molybdenum electrode at various scan rates of 0.025 to 0.5Vs⁻¹.</i>	123
5.9	<i>Back ground corrected cyclic voltammograms of LaCl₃-LiCl-KCl melt on molybdenum electrode at various scan rates of 0.025 to 0.5Vs⁻¹.</i>	124
5.10	<i>Variations of cathodic peak potentials with logarithm of sweep rate in LaCl₃-LiCl-KCl melt at 973K.</i>	125

5.11	<i>Variation of cathodic peak current vs. square root of scan rate in LaCl₃-NaCl-KCl melts.</i>	126
5.12	<i>Variations of cathodic peak potential with logarithm of sweep rate in LaCl₃-LiCl-KCl melt at 973K.</i>	128
5.13	<i>Verification of Arrhenius law. (1) LaCl₃ in equimolar LiCl-KCl melt. (2) LaCl₃ in equimolar NaCl-KCl melt.</i>	130
5.14	<i>Tafel plot for LaCl₃ in equimolar mixture of LiCl-KCl melt on molybdenum electrode.</i>	134
5.15	<i>Comparison of the cyclic voltammogram for pure LiCl-KCl melt and CeCl₃-LiCl-KCl melt in the potential range of 0 to -2.6V.</i>	136
5.16	<i>Energy dispersive X-ray fluorescence (EDXRF) spectra of the deposit (metallic cerium) obtained under potentiostatic condition in equimolar LiCl-KCl mixture at 963K</i>	136
5.17	<i>Comparison of the cyclic voltammogram for pure NaCl-KCl melt and CeCl₃-NaCl-KCl melt in the potential range of 0 to -2.6V. Working electrode: Molybdenum.</i>	137
5.18	<i>SEM micrograph of the deposit product (metallic cerium) obtained under potentiostatic condition in equimolar LiCl-KCl mixture at 963K.</i>	138
5.19	<i>Cyclic voltammogram for 2.1×10^{-4} molcm⁻³ of CeCl₃ in equimolar LiCl-KCl melt on molybdenum electrode at various scan rates at 963K.</i>	139
5.20	<i>Plot between the square root of scan rate and cathodic peak current for CeCl₃-LiCl-KCl melt.</i>	140

5.21	<i>Cyclic voltammogram of CeCl₃-NaCl-KCl melt on molybdenum electrode at various scan rates.</i>	140
5.22	<i>Plot between the square root of scan rate and cathodic peak current for CeCl₃-NaCl-KCl melt.</i>	141
5.23	<i>Square wave voltammogram for reduction of CeCl₃ at molybdenum electrode in LiCl-KCl melt.</i>	143
5.24	<i>Net square wave voltammogram for reduction of CeCl₃ at molybdenum electrode in NaCl-KCl melt.</i>	144
5.25	<i>Logarithm of the diffusion coefficient of Ce (III) as a function of inverse of temperature in (1) Equimolar LiCl-KCl melt (2) Equimolar NaCl-KCl melt.</i>	146
5.26	<i>Tafel for CeCl₃ in equimolar LiCl-KCl salt on Mo electrode</i>	148
5.27	<i>Tafel for CeCl₃ in equimolar NaCl-KCl salt on Mo electrode</i>	149
5.28	<i>Comparison of the cyclic voltammogram for pure LiCl-KCl melt and PrCl₃-LiCl-KCl melt in the potential range of 0 to -2.5V.</i>	152
5.29	<i>EDXRF spectra of the deposit (metallic Praseodymium) obtained under potentiostatic condition in equimolar LiCl-KCl mixture</i>	152
5.30	<i>Comparison of the cyclic voltammogram for pure NaCl-KCl melt and PrCl₃-NaCl-KCl melt in the potential range of 0 to -2.5V on Mo electrode.</i>	153

5.31	<i>Cyclic voltammogram of PrCl₃-LiCl-KCl melt on molybdenum electrode at various scan rates of 0.025 to 0.5Vs⁻¹.</i>	155
5.32	<i>Variations of cathodic peak current vs. square root of scan rate in PrCl₃-LiCl-KCl melt.</i>	156
5.33	<i>Cyclic voltammogram of PrCl₃-NaCl-KCl melt on molybdenum electrode at various scan rates of 0.025 to 0.5Vs⁻¹.</i>	157
5.34	<i>Variations of cathodic peak current vs. square root of scan rate for PrCl₃-NaCl-KCl melt.</i>	158
5.35	<i>Verification of Arrhenius law. (1) PrCl₃ in equimolar LiCl-KCl melt. (2) PrCl₃ in equimolar NaCl-KCl melt.</i>	160
5.36	<i>Tafel plot for PrCl₃ in equimolar mixture of LiCl-KCl melt on molybdenum electrode.</i>	162
5.37	<i>Comparison of the cyclic voltammogram for pure LiCl-KCl melt and NdCl₃-LiCl-KCl melt in the potential range of 1 to -2.5V on molybdenum electrode.</i>	164
5.38	<i>Comparison of the cyclic voltammogram for pure NaCl-KCl melt and NdCl₃-NaCl-KCl melt in the potential range of 0 to -2.75V on Mo electrode.</i>	165
5.39	<i>Cyclic voltammogram of NdCl₃-LiCl-KCl melt on molybdenum electrode at various scan rates of 0.025 to 0.5Vs⁻¹.</i>	166
5.40	<i>Variation of cathodic peak current vs. square root of scan rate for Nd (III)/Nd (II) in NdCl₃-LiCl-KCl melt.</i>	167

5.41	<i>Variation of cathodic peak current vs. square root of scan rate for Nd (II)/Nd (0) in NdCl₃-LiCl-KCl melt.</i>	167
5.42	<i>Cyclic voltammograms of NdCl₃-NaCl-KCl melt on molybdenum electrode at various scan rates of 0.025 to 0.5Vs⁻¹</i>	168
5.43	<i>Variations of cathodic peak current vs. square root of scan rate for NdCl₃-NaCl-KCl melt.</i>	169
5.44	<i>Tafel plot for NdCl₃ in equimolar mixture of LiCl-KCl melt on molybdenum electrode.</i>	171
6.1	<i>Schematic view of the molten salt electrochemical set-up</i>	178
6.2	<i>Electrodeposited product obtained from the electrolysis of LaCl₃ in LiCl-KCl flux.</i>	178
6.3	<i>Electrodeposited product obtained from the electrolysis of CeCl₃ in LiCl-KCl flux</i>	179
6.4	<i>Electrodeposited product obtained from PrCl₃-LiCl-KCl electrolyte.</i>	179
6.5	<i>Electrodeposited product obtained from NdCl₃-LiCl-KCl electrolyte.</i>	179
6.6	<i>EDXRF spectra of the electrodeposited product from LaCl₃-LiCl-KCl electrolyte</i>	181
6.7	<i>EDXRF spectra of the electrodeposited product obtained from CeCl₃-LiCl-KCl electrolyte.</i>	181

6.8	<i>EDXRF spectra of the electrodeposited product obtained from PrCl₃-LiCl-KCl electrolyte.</i>	183
6.9	<i>EDXRF spectra of the electrodeposited product obtained from NdCl₃-LiCl-KCl electrolyte.</i>	182
6.10	<i>XRD plot of the electrodeposited product from LaCl₃-LiCl-KCl electrolyte</i>	183
6.11	<i>XRD plot of the electrodeposited product obtained from CeCl₃-LiCl-KCl electrolyte.</i>	183
6.12	<i>Relationship between current efficiency and operating temperature in the electrowinning of RE metals using RECl₃(40wt%)-LiCl-KCl electrolytes.(RE=La, Ce, Pr and Nd)</i>	187
6.13	<i>Relationship between current efficiency and electrolyte composition of in the electrowinning of La, Ce, Pr and Nd in LiCl-KCl melt.</i>	189
6.14	<i>Relationship between CE and CCD obtained in the electrolysis of LiCl-KCl-RECl₃ systems.</i>	190
6.15	<i>Metal yield and current efficiency obtained with time in the electrowinning of lanthanum metal.</i>	192
6.16	<i>Relationship between CE and CCD obtained in the electrowinning of lanthanum in single carrier electrolyte like LiCl, KCl and NaCl respectively.</i>	193
7.1	<i>Cyclic voltammogramms obtained on molybdenum electrode in LiCl-KCl-MgCl₂ in the presence and absence of LaCl₃.</i>	206

7.2	<i>Open circuit potentiogram of $\text{LaCl}_3\text{-MgCl}_2\text{-LiCl-KCl}$ system at molybdenum electrode at 773K, $E_{\text{applied}}=-2.4\text{ V}$</i>	207
7.3	<i>XRD pattern of La-Mg alloys obtained by potentiostatic electrolysis at -1.80 V for 30 minutes from $\text{LiCl-KCl-LaCl}_3(2\text{wt}\%)\text{-MgCl}_2(5\text{wt}\%)$ electrolyte</i>	208
7.4	<i>Schematic of the molten salt electrolytic set-up used in our study for La-Mg alloy production.</i>	210
7.5	<i>X-ray diffraction pattern of the products obtained by electrolysis in $\text{LaCl}_3\text{-MgCl}_2\text{-KCl}$ (60wt %) melt containing a)10wt%, b)12.5wt%, c)15wt% and d)20wt% of MgCl_2.</i>	212
7.6	<i>SEM images of samples obtained in the electrolysis of $\text{LaCl}_3\text{-MgCl-KCl}$ with various compositions.</i>	214
7.7	<i>Effect of electrolysis temperature on current efficiency (CE) in the electrowinning of La-Mg alloys.</i>	216
7.8	<i>Effect of cathode current density (CCD) on current efficiency (CE) in the electrowinning of La-Mg alloys</i>	217
7.9	<i>The comparison of electrochemical domain of NaCl-KCl electrolyte on Fe electrode with that of molybdenum electrode</i>	220
7.10	<i>Comparison of the voltammogram obtained in NaCl-KCl molten media before and after addition of NdCl_3 on iron electrode at 973K.</i>	220
7.11	<i>Fluorescence (ED-XRF) analysis of the deposited product obtained</i>	221

after potentiostatic electrolysis at -2.0 V for 10 minutes in NdCl₃-NaCl-KCl melt on Fe cathode.

7.12	<i>Schematic of the electrolytic set-up used in the Nd-Fe alloy preparation</i>	222
7.13	<i>Photograph of the Nd-Fe product obtained in our experiment.</i>	223
7.14	<i>EDXRF spectra of the obtained Nd-Fe product</i>	223
7.15	<i>Current efficiency obtained in the electrowinning of Nd-Fe alloy with varying CCD</i>	225

List of Tables

Table No.	Table Caption	Page No.
1.1	<i>Metallic use of La, Ce, Pr and Nd by application</i>	3
2.1	<i>Summary of major work carried out in the electrolysis of rare earth chlorides</i>	16
2.2	<i>Summary of major work carried out in oxide-fluoride electrolysis</i>	19
2.3	<i>Theoretical decomposition potential of chloride salts</i>	23
2.4	<i>Temperature dependant equation for the specific conductance ($\text{ohm}^{-1}\text{cm}^{-1}$) of LiCl-KCl and NaCl-KCl mixtures.</i>	25
2.5	<i>Temperature dependant equation for density (g cm^{-3}) for LiCl-KCl and NaCl-KCl mixtures.</i>	25
2.6	<i>Temperature dependant equation for viscosity (cp) of LiCl-KCl and NaCl-KCl mixtures.</i>	26
2.7	<i>Temperature dependant equation for surface tension (dyne cm^{-1}) for LiCl-KCl and NaCl-KCl mixtures.</i>	26
2.8	<i>Electrochemical data on reduction of La (III) in LiCl-KCl electrolyte.</i>	30
4.1	<i>Measured and calculated mass loss for different vaporization reaction steps in the dehydration of $\text{LaCl}_3 \cdot 7\text{H}_2\text{O}$.</i>	66

4.2	<i>Mass loss data for the step-I, step-II and step-III of the vaporization reactions(in the decomposition of $\text{LaCl}_3 \cdot 7\text{H}_2\text{O}$) measured at carrier gas flow rate of 2.4 l/h</i>	70
4.3	<i>Comparison of values of standard molar enthalpies and entropies for the vaporization reactions steps 1,2 and 3 .(in the decomposition of $\text{LaCl}_3 \cdot 7\text{H}_2\text{O}$)</i>	72
4.4	<i>Comparison of values of standard molar enthalpies of formation of $\text{LaCl}_3 \cdot 7\text{H}_2\text{O}(s)$, $\text{LaCl}_3 \cdot 3\text{H}_2\text{O}(s)$, $\text{LaCl}_3 \cdot \text{H}_2\text{O}(s)$.</i>	75
4.5	<i>Comparison of measured and calculated mass loss for different vaporization steps in the dehydration of $\text{CeCl}_3 \cdot 7\text{H}_2\text{O}$.</i>	77
4.6	<i>Mass loss data for the step-I, step-II, step-III and step-IV of the vaporization reactions measured at carrier gas flow rate of 2.5 l/h. (in the dehydration of $\text{CeCl}_3 \cdot 7\text{H}_2\text{O}$).</i>	81
4.7	<i>Values of standard molar enthalpies and entropies for the vaporization reactions steps 1,2 ,3 and 4.(in the dehydration of $\text{CeCl}_3 \cdot 7\text{H}_2\text{O}$)</i>	84
4.8	<i>Measured and calculated mass loss for different vaporization reaction steps in the dehydration of $\text{PrCl}_3 \cdot 7\text{H}_2\text{O}$.</i>	89
4.9	<i>Mass loss data for the step-I, step-II, step-III and step-IV of the vaporization reactions measured at carrier gas flow rate of 2.4 l/h (in the dehydration of $\text{PrCl}_3 \cdot 7\text{H}_2\text{O}$).</i>	91
4.10	<i>Values of standard molar enthalpies and entropies for the</i>	94

vaporization reactions.(in the dehydration of $\text{PrCl}_3 \cdot 7\text{H}_2\text{O}$)

4.11	Values of standard molar enthalpies of formation of $\text{PrCl}_3 \cdot X\text{H}_2\text{O}(s)$.	95
4.12	Measured and calculated mass loss for different vaporization reaction steps in the dehydration of $\text{NdCl}_3 \cdot 6\text{H}_2\text{O}$.	97
4.13	Mass loss data for the step-I, step-II, step-III and step-IV of the vaporization reactions measured at carrier gas flow rate of 2.38 l/h (in the dehydration of $\text{NdCl}_3 \cdot 6\text{H}_2\text{O}$).	103
4.14	Comparison of values of standard molar enthalpies and entropies for the vaporization reactions steps 1, 2 3 and 4. (in the dehydration of $\text{NdCl}_3 \cdot 6\text{H}_2\text{O}$).	106
4.15	Comparison of values of standard molar enthalpies of formation of $\text{NdCl}_3 \cdot X\text{H}_2\text{O}(s)$.	108
4.16	Equilibrium decomposition temperatures of $\text{RECl}_3 \cdot X\text{H}_2\text{O}$. (RE =La, Ce, Pr and Nd).	109
4.17	Enthalpy of formation of $\text{RECl}_3 \cdot X\text{H}_2\text{O}$ (RE =La, Ce, Pr and Nd)	110
4.18	Enthalpy of formation of $\text{RECl}_3 \cdot X\text{H}_2\text{O}$ (RE =La, Ce, Pr and Nd)	110
5.1	The value of 'no' obtained at three different temperatures for the reduction of La (III) in LiCl-KCl and NaCl-KCl melts.	128
5.2	Diffusion coefficient of La (III) evaluated in equimolar LiCl-KCl and NaCl-KCl melt at 973K.	129

5.3	<i>Determination of rate constant (K_s) for the reduction of La (III) employing Nicholson method.(in $\text{LaCl}_3\text{-LiCl-KCl}$ and $\text{LaCl}_3\text{-NaCl-KCl}$ melts)</i>	133
5.4	<i>Values of exchange current density and transfer coefficients estimated at various temperatures (For the reduction of La (III) in $\text{LaCl}_3\text{-LiCl-KCl}$ and $\text{LaCl}_3\text{-NaCl-KCl}$ melts).</i>	134
5.5	<i>Rate constant (K_s) values obtained for the reduction of Ce (III) employing Nicholson method in $\text{CeCl}_3\text{-LiCl-KCl}$ and $\text{CeCl}_3\text{-NaCl-KCl}$ melts) using Nicholson method</i>	142
5.6	<i>Diffusion coefficient of Ce (III) evaluated from different cyclic voltammetry technique in equimolar LiCl-KCl and NaCl-KCl melt.</i>	145
5.7	<i>Variation of diffusion coefficient of Ce (III) with the temperature and activation energy of the diffusion process in equimolar LiCl-KCl and NaCl-KCl melts.</i>	147
5.8	<i>Evaluation of exchange current density for the reduction of Ce (III) on Mo and W at various temperatures in $\text{CeCl}_3\text{-LiCl-KCl}$ and $\text{CeCl}_3\text{-NaCl-KCl}$ melts.</i>	150
5.9	<i>Diffusion coefficient of Pr (III) evaluated in equimolar LiCl-KCl and NaCl-KCl melt at 973K.</i>	159
5.10	<i>Values of exchange current density and transfer coefficients estimated at various temperatures. (For the reduction of Pr (III) in $\text{PrCl}_3\text{-LiCl-KCl}$ and $\text{PrCl}_3\text{-NaCl-KCl}$ melts).</i>	162

5.11	<i>Diffusion coefficient of Nd ions evaluated in equimolar LiCl-KCl and NaCl-KCl melt at 973K.</i>	170
5.12	<i>Values of exchange current density and transfer coefficients estimated at various temperatures (For the reduction of Nd ion in NdCl₃-LiCl-KCl and NdCl₃-NaCl-KCl melts).</i>	172
6.1	<i>Typical operating data in electrowinning of RE metal from RECl₃-LiCl-KCl and RECl₃-NaCl-KCl electrolytes in the study of temperature effect on current efficiency.</i>	186
6.2	<i>Typical operating data in the v electrowinning of re metal from RECl₃-LiCl-KCl and RECl₃-NaCl-KCl electrolytes in the study of electrolyte composition on current efficiency.</i>	188
6.3	<i>Typical operating data in electrowinning of RE metal from RECl₃-LiCl-KCl and RECl₃-NaCl-KCl electrolytes in the study of CCD effect on current efficiency.</i>	190
6.4	<i>Typical operating data for electrowinning of La metal from LaCl₃-LiCl-KCl and LaCl₃-NaCl-KCl electrolytes in the study of duration of electrolysis on current efficiency and yield.</i>	192
6.5	<i>Standardized parameters in the electrowinning of La, Ce, Pr and Nd metals in LiCl-KCl and NaCl-KCl carrier electrolytes.</i>	194
6.6	<i>Taguchi parameters and their levels</i>	196
6.7	<i>L9 Orthogonal array according to Taguchi method</i>	197
6.8	<i>Effect of each parameter on current efficiency</i>	197

6.9	<i>Solubility of RECl₃ in LiCl-KCl electrolyte measured at 1173 K.</i>	199
6.10	<i>Solubility of RECl₃ in NaCl-KCl electrolyte measured at 1173 K.</i>	200
6.11	<i>Comparison of current efficiency value in chloride (present study) and oxide-fluoride media (literature).</i>	201
7.1	<i>ICP-AES analysis of the obtained products with varying concentration of LaCl₃ and MgCl₂.</i>	208
7.2	<i>Current efficiency obtained with change in composition of electrolyte in the electrodeposition of La-Mg alloys.</i>	211
7.3	<i>Phases of products obtained in the electrolysis of LaCl₃-MgCl₂-LiCl-KCl electrolyte at 850⁰C temperature at cathode current density (CCD) of 10A/cm² for 3 hours duration.</i>	213
7.4	<i>ICP-AES analysis of the samples obtained in the electrolysis of LaCl₃-MgCl₂-LiCl-KCl electrolyte at 850⁰C temperature at cathode current density (CCD) of 10A/cm² for 3 hours duration.</i>	213
7.5	<i>Effect of electrolysis duration on composition of the alloy obtained in the melt containing 25wt% of LaCl₃ and 15wt% MgCl₂ at 850⁰C temperature at CCD of 10A/cm².</i>	213
7.6	<i>Current efficiency obtained with varying conc. Of NdCl₃ in the electrodeposition of Nd-Fe alloy using NdCl₃-NaCl-KCl electrolyte and Fe cathode.</i>	224

List of symbols

Symbols	Parameters/Variables	Unit
T	Temperature	K
t	Time	hr
v	Flow rate	l/h
β	Heating rate	$^{\circ}\text{C}/\text{min}$
$P_{\text{H}_2\text{O}}$	Vapor pressure of water	atm
$\Delta H^{\circ}_{\text{r}}$	Change in enthalpy for the reaction	kJ mol^{-1}
$\Delta S^{\circ}_{\text{r}}$	Change in entropy for the reaction	$\text{J mol}^{-1}\text{K}^{-1}$
$\Delta_{\text{f}}G^{\circ}$	Gibbs free energy of formation of the compound	kJ mol^{-1}
$\Delta G^{\circ}_{\text{r}}$	Free energy change for the reaction	kJ/mol
K	Equilibrium constant	
$\Delta_{\text{f}}H^{\circ}$	Enthalpy of formation of the compound	kJ mol^{-1}
$\Delta_{\text{f}}S^{\circ}$	Entropy of formation of the compound	$\text{J mol}^{-1}\text{K}^{-1}$
I_{c}	Cathodic peak current	A
I_{a}	Anodic peak current	A

E_c^P	Cathodic peak potential	V
E_a^P	Anodic peak potential	V
ΔE_p	Difference between cathodic and anodic peak potential	V
v	Scan rate	$V s^{-1}$
I	Current	A
F	Faraday constant	Coulomb mol^{-1}
C	Concentration	$mol cm^{-3}$
D	Diffusion coefficient	$cm^2 s^{-1}$
D_0	Pre-exponential term	$cm^2 s^{-1}$
E_a	Activation energy	$kJ mol^{-1}$
R	Gas constant	$J mol^{-1} K^{-1}$
α	Transfer co-efficient	
n_α	Number of electrons involved in the reduction process	
K_s	Standard rate constant of electron transfer	$cm s^{-1}$
ΔE_p^{298}	Difference between cathodic and anodic peak potential at 298 K.	V

ΔE_p^T	Difference between cathodic and anodic peak potential at T K.	V
Ψ_{298}	Nicholson function at 298 K.	
Ψ_T	Nicholson function at T K.	
i_0	Exchange current density	$A\text{ cm}^{-2}$
η	Current efficiency	%
W	Mass of the metal deposited	g
e	Electrochemical equivalent of metal	g
e_{alloy}	Electrochemical equivalent of alloy	g
I	Current in the electrolysis process	A
T	Duration of electrolysis	hr
Q	Quantity of electricity passes	Col
e_{La}	Electrochemical equivalent of lanthanum	g
e_{Mg}	Electrochemical equivalent of magnesium.	g

INTRODUCTION

1.1 Back ground:

The term “Rare Earths” (RE) refers to the group of 17 metallic elements in the periodic table including the 15 lanthanides (La, $Z = 57$ to Lu, $Z = 71$), along with yttrium ($Z = 39$) and scandium ($Z = 21$) [1]. They possess unique set of physical and chemical properties that make them valuable for important industrial applications. Despite having the name “Rare Earth”, these elements are not so rare, as they have significant abundance in the Earth’s crust. Some of the rare earths such as cerium and yttrium are even more abundant than many common metals [2]. The word, ‘rare’ refer to the difficulty in isolating the metals from their ore [3,4]. These RE elements are divided into two sub-groups, i.e. light rare earth elements (LREEs) “cerium sub-group” and heavy rare earth elements (HREEs) “yttrium sub-group” [5,6].

Rare Earth metals find extensive uses in fields like in the production of clean energy, in electronic devices, aerospace and defense applications. Rare earth elements are essential for compact fluorescent lighting (CFLs) and LED lighting [7]. The use of rare earth in magnetic refrigeration [8] improves the energy efficiency of refrigerators and also reduces the emission of greenhouse gases. Rare earth elements are helpful in making high performance magnet which enable faster, smaller, and lighter products such as cell phones and computer hard drives. The luminescence properties of rare earths are employed to impart color in televisions and computer screens [9-13]. The powerful rare earth (REE) magnets also permit the miniaturization of products for use in loudspeakers, optical fibers, smart phones, and tablets [14]. Rare earth

elements (REEs) are key component in hybrid vehicles, which will become increasingly abundant on roads in coming years. Rare earth permanent magnets play an important role in new generation of automobile design to reduce energy consumption [15]. They are also found in catalytic converters in cars and can help in reducing harmful air pollutants. Rare earth based permanent magnets are suitable for defense applications such as jet fighter engines, missile guidance systems, antimissile defense, satellite and communication systems. Rare earth elements are also used for lasers and resolution technologies which is critical to modern aerospace systems [16-18]. The frontier technologies in transport and mass communication requires huge amount of rare earths. To meet the growing demand of rare earth based materials, better metallurgical technologies are required for the synthesis and engineering scale production of rare earth metals and their alloys in an efficient and economical way.

The present study deals with production of four light rare earth elements i.e. La, Ce, Pr and Nd. Among these metals 'La' finds applications in rechargeable nickel metal hydride (NiMH) battery. La-Ni alloy i.e. LaNi_5 can also be used as hydrogen storage [19]. Misch-metal which is a mixture of light rare earth elements (La, Ce, Pr, and Nd) can also be used in place of lanthanum for hydrogen storage [20]. Cerium metal is used as an additive in the metallurgical industry to increase the mechanical strength of the steel. Praseodymium is alloyed with magnesium to impart higher mechanical and good corrosion resistance properties in aircraft engines [21]. PrNi_5 exhibits a strong magneto caloric effect for the attainment of low temperature [22-23]. The most common rare earth magnets are based on Nd-Fe-B alloys. NdFeB magnets have the highest energy product ($\text{BH}_{\text{max}} > 440 \text{ kJ m}^3$) of all permanent magnets [24]. The uses of the light RE elements

are summarized in Table 1.1. Due to their extensive use and low availability, the demand for these light RE elements are increasing exponentially. This is creating huge pressure on the production of these metals economically.

REE application	La (%)	Ce (%)	Pr(%)	Nd(%)
Magnets			23.4	69.4
Battery alloys	50.0	33.4	3.3	10.0
Metallurgy	5.0	90.0		

Table 1.1 Metallic uses of La, Ce, Pr and Nd by application. Adapted from (Long et.al.2010) [25].

The light RE elements are generally found in the minerals bastansite and monazite which constitute majority of the world's total rare earth reserves.

The current methods for the extraction of light RE metals from their ores are efficient but not very convenient or economical. It is therefore, necessary to explore new processes and process modifications

1.2 Importance of rare earths to India:

In India, monazite is the principal source of rare earths containing 0.4 - 4.0% REO. India holds only 3% of the world reserves as compared to 36% by china and 13% by USA [26]. Establishment of rare earth metal industry to develop rare earth metals and alloys has special significance to India because of the availability of rich resource of monazite mineral. Existing rare earth plants in India are only producing individual rare earth oxide or chloride. At present, India is not producing on an industrial scale RE metals and alloys. Objective of this current work

is to investigate by molten salt electrolysis processes for the preparation of light rare earth metals and alloys because concentration of light rare earths in monazite, (India's primary rare earth resource) is high.

1.3 General Processing of RE minerals:

Processing REEs from mined ore is a very complex process and often varies considerably for different deposits. Initial step for ore processing typically include beneficiation process which does not alter the chemical composition of the ore; but helps to liberate the valuable mineral grains from the host lattice. Conventional physical separation methods such as electrostatic and magnetic separation, froth floatation and gravity separation are employed to concentrate rare earth minerals. The concentrated mineral is subsequently transformed into more valuable chemical forms through various thermal and chemical reactions known as cracking. The individual rare earth elements are selectively removed from the concentrated solution (mixed rare earth solution) and the step is known as separation step. Then last step is the reduction step where metal or alloy is produced from REO by reduction. Our focus is on the reduction process to prepare individual metal and alloys. General steps followed presently in the extractive metallurgy of rare earths are shown in Fig.1.1.

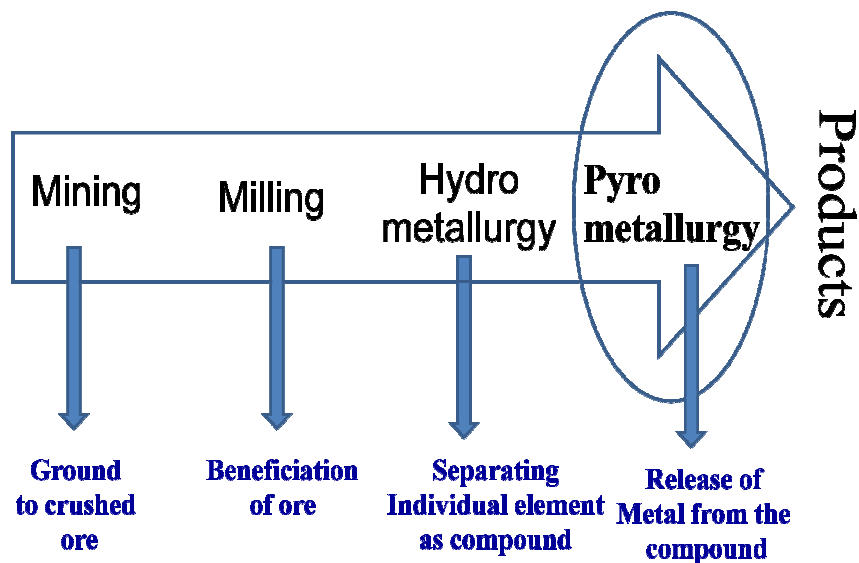


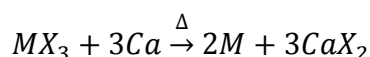
Fig.1.1 Steps of extractive metallurgy of REEs

1.4 Reduction of REEs

The separated REO is reduced to pure metal or alloy depending on the required end products. There are basically two methods employed for the preparation of rare earth metals from their separated oxide i.e. (i) molten salt electrolysis. (ii) Metallothermic reduction [27]. Results of this process are rare earth metals with 98- 99% purity. In the REEs supply chain, although many players are there in the market for the manufacturing of final products, but only few companies are there for mining and processing.

1.4.1 Metallothermic reduction process:

In the metallothermic reduction process, the most common approach is to prepare rare earth halide and then reduce it by calcium.



The purity of rare earth products using metallothermic processes depends on these preparation processes and reducing agents. Hence, the preparation processes are very critical in determining the quality of rare earth products.

1.4.2 Molten salt electrolysis process

In the molten salt electrolysis process, pure metal is deposited at the cathode by electrolytic decomposition of its compound dissolved in a molten salt media. The metallic salt which is to be reduced to the metal is known as functional electrolyte and the salt mixture which serves as a solvent for the metallic salt is known as the carrier electrolyte. These properties of carrier are normally obtained by using an alkali /alkaline earth fluoride or chloride or a mixture of these fluorides and chlorides.

1.4.3 Comparison between metallothermic-reduction and molten salt electrolysis in rare earth metal extraction

Although metallothermic reduction process is applicable for the production of most of the rare earth metals, but it has some limitations like small batch size and high operational cost. Molten salt electrolysis process for making rare earth metals offers an advantage of continuous operation over the batch mode of metallothermic reduction process [28]. Moreover molten salt electrolysis becomes particularly attractive for the extraction of light rare earth metals because their melting points facilitate their electrowinning in molten state [29]. There are two different types of molten salt electrolysis processes employed for the electrowinning of rare earth metals from molten salt media: (i) Chloride electrolysis (ii) Oxide-Fluoride electrolysis [6]. In oxide-fluoride system, low solubility of oxide in the fluoride salt and difficulty in controlling the material feed rate limit the easy implementation of this process [30]. Moreover, extreme corrosiveness of molten fluoride aggravates the problem of finding suitable container material. On the other hand, high solubility of rare earth chloride in molten alkali chlorides and low melting temperature of chloride salt

offers advantage over fluoride salt in the electrowinning process [31]. The major problem associated with the chloride electrolysis is low current efficiency and evolution of chlorine gas. These issues do not allow the widespread and easy implementation of this process.

1.5. Research Objectives

In the present work attempt has been made to increase the current efficiency in the extraction of light rare earth metals by molten chloride electrolysis process.

Purity of the starting material plays important in the production pure metals with high yield. Presence of oxychloride, in particular, reduces the efficiency of metal production in the chloride electrolysis process. The use of pure starting material, free of moisture and oxychloride is a prime a concern in the electrolysis process. Effective removal of adsorbed water responsible the formation of oxychloride is necessary to improve the yield of the metal. In this work detail investigations has been carried to establish procedure for the production of anhydrous RECl_3 salt free from oxychloride.

The other objective of this study is to analyze the behavior of RE metal ions in alkali chloride melts to determine the mechanism and kinetics of their deposition in the electrochemical reduction process. Understanding the mechanism of electrolytic process will help improving the yield and current efficiency of the electrolytic process.

The electrowinning of rare earth metal is an energy intensive process. There are many factors involve in the design of the cell to achieve high efficiency in the process. These include type of material of construction, shape of anode and cathode, collection of deposited material etc. The aim here is to develop a cell design for the electrowinning of RE metals in batch mode which may transform into continuous mode afterwards. There are various process parameters which also affect the current efficiency in the electrowinning process. These include temperature of

operation, composition of electrolyte and current density. One of the major aims of this present investigation is to suggest optimized process parameters for the electrowinning of all the four above mentioned metals and alloys.

Another objective of the present investigation is to study the possibility of in the extraction of rare earth alloys using molten chloride electrolysis. Here the aim was to explore two techniques (i) co-deposition technique and (ii) consumable cathode technique for the production of alloy.

1.6 Contribution from the thesis:

The contributions from the present study are

- 1- Determination of thermodynamic stability of RECl_3 hydrates (RE = La, Ce, Pr and Nd)
- 2- Establishment of easy and effective dehydration procedure
- 3- Determination of mechanism and kinetics of the electrochemical deposition of RE (La, Ce, Pr and Nd) metals in two molten chloride electrolytes i.e. LiCl-KCl and NaCl-KCl.
- 4- Establishment of reduction mechanism and estimation of kinetic parameters in the reduction of RE (III) ions in both LiCl-KCl and NaCl-KCl molten salt mixture.
- 5- Establishment of improved process parameters in the electrowinning of La, Ce, Pr and Nd metal in bulk scale with good current efficiency and yield
- 6- Determination of mechanism of La-Mg and Nd-Fe alloy formation by electrochemical co-deposition and consumable cathode technique respectively. Establishment of optimum conditions in the bulk preparation of these alloys.

LITERATURE REVIEW

2.1 Introduction

The present thesis focuses on improvement in the extraction efficiency of light rare earth metals i.e. La, Ce, Pr and Nd and alloys i.e. La-Mg and Nd-Fe by molten chloride electrolysis process. The first part of this chapter discusses about the methods available for the preparation of rare earth metals and advantage of molten salt electrowinning in the synthesis of light rare earth metals. Brief description about molten chloride salts are discussed in the subsequent portion. Literature data regarding physical properties of LiCl-KCl and NaCl-KCl mixture were also presented in this part.

The second part of this chapter describes about the different procedures available for the preparation of anhydrous rare earth chloride evaluating their advantages and disadvantages. The subsequent portions of the second part describes the previous work done on the mechanism of the dehydration of $RECl_3 \cdot XH_2O$ (RE= La, Ce, Pr and Nd). The detail thermodynamic investigation of $RECl_3$ hydrates carried out in this study are given in Chapter-IV.

Third part in this chapter discusses about the previous studies conducted on electrochemical investigations of RE (La, Ce, Pr & Nd) ions molten chloride electrolytes. The electroreduction mechanism and determination kinetic parameters are described in details in Chapter-V.

Literatures available in the design of the cell and effect of process parameters on current efficiency in the electrowinning of rare earth metals are presented in the fourth part of this chapter. Studies conducted to optimize these parameters to get high current efficiency are discussed in chapter-VI.

The next portions of this chapter review the previous work done on the preparation of alloys by molten chloride electrolysis route by using electrochemical co-deposition and consumable cathode techniques with specific reference to La-Mg alloy and Nd-Fe alloy. The mechanism and bulk preparation of the alloys are discussed in details in Chapter-VII.

2.2 Methods available for extraction of rare earth metals:

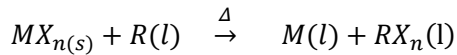
Rare earth (RE) metals are usually extracted from their corresponding oxides, fluorides and chlorides by reduction process. These compounds (RE oxides, fluorides and chlorides) are so stable that it is difficult to reduce them by carbon and hydrogen and therefore require stronger reducing agent. Only two methods found suitable for the reduction of rare earth compounds to obtain pure metal. i.e. (i) Metallothermic reduction (ii) Electrowinning.

2.2.1 Metallothermic reduction process:

Use of metal in the reduction process to get pure metal is usually called as metallothermic reduction process. RE oxides, fluorides and chlorides are employed in the metallothermic reduction processes to get pure metal. Calcium metal is found suitable in the reduction of RE_2O_3 and $RECl_3$. [32]. This process is called calciothermic reduction process. Similarly lanthanum is used as reductant in the reduction of RE oxides and the process called lanthanothermic reduction process. RE metals with high vapor pressure i.e. Sm, Eu, Tm and Yb are usually prepared employing lanthanothermic reduction method.

Basic fundamentals behind reduction process

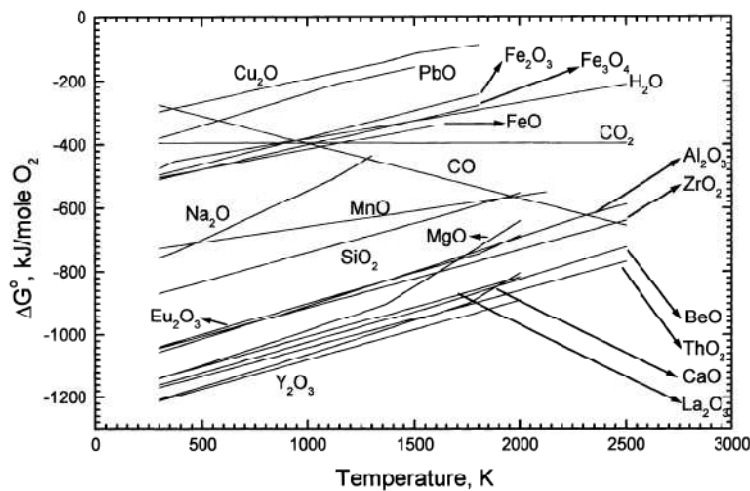
The process of liberation of a metal from its compound by reduction process can be represented by equation:



M is the rare earth metal to be obtained from reduction process, X may be either oxygen or halide atoms (chlorine or fluorine), R is reductant predominantly Ca and in some cases La. The above reaction is feasible only when, the change in free energy for the reaction is negative i.e.

$$\{\Delta_f G^0(RX_n) + \Delta_f G^0(M)\} - \{\Delta_f G^0(MX_n) + \Delta_f G^0(R)\} \leq 0$$

In order to find suitable metal for the reduction of RE metal oxides, chlorides and fluorides, the free energy versus temperature diagram (Ellingham diagram) for oxides fluorides and chlorides were searched. Fig.2.1, 2.2 and 2.3 show the standard free energy of formation of certain RE oxides, fluorides and chlorides respectively with certain common metals as a function of



temperature.

Fig.2.1 Standard free energy of formation of selected oxides of rare earths and certain common metals as a function of temperature.

Source: C. K. Gupta, N. Krishnamurthy, Extractive Metallurgy of Rare Earths, (2005) CRC Press pp-196.

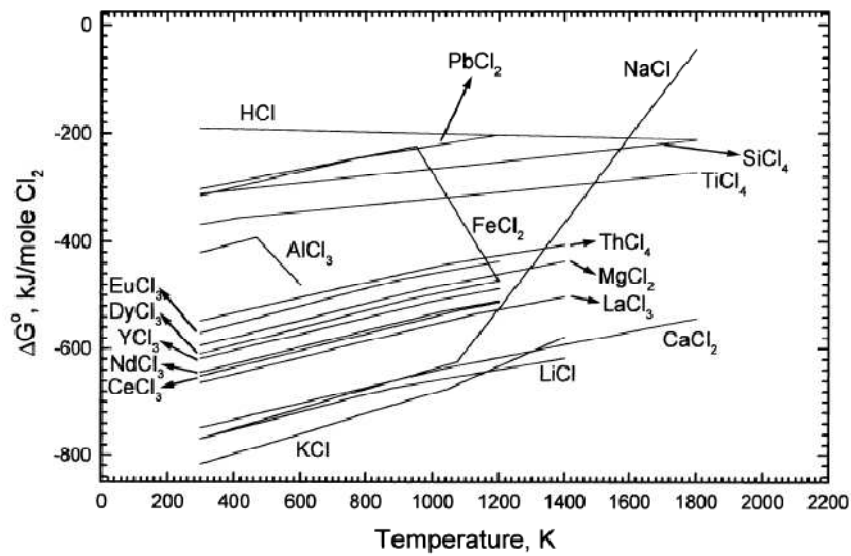


Fig.2.2 Standard free energy of formation of selected chlorides of rare earths and certain common metals as a function of temperature. Source: C.K.Gupta, N. Krishnamurthy, Extractive Metallurgy of Rare Earths, (2005) CRC Press pp-198

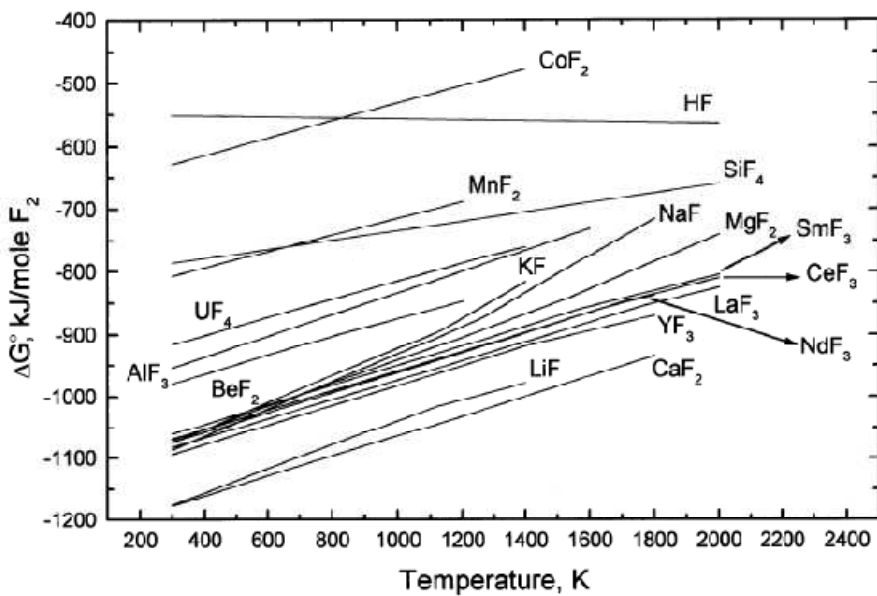


Fig.2.3 Standard free energy of formation of selected fluorides of rare earths and certain common metals as a function of temperature. Source: C. K.Gupta, N. Krishnamurthy, Extractive Metallurgy of Rare Earths, (2005) CRC Press pp-198

From the above Ellingham diagrams, it can be seen rare earth oxide and fluoride can be reduced only by calcium metal where as rare earth chloride can be reduced either by alkali metals (Na, K and Li) or by calcium metal.

2.2.1.1 Reduction of rare earth oxide:

Although Gibbs free energy for the reduction reaction evident from the Ellingham diagram qualifies calcium as suitable reductant for the reduction of REO, but the high melting point of CaO makes the process less efficient in making pure metal. In such cases, the heat evolved in the reaction is not sufficient to melt the products for better slag metal separation. Hence, rare earth metals found dispersed in the slag matrix. Therefore, oxide reduction of rare earth is rather used for the preparation of alloy than making of pure metal. In this method, neodymium metal has been produced by reacting Nd_2O_3 by calcium in molten $\text{CaCl}_2\text{-NaCl}$ bath, at about 800°C and extracting Nd metal as Nd-Zn or Nd-Fe alloy [33]. Calciothermic reduction of rare earth is also used for the preparation of Sm-Co and Nd-Fe-B alloy powder by reduction-diffusion process [34, 35]. It is also used for the preparation of RE-Ni alloy etc [36].

Reduction of REO by lanthanum is useful in the preparation of rare earth metals with high vapor pressure like Sm, Eu, Tm and Yb [37]. The oxides of these RE metals were reduced by lanthanum granules under high vacuum in the temperature zone of $1400\text{-}1600^\circ\text{C}$ [38]. Due to the difference in vapor pressure, the metal was distilled leaving La_2O_3 . In the process, lanthanum forms La_2O_3 which is non volatile in the operating temperature.

2.2.1.2 Reduction of rare earth fluoride:

The advantage of fluoride reduction process is the high metal yield due to the liberation of large amount of heat during the process. The greater stability and lower vapor pressure of CaF_2

permitted to increase the reduction temperature up to 1700⁰C. Therefore, it is possible to prepare Er, Ho, Dy, Tb and Tm in consolidated form by fluoride reduction process. On the other hand, the disadvantage is the high cost of RE_F₃ chemicals. This process was proved to be expensive due to the batch mode of operation and also due to the high cost of reductant (Ca) and container material [6]. Usually tantalum is used as container material to reduce the contamination [39]. Temperature required for the fluoride reduction process is sometimes reduced through the formation of an intermediate low melting alloy [40]. All the rare earth metals except Sm, Eu, Yb and Tm can be prepared by calciothermic reduction of RE_F₃.

2.2.1.3 Reduction of rare earth chloride:

The chloride reduction process is best suited for the extraction of rare earth metal having low melting temperature. This process cannot be applied to higher melting metal because excessive chloride volatilization during separation which reduces yield. This problem could be overcome by resorting to preparation of low melting alloys [41].

2.2.2 Electrolytic production of rare earth metals

Electrolytic reduction offers an effective alternate method for the synthesis of rare earth metals and alloys. Electrowinning of these metals in the aqueous solution is not possible due to the preferential reduction of hydrogen at cathode prior to the reduction of dissolved rare earth compound. Thus, electrolysis using molten salt media remains the preferred option for the electrowinning of rare earth metals.

Molten salt electrowinning of rare earth metal has a definite advantage over chemical reduction because large scale production of metal by electrolytic reduction is more economic than metallothermic reduction process.

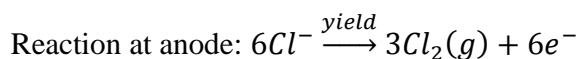
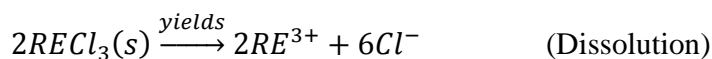
In the molten salt electrolysis process, pure metal is deposited at the cathode by electrolytic decomposition of its compound dissolved in a molten salt media. The metallic salt which is to be reduced to extract the metal is known as functional electrolyte and the salt mixture which serves as a solvent for the metallic salt is known as the carrier electrolyte. The carrier electrolyte should have suitable properties like (i) high solubility for the functional electrolyte (ii) greater stability at working temperature than functional electrolyte (iii) suitable physiochemical properties like low melting point, high conductivity and low viscosity and vapor pressure. These properties are normally obtained from alkali /alkaline earth fluoride or chloride or from the mixture of these fluorides and chlorides.

There are two different types of molten salt electrolysis processes employed for the electrowinning of rare earth metals from molten salt media: (i) Chloride electrolysis (ii) Oxide-Fluoride electrolysis.

2.2.2.1 Chloride electrolysis:

Chlorides system is suitable to produce the rare earth metals or their alloys with low melting point. The RE metals including La, Ce, Pr, and some mixed rare earth metal alloys have been produced from the chloride system. The disadvantages for the chlorides electrolysis lie in high hygroscopic and volatile nature of electrolyte which eventually results into the low current efficiency of the process.

Electrowinning in chloride salt is represented by following equation



The major work carried on the electrolysis of rare earth chlorides are summarized in the Table-2.1.

Year	Electrolyte	Electrodes	Cell	Product	Ref
1875	RECl ₃ -NaCl-KCl	Fe	Porcelain	Ce, La and Di	[42]
1902	RECl ₃ -NaCl-KCl	C	Water cooled Cu	Ce, La nodule	[43]
				Fail to produce Pr	[44]
1912	CeCl ₃ -NaCl-KCl- BaCl ₂	Graphite(A) Cell (C)	Iron	Ce	[45]
1923	LaCl ₃ -KF-NaCl	Carbon(A) W (C)	Iron	La metal	[46]
1926	RECl ₃ -KCl	Graphite(C) Graphite(A)		La, Ce, Pr, Nd ,Sm	[51]
1931	CeCl ₃ -CaF ₂	Carbon (A) Mo(C)	Fluorspar	Ce ingot	[52]
1940	RECl ₃ -NaCl-KCl	Graphite (A) Fe (C)	Refractory lining	La, Ce, Di, Misch metal	[47-50]
1961	LaCl ₃ -KCl	Graphite (A) Mo (C)	Ni can	La	[53]
1986	NdCl ₃ -LiCl-LiF	Graphite (A) W (C)	alumina	Nd	[54]
1986	RECl ₃ -NaCl-KCl RECl ₃ -LiCl-KCl	Graphite (A) Mo (C)	Inconel	Ce	[55]

Table-2.1 Summary of major work carried out in the electrolysis of rare earth chlorides

The electrolytic preparation of rare earth metal was first reported by Hillenbrand and Norton in 1875 [42]. This work is followed by Muthenana et.al [43] who produced several pounds of cerium, lanthanum and small quantity of neodymium metal using water cooled copper container with carbon as electrodes. But, they failed to prepare praseodymium employing the same method reportedly due to the formation of oxychloride [44]. A few years later Hirsh [45] synthesized huge amount of cerium employing graphite anode and iron cathode. Metals obtained in all these methods were not very pure due to contamination from cathode materials.

To reduce the contamination from electrode, Kremers et.al. [46] prepared lanthanum in LaCl_3 - NaCl - KF electrolytic bath using W cathode. They also produced La, Ce and Di using Fe cathode in a refractory line cell [47-50]. Metals obtained from above process were found to have Fe impurities. Small quantity of Ce, La, Pr, Nd and Sm were prepared by Schumacher using graphite crucible, graphite anode [51]. Later Trombay prepared high purity RE metal in a bath containing CeCl_3 - KCl - CeF_3 electrolyte using graphite anode and molybdenum cathode [52].

Lanthanum metal with purity around 98-99% was obtained by electrolysis of LaCl_3 - KCl at 900°C [53]. Preparation of neodymium metal was demonstrated in ceramic refractory cell using Fe cathode and graphite anode [54]. Singh et.al. [55] demonstrated the production of capability of cerium metal in LiCl - KCl and NaCl - KCl molten salt.

Advantage

1. High solubility of RECl_3 in chloride electrolyte.
2. Low cost of chloride chemicals makes the process more economic
3. The corrosion of cell material is comparatively low due to lower temperature of operation.

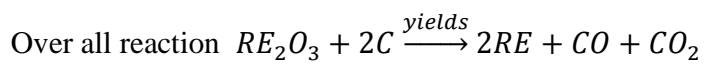
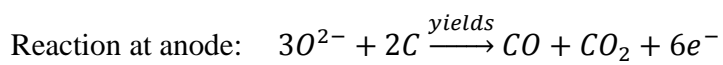
Disadvantage:

1. Chloride electrolyte system is unsuitable to produce high melting point rare earth metal.

2.2.2.2 Oxide-Fluoride electrolysis:

In the oxide-Fluoride electrolysis, functional electrolyte is RE_2O_3 and the carrier electrolyte is mixture of REF_3 and alkali or alkaline earth fluorides.

Electrolytic reaction in this process can be represented as:



The major work carried out on electrodeposition of metal in oxide-fluoride electrolysis is summarized in the Table-2.2.

Year	Electrolyte	Electrode	collector	product	Ref
1907	CeO ₂ -CeF ₃	Carbon(C)	Water cooled Cu	Ce	[56]
1951	CeO ₂ -CeF ₃ -LiF-BaF ₂	Graphite(A) Mo (C)	Mo crucible	Ce	[57]
1960	CeO ₂ -CeF ₃ -LiF-BaF ₂	Carbon (A) Mo (C)	Electrolyte skull	Ce	[58]
1962	La ₂ O ₃ -LaF ₃ -LiF-BaF ₂	Carbon (A) Mo (C)	Electrolyte skull	La	[59]
1964	Ce ₂ O ₃ -CeF ₃ -LiF-BaF ₂	Graphite(A) Mo (C)	Mo liner	Ce	[60]
1966	RE ₂ O ₃ -REF ₃ -LiF	Graphite(A) W (C)	Electrolyte skull	Dy,Y,Gd	[61]
1967	Nd ₂ O ₃ -NdF ₃ -LiF	Graphite(A) W (C)	Electrolyte skull	Nd	[62]
1980	Gd ₂ O ₃ -GdF ₃ -LiF	Graphite (C) Graphite (A)	Electrolyte skull	Gd	[63]

Table-2.2 Summary of major work carried out in oxide-fluoride electrolysis

In oxide-fluoride electrolysis, muthanan [56] was first to prepare Ce metal by electrolysis of CeO₂ in molten CeF₃. Grey [57] studied the process and was able to make pure cerium metal by electrolyzing CeO₂ at 880-890°C in the molten bath of CeF₃-LiF-BaF₂. Then Morrice in 1960 [58] was able to achieve a good current efficiency in the above mentioned process. He also prepared lanthanum metal in an electrolytic bath of LaF₃-LiF-BaF₂-La₂O₃ with current efficiency of 60%. Here electrolysis was carried out in an inert atmosphere at 950°C using carbon anode and molybdenum cathode. The container was a graphite crucible and the metal was collected in a

skull of frozen electrolyte. Later comparatively good yield was achieved by this process with careful control of oxide feed rate and atmosphere [59].

Cerium was prepared in kilogram quantity by continuous operation of the electrolytic bath containing $\text{REF}_3\text{-LiF-BaF}_2$. Metals were electrowon on Mo/W substrates and tapped into an inert casting chamber [60]. Shedd et.al. [61] in 1966 established the electrode geometry, oxide feed rate and optimum operating parameters for electrowinning of La metal.

High pure Nd, Pr and Di were electrowon from fluoride bath with good current efficiency where the operation was carried out under protective gas cover [62]. Preparation of Gadolinium in dendrite form was also reported by the electrolysis of Gd_2O_3 dissolved in a fluoride bath at a temperature lower than 1000°C [63].

Advantage

1. Oxide-fluoride electrolysis process is suitable to produce high melting point rare earth metal.
2. The current efficiency in this process is better than chloride electrolysis
3. Chance of emission of greenhouse gas at anode is less.

Disadvantage:

1. Low solubility of RE_2O_3 in fluoride electrolyte is a definite disadvantage
2. High cost of fluoride chemicals makes the process less economic
3. The corrosion of cell material is high due to high temperature of operation and also due to high reactivity of fluoride materials.

2.2.2.3 Current efficiency:

It was reported that current efficiency in chloride cell is usually low; in the range of 30-50%. The main cause for the low current efficiency is the presence of oxychloride present in the starting

material which is formed due to the reaction between chloride salt and water in the heating process [64]. Current efficiency also depends upon the other operational parameters like composition of electrolyte, temperature, current densities and impurities present in the salt.

Current efficiency of molten oxide-fluoride systems is better than chloride electrolysis process.

This was attributed to the high conductivity of fluoride salt and also due to the positive effect of F⁻ ion on the stability of higher +3 oxidation state of rare earth ion.

2.3 Reason for using chloride electrolytes

The major problems associated with oxide-fluoride systems are (i) High cost of fluoride chemicals (ii) high melting point (iii) extreme corrosiveness of fluoride salt and (iv) low solubility of oxide in fluoride. Chloride system was used in this study due to its inherent advantages like (i) low melting point (ii) low cost (iii) low corrosion rate compared to fluorides and (iv) high solubility of RECl₃ in molten alkali chlorides. Moreover, the lower melting point of chloride electrolytes enables the cell to be operated at temperature significantly above the melting point, where solubility of functional electrolyte (RECl₃) in solvent increases. The major objective of this work is to study various aspects in chloride electrolysis to get higher current efficiency in the electrodeposition of light rare earth metals and alloys and also to design an effective way for the efficient neutralization or reuse of chlorine gas generated at anode.

2.4 Electrolytes properties for chloride electrolysis

Molten salt is defined as a salt which is solid at ambient temperature and enters into liquid phase at elevated temperature. A molten salt has a low viscosity, high heat capacity, and high electric and thermal conductivity. This electrolyte is used for some applications like transferring heat in solar tower, as a catalyst in coal gasification, in a molten salt reactor. It is used for extraction of metals such as: aluminum, titanium, magnesium and rare earths by electrolysis. As the molten

salts are solid at room temperature, heat is required to raise the temperature above its melting point to ensure the system in molten state. Usually molten salts are ionic compounds which have high melting point. The high melting temperature of the molten salt requires more heat to come to the molten state. Therefore, mixture of molten salt system is usually preferred to lower the melting temperature of the system in order to reduce the energy consumption. A mixture of salts generally possesses a lower melting point than a single salt system. Therefore, lower heat will be needed to maintain molten state, which leads to cost efficiency. Binary and ternary systems are used as molten salt to satisfy the requirement of viscosity, density, conductivity and melting point of the molten salt. It was found that mixture of alkali or alkaline metal earth chlorides are fulfilling most of these properties.

The most important criteria for the carrier electrolyte are its decomposition potential which should be more than the decomposition potential of the functional electrolyte. The salt which decomposes to metal in the electrolysis process is called functional electrolyte and the mixture of salts which acts as solvent to dissolve the functional electrolyte is called carrier electrolyte. Table-2.3 gives the theoretical decomposition potentials of chloride salts. From the Table, it is evident that Li (Na, K, Rb, Cs) Cl or Be (Mg, Ca) Cl₂ are suitable for carrier (supporting) electrolyte. Between alkali and alkaline earth metal chlorides, alkali metal chlorides are preferred as it is difficult to get alkaline earth chlorides in anhydrous form. In order to achieve low melting point, eutectic mixture of LiCl-KCl and NaCl-KCl are usually employed as solvent for the electrowinning of RE metals. Electrodeposition of rare earth metal in different composition of LiCl-KCl and NaCl-KCl melts are not found in the literature. In this study, equimolar composition of electrolyte will be used to study its effect on current efficiency and yield. Equimolar composition of LiCl-KCl helps in more economic deposition of RE metals

because the amount of LiCl (which is more costly) require for the electrolysis is less in equimolar composition to that of eutectic composition. The phase diagram for LiCl-KCl and NaCl-KCl are presented in Fig.2.4 and 2.5. The temperature dependent equation of the physical parameters like specific conductance, density, viscosity and surface tension of both LiCl-KCl and NaCl-KCl are presented in Table-2.4 to 2.7 [65]. This provides an idea about the properties of different compositions of electrolyte.

Compound	Temperature / K			
	676	873	1073	1273
	Decomposition Potential, E/V			
LiCl	3.66	3.49	3.37	3.26
NaCl	3.61	3.42	3.24	3.14
KCl	3.86	3.66	3.48	3.35
RbCl	3.84	3.65	3.48	3.35
CsCl	3.90	3.71	3.56	3.43
BeCl ₂	2.04	1.92	1.81	1.72
MgCl ₂	2.77	2.61	2.47	2.36
CaCl ₂	3.59	3.44	3.29	3.17
SrCl ₂	3.74	3.59	3.44	3.31
BaCl ₂	3.90	3.74	3.58	3.43
LaCl ₃	3.12	2.96	2.81	2.68
CeCl ₃	3.06	2.90	2.75	2.63
PrCl ₃	3.07	2.91	2.76	2.64
NdCl ₃	3.03	2.87	2.72	2.60

Table-2.3 Theoretical decomposition potential of chloride salts

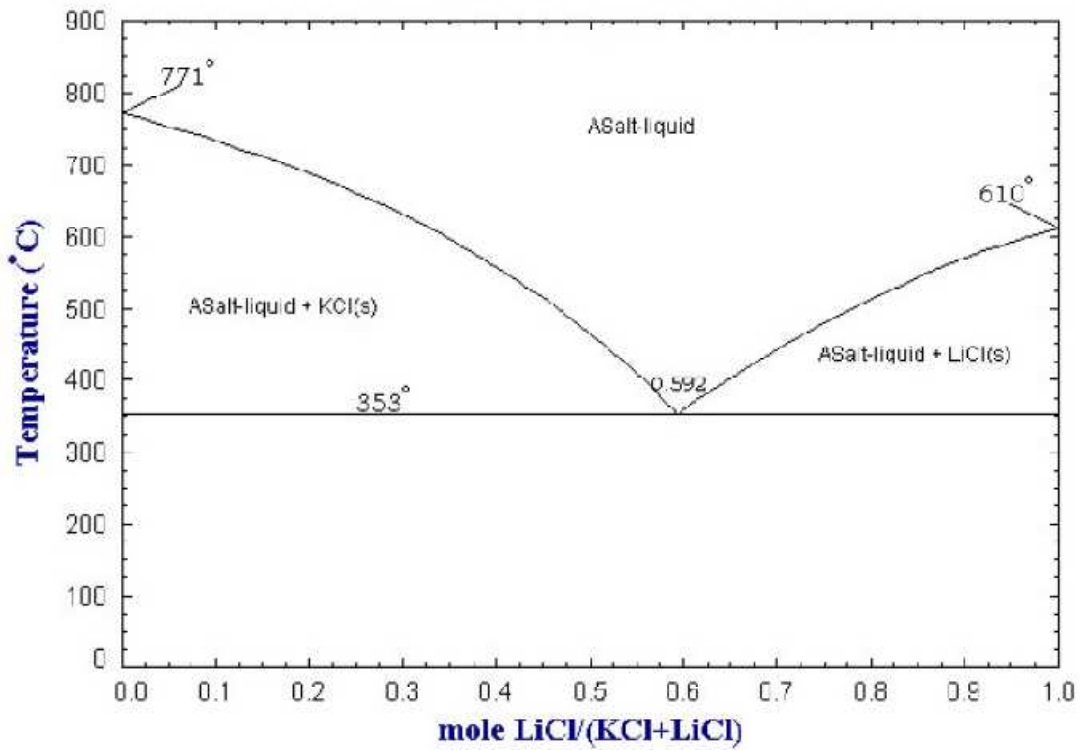


Fig.2.4 Phase diagram of LiCl-KCl [66]

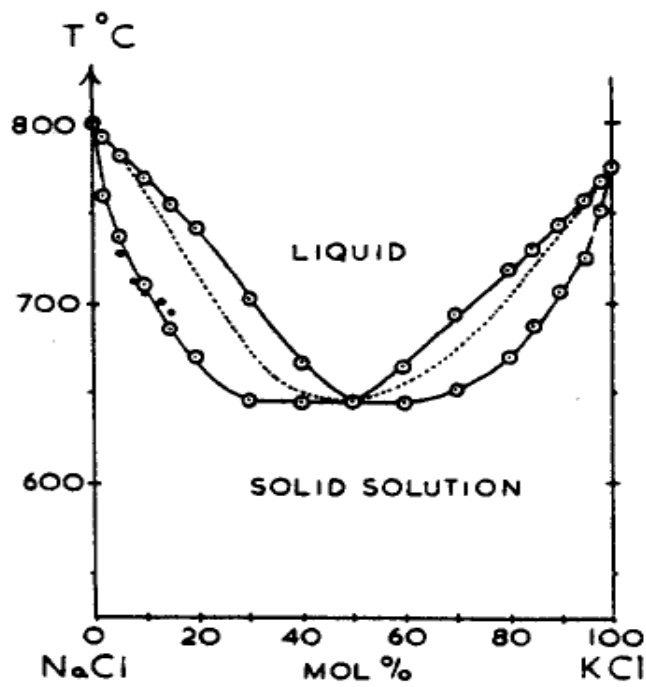


Fig.2.5 Phase diagram of NaCl-KCl melt [67]

LiCl-KCl			NaCl-KCl				
$\kappa = a + bT + cT^2$			$\kappa = a + bT + cT^2$				
Mole% LiCl	a	$b \times 10^2$	$C \times 10^6$	Mole% NaCl	a	$b \times 10^2$	$C \times 10^6$
0	-5.5231	1.1714	-4.1800	0	-5.5231	1.1714	-4.180
19.96	-5.9678	1.2866	-4.7560	20.4	-2.9567	0.7386	-2.270
40.45	-8.5932	1.8845	-7.8109	41.0	-6.3093	1.3765	-5.147
58.80	-5.6492	1.3732	-5.1788	51.23	-3.3119	0.8380	-2.641
70.36	-11.0108	2.7461	-13.2471	65.15	-3.1690	0.8265	-2.477
81.77	-6.7217	1.8182	-7.4002	84.77	-1.3797	0.5656	-1.274
100	-7.3766	2.2747	-9.0623	100	-2.2356	0.7783	-2.118

Table-2.4 Temperature dependant equation for the specific conductance ($\text{ohm}^{-1}\text{cm}^{-1}$) of LiCl-KCl and NaCl-KCl mixtures.

LiCl-KCl			NaCl-KCl		
$\rho = a + bT$			$\rho = a + bT$		
Mole% LiCl	a	$b \times 10^4$	Mole% NaCl	a	$b \times 10^4$
0	2.1376	-5.8445	0	2.1376	-5.8445
19.96	2.1172	-5.7764	20.4	2.1377	-5.8127
40.45	2.0768	-5.6120	41.0	2.1342	-5.7477
58.80	2.0286	-5.2676	51.23	2.1314	-5.6793
70.36	1.9945	-5.0738	65.15	2.1338	-5.5749
81.77	1.9689	-4.8908	84.77	2.1400	-5.5381
100	1.8832	-4.3182	100	2.1365	-5.4042

Table-2.5 Temperature dependant equation for density (g cm^{-3}) for LiCl-KCl and NaCl-KCl mixtures.

LiCl-KCl					NaCl-KCl				
$\eta = a + bT + cT^2 + dT^3$					$\eta = a + bT + cT^2 + dT^3$				
Mole% LiCl	a	b $\times 10^2$	C $\times 10^6$	d $\times 10^9$	Mole% NaCl	a	b $\times 10^2$	C $\times 10^6$	d $\times 10^9$
0	13.55	-2.00	7.86	0	0	1.70	1.58	-27.72	11.58
20					20.75	14.13	-1.90	5.07	1.29
30					41	11.64	-1.16	-1.94	3.41
40					51.23	18.35	-2.56	7.17	1.69
60	-8.51	-0.74	-4.86	4.81	65.15	16.27	-2.02	3.02	2.58
80					84.77	15.24	-1.49	-3.37	4.91
100	10.01	-0.51	-13.02	9.29	100				

Table-2.6 Temperature dependant equation for viscosity (cp) of LiCl-KCl and NaCl-KCl mixtures.

LiCl-KCl			NaCl-KCl		
$\gamma = a + bT$			$\gamma = a + bT$		
Mole% LiCl	a	b $\times 10^2$	Mole% NaCl	a	b $\times 10^2$
10	187.45	-8.309	10	178.1	-7.5
22	196.22	-9.16	25	178.0	-7.4
40	189.47	-8.45	40	177.0	-7.2
50	187.34	-8.08	50	179.3	-7.2
58	189.56	-8.23	60	180.4	-7.2
79	183.53	-7.10	75	181.2	-7.0
90	183.38	-6.75	90	183.5	-6.8

Table-2.7 Temperature dependant equation for surface tension (dyne cm⁻¹) for LiCl-KCl and NaCl-KCl mixtures.

2.5 Method for the production of anhydrous rare earth chloride:

The success in the chloride winning process depends upon the quality of raw material available for the extraction. Presence of impurities and moisture in the starting RE chlorides adversely affect the electrolysis process. Therefore, preparation of anhydrous $RECl_3$ is extremely important for the better efficiency of the process. Generally, anhydrous rare earth chlorides have been prepared from rare earth oxides using chlorinating agents like Cl_2 gas [68], $SOCl_2(g)$ [69], $CCl_4(g)$ [70], $COCl_2(g)$ [71] and $NH_4Cl(s)$ [72]. These chlorinating agents are corrosive at operating temperature of 600-700°C. Therefore, it is difficult to find suitable construction material for the design of reaction vessel. Hence, these methods are not suitable for the large production of anhydrous rare earth chlorides. Moreover, the high cost of these chlorinating agents make these process more expensive. Nolting et al. [73] (1960) reported preparation of $YCl_3 \cdot 6H_2O$ by dissolving yttrium oxide in concentrated hydrochloric acid and evaporating the solution up to crystallization. Various researchers have followed this method to prepare RE chloride for the electrolysis work [74].

Although the method of chlorination using HCl solution produce $RECl_3 \cdot XH_2O$ which needs dehydration to prepare anhydrous chloride, this method is simple and attractive for the industrial production of rare earth metal [75]. The next step is the dehydration of rare earth chloride hydrates. Various techniques i.e. (i) dehydration in presence of HCl vapor, (ii) in presence ammonium chloride and (iii) vacuum dehydration were found in the literature for the proper dehydration of $RECl_3 \cdot XH_2O$. Dehydration in presence of hydrogen chloride was found to be slow and tedious [76]. Although the rare earth chloride prepared in presence of NH_4Cl was free from any impurities, the metal obtained using this chloride was found to contaminate with

nitrogen [77-78]. Therefore, the vacuum dehydration method was found to be more suitable for the preparation of anhydrous rare earth chloride [79].

It is important to study the mechanism of dehydration relevant in fixing the condition for the dehydration of rare earth chloride hydrates. The mechanism of dehydration of hydrated rare earth chloride has been studied by many researchers [80-88].

In the mechanism of dehydration of $\text{LaCl}_3 \cdot \text{XH}_2\text{O}$, Powel and Burkholder [82] reported the existence of intermediates such as $\text{LaCl}_3 \cdot 3\text{H}_2\text{O}(\text{s})$ and $\text{LaCl}_3 \cdot \text{H}_2\text{O}(\text{s})$. The decomposition pattern of $\text{LaCl}_3 \cdot 7\text{H}_2\text{O}$ due to loss of water reported by Ashcroft and Mortimer [83] was found to $\text{LaCl}_3 \cdot 7\text{H}_2\text{O}(\text{s}) \rightarrow \text{LaCl}_3 \cdot 3\text{H}_2\text{O}(\text{s}) \rightarrow \text{LaCl}_3 \cdot 2\text{H}_2\text{O} \rightarrow \text{LaCl}_3 \cdot \text{H}_2\text{O}(\text{s}) \rightarrow \text{LaCl}_3(\text{s})$. Hong and Sundstrom [84] have shown the dehydration scheme as $\text{LaCl}_3 \cdot 7\text{H}_2\text{O}(\text{s}) \rightarrow \text{LaCl}_3 \cdot 3\text{H}_2\text{O}(\text{s}) \rightarrow \text{LaCl}_3 \cdot \text{H}_2\text{O}(\text{s}) \rightarrow \text{LaCl}_3(\text{s})$. GuahaoRen [85] have described the dehydration scheme of $\text{LaCl}_3 \cdot 7\text{H}_2\text{O}(\text{s})$ with the following steps: $\text{LaCl}_3 \cdot 7\text{H}_2\text{O}(\text{s}) \rightarrow \text{LaCl}_3 \cdot 6\text{H}_2\text{O}(\text{s}) \rightarrow \text{LaCl}_3 \cdot 3\text{H}_2\text{O}(\text{s}) \rightarrow \text{LaCl}_3 \cdot \text{H}_2\text{O} \rightarrow \text{LaCl}_3(\text{s})$ and also have reported that dehydration at higher temperature lead to formation of small amount of $\text{LaOCl}(\text{s})$.

The decomposition pattern of $\text{CeCl}_3 \cdot 7\text{H}_2\text{O}$ due to loss of water reported by Ashcroft and Mortimer [83] was found to $\text{CeCl}_3 \cdot 7\text{H}_2\text{O}(\text{s}) \rightarrow \text{CeCl}_3 \cdot 3\text{H}_2\text{O}(\text{s}) \rightarrow \text{CeCl}_3 \cdot 2\text{H}_2\text{O} \rightarrow \text{CeCl}_3 \cdot \text{H}_2\text{O}(\text{s}) \rightarrow \text{CeCl}_3(\text{s})$. V.V. Hong [84] reported the similar dehydration scheme of $\text{CeCl}_3 \cdot 7\text{H}_2\text{O}$.

The decomposition pattern of $\text{PrCl}_3 \cdot 7\text{H}_2\text{O}$ due to loss of water reported by Ashcroft and Mortimer [83] was found to $\text{PrCl}_3 \cdot 7\text{H}_2\text{O}(\text{s}) \rightarrow \text{PrCl}_3 \cdot 3\text{H}_2\text{O}(\text{s}) \rightarrow \text{PrCl}_3 \cdot 2\text{H}_2\text{O} \rightarrow \text{PrCl}_3 \cdot \text{H}_2\text{O}(\text{s}) \rightarrow \text{PrCl}_3(\text{s})$. V. V. Hong [84] reported the dehydration scheme as with following steps: $\text{PrCl}_3 \cdot 7\text{H}_2\text{O}(\text{s}) \rightarrow \text{PrCl}_3 \cdot 6\text{H}_2\text{O}(\text{s}) \rightarrow \text{PrCl}_3 \cdot 3\text{H}_2\text{O}(\text{s}) \rightarrow \text{PrCl}_3 \cdot \text{H}_2\text{O} \rightarrow \text{PrCl}_3(\text{s})$.

The decomposition pattern of $\text{NdCl}_3 \cdot 6\text{H}_2\text{O}$ due to loss of water reported by Kipouros and Sharma [86] was found to $\text{NdCl}_3 \cdot 6\text{H}_2\text{O}(\text{s}) \rightarrow \text{NdCl}_3 \cdot 5\text{H}_2\text{O}(\text{s}) \rightarrow \text{NdCl}_3 \cdot 4\text{H}_2\text{O} \rightarrow \text{NdCl}_3 \cdot \text{H}_2\text{O}(\text{s}) \rightarrow \text{NdCl}_3(\text{s})$. However, [87-88] have described the following dehydration scheme for $\text{NdCl}_3 \cdot 6\text{H}_2\text{O}(\text{s})$: $\text{NdCl}_3 \cdot 6\text{H}_2\text{O}(\text{s}) \rightarrow \text{NdCl}_3 \cdot 3\text{H}_2\text{O}(\text{s}) \rightarrow \text{NdCl}_3 \cdot 2\text{H}_2\text{O}(\text{s}) \rightarrow \text{NdCl}_3 \cdot \text{H}_2\text{O} \rightarrow \text{NdCl}_3(\text{s})$.

It is evident that mechanisms reported by previous researchers are not consistent. Moreover, data on thermodynamic stability of rare earth chloride hydrates are not available in the literature. Therefore questions like sequence of decomposition reactions in the dehydration of RECl_3 hydrates, and conditions to prevent oxy-chloride formation during dehydration process have remained unanswered. A systematic study on the decomposition mechanism and thermodynamic stability of $\text{RECl}_3 \cdot \text{XH}_2\text{O}$ are required to answer the above questions.

2.6 Kinetic parameters in the electrodeposition of RE (III) in molten alkali chloride melt:

Studies on electrochemical behavior of rare earths (RE) ions in molten chloride medium are important for the effective use of molten salt electrolysis technology in the extraction of RE metals. Many investigations have been carried out on electrochemical behavior of RE (La, Ce, Pr and Nd) ions molten chloride electrolytes [89-102]. Electrochemical data reported by these researchers are not consistent. For example, discrepancies on the data reported on reduction of La (III) have been highlighted in Table-2.8.

Researchers	D/10 ⁵ (cm ² s ⁻¹) At 723 K	Reversibility	Exchange current density (Acm ⁻²)
Y. Motto	0.72	-	-
F. Lantelme	1.47	-	-
Y. Catrillejo	1.17	Quasi-Reversible	-
P. Masset	0.8	-	-
Gao	0.67	Reversible to quasi reversible	-
Vandrakuzhali	1.16	Quasi reversible to irreversible	-
Tang	1.70	Quasi reversible	0.023

Table-2.8 Electrochemical data on reduction of La (III) in LiCl-KCl electrolyte.

The data reported for the reduction of Ce (III) and Pr (III) in LiCl-KCl molten salt is also found to be inconsistent. Apart from this, the temperature range studied in all the previous work is in between 650 to 850K which is much less than operational temperature in preparing rare earth metal by molten salt electrolysis process. Information on the exchange current for the reduction reaction RE (III)/RE (0) is rarely found in the literature. Moreover, electrochemical data of the reduction of RE (III) in NaCl-KCl are also not available in literature. Therefore, investigation on electrochemical behavior of RE (III) ions both in LiCl-KCl and NaCl-KCl melt on inert electrodes at higher operational temperatures are required to get the inherent mechanism and kinetics of electrochemical process.

In the present study, higher operational temperature will be used to probe the mechanism and to determine the kinetic parameters like diffusion coefficient and exchange current densities which are important and relevant in the formation of RE metal by electrochemical deposition from molten salts mixtures. Higher operational temperature will also allow us to compare the kinetic parameters of the electrochemical process in LiCl-KCl medium with that of NaCl-KCl medium.

2.7 Bulk preparation of rare earth metals:

Cell design is important in the electrowinning of metal to get high current efficiency which reduces the power consumption. Many researchers have suggested a number of cell designs for electrowinning of rare earth metals using molten chloride electrolytes [13-26]. Some of the important factors indicated in the extraction of RE metals are mentioned below

- 1- Provision of inert atmosphere within the cell.
- 2- High anodic to cathodic area to prevent anode effect.
- 3- Provision of collecting metal.
- 4- Arrangement for the removal of chlorine gas as soon as it forms.

Due to the high reactivity of rare earth metal, it is difficult to find suitable material for cathode, anode and cell for the electrolysis process. Tantalum, tungsten and molybdenum are found to be suitable for cathode as they do not form any alloy with the rare earth metal at operating temperature [103]. These materials are not suitable to be used as anode because these metals are highly reactive to chlorine gas. Graphite is widely accepted material for anode but cannot be used as cathode as it forms carbide with rare earth metals at operating temperature. The detail of cell design used in this present investigation is discussed in details chapter-VI.

In the actual electrowinning process, various factors including temperature, current density (for both cathode and anode), and duration of electrolysis affect the outcome of the product. Limited reports are found on the effect of these parameters in the electrowinning of lanthanum and cerium metal, in NaCl-KCl electrolytes [55, 74] but there is no data available on electrowinning of praseodymium and neodymium metal in molten chloride medium. It is therefore necessary to establish the optimum operating conditions for the electrowinning of four rare earth metals (La, Ce, Pr and Nd) and also to develop a method for effective neutralization of

chlorine gas. In this study, operational parameters have been verified maximize the current efficiency and yield for each of the four rare earth metal and also develop a method for the neutralization of chlorine gas. Experiments will, also be carried out to observe the effect of using single carrier electrolyte like KCl, NaCl and LiCl in preparing rare earth metal.

2.8 Recovery of rare earth alloys:

2.8.1 Electrochemical codeposition technique:

The electrolytic codeposition method involves simultaneous deposition of two ions in the electrolyte on the cathode. Several investigators [104-106] in the past have reported the formation of alloys like Co-Sn, Sm-Co and La-Co alloys by electrochemical codeposition in the molten salt media. Soare and co workers [107] investigated the electrochemical preparation of Mg-Nd alloy in molten oxy-fluoride media. Recently Cao et al. [108-109] succeeded in preparing Mg-Li-La alloys from LiCl-KCl-MgCl₂-LaCl₃ and LiCl-KCl-KF-MgCl₂-La₂O₃ melts. They carried out basic electrochemical studies to know the reduction behavior of lanthanum and magnesium ions in the chloride electrolyte. However, no information is available on the electrodeposition of pure La-Mg alloys required for various industrial applications. Therefore, in this study preparation of La-Mg alloy using LaCl₃-MgCl₂-KCl electrolyte was undertaken.

Here basic electrochemical study will be carried out to investigate the mechanism of co-reduction of Mg (II) and La (III) ions at lower operating temperature first. After verifying the feasibility of formation, bulk scale preparation of alloys will be carried out and also process parameters will be standardized to get maximum current efficiency.

2.8.2 Consumable cathode technique:

In this technique, cathode is solid at operating temperature which forms alloy in the liquid form with the electrodeposited rare earth metal. The previous works on electrodeposition of alloy employing consumable cathode technique were mostly carried out using fluoride as electrolyte. Rare earth alloys with Fe, Cr, Ni and Co were successfully prepared from the electrolysis of the bath comprising of $\text{REF}_3\text{-LiF-BaF}_2$ on consumable cathode [110-111]. Limited information is available in the deposition of RE alloys using chloride electrolysis. The preparation of neodymium-iron alloys has been reported by molten salt electrolysis of $\text{NdCl}_3\text{-KCl}$ bath using a consumable iron cathode [112]. The current efficiency reported here was low. Therefore, preparation of Nd-Fe alloy in NaCl-KCl molten chloride was undertaken with an aim to increase current efficiency and yield.

2.9 Scope of present thesis:

Several aspects like dehydration of process, kinetics of the electrode process, cell design, and effect of operational parameters in the extraction of light rare earth metals (i.e. La, Ce, Pr and Nd) from their corresponding chlorides by molten salt electrolysis process have been investigated in order to get maximum production efficiency.

Rare earth chlorides which are used as electrolytic precursor material in synthesis of rare earth metals and alloys are highly hygroscopic in nature. Finding a suitable and efficient way of dehydration is extremely important for the success of electrowinning process. The thermodynamic parameters provide useful information's in fixing the conditions for a desirable reaction to happen. In the present work, the equilibrium vapor pressure of water over various hydrates was measured employing dynamic transpiration technique. The standard molar Gibbs energy of formation of RE chloride hydrates have been derived using the measured equilibrium

vapor pressure data. This information is useful in fixing the conditions for dehydration of $\text{RECl}_3 \cdot x\text{H}_2\text{O}(\text{s})$ to form $\text{RECl}_3(\text{s})$ free of oxychloride.

Extensive research has not been carried out on behavior of RECl_3 (LaCl_3 , CeCl_3 , PrCl_3 , NdCl_3) in LiCl-KCl and NaCl-KCl electrolytes to know the mechanism and kinetics of the electro deposition of rare earth metal from these melts. Studies related to electro-kinetic parameters such as electron transfer co-efficient, electron transfer rate constant, diffusion co-efficient have been carried out to draw more insight into the process.

One of the major objectives of this current investigation was to determine the optimum operating conditions for the electrowinning of light rare earth metals from their corresponding chlorides in alkali chloride melts i.e. (i) LiCl-KCl and (ii) NaCl-KCl melts. Process parameters like temperature of operation, electrolytic composition and cathode current densities have been standardized to get maximum current efficiency and yield.

Electrochemical deposition in molten salt has been proven as an effective and economic way in producing RE alloys. Electrodeposition of two alloys namely La-Mg and Nd-Fe were studied by co-deposition and consumable cathode technique respectively. The electrochemistry and mechanism of the deposition process were studied by cyclic voltammetry, and open circuit potentiometry etc. The effects of various process parameters such as composition of electrolyte in the bath, temperature of electrolysis and cathode current density on current efficiency have been investigated to get maximum current efficiency in both the cases.

INSTRUMENTATIONS

3.1 Introduction:

This chapter deals with the various experimental techniques employed for the synthesis, characterization of metals and alloys. Various characterization techniques were used for the characterizations. They are as follows: Energy Dispersive X-ray-Fluorescence (EDXRF), X-Ray Diffraction (XRD), Scanning Electron Microscopy (SEM), Thermo Gravimetric Analysis (TGA), Differential Thermal Analysis (DTA), Differential Scanning Calorimetry (DSC), Evolved Gas Analysis (EGA) and Inductively Coupled Plasma-Atomic Emission Spectroscopy (ICP-AES). Electrochemical techniques like cyclic voltammetry and square wave voltammetry were also used in the study.

3.2 X-Ray Fluorescence Spectrometry

The X-ray fluorescence spectrometry is generally used for qualitative and quantitative determination of elemental composition. It is based on the principle of measurement of the energies or wavelengths of the X-ray spectral lines emitted from the sample, which are the characteristic or signature of the elements present in the sample. H.G.J. Mosley in 1913 discovered the relationship of photon energy and element [113] and laid down the basis of XRF. X-rays are proportional to the atomic number (Z). X-ray spectra originate from the inner orbitals, which are not affected substantially by the valency of the atom; normally the emitted X-ray lines are independent of the chemical state of the atom. However, in the case of low and medium atomic number elements, the energy of the characteristic X-rays depends on oxidation state.

In XRF, the primary beam from an X-ray source (or electrons or charged particles) irradiates the specimen thereby exciting each chemical element. These elements in turn emit secondary X-ray spectral lines having their characteristic energies or wavelengths in the X-ray region of the electromagnetic spectrum. The intensities of these emitted characteristic X-rays are proportional to the corresponding elemental concentrations. Since the X-rays penetrate to about 100 μm depth of the surface of the sample, XRF is near surface characterization technique. This method of elemental analysis is fast and has applications in a variety of fields. This technique has also got sample versatility as sample in the form of solid, liquids, slurry, powder, etc. can be analyzed with little or no sample preparation. In most cases, XRF is a non-destructive/non-consumptive technique. All elements having atomic number $Z > 11$ (Na) can be detected and analyzed in conventional XRF. But, nowadays, with the advances in the XRF instrumentation, like use of very thin or windowless tubes and detectors, multilayer analyzer crystals, reduction in the path length of X-rays (tube – to sample and sample – to- detector) and application of vacuum or helium atmosphere, elements up to B ($Z=6$) can be detected and quantified [114]. Further, with the development of synchrotron radiation technology, a vast improvement in terms of detection limits has been obtained by tuning of the excitation energies [115]. XRF method has a large dynamic range, sensitive up to microgram per gram level and is considerably precise and accurate. For these reasons, XRF has become a well established method of analysis. It has got a variety of applications in industries of material production, quality control laboratories, scientific research centers, environmental monitoring, medical, geological and forensic laboratories [116-119]. There are two major modes of analysis in X-ray spectrometry: Wavelength Dispersive X-Ray Fluorescence (WDXRF) and Energy Dispersive X-Ray Fluorescence (EDXRF) Spectrometry. The difference in these two modes of analysis lies in the detection component. In EDXRF, the detectors directly measures the energy of the X-rays with the help of multichannel analyzer, whereas in WDXRF, the X-rays emitted from the samples are dispersed spatially using a dispersion crystal and wavelength of the each emitted X-rays is

determined by the detector sequentially. Here, we will only discuss about the ED-XRF technique which was used in the present investigation.

3.2.1 Energy Dispersive X-Ray Fluorescence (EDXRF)

In Energy dispersive X-Ray fluorescence (EDXRF), the wavelengths of all the elements emitted by the specimen are not dispersed spatially prior to detection, but the detector receives the un-dispersed beam. The detector itself separates the different energies of the beam on the basis of their average pulse heights. Energy dispersive spectrometer consists of three basic units:

- (a) Excitation source,
- (b) Sample holder unit and
- (c) Detection system

In XRF spectrometers, X-ray beam emitted from X-ray tube or radioisotope sources. In tube excited XRF systems, the energy distribution of the spectrum arriving from the sample depends on the tube target element, voltage and current applied. Standard commercial EDXRF spectrometer comprise of the following components: an X-ray tube, sample holder with auto sampler unit, solid state semiconductor detector Si (Li) with liquid nitrogen cooled detectors and the spectrometer electronics. Unfiltered direct excitation leads to a combination of both continuum and characteristic peak to fall on the sample. The spectrum shape can be altered by use of various filters and secondary targets present in the filter changer unit. Optimum selection of target, current, voltage and primary beam filter / secondary target are important in obtaining the best data from an EDXRF system. In XRF, primary beam filters are used to eliminate the scattered background drastically and improve the signal to noise ratio at the region of interest (ROI). Apart from this, it also reduces the dead time of the detector significantly [120]. All these features ultimately improve the detection limits. Schematic of EDXRF equipment is shown in Fig.3.1. In

the present investigation, EDXRF was carried out using EX-3600 M spectrometer from Xenometrix.

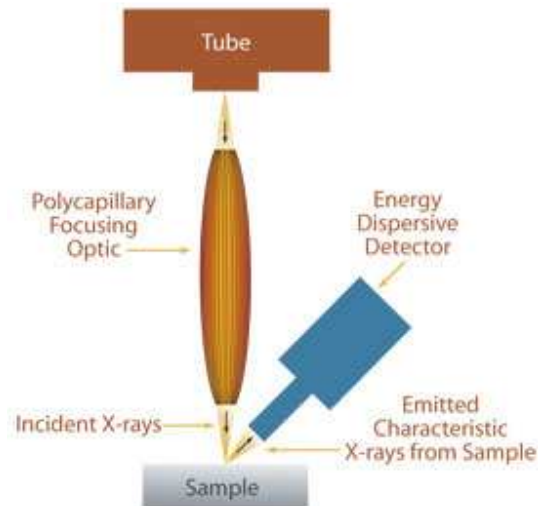


Fig.3.1 Schematic of ED-XRF equipment.

3.3 X-ray diffraction (XRD):

X-ray diffraction (XRD) is the most extensively used technique to identify the crystalline phases and to determine the crystal structures of condensed matter. It is the most commonly used technique for fingerprint characterization of the crystalline materials, as well as for determination of their unit cell, lattice parameters, phase and probable crystal structure. In our present study we have used the technique to identify the phase rare earth metals and alloys synthesized in the study.

The German physicist Max von Laue recognized that the wavelength of X-ray are comparable to the spacing between adjacent atoms in crystal and thus proposed that a crystal could be used as a diffraction grating in three dimensions. X-rays are electromagnetic radiation with typical photon

energies in the range of 100 eV - 100 keV. For the diffraction applications, only short wavelength X-rays (hard X-rays) in the range of a few angstroms to 0.1 angstrom (1 keV - 120 keV) are used. As the wavelength of X-rays is comparable to the size of atoms, they are ideally suited for probing the structural arrangement of atoms and molecules in a wide range of materials. The energetic X-rays can penetrate deep into the materials and provide information about the bulk structure.

The theory of diffraction is based on the Bragg's law, which describes how the electromagnetic waves of a certain wavelength λ interfere with a regular lattice. At a certain angle of incidence, also called as Bragg's angle (θ), with regard to a set of parallel crystal planes, which are, therefore, called reflectors, constructive interference take place according to the equation (3.1) where n is a positive integer, d_{hkl} represents the inter planer spacing between the crystal planes that cause constructive interference, and λ is the wavelength of the incident X-ray beam.

$$n\lambda = 2d \sin\theta \quad (3.1)$$

In XRD, the sample is irradiated by a monochromatic X-ray beam, which are generated by a cathode ray tube, by heating a filament to produce electrons, accelerating the electrons toward a target, by applying a voltage, and bombarding the target material (Cu, Fe, Mo, Cr) with the electrons. When the electrons have sufficient energy, to dislodge inner shell electrons of the target material, characteristic X-ray spectra are produced. The typical X-ray spectrum of elemental Cu is given in Fig. 3.2.

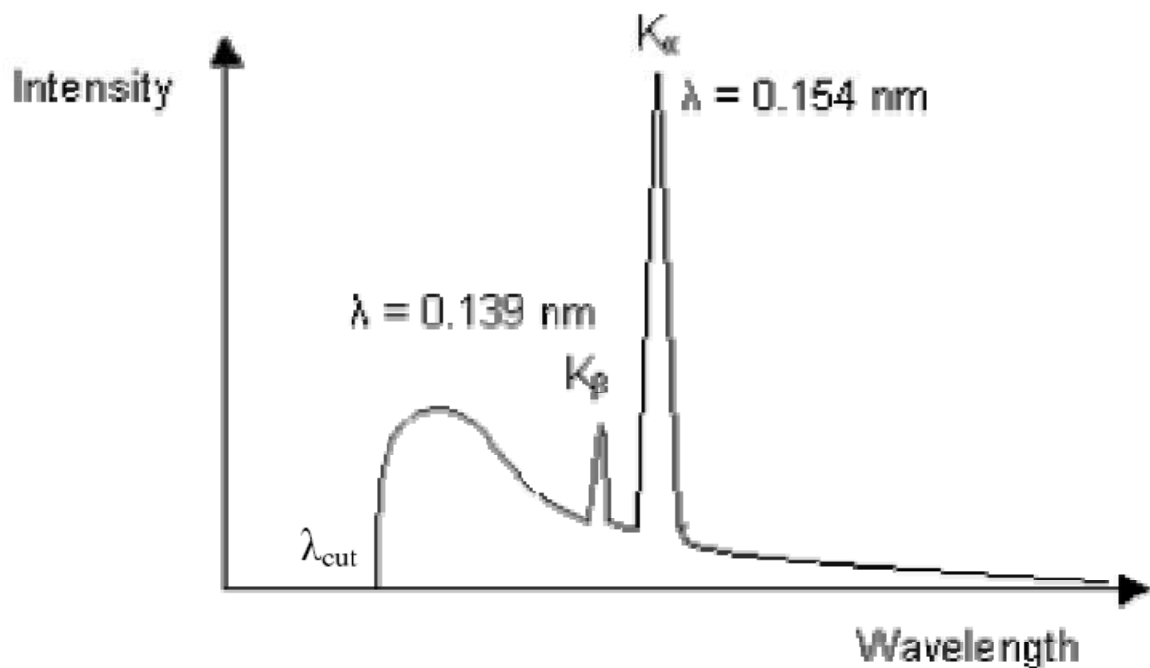


Fig.3.2 Typical X-ray of Cu target

Though the X-rays are produced in all the directions, it is allowed to escape from a particular direction (commonly using a beryllium window) for experiments. The background and radiations are filtered using β -filters. The beam of X-rays is passed through the divergence slits and then allowed to fall on the sample. The interaction of the incident rays with the sample produces constructive interference (and a diffracted ray), when conditions satisfy the Bragg's law. These diffracted X-rays are then detected, processed and counted. For the detection of X-ray, the gas filled tube or scintillation counters are commonly used. These tubes can either be the proportional counter or Geiger-Muller counter. This particular tube is usually filled with a gas, which gets ionized by the impact of the radiation. Applying a potential difference between the two electrodes, the ions are collected. The typical current obtained is proportional to the number of photons reaching to the detector. The diffracted rays are scanned by sweeping the detector

from one angle to another. By scanning the sample through a range of 2θ angles, all the possible diffraction directions of the lattice can be attained due to the random orientation of the powdered material. The conversion of the diffraction peaks to d-spacing allows identification of the material, because each material has a set of unique d-spacing. Typically, this is achieved by comparison of the d-spacing with the standard reference patterns. The intensity distribution of the peaks is governed by the nature and the kind of distribution of the atoms/ions in the unit cell. The absolute intensities of the peaks depend on the source intensity and counting time, in addition to the nature and the kind of distribution of the atoms/ions in the unit cell. A schematic diagram of XRD equipment is shown in Fig.3.3.

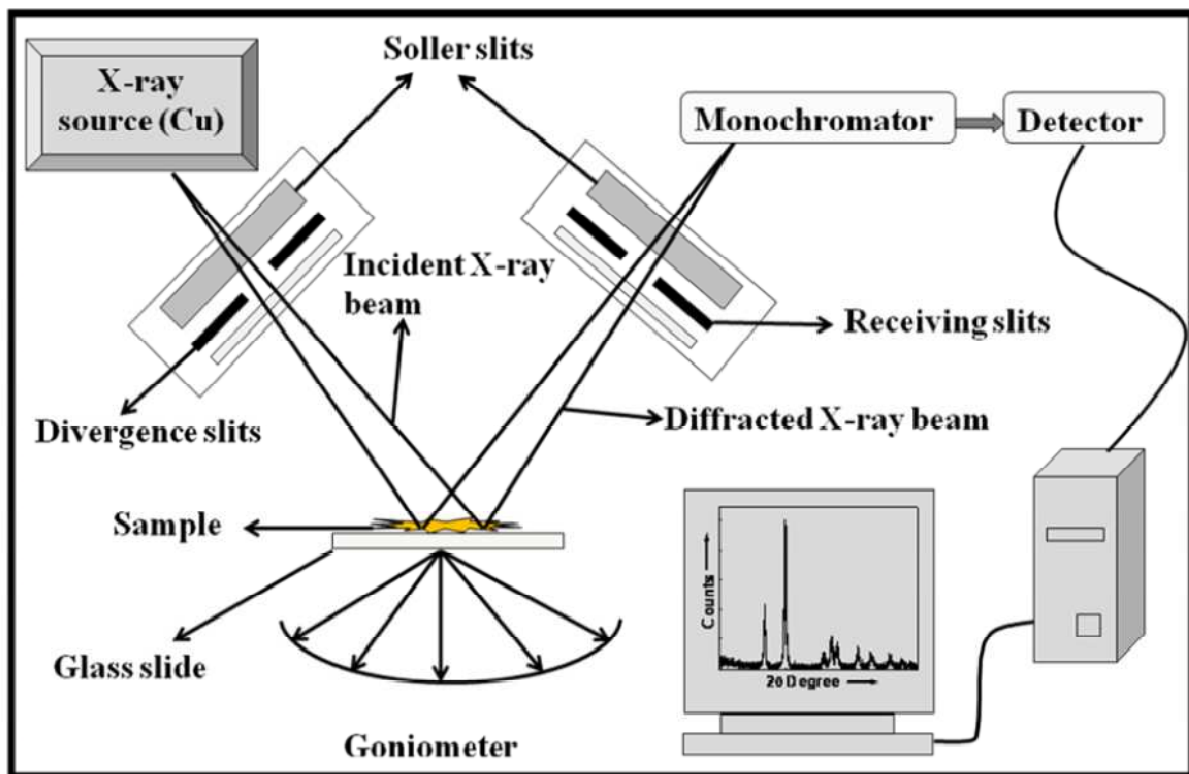


Fig.3.3 Schematic of a XRD equipment

The peaks (also called as reflections) in the plot correspond to a set of parallel planes with interplanar spacing d_{hkl} . The d-values are calculated from the position of the peaks. Thus, for a particular sample a set of d-values giving constructive interference is observed. The peak positions (d values) are related with the unit cell parameters of the lattice. Hence they can be used for identification of the materials and they generally act as the finger print for the crystalline materials. The intensity distribution of the reflections is governed by the nature and kind of distribution of atoms in the unit cell.

The data collection protocols often depend on the specific purpose of the data collections. In general a short time scan in the two-theta (2θ) range of 10 to 80° is sufficient for the identification of a well crystalline inorganic material. However, low symmetry samples and samples with not good X-ray scattering power may need a slow scan. The scan time was optimized for getting good intensity peaks. After the data collection, the observed d-values were fitted to standard patterns and the unit cell parameters were refined with respect to the standard values. By comparing the observed diffraction pattern with JCPDS (Joint Committee on Powder Diffraction Standards, 1974) files available for reported crystalline samples, fingerprinting of sample materials is normally done. The unit cell parameters are made free to adjusting the best way to fit the observed experimental data. The use and interpretation of the powder diffraction patterns are explained in several books [121-123]. In our study, XRD characterizations were carried out using Philips (Panalytical X-pert-pro) equipment.

3.4 Electron Microscopy:

Micro-structural characterization has become important for all types of materials as it give substantial information about the structure-property correlation. Micro-structural characterization broadly means ascertaining the morphology, identification of crystallographic defects and

composition of phases, estimating the particle size, etc. Electron microscopic techniques are extensively used for this purpose. Electron microscopy is based on the interaction between electrons (matter wave) and the sample. In the present study, Scanning Electron Microscopy (SEM) has been used to characterize the alloy powders. The principle and experimental details of the SEM technique is given below.

3.4.1 Scanning Electron Microscopy (SEM):

In a typical scanning electron microscope, a well-focused electron beam is incident and scanned over the sample surface by two pairs of electro-magnetic deflection coils. The signals generated from the surface by secondary electrons are detected and fed to a synchronously scanned cathode ray tube (CRT) as intensity modulating signals [124-125]. Thus, the specimen image is displayed on the CRT screen. Changes in the brightness represent changes of a particular property within the scanned area of the specimen. Schematic representation of SEM is shown in Fig.3.4.

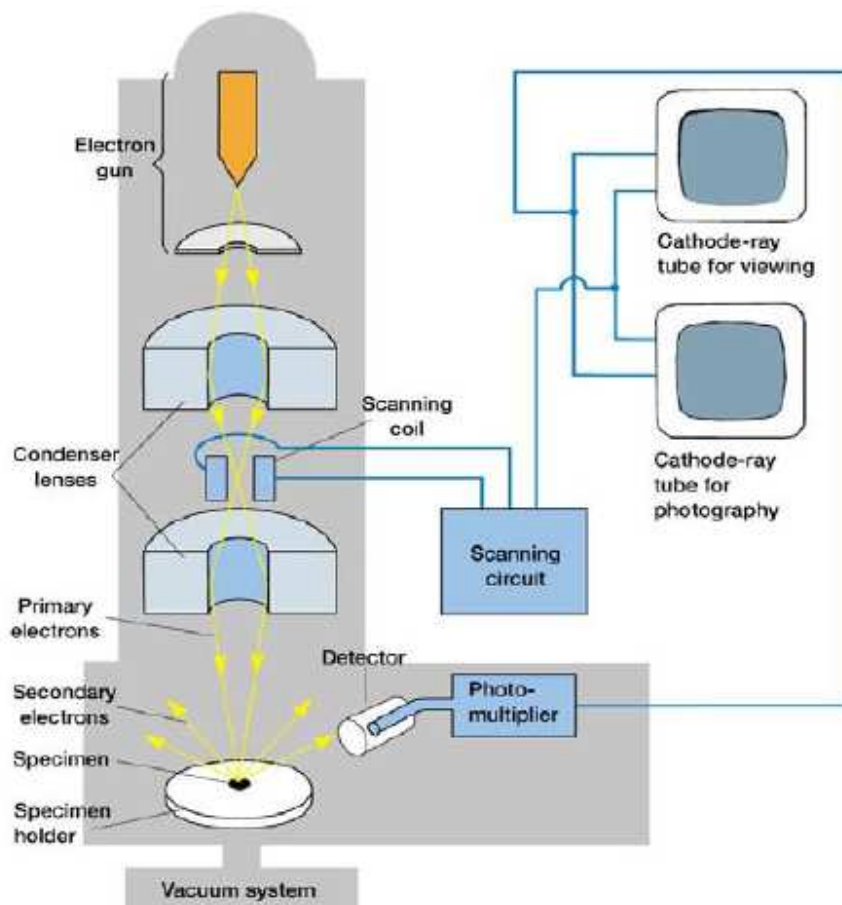


Fig.3.4 Schematic of SEM equipment

For carrying out SEM analysis, the sample must be vacuum compatible ($\sim 10^{-6}$ Torr or more) and electrically conducting. The surfaces of non-conductive materials are made conductive by coating with a thin film of gold or platinum or carbon. In this study, the SEM technique was used to study the microstructure evolution of rare earth metal and alloys. EDS (energy dispersive X-ray spectroscopy) was used for the compositional analysis.

In the present study, SEM instrument used was from Seron Inc. (Model AIS 2100) having standard tungsten filament. An accelerating voltage of 20 kV and magnification of 10kx was used for recording the micrographs.

3.5 Thermal analysis:

Thermal analysis methods are essential for understanding the compositional and heat changes involved during reaction. They are useful for investigating phase changes, decomposition, and loss of water or oxygen and for constructing phase diagrams.

3.5.1 Thermo gravimetric analysis (TGA):

In thermo gravimetric analysis the sample is heated at a constant heating rate and the sample weight is measured as function of temperature [126]. In this technique the heating can be done under air (oxidative) or nitrogen/argon (inert) atmosphere. Loss of water of crystallization or volatiles (such as oxygen, CO₂, etc.) is revealed by a weight loss. Oxidation or adsorption of gas shows up as a weight gain.

3.5.2 Differential thermal analysis (DTA):

Differential Thermal Analysis measures the temperature difference between a sample and a reference material as a function of temperature, when they are heated or cooled at a constant heating rate. A phase change is generally associated with either absorption or evolution of heat. In DTA experiments, the sample is placed in one cup, and a standard sample (like Al₂O₃) in the other cup. Both cups are heated at a controlled uniform rate in a furnace, and the difference in temperature (ΔT) between the two is monitored and recorded against time or temperature. Any reaction involving heat change in the sample will be represented as a peak in the plot of ΔT vs. T. Exothermic reactions give an increase in temperature, and endothermic reaction leads to a decrease in temperature and the corresponding peaks appear in opposite directions.

3.5.3 Differential Scanning Calorimetry (DSC)

Differential scanning calorimetric technique is quite similar to DTA, except that, it is an isothermal measurement. It means that, during the measurement the sample and reference

material are simultaneously heated or cooled at a constant rate just like DTA [127]. But here the amount of heat absorbed or released by a sample, to keep both the sample and reference at the same temperature is measured. In case of any exothermic/endothermic transition, the amount of heat flow from the system varies in order to keep both the sample and the reference at same temperature. The difference in temperature between them is proportional to the difference in heat flow (from the heating source i.e. furnace), between the two materials. This technique is applied to most of the polymers in evaluating the curing process of the thermoset materials as well as in determining the heat of melting and melting point of thermoplastic polymers, glass transition temperature (T_g), endothermic & exothermic behaviour. As desorption of hydrogen occurs with absorption of heat, so it can be detected for the endothermic peak of DSC. The instrumentation of DSC [Fig. 3.5] is exactly similar to that of DTA, except for the difference in obtaining the result.

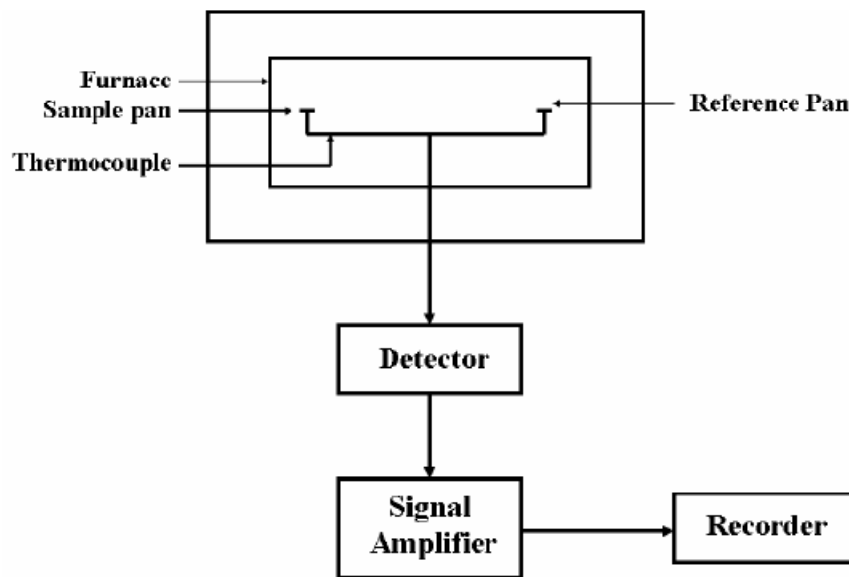


Fig.3.5 Schematic diagram of DTA/DSC

In the present study, thermo-gravimetric-differential thermal analysis (TG-DTA) of samples was carried out in platinum crucibles using a Setaram, 92-16.18 make TG-DTA instrument.

3.5.4 Evolved Gas Analysis

Evolved gas analysis (EGA) is a method used to study the gas evolved from a heated sample that undergoes decomposition. The identification of the compound is performed by mass spectrometry, Fourier transform spectroscopy, gas chromatography, or Optical In-Situ Evolved Gas Analysis. Here, the gas analyzer used was a quadruple mass spectrometer to identify the emitted vapors at different temperatures and understand the underlying mechanism. In quadruple spectrometer, an electrical field is formed in the system. Ions of varying mass are shot axially into the system at approximately equal energy and move through the system at uniform velocity. The applied quadruple field deflects the ions in the X and Y directions, causing them to describe helical trajectories through the mass filter. Ions are separated by the m/e ration in the rod system and then detected at the detector. Here EGA study was carried out using QMS coupled to a TG-DTA, (model-SETSYS Evolution-1750, SETARAM).

3.6 Inductively coupled plasma atomic emission spectroscopy (ICP-AES)

ICP-AES is a spectral method used to determine very precisely the presence of metal analyte and the elemental concentration. There are numerous reports on utilization of this technique for analysis of rare earth elements [128-130]. ICP-AES analysis requires a sample to be in solution. It works by the emission of photons from analytes that are brought to an excited state by the use of high-energy plasma. The plasma source is induced when passing argon gas through an alternating electric field that is created by an inductively couple coil. A peristaltic pump delivers the sample into a nebulizer where it is atomized and introduced directly inside55the plasma

flame. When the analyte is excited, the electrons try to dissipate the induced energy by moving to a ground state of lower energy and in doing this they emit the excess energy in the form of light. The wavelength of light emitted depends on the energy gap between the excited energy level and the ground state and is thus specific to the element. In this way, the wavelength of light can be used to determine what elements are present by detection of the light at specific wavelengths. In order to determine the concentration of elements present, a calibration curve is developed using analyte solutions of known concentrations, whereby the intensity of the signal changes as a function of the concentration of the material that is present. When measuring the intensity from a sample of unknown concentration, the intensity from this sample can be compared with the calibration curve to determine the concentration of the analytes within the sample. An ICP-AES system can be divided up into two basic parts; the inductively coupled plasma source and the atomic emission spectrometry detector. Here ICP-AES analyses were carried out using high Ultima 2, Horiba Jobinyvon, France make high resolution ICP-AES. Figure 3-5 shows the common components of an ICP-AES system.

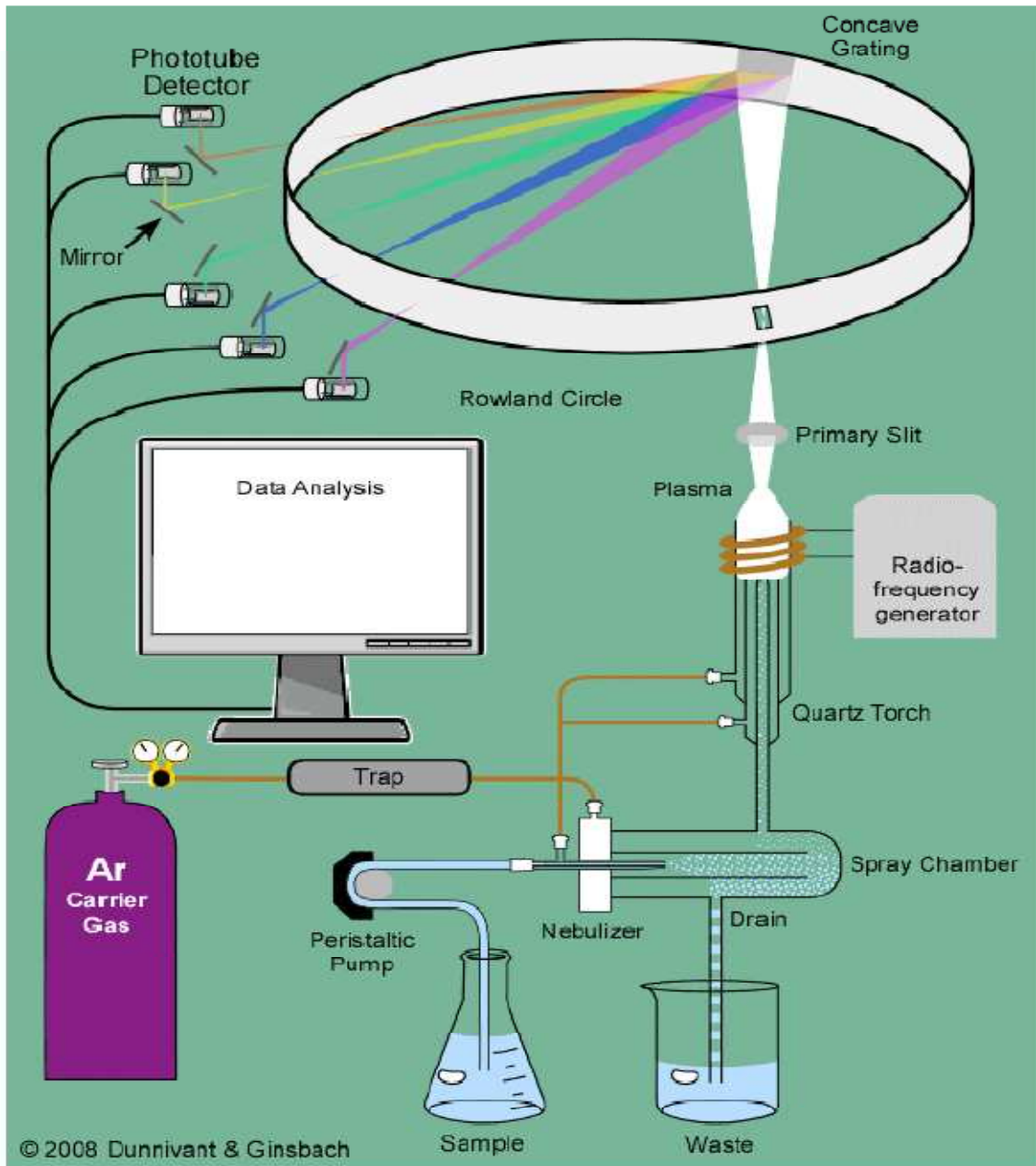


Figure 3.6. Schematic of an ICP-AES equipment

3.7 Background of Voltammetric studies

During voltammetric studies involving a three electrode assembly, the electrochemical response is dependent on the mode of mass transport. These mass transport phenomena are diffusion, migration and convection [131]. Convection is eliminated by carrying out the experiment under quiescent conditions. Migration is eliminated by adding large excess of inert supporting electrolyte. In voltammetric studies the species that responds to the applied potential or current are known as electro active species. Thus, the essential mode of mass transfer occurs only by diffusion of electroactive species. Such electrode reactions are known as diffusion controlled processes.

3.7.1 Potentiostat

A potentiostat is an electronic amplifier which controls the potential drop between the working electrode and the electrolyte [132]. All the three electrodes as mentioned earlier are controlled by a potentiostat which acts in the manner shown in Fig. 3.7.

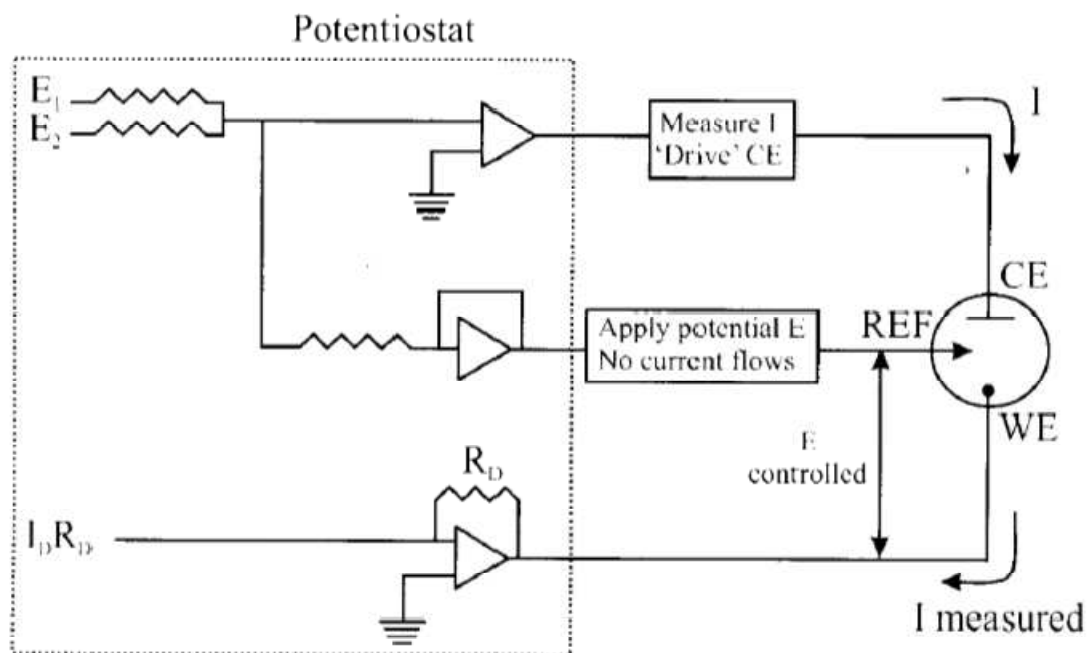


Fig.3.7 A schematic of a potentiostat connected to a three electrode assembly. R_D is variable resistance, CE is counter electrode, WE is working electrode and REF is reference electrode

The potentiostat imposes a fixed potential, E , between the working (WE) and the reference (REF) electrode and draws negligible current through the latter electrode.

$$E = (\Phi_M - \Phi_S)_{working} - (\Phi_M - \Phi_S)_{reference} \quad (3.2)$$

Where Φ_M is the electrical potential and Φ_S is the solution potential. Since the reference electrode serves to provide a constant value of $(\Phi_M - \Phi_S)_{reference}$, any changes in E are reflected as changes in $(\Phi_M - \Phi_S)_{working}$. The imposition of the potential drop $(\Phi_M - \Phi_S)_{working}$ on the working electrode-solution interface will typically cause a current to flow. The counter electrode (CE) serves to pass the same current as that induced to flow through the working electrode. Accordingly, the potentiostat drives the counter electrode to whatever voltage is required to pass

this current. The introduction of the third electrode is the only reason why a controlled potential can be applied to the working electrode as expressed by the Eqn. 3.2.

All the electrochemical measurements were carried out using IM6 electrochemical workstation (ZahnerCo.Ltd. Germany). The voltammograms were recorded and analyzed using THALES 2.10 software package.

3.7.2 Cyclic voltammetry (CV)

Principle: Cyclic voltammetry involves applying a potential to the working electrode which changes with time as shown in Fig. 3.8.

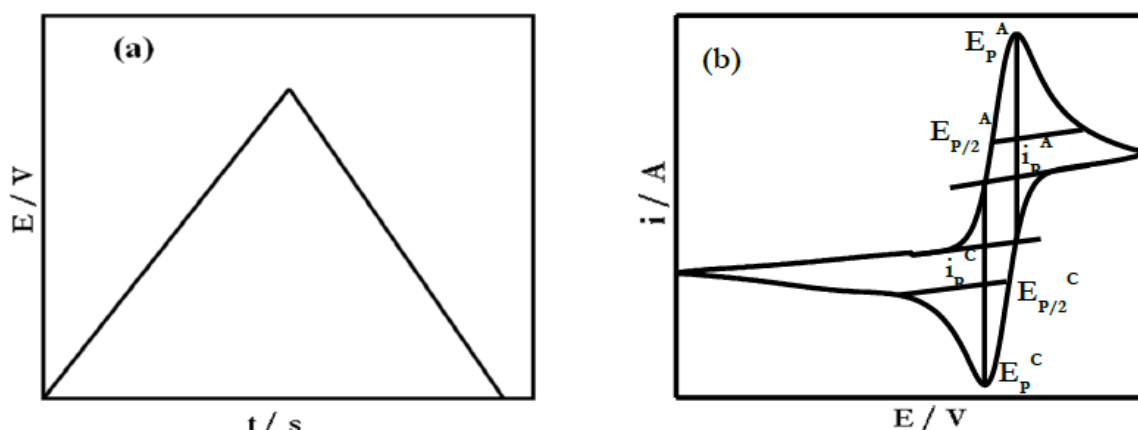


Fig. 3.8 Potential simulation (a) and resulting current response (b) in a cyclic voltammetry experiment.

The current flowing through the working electrode as a function of the applied potential and a plot of current versus potential is recorded which is known as the voltammogram. The initial voltage is selected such that the chemical species under investigation are not initially oxidized or reduced. The potential is swept in a linear manner to a certain value and then the direction of scan is reversed usually to its original value. The potential range is usually selected such that the

range contains an oxidation or reduction process of interest. The observed voltammogram depends on the parameters such as the electron transfer coefficient, standard electrochemical rate constant (K_s), formal potential of the redox couple, diffusion coefficient (D) of the redox species and the voltage scan rate (v).

Procedure: In the present study, voltammetric studies were carried out over the temperature range 963 – 1053 K. The electrochemical cell was operated under argon during the measurement. The experiments were conducted using a three-electrode assembly, where the alumina crucible served as the container for the electrolyte.

The working electrode consists of 1mm (diameter) molybdenum or tungsten wires. Other Tungsten wires of 2mm and 1 mm diameter were employed as the counter and quasi reference electrode respectively. The surface of each electrode were polished with emery paper of 1200 grit and then cleaned with acetone.

3.7.3 Electron transfer coefficient

The electron transfer coefficient (α) gives the ratio of the change of the height of the energy barrier the electron has to surmount during charge transfer with respect to the change of electrode potential ΔE [132]. A value of $\alpha = 0$ implies no influence of the electrode potential change on the barrier height. $\alpha = 1$ implies that the change of electrode potential causes an exactly equal change of barrier height. The value of αn (αn is the number of electrons transferred for the reduction process in the rate determining step) can be determined from the equation given by Matsuda and Ayabe (Eqn. 2.2) [133-134].

$$E_{P/2}^C - E_P^C = \frac{1.857RT}{\alpha n F} \quad (3.3)$$

E_p^C is cathodic peak potential, $E_{p/2}^C$ is cathodic half potential, R is the molar gas constant, T is absolute temperature and F is Faraday constant.

The αn_α also can be evaluated from the following equation

$$\frac{\Delta E_p^C}{\Delta \log v} = \frac{2.3 RT}{2\alpha n_\alpha F} \quad (3.4)$$

$\frac{\Delta E_p^C}{\Delta \log v}$ is determined from the slope of E_p^C vs $\log v$ plots.

The current function ($i_p^C/v^{1/2}$) i.e. the ratio of cathodic peak current to the square root of scan rate can be measured to determine the mechanism of electrochemical reaction. If the current and peak potential are independent of scan rate, then the electrode process is said to be reversible. In case of quasi reversible process, the current function is virtually independent of scan rate but the peak potential shift with scan rate. The difference between anodic and cathodic peak potential is useful criterion for Nerstian behavior. The electrochemical behavior is said to Nerstian if ΔE_p is very close to $2.3RT/nF$ and the ratio of anodic to cathodic peak current is approximately 1 regardless of scan rate and switching potential.

3.7.4 Square wave voltammetry (SWV):

Square wave voltammetry is one of the recent technique used by electrochemist for analytical, kinetics and mechanistic work. The form of SWV most electrochemists use today, called Osteryoung square wave which is based on work done by Ramaley and Krause in 1969 [135-136].

Fig.2.10 shows the excitation waveform used in Osteryoung SWV. With this waveform, current response to the potential excitation once on each forward pulse and once on each reverse pulse can be recorded. Using this technique, three possible current potential plots can be generated– forward current versus potential, reverse current versus potential or difference current versus potential. The resulting combination plot has been suggested as the most useful form for investigating kinetics and mechanisms.

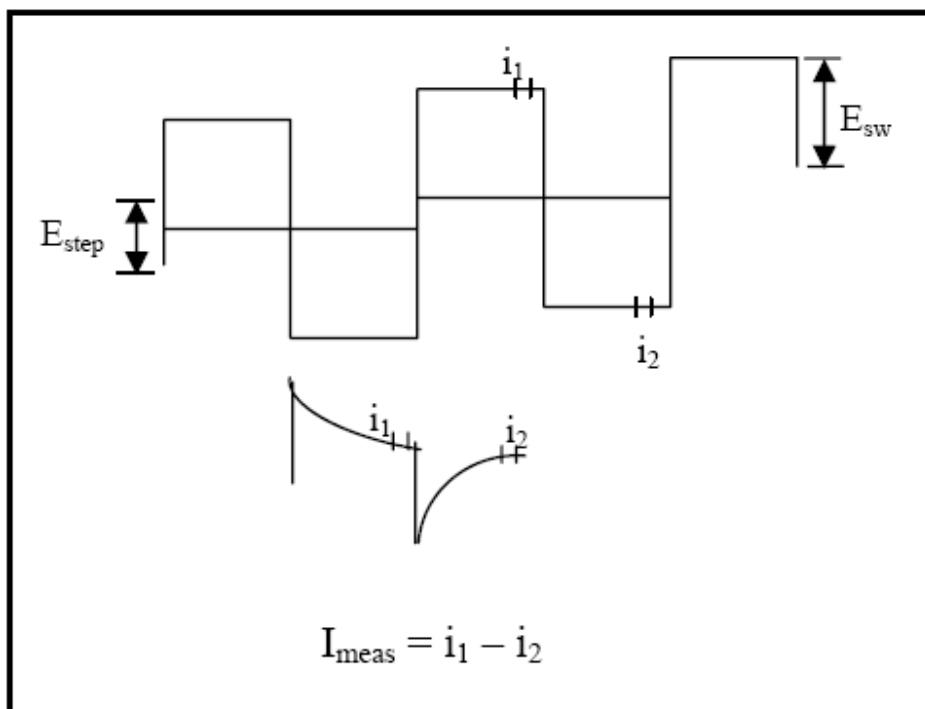


Fig.3.9: Excitation waveform and current sampling points for Osteryoung square wave.

Advantages

One of the drawbacks of rapid scanning in CV is that it introduces a large capacitive background current. This background current (or noise) makes it hard to detect the faradic current, which is the signal of interest, and severely affects the signal to noise ratio. Since SWV is a pulsed technique, it can discriminate against the charging current and eliminate this drawback.

3.7.5 Exchange current density:

When a metal in solution is at equilibrium, it implies rates of dissolution and deposition reactions are equal. When the above two reactions (anodic and cathodic) are in equilibrium, the rates (equal and opposite) of each of the two reactions are referred to as exchange current density.

Expressing reaction rates in terms of current density, $r_{\text{oxid}} = r_{\text{red}} = \frac{i_0}{nF}$ (3.5)

r_{oxid} and r_{red} are equilibrium oxidation and reduction rates. i_0 is termed exchange current density which is the rate of oxidation and reduction at equilibrium. There is no net current under the above conditions even though the concept is a useful method of representing rates at equilibrium.

at equilibrium: $i_c = i_a = i_0$

$$\text{net} = i_a - i_c = 0$$

A Kinetic expression for i_0 is given as

$$i_0 = nFAK_s(C_{\text{oxd}})^{1-\alpha}(C_{\text{red}})^\alpha \quad (3.6)$$

K_s is rate constant for the redox reaction, α = transfer coefficient and A = Area of electrode.

Exchange current density (i_0) is dependent on a) Nature of the redox reaction b) Electrode composition / surface c) Concentration ratio of oxidized and reduced species and d) Temperature.

DEHYDRATION OF RARE EARTH (RE) CHLORIDE HYDRATES

4.1 Introduction:

One of the most important aspects in the preparation of rare earth metals and their alloys is the quality of precursor used in the production process. Anhydrous rare earth chloride is widely used as the precursor for producing rare earth metal in electrolytic reduction processes [137-138]. However, preparation of pure and anhydrous rare earth (RE) chloride is extremely difficult. Rare earth chlorides are highly hygroscopic in nature and absorb moisture when exposed to atmosphere even for short duration. These compounds can absorb more than 30-35 weight % crystallized water and adsorbed moisture. Although, anhydrous RE chloride can be prepared from their corresponding oxides using different chlorinating agents, but dehydration of hydrated RE chloride is an interesting option for industrial applications[75]. Therefore, dehydration of hydrated RE chloride ($RECl_3 \cdot xH_2O$) to get anhydrous RE chloride ($RECl_3$) is an important step in the success of electrolytic reduction processes. Anhydrous rare earth chloride is prepared by heating hydrated RE chloride for several hours in vacuum or under flowing inert gas. The main difficulty in obtaining anhydrous RE chloride in pure form is the formation of oxychloride $REOCl(s)$ during dehydration process through the reaction $RECl_3 \cdot nH_2O(s) \rightarrow REOCl(s) + 2HCl(g) + (n-1) H_2O(g)$. Presence of RE oxychloride impairs the reduction process and thereby affects both yield and product purity. Therefore, it is necessary to find out an effective way to remove moisture from the starting material. Knowledge of thermodynamic stability of the RE

chloride hydrates and the mechanism of the dehydration processes is of great interest for the production of anhydrous chloride.

The mechanism of dehydration of hydrated rare earth chloride has been studied by many researchers [80-88] but the mechanisms reported by them are not consistent. In view of the conflicting reports on the decomposition pattern of $\text{RECl}_3 \cdot \text{XH}_2\text{O}$, the sequence of decomposition was reinvestigated in the present study by thermal and high temperature X-ray techniques.

In the present study, the equilibrium vapor pressure of water over various hydrates was measured employing dynamic transpiration technique. The standard molar Gibbs energy of formation of RE chloride hydrates have been derived using the measured equilibrium vapor pressure data. The derived thermodynamic properties have been compared with the existing literature. This information is very much useful in fixing the conditions for dehydration of $\text{RECl}_3 \cdot \text{XH}_2\text{O}(\text{s})$ to form $\text{RECl}_3(\text{s})$ free of oxychloride.

Experimental Details

$\text{RECl}_3 \cdot \text{XH}_2\text{O}(\text{s})$ (99% purity) used for the vapor pressure measurement experiments were supplied by Indian Rare Earth Limited (IREL). The samples were characterized by thermal and X-ray diffraction (XRD) techniques. HT-XRD patterns were recorded at various temperatures starting from 298 to 473 K in the 2θ range 10 to 70° in static air atmosphere with a step width 0.02° . The samples spread over platinum metal substrate using collodion solution were heated at a heating rate $5^\circ\text{C}/\text{min}$ and held isothermally at the predetermined temperature with an accuracy of ± 0.5 K during the measurement. In each HTXRD measurement, the samples were equilibrated for 30 minutes at the pre-set temperature prior to the measurement.

4.2 Vapor Pressure Measurement

Vapor pressure measurement was carried out by a dynamic thermo-gravimetric transpiration instrument using a micro-thermo balance (SETARAM, Model B24) described elsewhere [139]. In the present experiment the vapor pressure of water (p_{H_2O}) over the sample was determined from the total mass loss (Δm) recorded at constant temperature (T) for known time interval (t) and carrier gas flow rate (v), following the equation

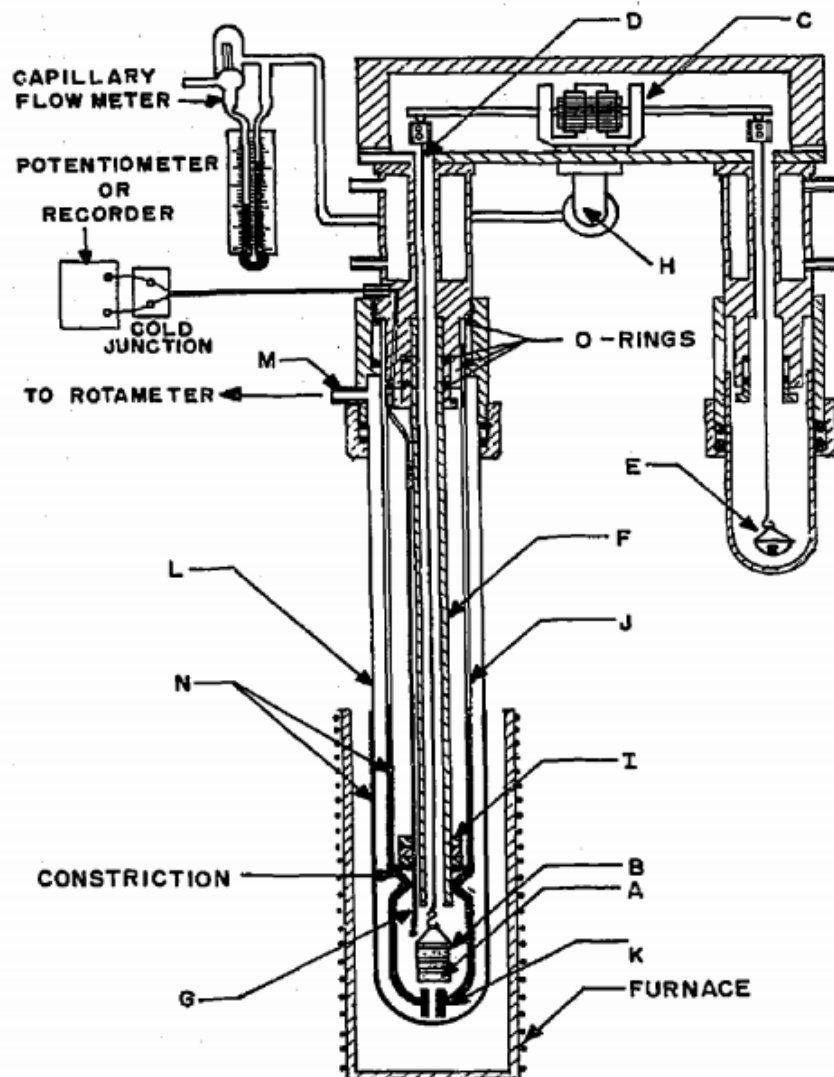
$$P_{H_2O} = \frac{\Delta m}{t} \times \frac{1}{M_{H_2O}} \times \frac{RT}{v}$$

Here, M_{H_2O} is the molecular weight of water, T is the room temperature and R is the universal gas constant. **Fig.4.1** gives the sketch diagram of the micro-thermo balance assembly used in the present study. A Pt, Pt-10%Rh thermocouple used for measuring the sample temperature located about 1 mm away from the sample which was well within the isothermal zone of the reaction tube. The equilibrium condition for the measurement of vapor pressure was established by determining the apparent pressure of water vapor over sample calculated from the mass loss of the sample per unit volume of the carrier gas (argon) swept over it as a function of flow rate at the mean temperatures of mass loss corresponding to each vaporization step. The region where the apparent vapor pressure of water is independent of flow rate of the carrier gas was determined to ascertain the saturation of the carrier gas by the vapor. The measurement of vapor pressure at different temperatures was carried out using the constant flow rate of the carrier gas in the plateau region.

$RECl_3 \cdot XH_2O$ is highly hygroscopic and loose water molecules in quick successive steps with narrow range of stability. Hence, it was difficult to isolate the decomposed products to establish the respective coexisting phase fields separately. Therefore, we have tried to measure the vapor pressure of sample with desired composition in the two phase region. This was done by

monitoring the total mass loss from the sample carried out in the transpiration apparatus using direct program mass loss technique. During vapor pressure measurement the mass loss was confined to 10 to 30 % of the total expected mass loss for any given steps. We presumed here that during the first 10 % wt loss process, the contributions due to the mass loss from the previous step gets over. By confining the measurements to 30 wt % loss, it is expected that the kinetic hindrances can be avoided. Further, it was assumed that there is no mutual solubility of among the co-existing phases during the vaporization reaction and the activity of the each of the solid phase is unity.

The sample was spread on a double stranded platinum crucible to increase the surface area. For calculation of vapor pressure, the mass loss was considered for the time interval of 60 seconds at a given mean temperature. Since the heating rate was maintained at a rate $0.5^{\circ}\text{C}/\text{min}$, in the time interval of 60 seconds the maximum variation in the temperature is expected to be 0.5 K which is well within the experimental uncertainty of temperature measurements. Therefore, it can be assumed that the mass loss process is nearly isothermal for a given measurement. The plots of the observed mass loss with respect to time in isothermal runs at given flow rate of the carrier gas were used to calculate the vapor pressure. The schematic of the vapor pressure measuring equipment is shown in **Fig.4.1**.



A. Sample, B. Tired sample holder, C. Electronic recording-type microbalance, D. Hang down wire (0.2 mm in diameter), E. Silica pan for weight tarring), F. 4 mm internal diameter (ID) silica tube, G. Thermocouple, H. Rear port in the balance housing, I. Baffles made of (i) Pt-20%Rh plate and (ii) alumina discs. 14 mm ID silica tube, K. capillary (1.5 mm diameter hole), L. 28 mm ID silica tube, M. 8 mm diameter hole, N. Layers of platinum coating.

Fig.4.1 Sketch diagram of the micro thermo-balance assembly used for dynamic transpiration vapor measurements.

4.3 Results and discussion

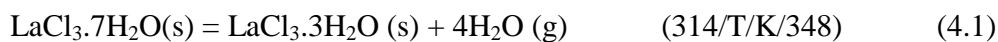
4.3.1 Determination of thermodynamic stability of LaCl_3 hydrates

4.3.1.1 Dehydration Mechanism

First the sequence of decomposition of $\text{LaCl}_3 \cdot X\text{H}_2\text{O}$ to form anhydrous LaCl_3 was investigated by thermal and high temperature X-ray diffraction technique. **Fig.4.2** gives the TG plot of $\text{LaCl}_3 \cdot 7\text{H}_2\text{O}(\text{s})$ recorded at the heating rates of 0.5, 2, 5 and 10 °C/min under 2 l/h flowing argon atmosphere. The figure indicates that the compound undergoes mass losses in three successive steps corresponding to the loss of 4, 2 and 1 number of water molecules. From Fig.2, it could also be observed that the decomposition temperature for each mass loss step is heating rate (β) dependent and progressively decrease with decrease in β . **Fig.4.3** gives the plot decomposition temperature versus heating rate for step-1, step-2 and step-3 of $\text{LaCl}_3 \cdot 7\text{H}_2\text{O}$ decomposition. The extrapolated decomposition temperatures to zero heating rate for step-1, step-2 and step-3 are found to be 314, 359 and 393 K respectively and the corresponding temperature ranges for mass loss steps are found to be 314-348 K, 359-378 K and 393-413 K, respectively. DTA plot of the sample (**Fig.4.4**) showed three endothermic peaks with initiation temperatures 314, 358 and 393 K, which correspond to the endothermic effects caused by the loss of 4, 2 and 1 water molecules in mass loss step-1, step-2 and step-3 respectively. The decomposition temperatures obtained from this work are found to be significantly lower compared to the earlier reported values [83-85]. This could be due to higher heating rate leading to non-equilibrium decomposition of lanthanum hydrate. Evolved gas analysis (**Fig.4.5**) of the sample indicates the loss of only water molecule over the entire range of mass loss steps. No mass peak for the mass numbers 36 and 38 due to HCl molecules produced by the hydrolysis of the $\text{LaCl}_3(\text{s})$ with the evolved water vapor could be observed. The onset temperatures for different mass loss steps was further verified by

recording TG-DSC (Mettler Toledo, TG-DSC-1) run at heating rate of 0.5 °C/min under 2 l/h flowing argon in a commercial instrument.

From **Fig.4.2**, it could be observed that the sample decomposes in three successive steps in the temperature ranges 314-348 K, 359-378 K and 393-413 K, respectively with 19.5 %, 9.5 % and 4.8 % mass loss respectively. The 19.5 % mass loss in the first step is attributed to loss of four water molecules. Similarly, 9.7 and 4.8 % mass loss observed in the second and third steps correspond to the loss of two and one water molecules, respectively. **Table-4.1** gives the comparison of measured and calculated mass loss for different vaporization steps. Based on the above observations the decomposition mechanism of the $\text{LaCl}_3 \cdot 7\text{H}_2\text{O}$ can be described as



The above mechanism of decomposition of $\text{LaCl}_3 \cdot 7\text{H}_2\text{O}(\text{s})$ matches well with the reported data [84].

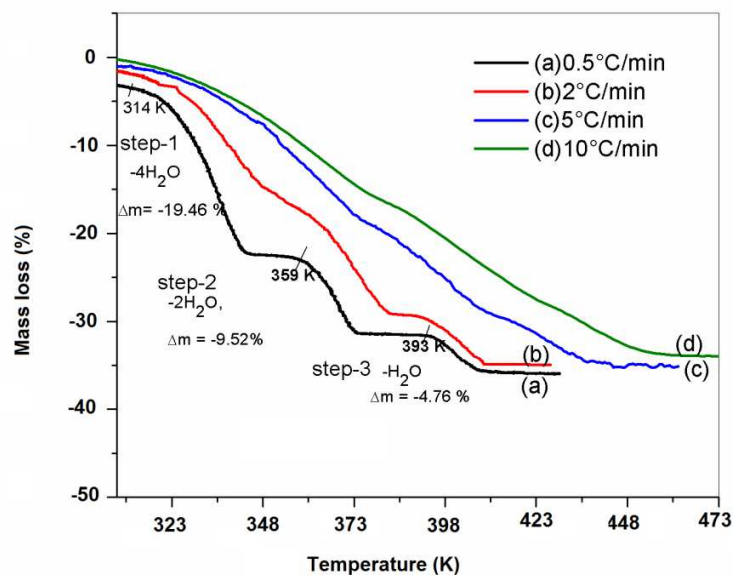


Fig.4.2 TG plot of $\text{LaCl}_3 \cdot 7\text{H}_2\text{O}$ recorded at the heating rate of 0.5, 2, 5 and 10 °C/min under 2 l/h flowing argon atmosphere.

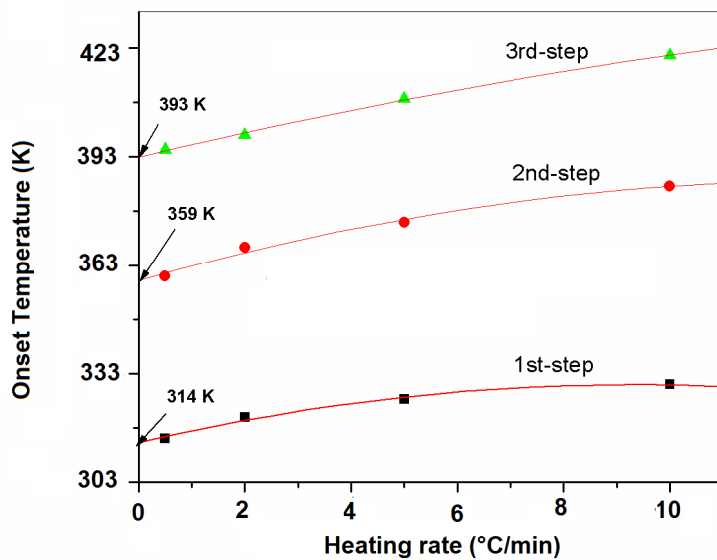


Fig.4.3 Plot of decomposition temperature versus heating rate for step-1, step-2 and step-3 of $\text{LaCl}_3 \cdot 7\text{H}_2\text{O}$ decomposition.

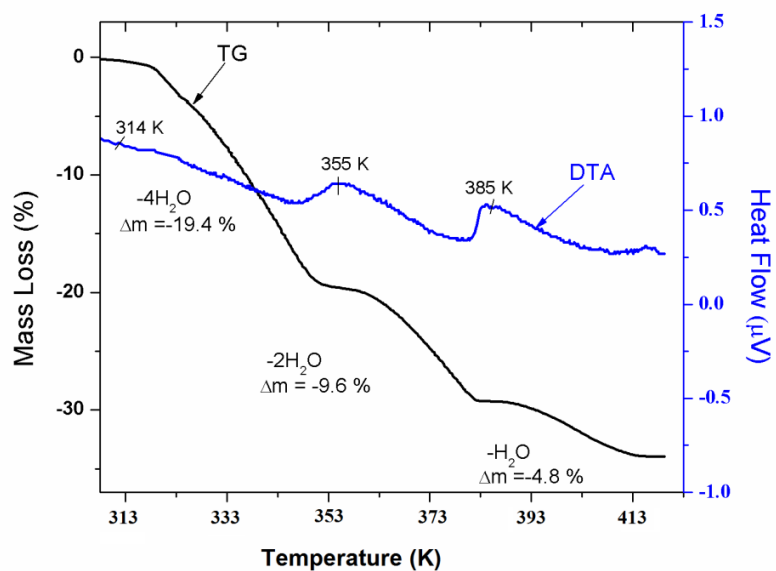


Fig.4.4 DTA plot of $\text{LaCl}_3 \cdot 7\text{H}_2\text{O}$ recorded at a heating rate of $0.5^\circ \text{C}/\text{min}$ under 2l/h flowing argon atmosphere

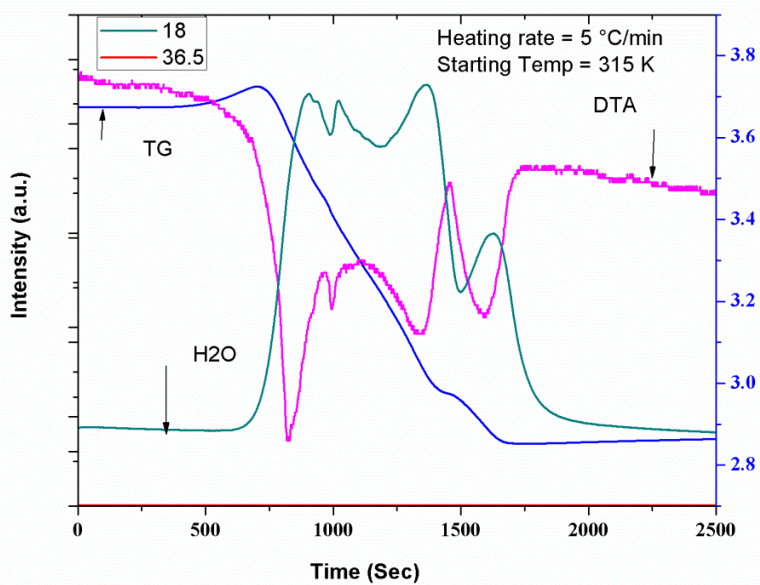


Fig.4.5 TGA-EGA plot of $\text{LaCl}_3 \cdot 7\text{H}_2\text{O}$ recorded at the heating rate of $5^\circ \text{C}/\text{min}$ under 2l/h flowing argon atmosphere.

Reaction Steps	Temperature range (K)	Measured mass loss (%)	Vaporization reaction	Calculated mass loss (%)
1	314-348	19.5	$\text{LaCl}_3 \cdot 7\text{H}_2\text{O} = \text{LaCl}_3 \cdot 3\text{H}_2\text{O} + 4\text{H}_2\text{O}$	19.2
2	359-378	9.7	$\text{LaCl}_3 \cdot 3\text{H}_2\text{O} = \text{LaCl}_3 \cdot \text{H}_2\text{O} + 2\text{H}_2\text{O}$	9.6
3	393-413	4.8	$\text{LaCl}_3 \cdot \text{H}_2\text{O} = \text{LaCl}_3 + \text{H}_2\text{O}$	4.8

Table-4.1 Measured and calculated mass loss for different vaporization reaction steps in the dehydration of $\text{LaCl}_3 \cdot 7\text{H}_2\text{O}$.

4.3.1.2 Characterization of LaCl_3 hydrates:

In order to ascertain the nature of decomposition product and decomposition temperature, high temperature x-ray diffraction patterns were recorded at the end each decomposition step. **Fig.4.6a** gives the HTXRD patterns of $\text{LaCl}_3 \cdot 7\text{H}_2\text{O}(\text{s})$ at room temperature and its decomposed daughter products recorded at 348 and 378 K whereas **Fig.4.6b** gives XRD patterns at 413 and 453 K, which corresponds to LaCl_3 . The XRD patterns at room temperature and 348 K are found to match well with the reported pattern of $\text{LaCl}_3 \cdot 7\text{H}_2\text{O}(\text{s})$ (JCPDF # 03-0069), $\text{LaCl}_3 \cdot 3\text{H}_2\text{O}(\text{s})$ (JCPDF # 82-1200). However, the XRD plot for the compound $\text{LaCl}_3 \cdot \text{H}_2\text{O}$ recorded at 378 K does not have any reported pattern for comparison. The XRD pattern recorded at 413 and 453 K matched well with reported pattern of $\text{LaCl}_3(\text{s})$ (JCPDF #73-2063) with some peaks due to LaOCl . The small amount of $\text{LaOCl}(\text{s})$ present in the sample could be due to the reaction of the water vapor with freshly produced $\text{LaCl}_3(\text{s})$ in static air condition. The formation of $\text{LaOCl}(\text{s})$ may not be possible when the water vapor is effectively flushed out. Further, **Fig.4.6** indicates that the room temperature pattern has sharp and well defined XRD peaks and the peak intensity and sharpness decreases as sample temperature of the sample increases. This is due to progressive loss of water molecules crumbling of the crystal structure and formation new crystal

lattice with smaller crystallite size. No line due parent compound could be seen all these XRD patterns, which is in confirmation with our TG results.

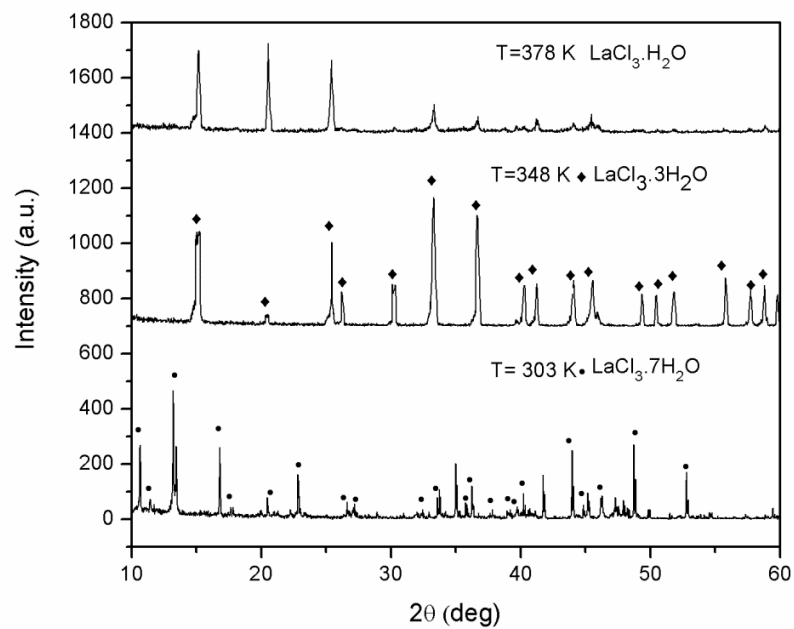


Fig.4.6a HTXRD patterns of $\text{LaCl}_3 \cdot x\text{H}_2\text{O}$ (s) sample recorded at 303, 348 and 378 K.

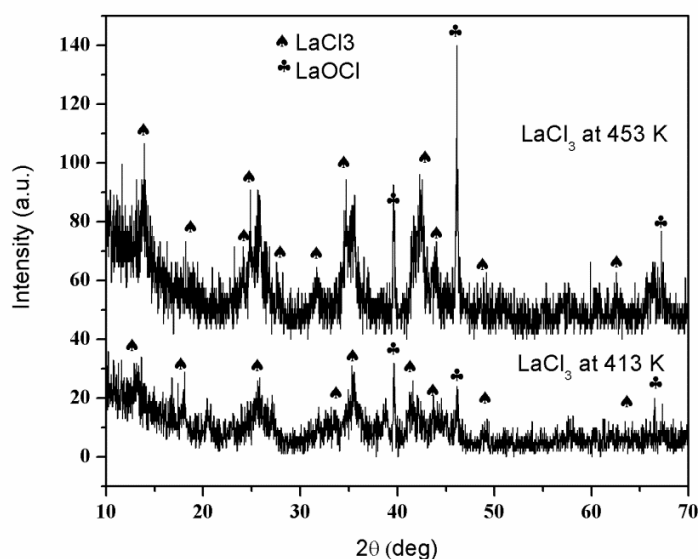


Fig.4.6b HTXRD patterns of $\text{LaCl}_3(\text{s})$ sample recorded at 413 and 453 K.

4.3.1.3 Establishment of equilibrium condition:

Fig.4.7 gives the apparent pressure versus flow rate of the carrier gas for $\text{LaCl}_3 \cdot 7\text{H}_2\text{O}(\text{s}) = \text{LaCl}_3 \cdot 3\text{H}_2\text{O}(\text{s}) + 4\text{H}_2\text{O}(\text{g})$ reaction measured at 330K for eq. (4.1). From the figure it can be observed that the apparent pressure of water over the sample is independent of flow rate of the carrier gas in the flow rate region, 1.90 to 2.7 l/h, indicating the establishment of equilibrium condition. A carrier gas flow rate of 2.4 l/h was therefore, chosen in the vapor pressure measurement experiments. Similar experiments were carried for the vaporization reactions given in eq (4.2) and eq. (4.3) under exactly similar conditions. Care was taken in all these steps to restrict the total mass loss in the range 10- 30% of the expected weight loss in respective cases. It was observed that in all these steps the flow rate independent region of the apparent pressure (plateau) also falls within 1.8 to 2.7 l/h. Hence a constant flow rate of 2.4 l/h was chosen for the

measurement of temperature coefficient of vapor pressure in all the cases. Similar experiments were carried out at flow rates i.e.2.2 and 2.4 l/hr to ascertain the reproducibility.

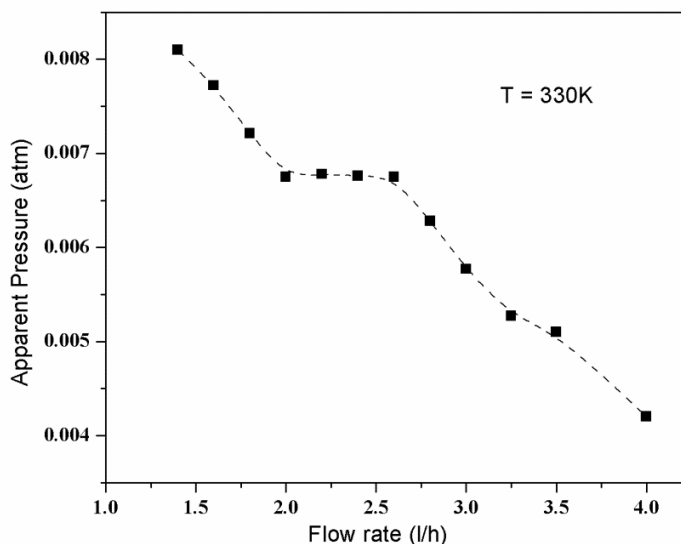


Fig.4.7 The apparent pressure versus flow rate of the carrier gas for $\text{LaCl}_3 \cdot 7\text{H}_2\text{O}(\text{s}) \rightarrow \text{LaCl}_3 \cdot 3\text{H}_2\text{O}(\text{s}) + 4\text{H}_2\text{O}(\text{g})$ reaction measured at 330 K.

4.3.1.4 Vapor pressure analysis

The vapor pressure of water as function of temperature was calculated from the rate of mass loss for given volume of carrier gas passed over the sample. **Table-4.2** gives the mass loss data for vaporization reactions eqs.4.1, 4.2 and 4.3 respectively. The plots of $\ln p_{\text{H}_2\text{O}}$ versus $1/T$ for the above processes are given in **Fig.4.8-4.10**. The least square fitted linear equations could be expressed as

$$\ln P_{\text{H}_2\text{O}}(\pm 0.01) = \frac{-7422(\pm 211)}{T} + 17.5(\pm 0.6) \quad (327 < T/\text{K} < 334) \quad (4.4)$$

$$\ln P_{\text{H}_2\text{O}}(\pm 0.03) = \frac{-8287(\pm 566)}{T} + 17.5(\pm 1.5) \quad (365 < T/\text{K} < 369) \quad (4.5)$$

$$\text{and } \ln P_{H_2O} (\pm 0.01) = \frac{-8566(\pm 346)}{T} + 16.4(\pm 0.9) \quad (391 < T/K < 396) \quad (4.6)$$

Mass loss step	Avg.Temp. (T/K)	Mass loss ($\Delta m/\mu\text{g}$)	Time ($\Delta t/\text{s}$)	Pressure (P_{H_2O}/atm)
Step-I	327	220	85	0.00527
	328	255	90	0.00577
	329	231	75	0.00628
	330	283	85	0.00678
	331	354	100	0.00721
	332	303	80	0.00772
	333	318	80	0.0081
	334	416	100	0.00848
Step-II	365	180	65	0.00564
	366	166	55	0.00615
	367	244	75	0.00663
	368	172	50	0.00701
	369	264	75	0.00717
Step-III	391.5	146	71.5	0.00416
	392.5	127	58.5	0.00442
	393.5	151	65	0.00473
	394.5	192	78	0.00502
	395.5	180	71	0.00517

Table-4.2 Mass loss data for the step-I, step-II and step-III of the vaporization reactions (in the decomposition of $\text{LaCl}_3 \cdot 7\text{H}_2\text{O}$) measured at carrier gas flow rate of 2.4 l/h

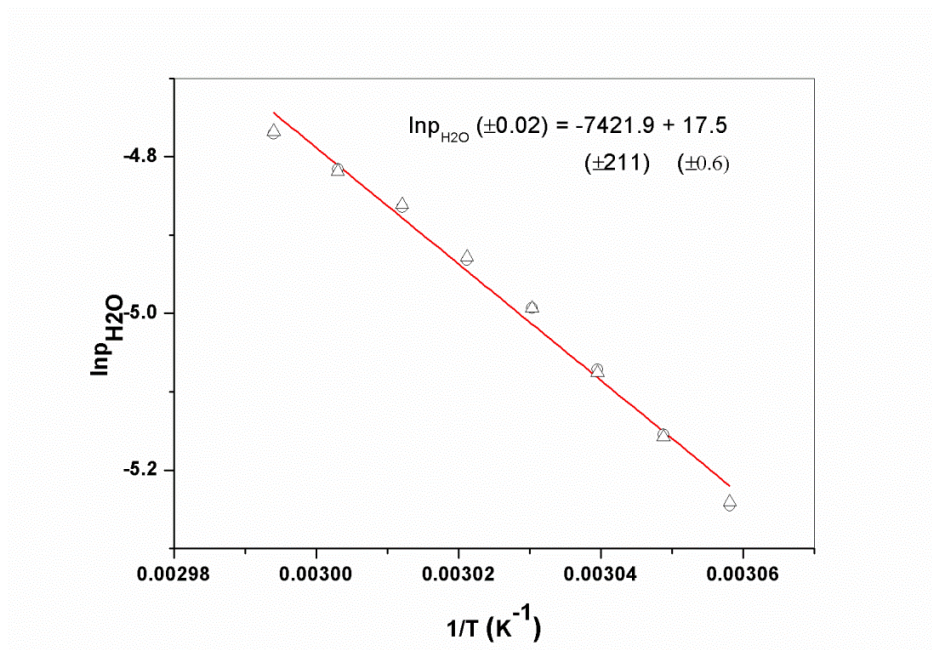


Fig.4.8 Plot of $\ln p$ versus $1/T$ for the vaporization reaction $\text{LaCl}_3 \cdot 7\text{H}_2\text{O}(\text{s}) \rightarrow \text{LaCl}_3 \cdot 3\text{H}_2\text{O}(\text{s}) + 4\text{H}_2\text{O}(\text{g})$ (Step-I).

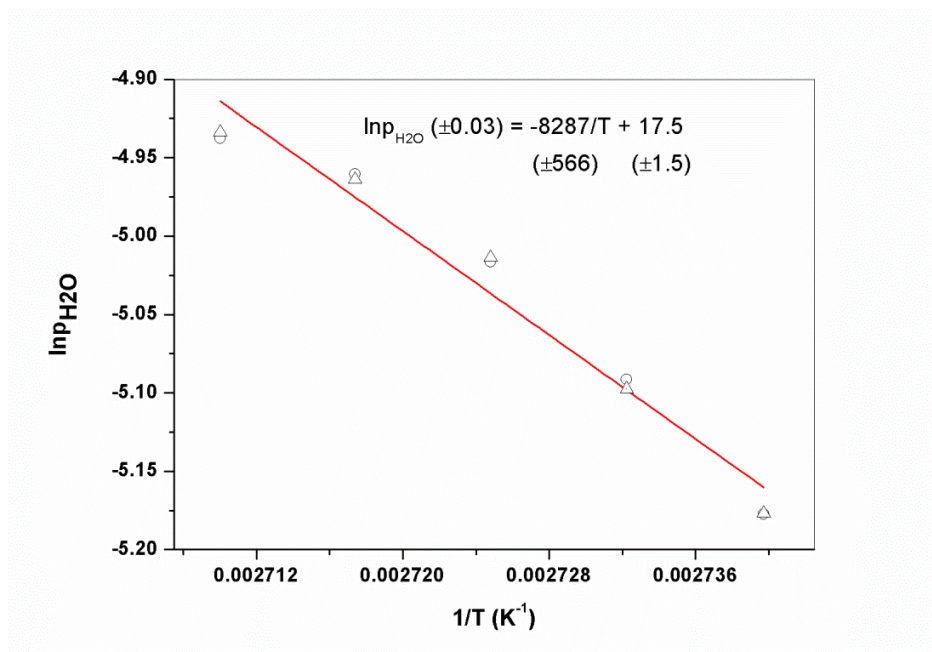


Fig.4.9 Plots of $\ln p$ versus $1/T$ for the vaporization reaction $\text{LaCl}_3 \cdot 3\text{H}_2\text{O}(\text{s}) \rightarrow \text{LaCl}_3 \cdot \text{H}_2\text{O}(\text{s}) + 2\text{H}_2\text{O}(\text{g})$ (Step-II)

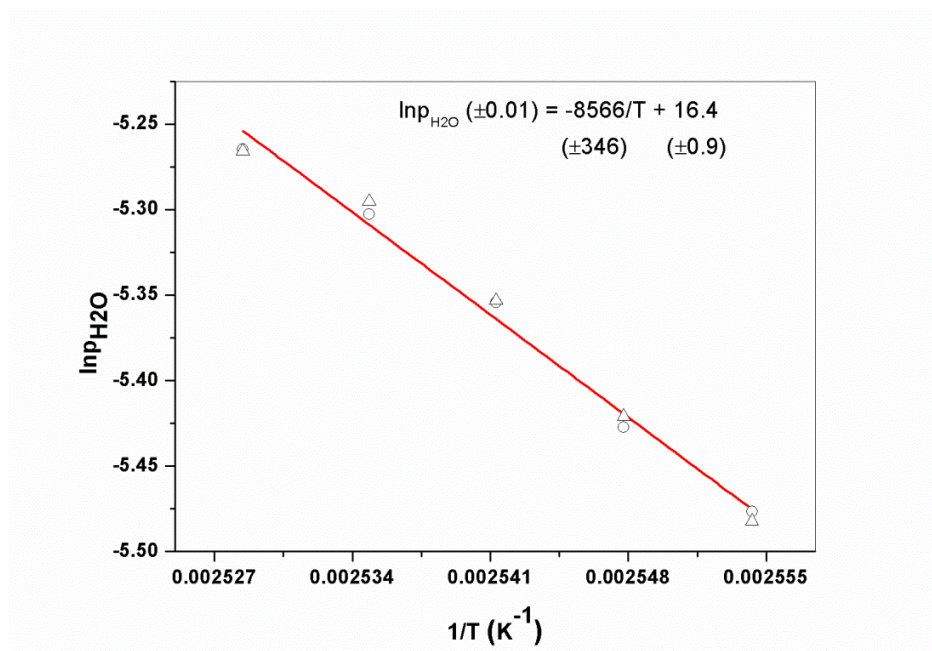


Fig.4.10 Plots of $\ln p$ versus $1/T$ for the vaporization reaction $\text{LaCl}_3 \cdot \text{H}_2\text{O}(\text{s}) \rightarrow \text{LaCl}_3(\text{s}) + \text{H}_2\text{O}(\text{g})$ (Step-III).

Comparison of values of standard molar enthalpies and entropies for the vaporization reactions steps 4.1, 4.2 and 4.3 are shown in **Table-4.3**. These values have been compared with the reported data.

Reaction steps	Vaporization reaction	ΔH_r° (kJ mol ⁻¹)	ΔH_r° (kJ mol ⁻¹)	ΔS_r° (J mol ⁻¹ K ⁻¹)	ΔS_r° (J mol ⁻¹ K ⁻¹)
		This work	(Literature)	(This work)	(Literature)
1	$\text{LaCl}_3 \cdot 7\text{H}_2\text{O}(\text{s}) =$	246.8 ± 1.7	229.8	581.8 ± 4	569.4
	$\text{LaCl}_3 \cdot 3\text{H}_2\text{O}(\text{s}) + 4\text{H}_2\text{O}(\text{g})$		[140-141]		[142-143]
2	$\text{LaCl}_3 \cdot 3\text{H}_2\text{O}(\text{s}) =$	141.4 ± 4.7	120.4	290.8 ± 12	284.7
	$\text{LaCl}_3 \cdot \text{H}_2\text{O}(\text{s}) + 2\text{H}_2\text{O}(\text{g})$		[140-141]		[142-143]
3	$\text{LaCl}_3 \cdot \text{H}_2\text{O}(\text{s}) =$	72.5 ± 2.9	72.5	136.3 ± 8	142.4
	$\text{LaCl}_3(\text{s}) + \text{H}_2\text{O}(\text{g})$		[140-141]		[142-143]

Table-4.3 Comparison of values of standard molar enthalpies and entropies for the vaporization reactions steps I, II and III (in the decomposition of $\text{LaCl}_3 \cdot 7\text{H}_2\text{O}$).

4.3.1.5 Estimation of thermodynamic parameters

The Gibbs energy of formation ($\Delta_f G^\circ$) of $\text{LaCl}_3 \cdot 7\text{H}_2\text{O}$ and its decomposition products such as $\text{LaCl}_3 \cdot 3\text{H}_2\text{O}$ and $\text{LaCl}_3 \cdot \text{H}_2\text{O}$ were calculated using the measured equilibrium vapor pressures of water over the samples and the value of standard Gibbs energy of formation of LaCl_3 from literature [144]. Considering $\text{LaCl}_3(\text{s})$ as anchoring point, the value of $\Delta_f G^\circ$ of the co-existing phase $\text{LaCl}_3 \cdot \text{H}_2\text{O}$ was first derived by using the vapor eq. 4.6, following the reaction $\text{LaCl}_3 \cdot \text{H}_2\text{O}(\text{s}) \rightarrow \text{LaCl}_3(\text{s}) + \text{H}_2\text{O}(\text{g})$. The free energy change for the reaction, $\Delta G_r^\circ = -RT \ln K$, (K is the equilibrium constant for the vaporization reaction) can be expressed as

$$\Delta G_r^\circ = \Delta_f G_{\text{LaCl}_3, \text{s}}^\circ + \Delta_f G_{\text{H}_2\text{O}, \text{g}}^\circ - \Delta_f G_{\text{LaCl}_3 \cdot \text{H}_2\text{O}, \text{s}}^\circ$$

$$\Delta_f G_{\text{LaCl}_3}^\circ (\pm 0.03) = -1066.8 (\pm 0.25) + 0.242 (0.0003) \times T$$

$$\Delta_f G_{\text{H}_2\text{O}}^\circ (\pm 0.03) = -243.3 (\pm 0.05) + 0.048 (\pm 0.0001) \times T$$

Equating $\Delta G_r^\circ = -RT \ln P_{\text{H}_2\text{O}}$, the free energy of formation of $\text{LaCl}_3 \cdot \text{H}_2\text{O}(\text{s})$ could be expressed

$$\text{as } \Delta_f G_{\text{LaCl}_3 \cdot \text{H}_2\text{O}, \text{s}}^\circ = \Delta_f G_{\text{LaCl}_3, \text{s}}^\circ + \Delta_f G_{\text{H}_2\text{O}, \text{g}}^\circ + RT \ln P_{\text{H}_2\text{O}}$$

Putting the value of $\ln p_{\text{H}_2\text{O}}$ from eq. (4.6), the molar Gibbs free energy of formation of $\text{LaCl}_3 \cdot \text{H}_2\text{O}$ was found to be

$$\Delta_f G_{\text{LaCl}_3 \cdot \text{H}_2\text{O}}^\circ (\pm 0.03) = -1381 (\pm 10) + 0.43 (\pm 0.01) \times T \quad (391 < T/\text{K} < 396) \quad (4.7)$$

The standard deviation of Gibbs free energy of formations was derived from the least square fitting of experimental data only.

The standard molar Gibbs energy of formation of $\text{LaCl}_3 \cdot 3\text{H}_2\text{O}(\text{s})$ was similarly derived following the vaporization reaction $\text{LaCl}_3 \cdot 3\text{H}_2\text{O}(\text{s}) \rightarrow \text{LaCl}_3 \cdot \text{H}_2\text{O}(\text{s}) + 2\text{H}_2\text{O}(\text{g})$. The expression for free energy of the compound in terms of vapor pressure of H_2O could be expressed as

$$\Delta_f G_{\text{LaCl}_3 \cdot 3\text{H}_2\text{O}, \text{S}}^0 = \Delta_f G_{\text{LaCl}_3 \cdot \text{H}_2\text{O}, \text{S}}^0 + 2\Delta_f G_{\text{H}_2\text{O}, \text{g}}^0 + 2RT \ln P_{\text{H}_2\text{O}}$$

Putting the value of $\ln p(\text{H}_2\text{O})$ for the above vaporization reaction from eq.(4.5), the value of standard Gibbs free energy of formation of $\text{LaCl}_3 \cdot \text{H}_2\text{O}(\text{s})$ derived from previous section, the molar Gibbs free energy of formation of $\text{LaCl}_3 \cdot 3\text{H}_2\text{O}$ was found to be

$$\Delta_f G_{\text{LaCl}_3 \cdot 3\text{H}_2\text{O}}^0 (\pm 0.03) = -2006(\pm 11) + 0.8(\pm 0.1) \times T \quad (365 < T/\text{K} < 369) \quad (4.8)$$

Similarly the standard molar Gibbs energy of $\text{LaCl}_3 \cdot 7\text{H}_2\text{O}(\text{s})$ was derived by considering the vaporization reaction $\text{LaCl}_3 \cdot 7\text{H}_2\text{O}(\text{s}) \rightarrow \text{LaCl}_3 \cdot 3\text{H}_2\text{O}(\text{s}) + 3\text{H}_2\text{O}(\text{g})$. The expression $\text{LaCl}_3 \cdot 7\text{H}_2\text{O}(\text{s})$ in terms of vapor pressure of H_2O could be expressed as

$$\Delta_f G_{\text{LaCl}_3 \cdot 7\text{H}_2\text{O}, \text{S}}^0 = \Delta_f G_{\text{LaCl}_3 \cdot 3\text{H}_2\text{O}, \text{S}}^0 + 4\Delta_f G_{\text{H}_2\text{O}, \text{g}}^0 + 4RT \ln P_{\text{H}_2\text{O}}$$

Putting the values of $\ln p(\text{H}_2\text{O})$ from eq. (4.4), the standard Gibbs free energy of formation of $\text{LaCl}_3 \cdot 7\text{H}_2\text{O}(\text{s})$ could be expressed as

$$\Delta_f G_{\text{LaCl}_3 \cdot 7\text{H}_2\text{O}}^0 (\pm 0.06) = -3226(\pm 13) + 1.6(\pm 0.1) \times T \quad (327 < T/\text{K} < 334) \quad (4.9)$$

The standard molar enthalpy of formation of $\text{LaCl}_3 \cdot 7\text{H}_2\text{O}(\text{s})$, $\text{LaCl}_3 \cdot 3\text{H}_2\text{O}(\text{s})$, $\text{LaCl}_3 \cdot \text{H}_2\text{O}(\text{s})$ at the mean temperature of measurements have been presented in **Table-4.4**. These values have also been compared with the available data in the literature.

Compound	T mean (T/K)	$\Delta_f H^0$ (kJ mol ⁻¹)	$\Delta_f H^0$ (kJ mol ⁻¹)
		(This work)	(Literature)
LaCl ₃ .7H ₂ O	329	-3226±13	-3182 [145]
LaCl ₃ .3H ₂ O	367	-2006±11	-1985 [146]
LaCl ₃ .H ₂ O	393	-1381±10	-1381 [147]

Table-4.4 Comparison of values of standard molar enthalpies of formation of LaCl₃.7H₂O(s), LaCl₃.3H₂O(s) and LaCl₃.H₂O(s).

4.3.2 Thermodynamic stability of CeCl₃ hydrates

4.3.2.1 Dehydration Mechanism

Fig.4.11 shows the TG plot of CeCl₃·7H₂O(s) recorded at the heating rates of 0.5 °C/min under 2.5 l/h flowing argon atmosphere. From **Fig.4.11** it could be observed that the sample decomposes in four successive steps in the temperature range 315-345 K, 345-360 K, 360-370K and 395-418 K respectively with 19.0%, 5.0%, 5.2% and 4.6 % mass loss respectively. The mass loss steps are correspond to the loss of 4, 1, 1, 1 water molecules in the 1st, 2nd, 3rd and 4th step respectively. **Table-4.5** gives the comparison of measured and calculated mass loss for different vaporization steps.

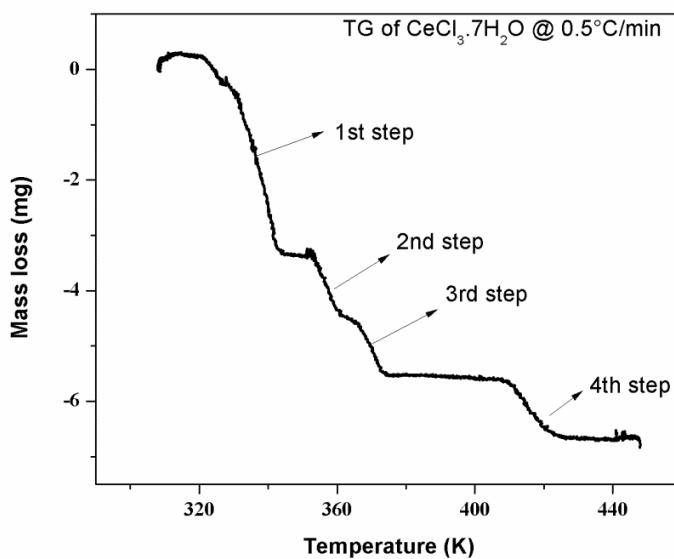


Fig.4.11 TG plot of CeCl₃·7H₂O(s) recorded at the heating rates of 0.5 °C/min under 2.5 l/h flowing argon atmosphere.

Reaction steps	Temp. Range (K)	Measured mass loss (%)	Vaporization reaction	Calculated mass loss (%)
1	315-345	19.4	$\text{CeCl}_3 \cdot 7\text{H}_2\text{O}(\text{s}) = \text{CeCl}_3 \cdot 3\text{H}_2\text{O}(\text{s}) + 4\text{H}_2\text{O}(\text{g})$	19.0
2	345-360	4.8	$\text{CeCl}_3 \cdot 3\text{H}_2\text{O}(\text{s}) = \text{CeCl}_3 \cdot 2\text{H}_2\text{O}(\text{s}) + \text{H}_2\text{O}(\text{g})$	5.0
3	360-370	4.8	$\text{CeCl}_3 \cdot 2\text{H}_2\text{O}(\text{s}) = \text{CeCl}_3 \cdot \text{H}_2\text{O}(\text{s}) + \text{H}_2\text{O}(\text{g})$	5.2
4	395-418	4.8	$\text{CeCl}_3 \cdot \text{H}_2\text{O}(\text{s}) = \text{CeCl}_3(\text{s}) + \text{H}_2\text{O}(\text{g})$	4.6

Table-4.5 Comparison of measured and calculated mass loss for different vaporization steps in the dehydration of $\text{CeCl}_3 \cdot 7\text{H}_2\text{O}$.

DTA plot of $\text{CeCl}_3 \cdot 7\text{H}_2\text{O}$ recorded at a heating rate of $5\text{ }^\circ\text{C}/\text{min}$ (**Fig.4.12**) showed four endothermic peaks, corresponding to the loss of water molecules in four successive steps. The initial endothermic base line shift before the initiation of first peak in the DTA plot could be due to loss of adsorbed surface water. Evolved gas analysis (**Fig.4.13**) of the sample indicates the loss of only water molecule over the entire range of mass loss steps. No mass peak for the mass numbers 36 and 38 due to HCl molecules produced by the hydrolysis of the $\text{CeCl}_3(\text{s})$ with the evolved water vapor could be observed.

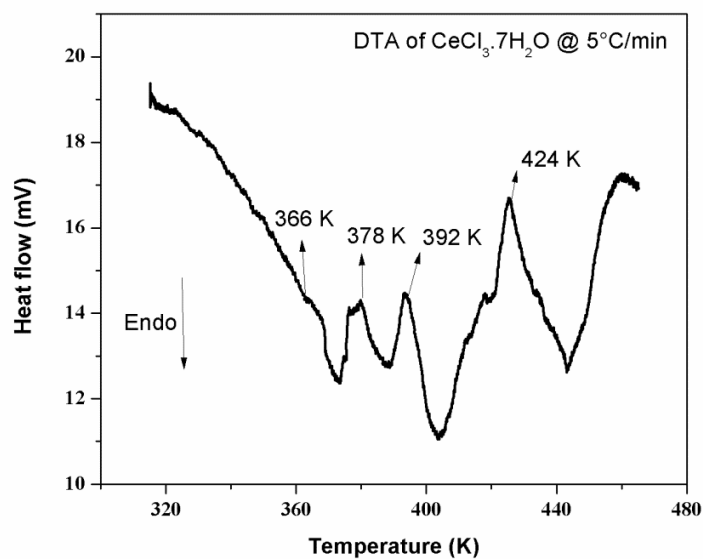


Fig.4.12 DTA plot of $\text{CeCl}_3 \cdot 7\text{H}_2\text{O}$ recorded at a heating rate of $5^\circ\text{C}/\text{min}$ under 2.5l/h flowing argon atmosphere

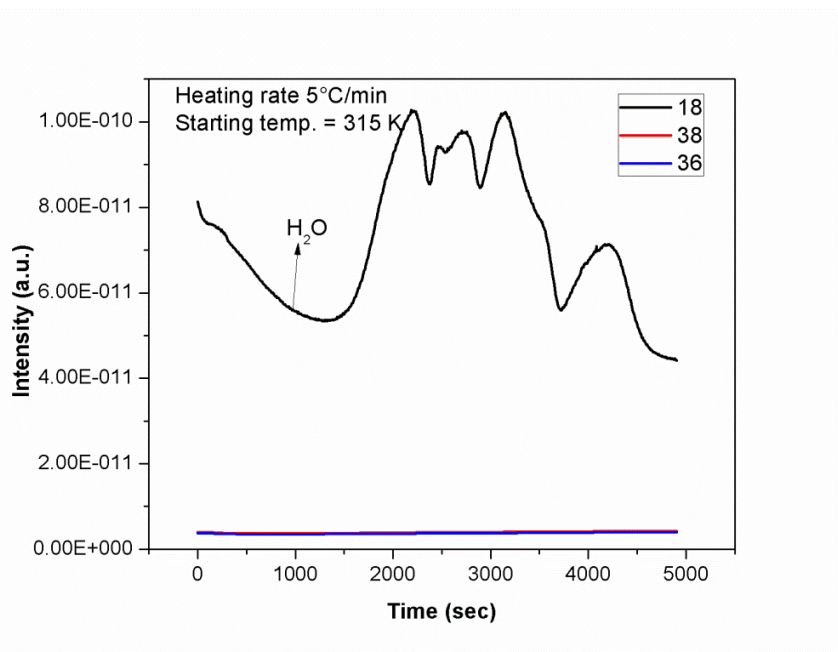
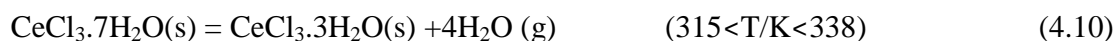


Fig.4.13 EGA plot of $\text{CeCl}_3 \cdot 7\text{H}_2\text{O}$ recorded at the heating rate of $5^\circ\text{C}/\text{min}$ under 2.5l/h flowing argon atmosphere.

Based on the above observations the decomposition mechanism of the $\text{CeCl}_3 \cdot 7\text{H}_2\text{O}$ can be described as



4.3.2.2 Establishment of equilibrium condition

Fig.4.14 gives the apparent pressure versus flow rate of the carrier gas for $\text{CeCl}_3 \cdot 7\text{H}_2\text{O}(\text{s}) = \text{CeCl}_3 \cdot 3\text{H}_2\text{O}(\text{s}) + 4\text{H}_2\text{O}(\text{g})$ reaction measured at 330 K for eq. (4.10). From the figure it can be observed that the apparent pressure of water over the sample is independent of flow rate of the carrier gas in the flow rate region, 2 to 3.0 l/h, indicating the establishment of equilibrium condition. Similar experiments were carried for the vaporization reactions given in eq. (4.11), eq. (4.12) and eq. (4.13) under exactly similar conditions. It was observed that in all these steps the flow rate independent region of the apparent pressure (plateau) also falls within 2 to 3 l/h. A carrier gas flow rate of 2.5 l/h was therefore, chosen in the vapor pressure measurement experiments. Care was taken in all these steps to restrict the mass loss measurements in the range 10- 30% of the expected total mass loss in respective cases. Similar experiments were carried out at flow rates i.e.2.2 and 2.7 l/h to ascertain the reproducibility.

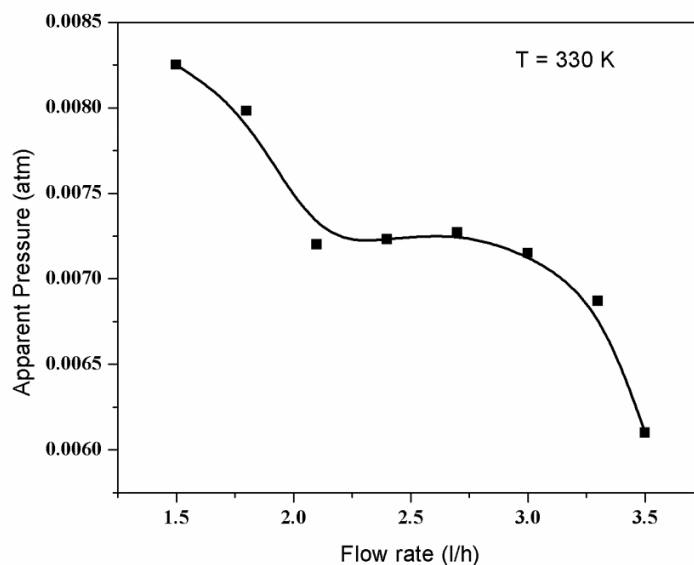


Fig.4.14 The apparent pressure versus flow rate of the carrier gas for $\text{CeCl}_3 \cdot 7\text{H}_2\text{O}(\text{s}) \rightarrow \text{CeCl}_3 \cdot 3\text{H}_2\text{O}(\text{s}) + 4\text{H}_2\text{O}(\text{g})$ reaction measured at 330 K.

4.3.2.3 Vapor pressure analysis

The vapor pressure of water as a function of temperature was calculated from the rate of mass loss for given volume of carrier gas passed over the sample. **Table-4.6** gives the mass loss data for vaporization reactions eqns. 4.10, 4.11, 4.12 and 4.13 respectively. The plots of $\ln p_{\text{H}_2\text{O}}$ versus $1/T$ for the above processes are given in Fig.8. The least square fitted linear equations could be expressed as

$$\ln P_{\text{H}_2\text{O}}(\pm 0.02) = \frac{-7487(\pm 487)}{T} + 17.7(\pm 1.5) \quad (331 < T/\text{K} < 335) \quad (4.14)$$

$$\ln P_{\text{H}_2\text{O}}(\pm 0.02) = \frac{-7828(\pm 604)}{T} + 17.3(\pm 1.8) \quad (352 < T/\text{K} < 355) \quad (4.15)$$

$$\ln P_{\text{H}_2\text{O}}(\pm 0.02) = \frac{-8676(\pm 130)}{T} + 18.0(\pm 0.35) \quad (362 < T/\text{K} < 366) \quad (4.16)$$

and

$$\ln P_{H_2O}(\pm 0.02) = \frac{-9281(\pm 828)}{T} + 17.4(\pm 2.08) \quad (397 < T/K < 400) \quad (4.17)$$

Mass loss step	Avg. Temp. (T/K)	Mass loss ($\Delta m/\mu g$)	Time ($\Delta t/s$)	Apparent pressure (P_{H_2O}/atm)
Step-I	325	157.2	60	0.00511
	326	169.2	60	0.00552
	327	180.6	60	0.00588
	328	187.2	60	0.0061
	329	211.2	60	0.00687
	330	222.6	60	0.00725
Step-II	344	130.2	60	0.00423
	345	141.6	60	0.00461
	346	150.6	60	0.00489
	347	158.4	60	0.00516
Step-III	362	114.0	60	0.00371
	363	121.8	60	0.00397
	364	129.6	60	0.00421
	365	139.2	60	0.00452
	366	148.2	60	0.00483
Step-IV	397	82.8	60	0.00269
	398	87.6	60	0.00285
	399	92.4	60	0.00301
	400	97.8	60	0.00318

Table-4.6 Mass loss data for the step-1, step-II, step-III and step-IV of the vaporization reactions measured at carrier gas flow rate of 2.5 l/h (in the dehydration of $CeCl_3 \cdot 7H_2O$).

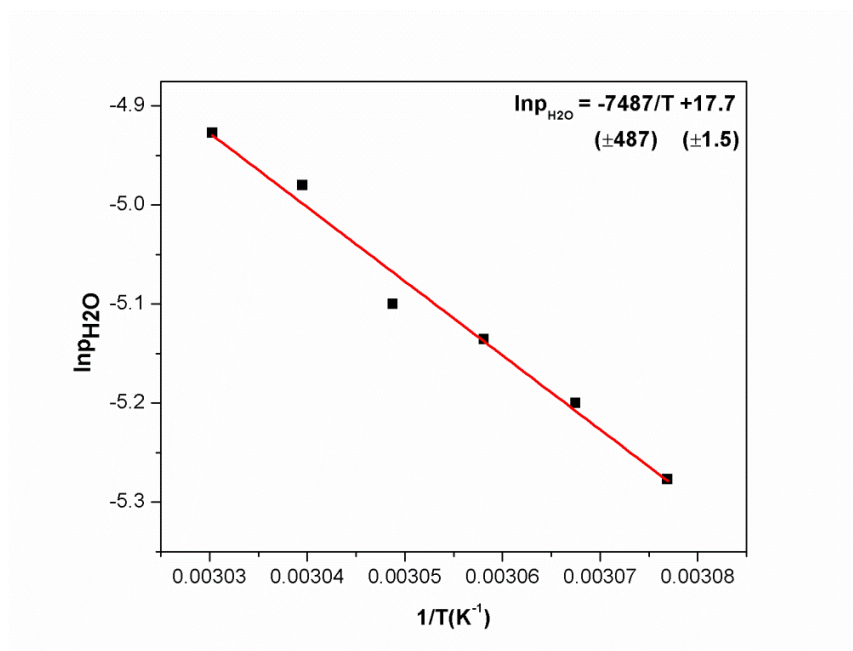


Fig.4.15 Plots of $\ln p$ versus $1/T$ for the vaporization reaction $\text{CeCl}_3 \cdot 7\text{H}_2\text{O}(\text{s}) \rightarrow \text{CeCl}_3 \cdot 3\text{H}_2\text{O}(\text{s}) + 4\text{H}_2\text{O}(\text{g})$ (Step-I)

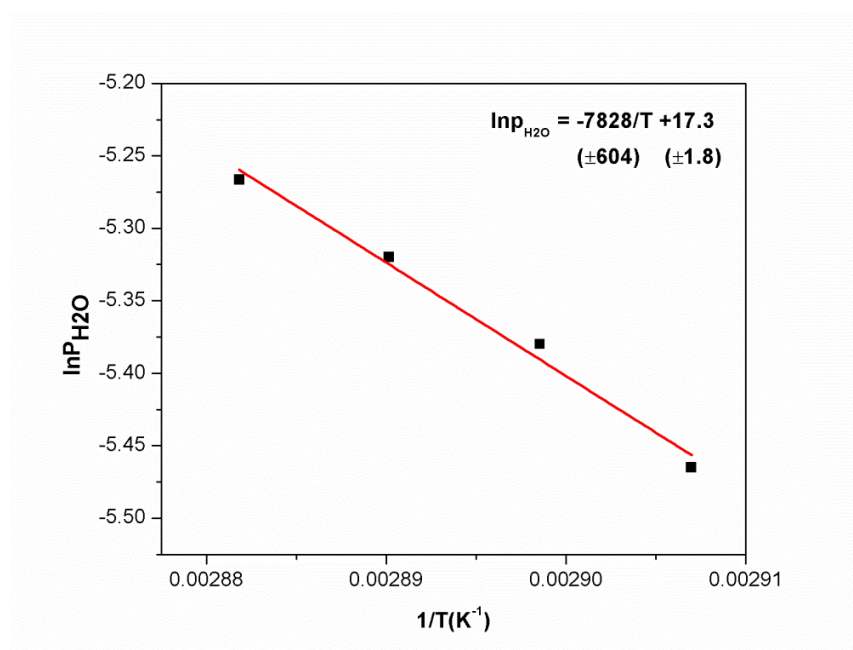


Fig.4.16 Plots of $\ln p$ versus $1/T$ for the vaporization reaction $\text{CeCl}_3 \cdot 3\text{H}_2\text{O}(\text{s}) \rightarrow \text{CeCl}_3 \cdot 2\text{H}_2\text{O}(\text{s}) + \text{H}_2\text{O}(\text{g})$ (Step-II),

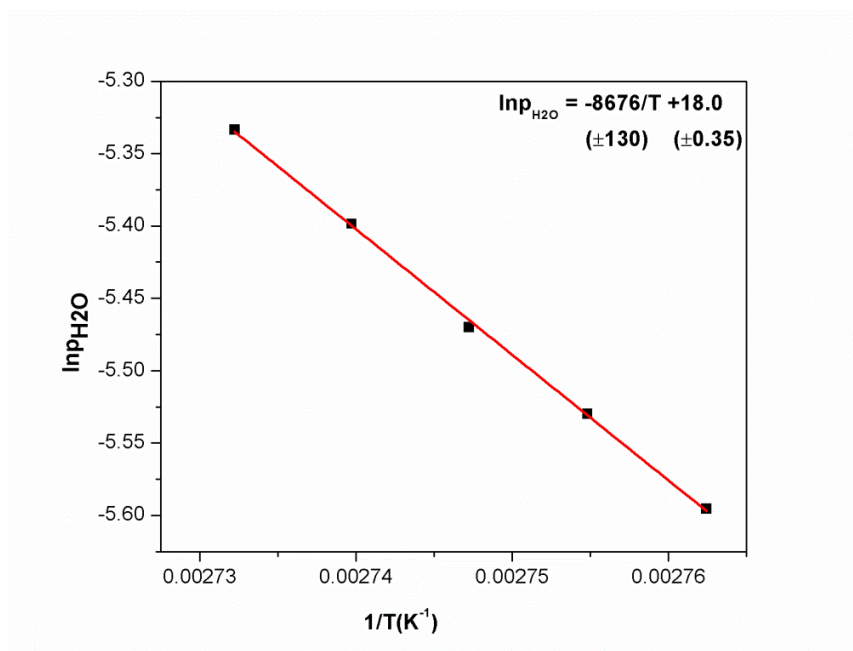


Fig.4.17 Plots of $\ln p$ versus $1/T$ for the vaporization reaction $\text{CeCl}_3 \cdot 2\text{H}_2\text{O}(\text{s}) \rightarrow \text{CeCl}_3 \cdot \text{H}_2\text{O}(\text{s}) + \text{H}_2\text{O}(\text{g})$ (Step-III).

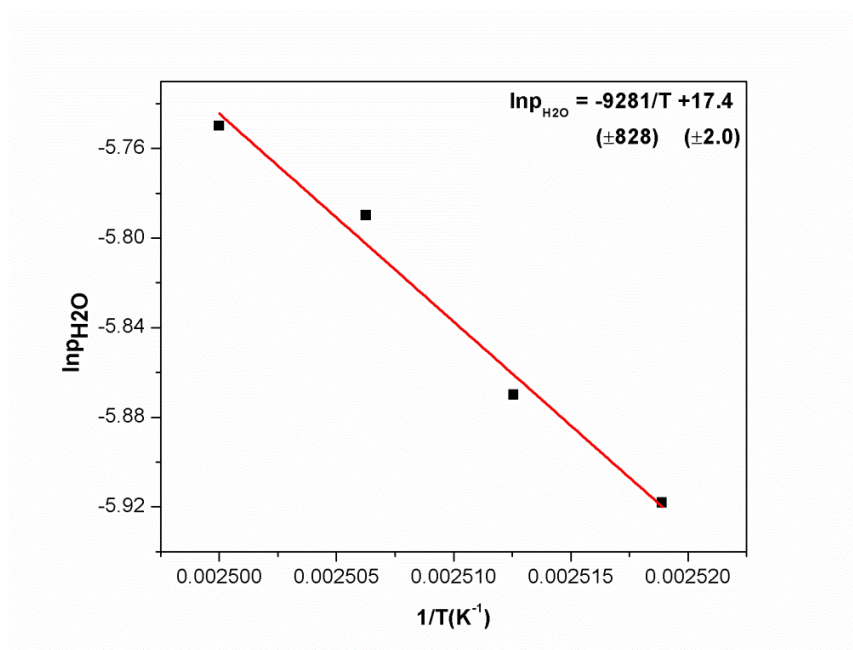


Fig.4.18 Plots of $\ln p$ versus $1/T$ for the vaporization reaction $\text{CeCl}_3 \cdot \text{H}_2\text{O}(\text{s}) \rightarrow \text{CeCl}_3(\text{s}) + \text{H}_2\text{O}(\text{g})$ (Step-IV).

The average standard molar enthalpy and entropy of vaporization for the respective reactions described in Eqns. (4.10) - (4.13) are given in **Table-4.7**.

Reaction steps	Vaporization reaction	ΔH^0_r (kJ mol ⁻¹)	ΔS^0_r (J mol ⁻¹ K ⁻¹)
		This work	(This work)
1	CeCl ₃ .7H ₂ O(s)= CeCl ₃ .3H ₂ O(s)+4H ₂ O(g)	248.9 ±20.0	588.6±12.5
2	CeCl ₃ .3H ₂ O(s) = CeCl ₃ .2H ₂ O(s)+H ₂ O(g)	65.08±5.0	143.8±15.0
3	CeCl ₃ .2H ₂ O(s) = CeCl ₃ .H ₂ O(s)+H ₂ O(g)	72.1±1.0	149.6±3.0
4	CeCl ₃ . H ₂ O(s) = CeCl ₃ (s)+H ₂ O(g)	77.2±07	144.6±16.7

Table-4.7 Values of standard molar enthalpies and entropies for the vaporization reactions steps 4.10, 4.11, 4.12 and 4.13 (in the dehydration of CeCl₃.7H₂O).

4.3.2.4 Estimation of thermodynamic parameters

Gibbs energy of formation of CeCl₃ hydrates estimated as per the method described in section 4.3.1.5.were given below.

$$\Delta_f G^0_{CeCl_3.H_2O} (\pm 0.03) = -1367(\pm 09) + 0.42(\pm 0.02) \times T \quad (396 < T/K < 400) \quad (4.18)$$

$$\Delta_f G^0_{CeCl_3.2H_2O} (\pm 0.03) = -1683(\pm 10) + 0.62(\pm 0.03) \times T \quad (362 < T/K < 366) \quad (4.19)$$

$$\Delta_f G^0_{CeCl_3.3H_2O} (\pm 0.05) = -1991(\pm 10) + 0.80(\pm 0.03) \times T \quad (352 < T/K < 355) \quad (4.20)$$

$$\Delta_f G^0_{CeCl_3.7H_2O} (\pm 0.08) = -3213(\pm 17) + 1.6(\pm 0.09) \times T \quad (330 < T/K < 337) \quad (4.21)$$

The standard molar enthalpy of formation of $\text{CeCl}_3 \cdot 7\text{H}_2\text{O}(\text{s})$, $\text{CeCl}_3 \cdot 3\text{H}_2\text{O}(\text{s})$, $\text{CeCl}_3 \cdot 2\text{H}_2\text{O}(\text{s})$ and $\text{CeCl}_3 \cdot \text{H}_2\text{O}$ at the mean temperature of measurements i.e. 333 K, 353 K, 364 K and 398 K are found to be -3213 ± 17 , -1991 ± 10 and -1683 ± 10 and -1367 ± 09 kJ mol^{-1} , respectively. The standard molar entropies of formation at mean temperature of measurement are found to be -1600 ± 90 , -800 ± 30 , -600 ± 20 and -400 ± 20 $\text{J mol}^{-1} \text{K}^{-1}$, respectively.

4.3.3 Thermodynamic stability of PrCl₃ hydrates

4.3.3.1 Dehydration Mechanism

Fig.4.19 gives the TG plot of PrCl₃.7H₂O(s) recorded at the heating rates of 0.5, 2, 5 and 10 °C/min under 2.5 l/h flowing argon atmosphere. From **Fig.4.19** it could be observed that the sample decomposes in four successive steps in the temperature range 323-348 K, 348-368 K, 368-383 K and 413-443 K respectively with 19.1%, 5.2%, 4.8 and 4.5 % mass loss respectively. The mass loss steps are corresponding to the loss of 3, 1, 1, 1 water molecules in the 1st, 2nd, 3rd and 4th step respectively. **Table-4.8** gives the comparison of measured and calculated mass loss for different vaporization steps. **Fig.4.20** gives the plot of decomposition temperature versus heating rate for step-1, step-2, step-3 and step-4 for PrCl₃.7H₂O dehydration. The extrapolated decomposition temperatures to zero heating rate for step-1, step-2 and step-3 and step-4 are found to be 321, 345, 360 and 408 K respectively.

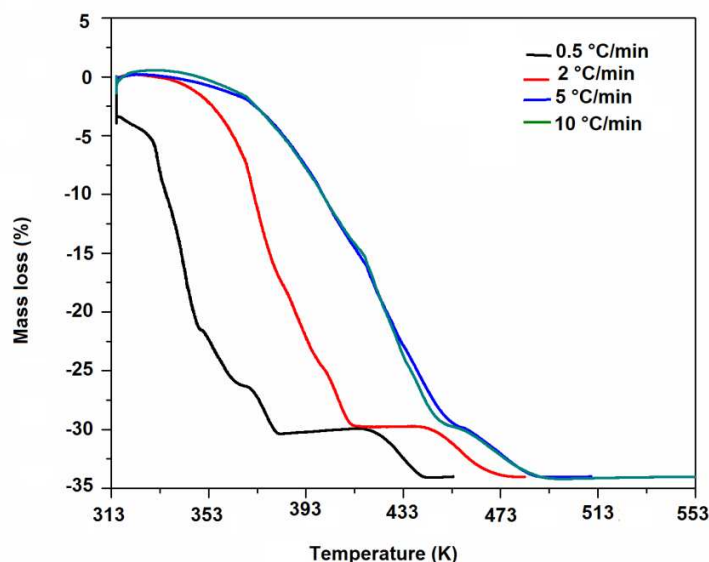


Fig.4.19 TG plot of PrCl₃.7H₂O recorded at the heating rate of 0.5, 2, 5 and 10 °C/min under 2.5 l/h flowing argon atmosphere.

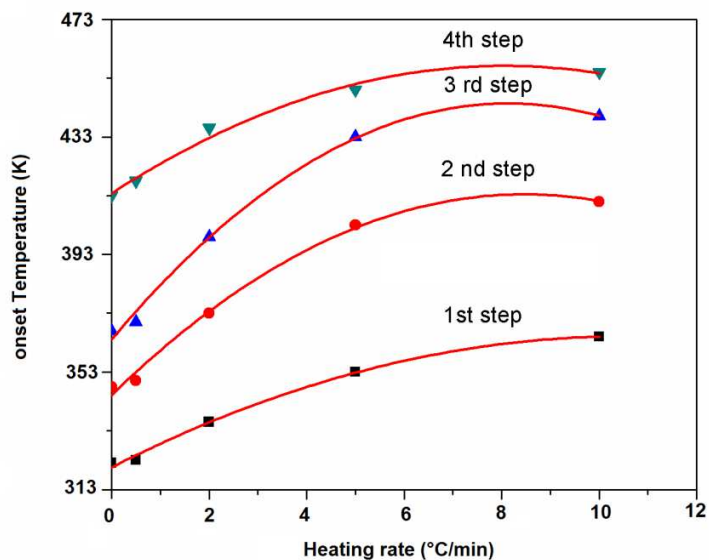


Fig.4.20 Plot of decomposition temperature versus heating rate for step-1, step-2, step-3 and step-IV of $\text{PrCl}_3 \cdot 7\text{H}_2\text{O}$ decomposition.

DTA plot of $\text{PrCl}_3 \cdot 7\text{H}_2\text{O}$ recorded at a heating rate of $5\text{ }^\circ\text{C}/\text{min}$ (**Fig.4.21**) showed four endothermic peaks, corresponding to the loss of water molecules in four successive steps. The initial endothermic base line shift in the DTA plot in the temperature range 298 to 343 K is due to loss of adsorbed surface water.

Evolve gas analysis of the sample (**Fig.4.22**) indicates the loss of only water molecule over the entire range of mass loss steps. No mass peak for the mass number 36.5 and 38.5 due to HCl molecules produced by the hydrolysis reaction could be observed.

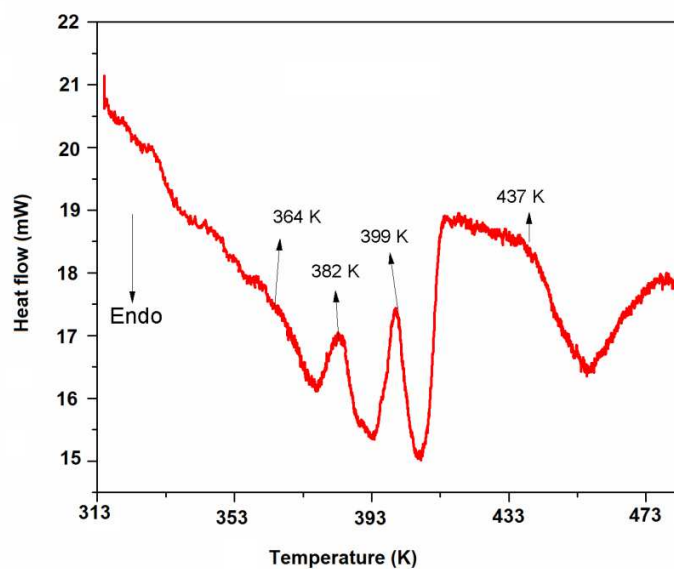


Fig.4.21 DTA plot of $\text{PrCl}_3 \cdot 7\text{H}_2\text{O}$ recorded at a heating rate of $5\text{ }^\circ\text{C}/\text{min}$ under 2.5 l/h flowing argon atmosphere

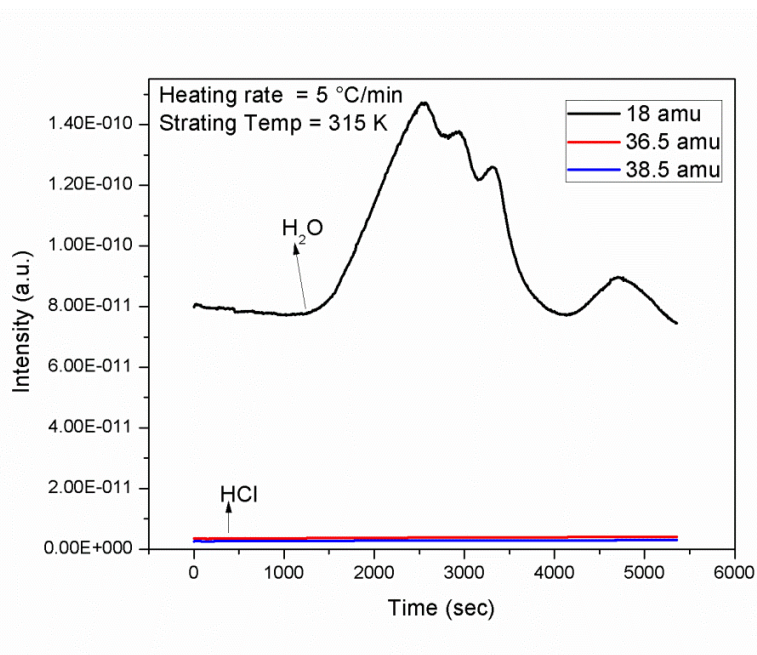


Fig.4.22 EGA plot of $\text{PrCl}_3 \cdot 7\text{H}_2\text{O}$ recorded at the heating rate of $5\text{ K}/\text{min}$ under 2.5 l/h flowing argon atmosphere.

Reaction Steps	Temperature range (K)	Calculated mass loss (%)	Vaporization reaction	Measured mass loss (%)
1	323-350	19.3	$\text{PrCl}_3 \cdot 7\text{H}_2\text{O}(\text{s}) = \text{PrCl}_3 \cdot 3\text{H}_2\text{O}(\text{s}) + 4\text{H}_2\text{O}(\text{g})$	19.1
2	350-368	4.8	$\text{PrCl}_3 \cdot 3\text{H}_2\text{O}(\text{s}) = \text{PrCl}_3 \cdot 2\text{H}_2\text{O}(\text{s}) + \text{H}_2\text{O}(\text{g})$	5.2
3	368-380	4.8	$\text{PrCl}_3 \cdot 2\text{H}_2\text{O}(\text{s}) = \text{PrCl}_3 \cdot \text{H}_2\text{O}(\text{s}) + \text{H}_2\text{O}(\text{g})$	4.8
4	410-445	4.8	$\text{PrCl}_3 \cdot \text{H}_2\text{O}(\text{s}) = \text{PrCl}_3(\text{s}) + \text{H}_2\text{O}(\text{g})$	4.5

Table-4.8 Measured and calculated mass loss for different vaporization reaction steps in the dehydration of $\text{PrCl}_3 \cdot 7\text{H}_2\text{O}$.

Based on the above observations the decomposition mechanism of the $\text{PrCl}_3 \cdot 7\text{H}_2\text{O}$ can be described as



4.3.3.2 Establishment of equilibrium condition

Fig.4.23 gives the apparent pressure versus flow rate of the carrier gas for $\text{PrCl}_3 \cdot 7\text{H}_2\text{O}(\text{s}) = \text{PrCl}_3 \cdot 3\text{H}_2\text{O}(\text{s}) + 4\text{H}_2\text{O}(\text{g})$ reaction measured at 335 K for eq. (4.22). From the figure it can be observed that the apparent pressure of water over the sample is independent of flow rate of the carrier gas in the flow rate region, 1.5 to 3.5 l/h, indicating the establishment of equilibrium condition. Similar experiments were carried for the vaporization reactions given in eq. (4.23), eq. (4.24) and eq. (4.25) under exactly similar conditions. A carrier gas flow rate of 2.4 l/h was therefore, chosen in the vapor pressure measurement experiments.

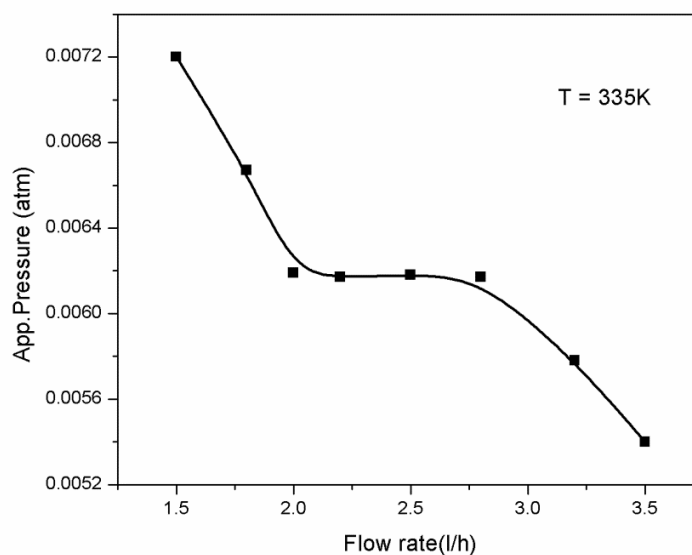


Fig.4.23 The apparent pressure versus flow rate of the carrier gas for $\text{PrCl}_3 \cdot 7\text{H}_2\text{O}(\text{s}) \rightarrow \text{PrCl}_3 \cdot 3\text{H}_2\text{O}(\text{s}) + 4\text{H}_2\text{O}(\text{g})$ reaction measured at 335 K.

4.3.3.3 Vapor pressure analysis

Table-4.9 gives the mass loss data for vaporization reactions steps. 4.22, 4.23, 4.24 and 4.25 respectively. The plots of $\ln p_{\text{H}_2\text{O}}$ versus $1/T$ for the above processes are given in **Fig.4.24-4.27**.

Mass loss step	Avg. Temp. (T/K)	Mass loss ($\Delta m/\mu\text{g}$)	Time ($\Delta t/\text{s}$)	Pressure ($P_{\text{H}_2\text{O}}/\text{atm}$)
Step-I	332	148.5	60	0.00504
	333	159.3	60	0.00541
	334	170.0	60	0.00577
	335	181.4	60	0.00616
	336	196.5	60	0.00667
	337	206.6	60	0.00701
	338	219.4	60	0.00745
	339	236.8	60	0.00804
Step-II	350	125.7	60	0.00427
	351	135.8	60	0.00461
	352	145.6	60	0.00494
	353	152.6	60	0.00518
Step-III	370	173.9	60	0.0059
	371	187.0	60	0.00635
	372	196.2	60	0.00666
	373	210.8	60	0.00715
	374	221.1	60	0.0075
Step-IV	416	150.67	60	0.00511
	417	160.95	60	0.00546
	418	167.78	60	0.00569
	419	179.66	60	0.0061
	420	186.64	60	0.00633

Table-4.9 Mass loss data for the step-I, step-II, step-III and step-IV of the vaporization reactions measured at carrier gas flow rate of 2.4 l/h (in the dehydration of $\text{PrCl}_3 \cdot 7\text{H}_2\text{O}$)

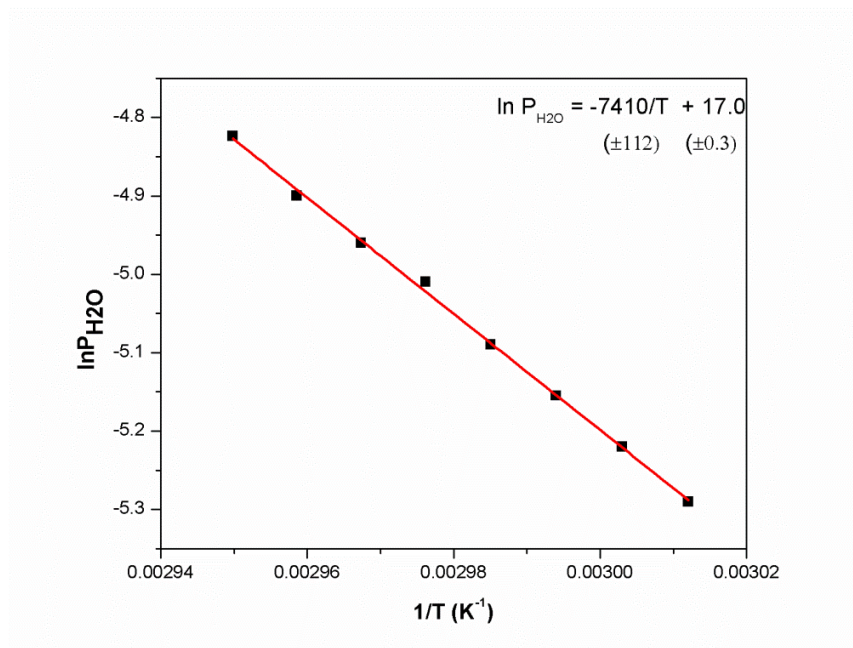


Fig.4.24 Plots of $\ln p$ versus $1/T$ for the vaporization reaction $\text{PrCl}_3 \cdot 7\text{H}_2\text{O}(\text{s}) \rightarrow \text{PrCl}_3 \cdot 3\text{H}_2\text{O}(\text{s}) + 4\text{H}_2\text{O}(\text{g})$ (Step-I).

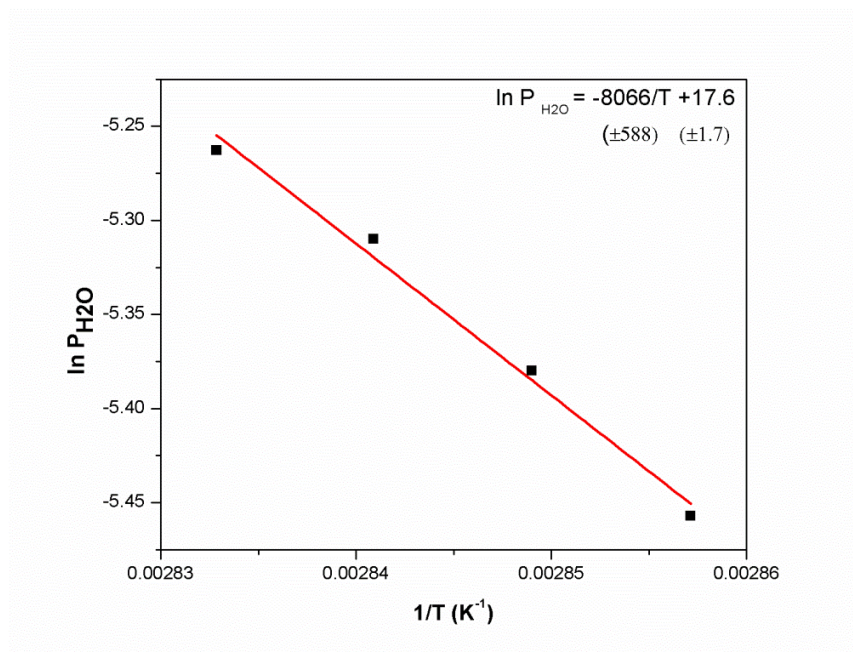


Fig.4.25 Plots of $\ln p$ versus $1/T$ for the vaporization reaction $\text{PrCl}_3 \cdot 3\text{H}_2\text{O}(\text{s}) \rightarrow \text{PrCl}_3 \cdot 2\text{H}_2\text{O}(\text{s}) + \text{H}_2\text{O}(\text{g})$ (Step-II)

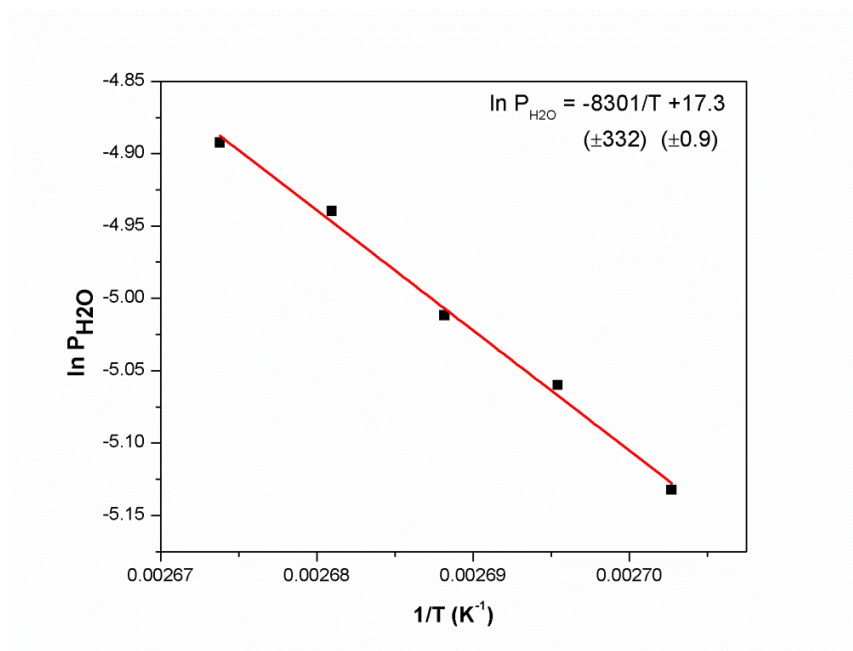


Fig.4.26 Plots of $\ln p$ versus $1/T$ for the vaporization reaction $\text{PrCl}_3 \cdot 2\text{H}_2\text{O}(\text{s}) \rightarrow \text{PrCl}_3 \cdot \text{H}_2\text{O}(\text{s}) + \text{H}_2\text{O}(\text{g})$ (Step-III)

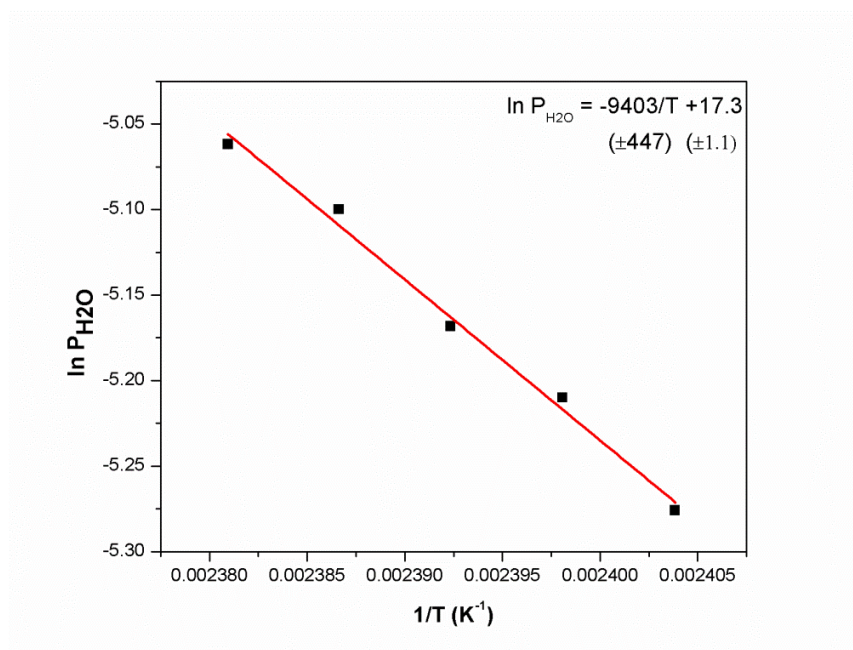


Fig.4.27 Plots of $\ln p$ versus $1/T$ for the vaporization reaction $\text{PrCl}_3 \cdot \text{H}_2\text{O}(\text{s}) \rightarrow \text{PrCl}_3(\text{s}) + \text{H}_2\text{O}(\text{g})$ (Step-IV)

The least square fitted linear equations could be expressed as

$$\ln P_{H_2O}(\pm 0.02) = \frac{-7410(\pm 112)}{T} + 17.0(\pm 0.3) \quad (332 < T/K < 339) \quad (4.26)$$

$$\ln P_{H_2O}(\pm 0.02) = \frac{-8066(\pm 588)}{T} + 17.6(\pm 1.7) \quad (350 < T/K < 353) \quad (4.27)$$

$$\ln P_{H_2O}(\pm 0.02) = \frac{-8301(\pm 332)}{T} + 17.3(\pm 0.9) \quad (370 < T/K < 374) \quad (4.28)$$

$$\text{and } \ln P_{H_2O}(\pm 0.02) = \frac{-9403(\pm 447)}{T} + 17.3(\pm 1.1) \quad (416 < T/K < 420) \quad (4.29)$$

The average standard molar enthalpy and entropy of vaporization for the respective reactions calculated from the slope and intercept of the plots are given in **Table-4.10** and have been compared with the available literature.

Reaction Steps	Vaporization reactions	ΔH^0_r (kJ mol ⁻¹) (This work)	ΔS^0_r (J mol ⁻¹ K ⁻¹) (This work)
1	$\text{PrCl}_3 \cdot 6\text{H}_2\text{O}(\text{s}) = \text{PrCl}_3 \cdot 3\text{H}_2\text{O}(\text{s}) + 4 \text{H}_2\text{O}(\text{g})$	246(±04)[335K]	562 (±10)[335 K]
2	$\text{PrCl}_3 \cdot 3\text{H}_2\text{O}(\text{s}) = \text{PrCl}_3 \cdot 2\text{H}_2\text{O}(\text{s}) + \text{H}_2\text{O}(\text{g})$	67 (±05) [352K]	146 (±14)[352K]
3	$\text{PrCl}_3 \cdot 2\text{H}_2\text{O}(\text{s}) = \text{PrCl}_3 \cdot \text{H}_2\text{O}(\text{s}) + \text{H}_2\text{O}(\text{g})$	69 (±03) [372K]	144 (±08)[372K]
4	$\text{PrCl}_3 \cdot \text{H}_2\text{O}(\text{s}) = \text{PrCl}_3(\text{s}) + \text{H}_2\text{O}(\text{g})$	78 (±07)[418K]	144 (±09)[418K]

Table-4.10 Values of standard molar enthalpies and entropies for the vaporization reactions in the dehydration of $\text{PrCl}_3 \cdot 7\text{H}_2\text{O}$.

4.3.3.4 Estimation of thermodynamic parameters

Gibbs energy of formation of PrCl_3 hydrates estimated as per the method described in section 4.3.1.5. were given below.

$$\Delta_f G_{\text{PrCl}_3 \cdot \text{H}_2\text{O}}^0 (\pm 0.03) = -1365 (\pm 04) + 0.43 (\pm 0.02) \times T \quad (416 < T/\text{K} < 420) \quad (4.30)$$

$$\Delta_f G_{\text{PrCl}_3 \cdot 2\text{H}_2\text{O}}^0 (\pm 0.03) = -1683 (\pm 05) + 0.43 (\pm 0.01) \times T \quad (370 < T/\text{K} < 374) \quad (4.31)$$

$$\Delta_f G_{\text{PrCl}_3 \cdot 3\text{H}_2\text{O}}^0 (\pm 0.06) = -1993 (\pm 07) + 0.62 (\pm 0.02) \times T \quad (350 < T/\text{K} < 353) \quad (4.32)$$

$$\Delta_f G_{\text{PrCl}_3 \cdot 7\text{H}_2\text{O}}^0 (\pm 0.07) = -3208 (\pm 10) + 1.4 (\pm 0.08) \times T \quad (336 < T/\text{K} < 342) \quad (4.33)$$

The standard molar enthalpy and entropy of formation of praseodymium chloride hydrates at mean temperature of measurements were given in the **Table-4.11**.

Compounds	$\Delta_f H^0$ (kJ mol ⁻¹) (This work)
$\text{PrCl}_3 \cdot 7\text{H}_2\text{O}$	-3208 (± 10) at 339 K
$\text{PrCl}_3 \cdot 3\text{H}_2\text{O}$	-1993 (± 07) at 352 K
$\text{PrCl}_3 \cdot 2\text{H}_2\text{O}$	-1683 (± 05) at 372 K
$\text{PrCl}_3 \cdot \text{H}_2\text{O}$	-1365 (± 04) at 418 K

Table-4.11 Values of standard molar enthalpies of formation of $\text{PrCl}_3 \cdot \text{XH}_2\text{O}(\text{s})$.

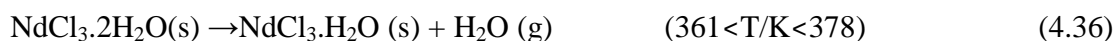
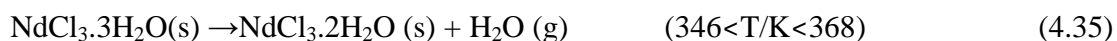
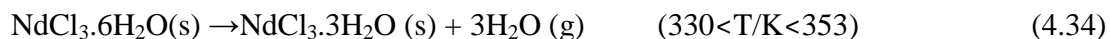
4.3.4 Determination of thermodynamic stability of NdCl₃ hydrates

4.3.4.1 Dehydration Mechanism

Fig.4.28 gives the TG plot of NdCl₃.6H₂O(s) recorded at the heating rates of 0.5, 2, 5 and 10 °C/min under 2.5 l/h flowing argon atmosphere. From **Fig.4.28** it could be observed that the sample decomposes in four successive steps in the temperature ranges 338-353 K, 353-368 K, 368-378 K and 413-448 K respectively with 15.06%, 5.1%, 5.02 and 4.9 % mass loss respectively. The mass loss steps are corresponding to the loss of 3, 1, 1, 1 water molecules in the 1st, 2nd, 3rd and 4th step respectively. **Table-4.11** gives the comparison of measured and calculated mass loss for different vaporization steps. **Fig.4.29** gives the plot of decomposition temperature versus heating rate for step-1, step-2, step-3 and step-4 for NdCl₃.6H₂O dehydration. The extrapolated decomposition temperatures to zero heating rate for step-1, step-2 and step-3 and step-4 are found to be 330, 346, 361 and 409 K respectively.

DTA plot of NdCl₃.6H₂O recorded at a heating rate of 5 °C/min (**Fig.4.30**) showed four endothermic peaks, corresponding to the loss of water molecules in four successive steps. The initial endothermic base line shift in the DTA plot in the temperature range 298-338 K is due to loss of adsorbed surface water.

Based on the above observations the decomposition mechanism of the NdCl₃.6H₂O can be described as



The above mechanism of decomposition of NdCl₃.6H₂O matches well with the reported data [87-88].

Reaction Steps	Temperature range (K)	Calculated mass loss (%)	Vaporization reaction	Measured mass loss (%)
1	338-353	15.7	$\text{NdCl}_3 \cdot 6\text{H}_2\text{O}(\text{s}) \rightarrow \text{NdCl}_3 \cdot 3\text{H}_2\text{O}(\text{s}) + 3\text{H}_2\text{O}(\text{g})$	15.06
2	353-368	5.02	$\text{NdCl}_3 \cdot 3\text{H}_2\text{O}(\text{s}) \rightarrow \text{NdCl}_3 \cdot 2\text{H}_2\text{O}(\text{s}) + \text{H}_2\text{O}(\text{g})$	5.1
3	368-372	5.02	$\text{NdCl}_3 \cdot 2\text{H}_2\text{O}(\text{s}) \rightarrow \text{NdCl}_3 \cdot \text{H}_2\text{O}(\text{s}) + \text{H}_2\text{O}(\text{g})$	5.02
4	413-448	5.02	$\text{NdCl}_3 \cdot \text{H}_2\text{O}(\text{s}) \rightarrow \text{NdCl}_3(\text{s}) + \text{H}_2\text{O}(\text{g})$	4.9

Table-4.12 Measured and calculated mass loss for different vaporization reaction steps in the dehydration of $\text{NdCl}_3 \cdot 6\text{H}_2\text{O}$.

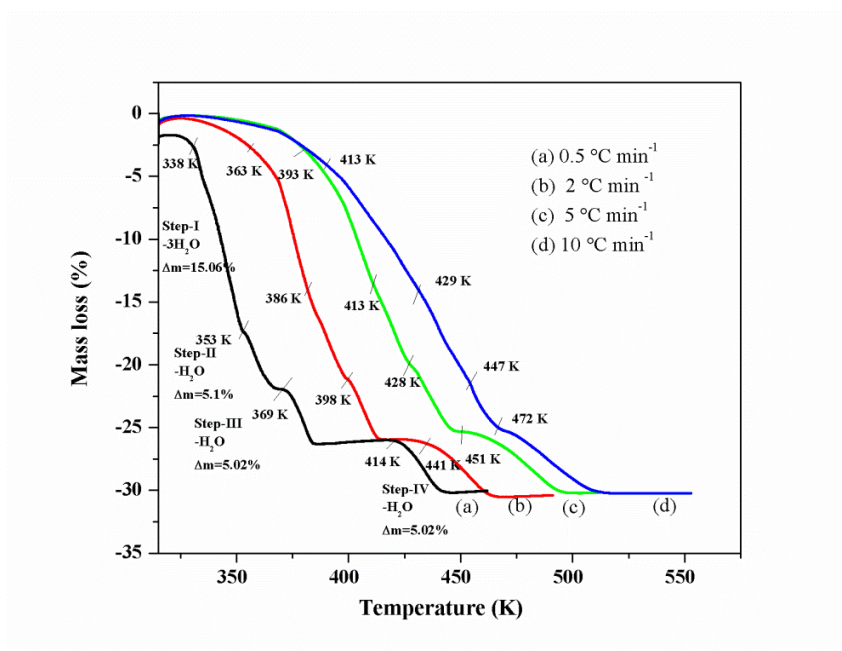


Fig.4.28 TG plot of $\text{NdCl}_3 \cdot 6\text{H}_2\text{O}$ recorded at the heating rate of 0.5, 2, 5 and 10 °C/min under 2.5 l/h flowing argon atmosphere.

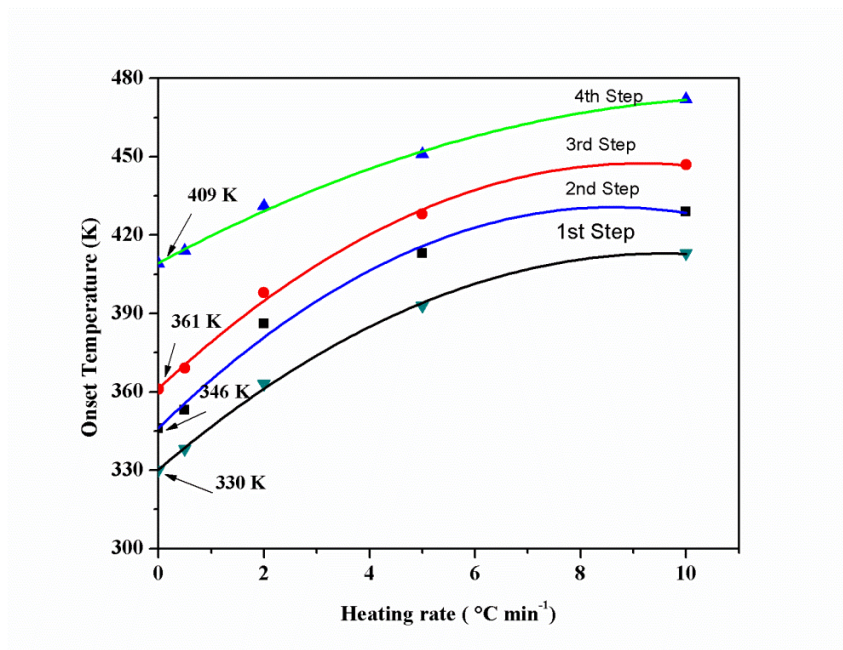


Fig.4.29 Plot of decomposition temperature versus heating rate for step-1, step-2, step-3 and step-4 of $\text{NdCl}_3 \cdot 6\text{H}_2\text{O}$ decomposition.

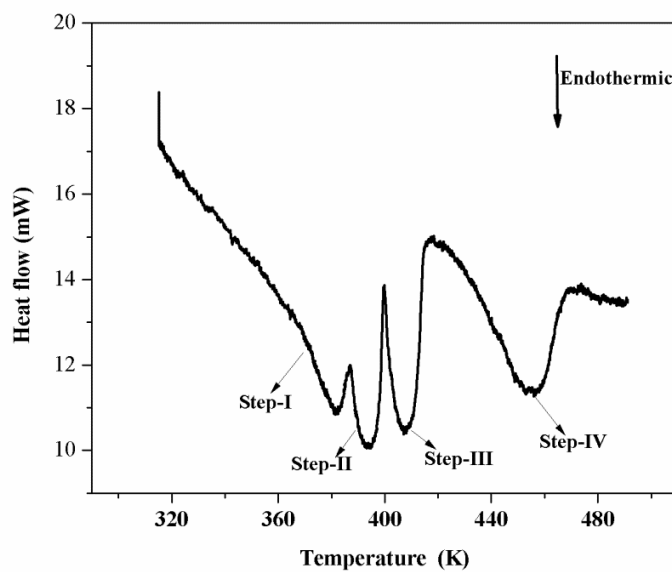


Fig.4.30 DTA plot of $\text{NdCl}_3 \cdot 6\text{H}_2\text{O}$ recorded at a heating rate of $5\text{ }^\circ\text{C}/\text{min}$ under $2.51/\text{h}$ flowing argon atmosphere

4.3.4.2 Characterization of NdCl_3 hydrates

In order to ascertain the decomposition mechanism, high temperature XRD patterns were recorded at the end each decomposition step. **Fig.4.31a** gives the HTXRD patterns of neodymium chloride hydrates recorded at 323, 353 and 368 K, whereas **Fig.4.31b** gives XRD patterns NdCl_3 hydrates recorded at 393 and 453 K. The XRD patterns recorded at 323 K is found to match well with the reported pattern of $\text{NdCl}_3 \cdot 6\text{H}_2\text{O}(\text{s})$ (JCPDF # 01-0131). However, no XRD data for the intermediate products recorded at 353 and 368 K corresponding to the intermediate compounds $\text{NdCl}_3 \cdot 3\text{H}_2\text{O}$ and $\text{NdCl}_3 \cdot 2\text{H}_2\text{O}$ are available in the literature for comparison. The XRD plots for these two products are found to be different from each other as well as from $\text{NdCl}_3 \cdot 6\text{H}_2\text{O}$ and $\text{NdCl}_3 \cdot \text{H}_2\text{O}$. Due to small intensity of the XRD plot it was not possible to refine the XRD data to derive crystallographic information and hence the data was used only for identification of the compounds. The XRD pattern recorded at 393 K matched well with reported pattern of $\text{NdCl}_3 \cdot \text{H}_2\text{O}(\text{s})$ (JCPDF #03-0139). XRD pattern recorded at 453 K shows the presence of NdCl_3 (JCPDF #75-1893) with small amount of NdOCl (JCPDF #08-0046). $\text{NdOCl}(\text{s})$ present in the sample could be due to the hydrolysis reaction in static air condition. The formation of $\text{NdOCl}(\text{s})$ could be avoided if the evolved water vapor is effectively flushed out and the heating temperature is controlled below 453 K. Thermal analyses of $\text{NdCl}_3 \cdot \text{XH}_2\text{O}$ experiments were carried out under the flow of argon gas to prevent the formation of oxychloride. The final products obtained after each transpiration measurement were verified not to have any NdOCl by HCl dissolution test which shows the complete solubility of NdCl_3 in HCl solution without any precipitate. The XRD pattern showed in Fig.4.31 also indicates that, the spectral peak intensity and sharpness decreases as temperature of the sample increases. This is due to progressive loss of water molecules crumbling of the crystal structure and formation

new crystal lattice with smaller crystallite size. Evolved gas analysis (**Fig.4.32**) of the sample indicates the loss of only water molecule over the entire range of mass loss steps. No mass peak for HCl molecules corresponding to the mass numbers 36 and 38 which could be produced by the hydrolysis of the $\text{NdCl}_3(\text{s})$ with the evolved water vapor could be observed, indicating that the moisture can be effectively removed if the sample is heated at slow rate under flowing argon atmosphere.

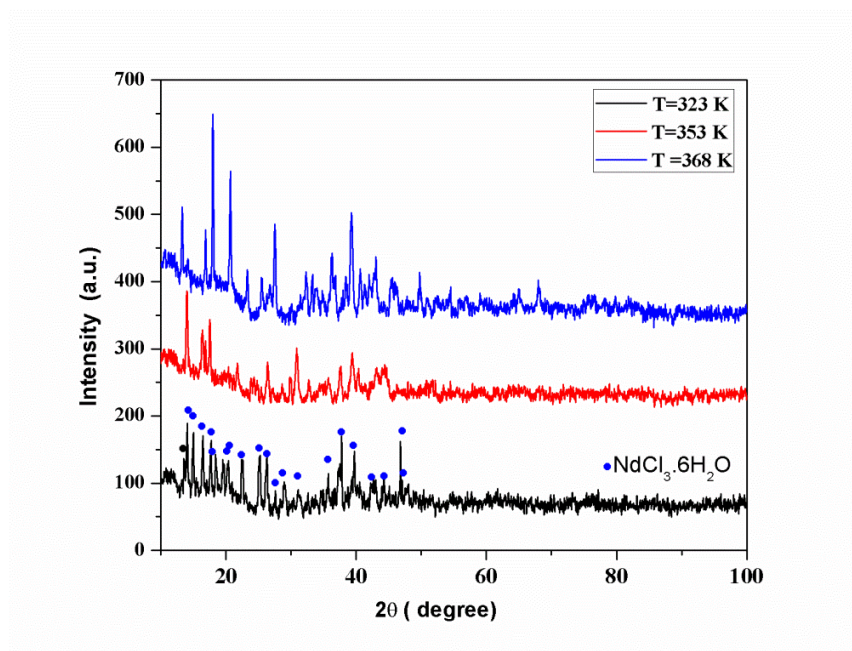


Fig.4.31a HTXRD patterns of $\text{NdCl}_3 \cdot x\text{H}_2\text{O}(\text{s})$ sample recorded at 323, 353 and 368 K.

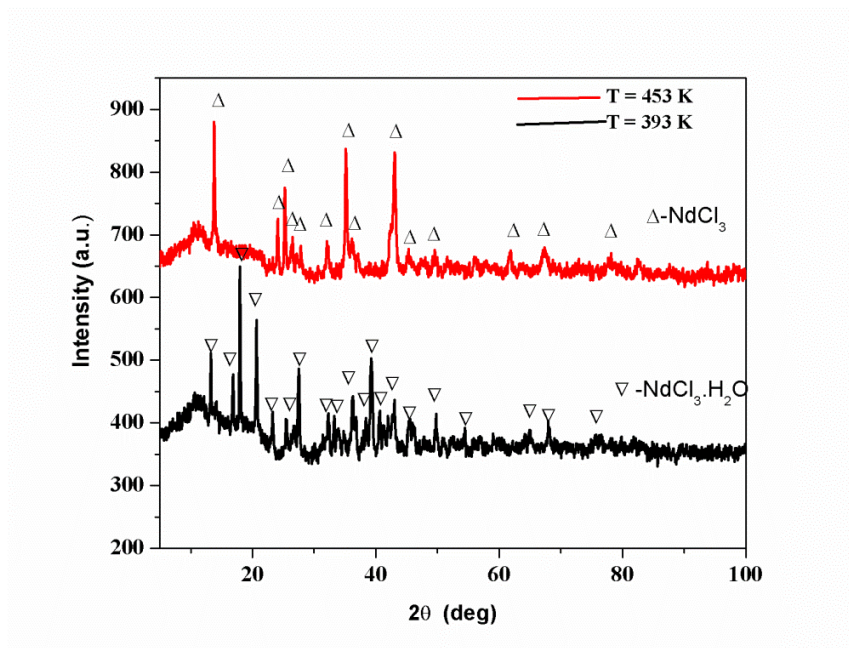


Fig.4.31b HTXRD patterns of $\text{NdCl}_3(\text{s})$ sample recorded at 393 and 453K.

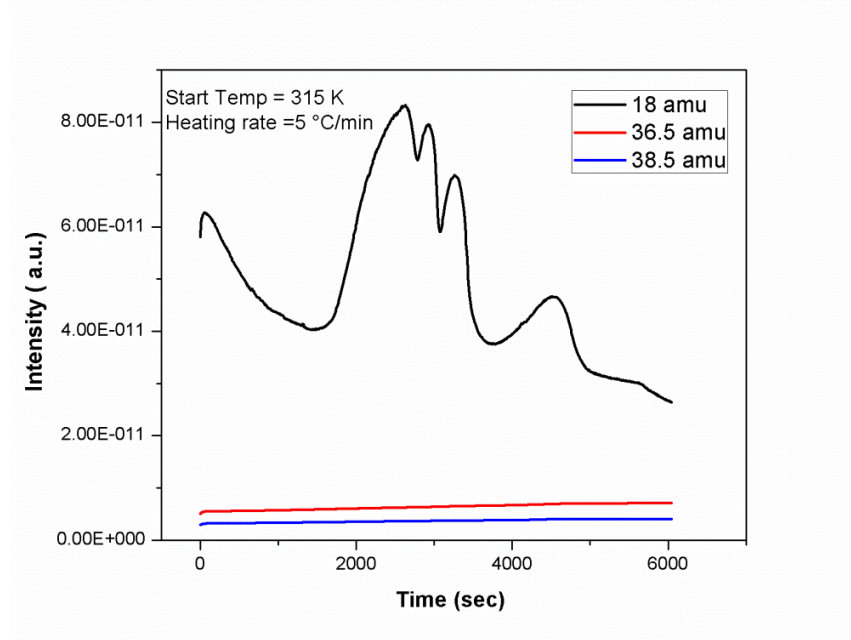


Fig.4.32 EGA plot of $\text{NdCl}_3 \cdot 6\text{H}_2\text{O}$ recorded at the heating rate of 5 °C/min under 2.5 l/h flowing argon atmosphere.

4.3.4.3 Establishment of equilibrium condition

Fig.4.33 gives the apparent pressure versus flow rate of the carrier gas for $\text{NdCl}_3 \cdot 6\text{H}_2\text{O}(\text{s}) = \text{NdCl}_3 \cdot 3\text{H}_2\text{O}(\text{s}) + 3\text{H}_2\text{O}(\text{g})$ reaction measured at 340 K for eq. (4.34). From the figure it can be observed that the apparent pressure of water over the sample is independent of flow rate of the carrier gas in the flow rate region, 2.0 to 3.5 l/h, indicating the establishment of equilibrium condition. Similar experiments were carried for the vaporization reactions given in eq. (4.35), eq. (4.36) and eq. (4.37) under exactly similar conditions. It was observed that in all these steps the flow rate independent region of the apparent pressure (plateau) also falls within 2 to 3.5 l/h. A carrier gas flow rate of 2.38 l/h was therefore, chosen in the vapor pressure measurement experiments. Care was taken in all these steps to restrict the mass loss measurements in the range 10- 30% of the expected total mass loss in respective cases. Similar experiments were carried out at flow rates i.e. 2.7 and 3.0 l/hr to ascertain the reproducibility.

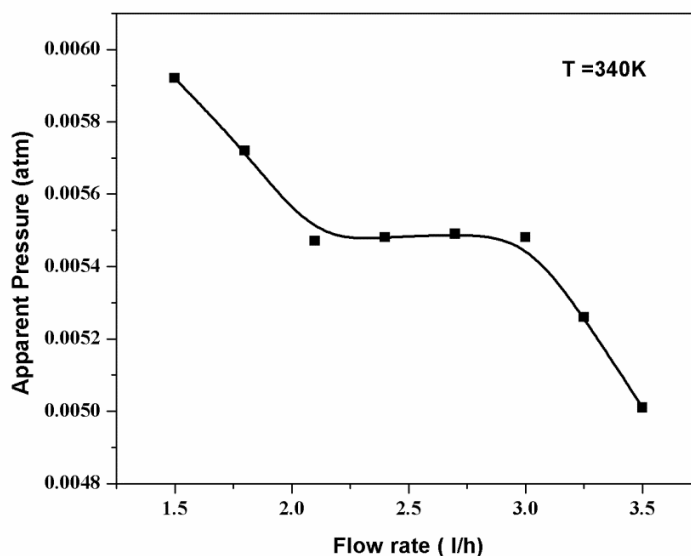


Fig.4.33 The apparent pressure versus flow rate of the carrier gas for $\text{NdCl}_3 \cdot 6\text{H}_2\text{O}(\text{s}) \rightarrow \text{NdCl}_3 \cdot 3\text{H}_2\text{O}(\text{s}) + 3\text{H}_2\text{O}(\text{g})$ reaction measured at 340 K.

4.3.4.4 Vapor pressure analysis

Table-4.13 gives the mass loss data for vaporization reactions eqns. 4.34 to 4.37 respectively.

The plots of $\ln p_{\text{H}_2\text{O}}$ versus $1/T$ for the above processes are given in Fig.4.34-4.37.

Mass loss step	Average Temp.(T/K)	Mass loss ($\pm\Delta m/\mu\text{g}$)	Time (At/s)	Apparent pressure $P(\text{H}_2\text{O})/\text{tam}$
Step-I	338	140.4	60	0.00481
	339	151.8	60	0.0052
	340	160.8	60	0.0055
	341	171	60	0.00586
	342	184.2	60	0.0063
Step-II	353	91.2	60	0.00312
	354	96.6	60	0.00331
	355	103.8	60	0.00355
	356	110.4	60	0.00378
Step-III	369	74.4	60	0.00254
	370	78.6	60	0.00269
	371	85.2	60	0.00291
	372	89.4	60	0.00149
Step-IV	423	68.4	60	0.00233
	424	72.6	60	0.00248
	425	75.6	60	0.00259
	426	79.8	60	0.00274

Table-4.13 Mass loss data for the step-1, step-II, step-III and step-IV of the vaporization reactions measured at carrier gas flow rate of 2.38 l/h (in the dehydration of $\text{NdCl}_3 \cdot 6\text{H}_2\text{O}$).

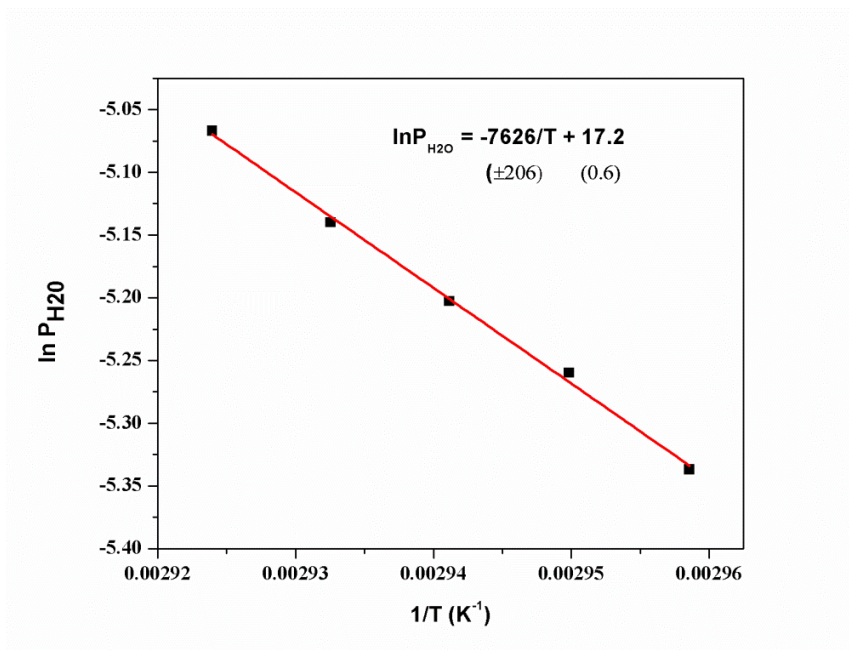


Fig.4.34 Plots of $\ln p$ versus $1/T$ for the vaporization reaction $\text{NdCl}_3 \cdot 6\text{H}_2\text{O}(\text{s}) \rightarrow \text{NdCl}_3 \cdot 3\text{H}_2\text{O}(\text{s}) + 3\text{H}_2\text{O}(\text{g})$ (Step-I).

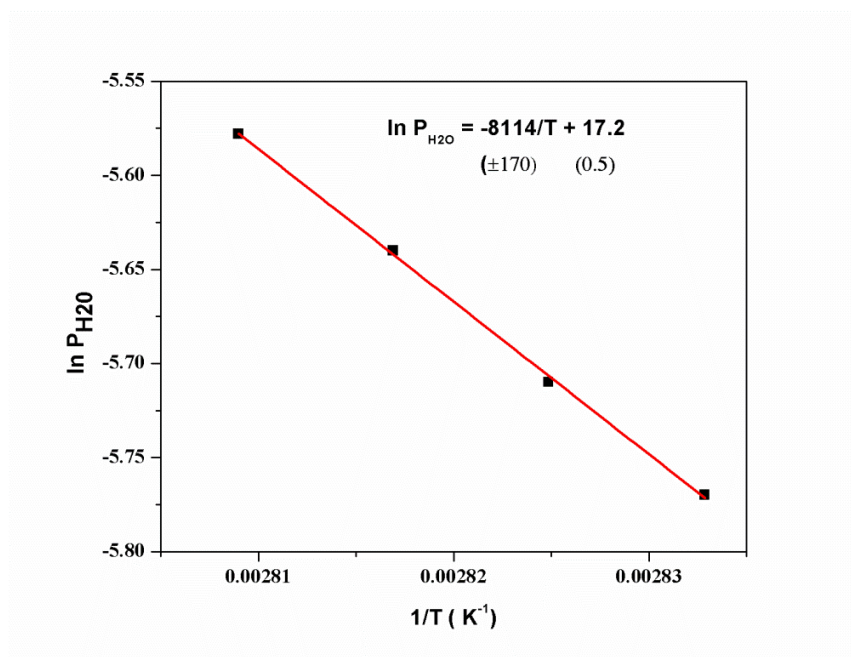


Fig.4.35 Plots of $\ln p$ versus $1/T$ for the vaporization reaction $\text{NdCl}_3 \cdot 3\text{H}_2\text{O}(\text{s}) \rightarrow \text{NdCl}_3 \cdot 2\text{H}_2\text{O}(\text{s}) + \text{H}_2\text{O}(\text{g})$ (Step-II),

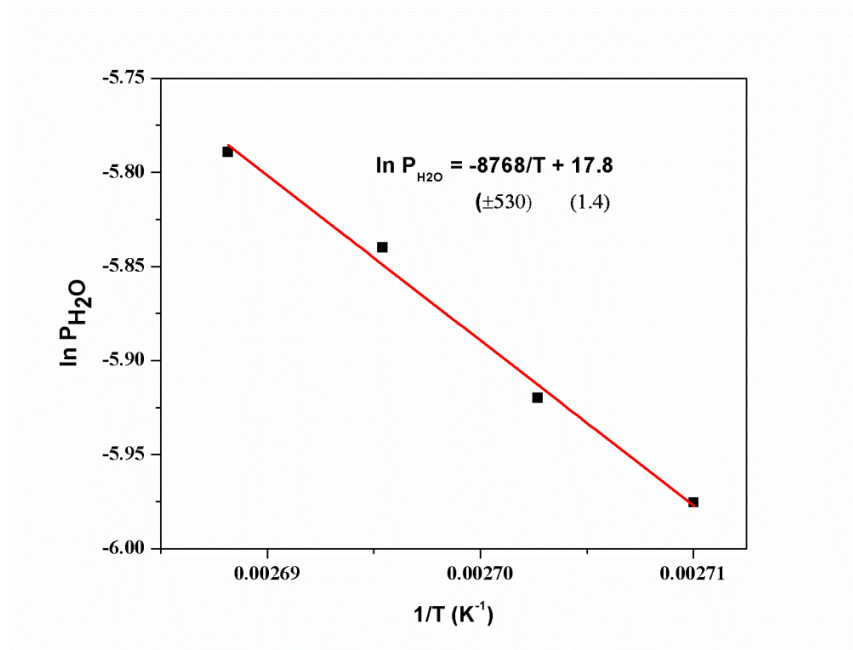


Fig.4.36 Plots of $\ln p$ versus $1/T$ for the vaporization reaction $\text{NdCl}_3 \cdot 2\text{H}_2\text{O}(\text{s}) \rightarrow \text{NdCl}_3 \cdot \text{H}_2\text{O}(\text{s}) + \text{H}_2\text{O}(\text{g})$ (Step-III),

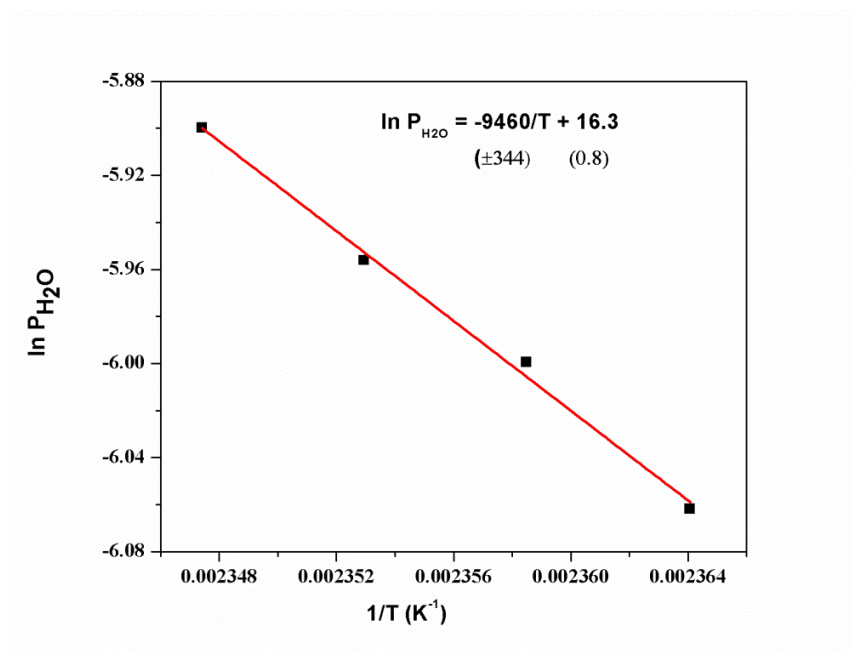


Fig.4.37 Plots of $\ln p$ versus $1/T$ for the vaporization reaction $\text{NdCl}_3 \cdot \text{H}_2\text{O}(\text{s}) \rightarrow \text{NdCl}_3(\text{s}) + \text{H}_2\text{O}(\text{g})$ (Step-IV),

The least square fitted linear equations could be expressed as

$$\ln P_{H_2O}(\pm 0.02) = \frac{-7626(\pm 206)}{T} + 17.2(\pm 0.6) \quad (338 < T/K < 342) \quad (4.38)$$

$$\ln P_{H_2O}(\pm 0.02) = \frac{-8114(\pm 170)}{T} + 17.2(\pm 0.5) \quad (353 < T/K < 356) \quad (4.39)$$

$$\ln P_{H_2O}(\pm 0.02) = \frac{-8768(\pm 530)}{T} + 17.8(\pm 1.4) \quad (369 < T/K < 372) \quad (4.40)$$

$$\ln P_{H_2O}(\pm 0.02) = \frac{-9460(\pm 344)}{T} + 16.3(\pm 0.8) \quad (423 < T/K < 427) \quad (4.41)$$

The average standard molar enthalpy and entropy of vaporization for the respective reactions described in Eqns. (4.34) - (4.37) calculated from the slope and intercept of the plots are given in **Table-4.14** and have been compared with the available literature.

Reaction Steps	Vaporization reactions	ΔH_r^0 (kJ mol ⁻¹) (This work)	ΔH_r^0 (kJ mol ⁻¹) (Literature) [148] at 298K	ΔS_r^0 (J mol ⁻¹ K ⁻¹) (This work)	ΔS_r^0 (J mol ⁻¹ K ⁻¹) (Literature) [148] At 298 K
1	NdCl ₃ .6H ₂ O(s) = NdCl ₃ .3H ₂ O(s) + 3 H ₂ O (g)	191(±7) [340K]	176.7	431 (±19) [340 K]	427.1
2	NdCl ₃ .3H ₂ O(s) = NdCl ₃ .2H ₂ O(s) + H ₂ O (g)	68 (±2) [355K]	66.1	144 (±05) [355K]	142.4
3	NdCl ₃ .2H ₂ O(s) = NdCl ₃ .H ₂ O(s) + H ₂ O (g)	71 (±4) [370K]	68.3	145 (±10) [370K]	144.8
4	NdCl ₃ .H ₂ O(s) = NdCl ₃ (s) + H ₂ O (g)	80 (±2) [425K]	73.0	139 (±03) [425K]	142.4

Table-4.14 Comparison of values of standard molar enthalpies and entropies for the vaporization reactions steps 4.34 to 4.37 (in the dehydration of NdCl₃.6H₂O).

4.3.4.5 Estimation of thermodynamic parameters

Gibbs energy of formation of NdCl₃ hydrates estimated as per the method described in section 4.3.1.5. were given below.

$$\Delta_f G_{NdCl_3, H_2O}^0 (\pm 0.03) = -1357(\pm 03) + 0.42(\pm 0.02) \times T \quad (423 < T/K < 427) \quad (4.42)$$

$$\Delta_f G_{NdCl_3, 2H_2O}^0 (\pm 0.03) = -1673(\pm 05) + 0.61(\pm 0.02) \times T \quad (369 < T/K < 372) \quad (4.43)$$

$$\Delta_f G_{NdCl_3, 3H_2O}^0 (\pm 0.06) = -1984(\pm 05) + 0.80(\pm 0.02) \times T \quad (353 < T/K < 356) \quad (4.44)$$

$$\Delta_f G_{NdCl_3, 6H_2O}^0 (\pm 0.07) = -2904(\pm 07) + 1.4(\pm 0.04) \times T \quad (336 < T/K < 342) \quad (4.45)$$

Compounds	$\Delta_f H^0$ (kJ mol ⁻¹) (This work)	$\Delta_f H^0_{298K}$ (kJ mol ⁻¹) (Literature) [154]
NdCl ₃ .6H ₂ O	-2904 (±07) [339K]	-2866
NdCl ₃ .3H ₂ O	-1984 (±05) [355K]	-1964
NdCl ₃ .2H ₂ O	-1673 (±05) [370]	-1657
NdCl ₃ .H ₂ O	-1357 (±03) [425K]	-1347

Table-4.15 Comparison of values of standard molar enthalpies of formation of NdCl₃.XH₂O(s).

4.4 Summary:

The equilibrium decomposition temperature of $\text{LaCl}_3 \cdot 7\text{H}_2\text{O}$, $\text{CeCl}_3 \cdot 7\text{H}_2\text{O}$, $\text{PrCl}_3 \cdot 7\text{H}_2\text{O}$ and $\text{NdCl}_3 \cdot 6\text{H}_2\text{O}$ obtained from TG curve with extrapolated heating rate $0^\circ\text{C}/\text{min}$ to the corresponding intermediate hydrates are listed in **Table-4.16**.

Compound	$7\text{H}_2\text{O}$ (K)	$6\text{H}_2\text{O}$ (K)	$3\text{H}_2\text{O}$ (K)	$2\text{H}_2\text{O}$ (K)	$\Delta \text{H}_2\text{O}$ (K)
$\text{LaCl}_3 \cdot \text{XH}_2\text{O}$	314		359		393
$\text{CeCl}_3 \cdot \text{XH}_2\text{O}$	318		346	359	407
$\text{PrCl}_3 \cdot \text{XH}_2\text{O}$	318		345	360	408
$\text{NdCl}_3 \cdot \text{XH}_2\text{O}$		330	346	361	409

Table-4.16 Equilibrium decomposition temperatures of $\text{RECl}_3 \cdot \text{XH}_2\text{O}$ (RE =La, Ce, Pr and Nd).

From the Table-4.16, it could be observed the decomposition temperatures of the corresponding hydrates do not vary much from La to Nd. This indicates that the water molecules are bound to the crystal lattice with similar bond energy, which could be explained by the negligible difference in the charge to radius ratio between La^{3+} , Ce^{3+} , Pr^{3+} and Nd^{3+} ; the crystal structure being remain same.

$\text{RECl}_3 \cdot \text{XH}_2\text{O}$ was found to lose water in molecules in multiple steps leading to the formation of 2-3 intermediate products. The enthalpies and entropies of formation of compounds obtained in the present study are summarized in **Table-4.17** and **4.18** respectively.

Compound	$\Delta_f H^0$	$\Delta_f H^0$	$\Delta_f H^0$ of	$\Delta_f H^0$	$\Delta_f H^0$
	7H ₂ O	6H ₂ O	3H ₂ O	2H ₂ O	1 H ₂ O
	in kJ mol ⁻¹				
LaCl ₃ .XH ₂ O	-3226±13		-2006±11		-1381±10
CeCl ₃ .XH ₂ O	-3213±19		-1991±10	-1683±09	-1367±09
PrCl ₃ .XH ₂ O	-3208±10		-1989±07	-1677±05	-1365±04
NdCl ₃ .XH ₂ O		-2904±07	-1984±05	-1677±05	-1357±03

Table-4.17 Enthalpy of formation of RECl₃.XH₂O (RE =La, Ce, Pr and Nd)

Compound	$\Delta_f S^0$ of 7H ₂ O	$\Delta_f S^0$ of 6H ₂ O	$\Delta_f S^0$ of 3H ₂ O	$\Delta_f S^0$ of 2H ₂ O	$\Delta_f S^0$ of H ₂ O
	in J mol ⁻¹ K ⁻¹				
LaCl ₃ .XH ₂ O	1100±100		600±10		360±10
CeCl ₃ .XH ₂ O	1600±90		800±30	620±20	420±20
PrCl ₃ .XH ₂ O	1400±80		820±20	630±20	430±20
NdCl ₃ .XH ₂ O	1400±40		800±20	610±20	420±20

Table-4.18 Enthalpy of formation of RECl₃.XH₂O (RE =La, Ce, Pr and Nd)

The trend in enthalpy of formation RECl₃.XH₂O were found to in the same order as that of pure RECl₃. This indicates that configurational arrangement and the bond strength of molecules in respective RECl₃ hydrates are same.

The equilibrium vapor pressure of water measured in the present investigation over RECl₃ hydrates is found to be in the order 10⁻³ atm at 425 K. This means that, if the sample can be dried under a dynamic vacuum less than 10⁻³ atm it is possible to effectively remove the crystallized water by heating at 425 K, where the possibility of oxychloride formation is negligible.

The present study suggests that for the effective removal of crystallized water, the sample should be heated maximum up to 473 K in dynamic vacuum of 10^{-4} atm. This is a simple and effective method.

To prove the above point, experiment was carried out to dehydrate $RECl_3 \cdot xH_2O$ (RE = La, Ce, Pr and Nd) by slowly heating the samples up to 473 K under dynamic vacuum of 0.1 mbar to obtain $RECl_3$. The schematic diagram for removal of water molecules is shown in Fig.4.38. The escaping water vapor was collected by using liquid nitrogen traps.

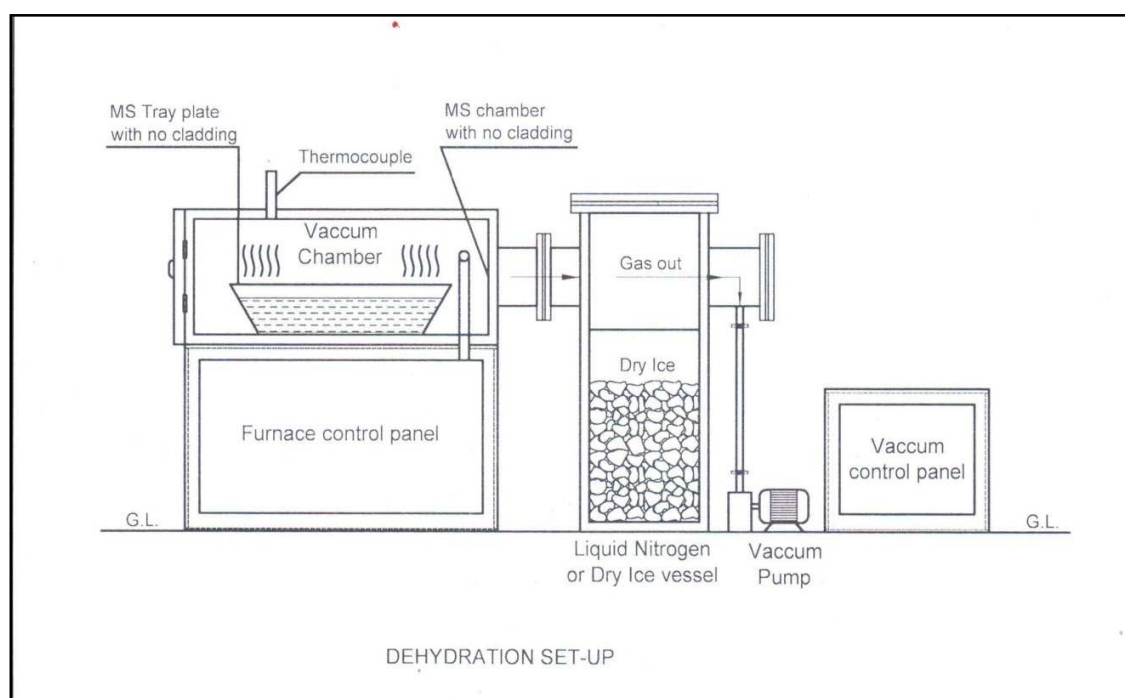


Fig.4.38 Schematic of the dehydration set-up used in the present investigation

Two measurements were taken to avoid the formation of oxychloride in the present study. First, the dehydration was carried out under a slow heating rate ($2\text{ }^{\circ}\text{C}/\text{min}$) and maximum temperature of dehydration was kept below 473 K. As the hydrolysis reaction begins to take place above 473

K, the heating temperature was controlled below. Secondly, large surface area was provided to the sample and step wise dehydration was carried out to prevent the hydrolysis reaction which could occur due the kinetic hindrance in the evacuation of decomposed water molecules. The dehydrated RECl_3 obtained in our study were dissolved in dilute HCl solution to check the purity of the compound. It was observed that the chlorides were completely dissolved in dilute HCl without any precipitate which could form due to the presence of oxychloride.

ELECTROCHEMICAL BEHAVIOR OF RE (III) IONS IN ALKALI CHLORIDE MELTS

5.1 Introduction:

Molten chloride electrolysis for making rare earth metals is attractive because of low cost, ease of operation, batch size and purity of the product. The process is particularly attractive for the synthesis of light rare earth metals and alloys [55]. The electrolytes used in such process are mostly rare earth chlorides with mixtures of alkali or alkaline chlorides. The hygroscopic nature of alkaline earth chlorides makes them unfavorable over alkali earth chlorides. LiCl-KCl and NaCl-KCl are the most common solvents used for such purposes [74]. The major problem associated with molten chloride electrolysis is the low current efficiency which limits the wide spread and easy implementation of this process. The motivation of this research is to study the kinetic properties of molten salt-electrode reaction which could affect current efficiency in the electrowinning of rare earth metals.

It is important to study the electrochemistry of rare earth (RE) ions in molten chloride medium for the effective use of molten salt electrolysis technology in the extraction of RE metals. In the present work, the electrochemical behavior of RE ions in LiCl-KCl and NaCl-KCl melts has been investigated using molybdenum and tungsten electrodes. Various studies were carried out on electrochemical investigations of RE (La, Ce, Pr and Nd) ions molten chloride electrolytes [89-102]. Most of these literatures reported the thermodynamic properties compared to kinetic parameters. Moreover, the kinetic data reported by some researchers are not consistent due to

different experimental conditions like salt composition and material of working electrodes. Apart from that, electrochemical data of the reduction of RE (III) in NaCl-KCl are rarely found in the literatures, although it is considered as a better media to get the metal ingot. Therefore, Present study was carried out to investigate the electrochemical properties of RE (III) both in LiCl-KCl and NaCl-KCl melt on inert electrodes (Tungsten and Molybdenum) at higher operational temperatures compared to previous studies to get the inherent mechanism and kinetics of electrochemical process. Higher operational temperature also allowed us to compare the kinetic parameters of the electrochemical process in LiCl-KCl medium with that of NaCl-KCl medium. The aim was to first probe the reaction mechanism and to determine the kinetic parameters like diffusion coefficient and exchange current densities which are important and relevant in the formation of RE metal by electrochemical deposition from molten salts mixtures. The results may help to do further research in the efficient extraction of rare earth metals by electrolytic reduction process.

5.2 Experimental Details

5.1.1 Preparation and purification of the electrolyte

The starting materials used were $\text{RECl}_3 \cdot \text{XH}_2\text{O}$ (99% pure) from Indian Rare Earths Limited. Potassium chloride, sodium chloride and lithium chloride having 99.5% purity of LR Grade used in the study were procured from Local supplier in Mumbai.

RECl_3 available in the market are highly hygroscopic and contains more than 35 weight % crystallized water and adsorbed moisture. The hydrated chlorides ($\text{RECl}_3 \cdot \text{XH}_2\text{O}$) were dehydrated by step wise heating under dynamic vacuum of 0.1mbar up to 473 K for 24 hours as discussed in the section 4.4. The final product obtained were verified not to have any REOCl by

HCl dissolution test which shows the complete solubility of RECl_3 in HCl solution without any precipitate.

Mixture of LiCl-KCl (in 1:1 molar ratio) was dehydrated at 473 K for 12 hours to remove adsorbed moisture. Similar procedure was followed to dehydrate equimolar mixture of NaCl-KCl. The chloride mixtures LiCl-KCl and NaCl-KCl were melted in an alumina crucible placed inside a tubular furnace under the inert Argon atmosphere. Inside temperature of the furnace was measured with a K-type thermocouple protected by an alumina tube. Calculated amount of anhydrous RECl_3 was put into the treated LiCl-KCl and NaCl-KCl melts. The total concentrations of lanthanum ion in both the prepared salts were measured by ICP-AES analysis.

5.1.2 Electrolytic cell

The experiments were carried out under inert argon atmosphere using a specially designed electrochemical cell. It consists of a vacuum tight inconel retort of 70 mm diameter and 500mm length fitted with a stainless steel flange which is having provisions for placing of working electrode, counter electrode, reference electrode, and thermocouple. Electrolytic mixture was charged into an alumina crucible which was kept inside the inconel retort. The whole electrochemical cell was kept inside a tubular vertical resistance furnace. The resistance furnace with electronic temperature control unit (± 2 K) was used to heat the cell up to the operating temperature. The schematic of the electrolytic set-up is shown in **Fig.5.1**.

5.1.3 Electrochemical apparatus and electrodes:

A three electrode system was used for the electrochemical measurements. The working electrode consists of 1mm (diameter) molybdenum or tungsten wires. Other Tungsten wires of 2mm and 1 mm diameter were employed as the counter and quasi reference electrode

respectively. The surface of each electrode were polished with emery paper of 1200 grit and then cleaned with acetone. The surface area of the working electrode was measured by standard area addition method together with CV. Cyclic voltammtery plots were generated for different immersion depth of working electrode and corresponding current was monitored keeping all other parameters constant like temperature, concentration of the electrolyte and value of applied potential. Plotting the cathodic peak current as a function of immersion depth (surface area) of the working electrode generated a linear plot (**Fig.5.2**) from which initial area of the electrode was calculated. Consistent results were obtained in measuring the surface area of the working electrode when similar experiments were carried out different temperature also.

All the electrochemical measurements were carried out using IM6 electrochemical workstation (Zahner Co. Ltd. Germany). The voltammograms were recorded and analyzed using THALES 2.10 software package.

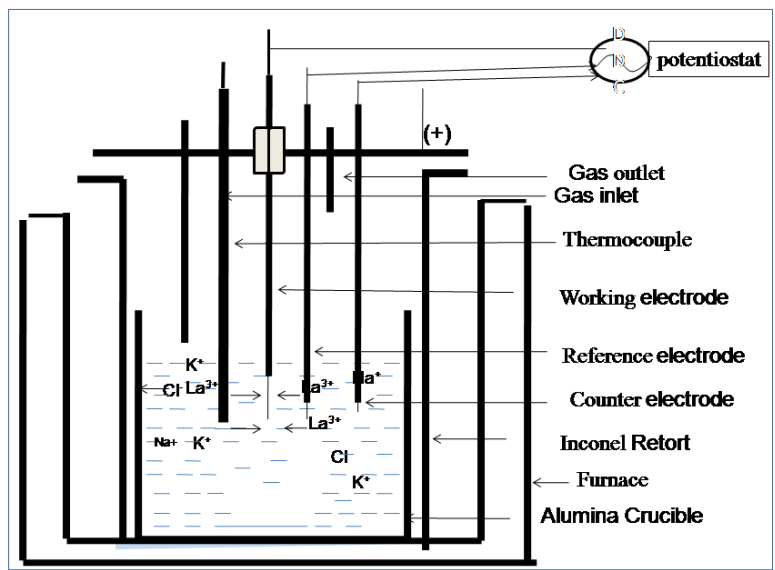


Fig.5.1 The schematic view of the electrochemical set-up used in the cyclic voltammetry measurement.

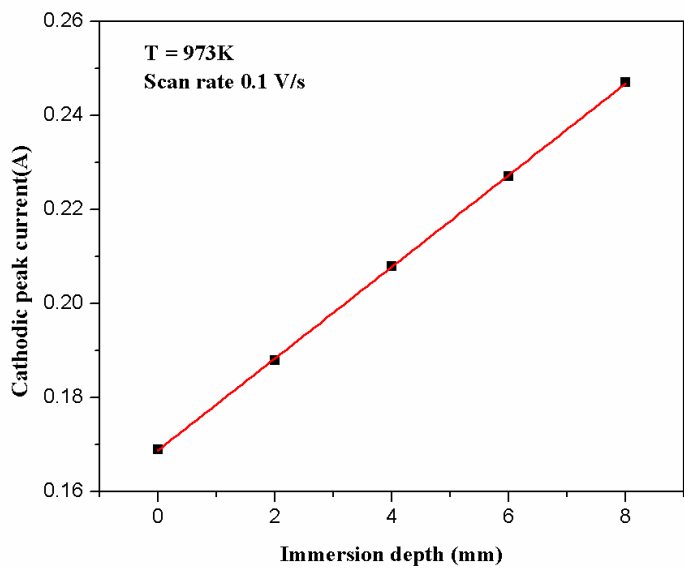


Fig.5.2 Variations of cathodic peak current vs. immersion depth of working electrode in LaCl_3 - LiCl-KCl melt. Concentration of La: 2.5×10^{-4} mole per cc, Temperature: 973K.

5.2 Results and discussion

5.2.1 Electrochemical investigation of LaCl_3 in alkali chloride melts

In this subsection the electrochemical characteristics of La (III) in molten salt electrolyte media was discussed.

5.2.1.1 Reduction behavior of La (III) in LiCl-KCl and NaCl-KCl system characterized by cyclic voltammetry technique

Fig.5.3 shows the comparison between the voltammograms obtained using LiCl-KCl electrolyte before and after addition of LaCl_3 over a potential range of 1 to -2.5V. The dashed curve of **Fig.5.3** shows the electrochemical window obtained in equimolar LiCl-KCl melt. The anodic discharge was observed at more positive potential to 0.5 V during anodic potential scan in blank molten salt electrolyte. This was due to the evolution of Cl_2 gas, thus 0.5 V is the anodic limit of the melt. Similarly, cathodic discharge was observed at around more negative to -2.4 V, this cathodic discharge was due to the deposition of Li ion, thus -2.4 V was attributed to the cathodic limit of the melt. After addition of LaCl_3 , a cathodic peak (I_c) at -2.05 V and the corresponding anodic peak (I_a) at -1.87 V were observed. The sharp anodic peak observed in the reverse scan is typical signature of the dissolution of the deposited metal. Thus, the observed pair of peaks could be due to the deposition and dissolution of lanthanum metal. To substantiate this assumption, energy dispersive X-ray fluorescence (EDXRF) analysis was employed to characterize the deposited product obtained after potentiostatic electrolysis at -2.1 V for 10 minutes. **Fig.5.4** shows the EDXRF analysis of the deposited product which confirmed the formation of lanthanum metal on electrochemical deposition.

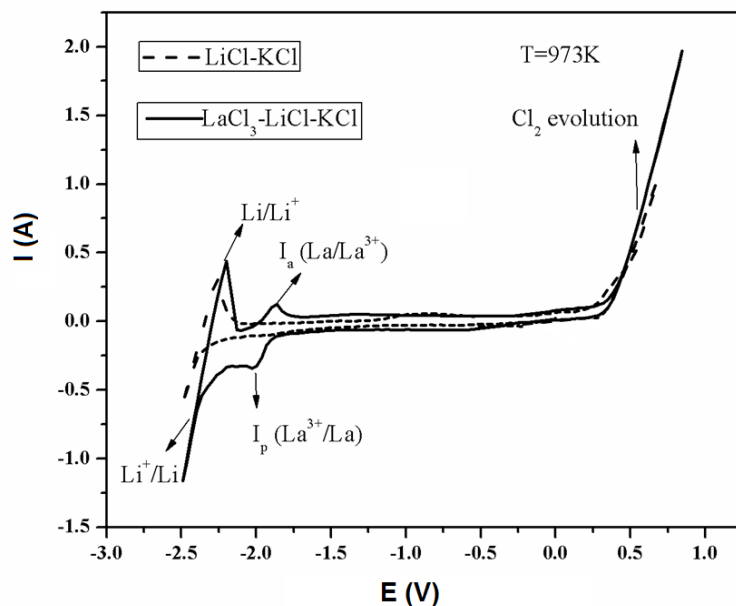


Fig.5.3 Comparison of the cyclic voltammogram for pure LiCl-KCl melt and LaCl₃-LiCl-KCl melt in the potential range of 1 to -2.5V. Working electrode: molybdenum, apparent electrode area: 0.77 cm², Temperature: 973K, Conc.: 2.5×10^{-4} mol/cc, scan rate: 0.1 Vs⁻¹.

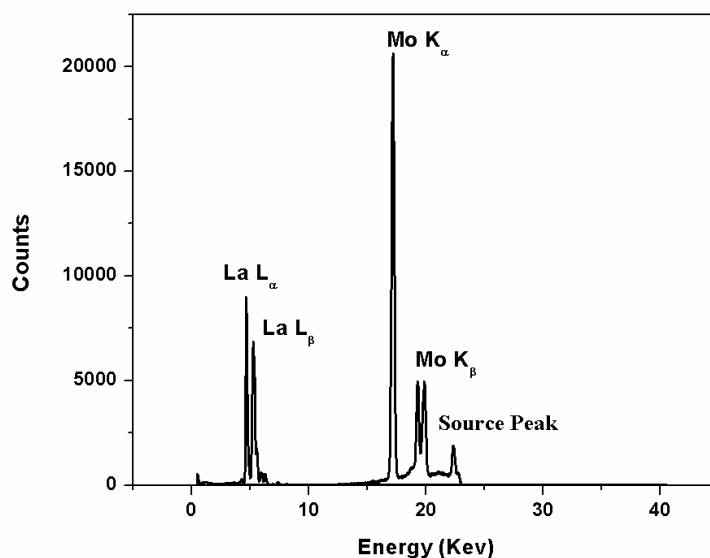


Fig.5.4 EDXRF spectra of the deposit (metallic lanthanum) on Mo electrode obtained under potentiostatic condition in equimolar LiCl-KCl mixture at 973K (-2.1V).

This substantiated the fact that the observed peak at -2.05 V after addition of LaCl_3 was due to the reduction of lanthanum ion to metallic lanthanum and the peak obtained in the reverse scan at -1.87 V was due to the dissolution of metallic lanthanum in the melt. The shapes of cathodic and anodic peaks are typical characteristics of soluble-insoluble exchange as described by Vandrakuzhali et.al. [97]. Morphology of the deposited lanthanum metal was investigated from scanning electron microscopy (SEM) and the micrograph is shown in **Fig.5.5**. The solidified melt was washed out with hexane prior to SEM characterization. Uniform crystallite size was observed with the average crystal diameter of $5\text{-}8\ \mu\text{m}$

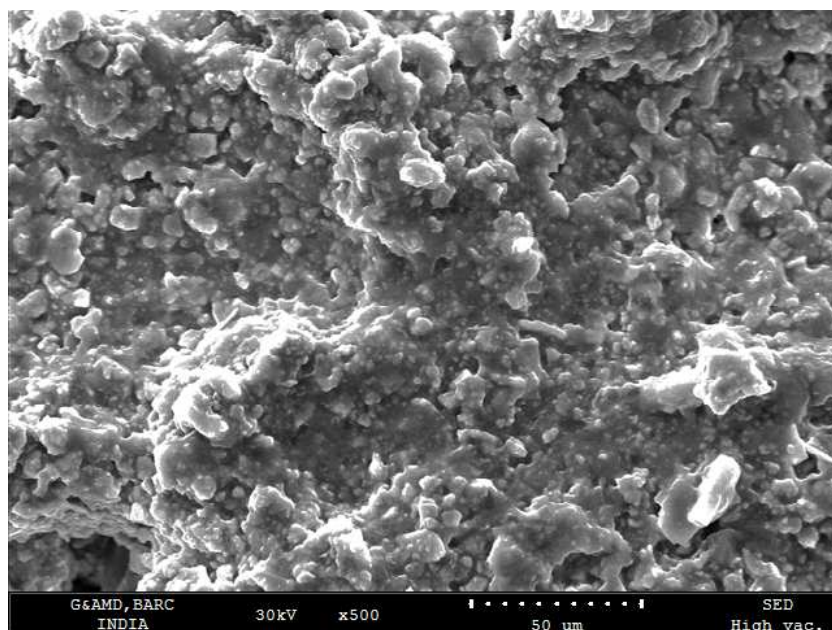


Fig.5.5 SEM micrograph of the deposit product (metallic lanthanum) obtained under potentiostatic condition in equimolar LiCl-KCl mixture at 973K (-2.1 V).

Though the electrochemical processes might be happening through multiple steps, present investigations could not resolve those elementary steps rather a broad peak due to the three

electron transfer process was observed. Electrochemical reduction of La (III) to La (0) was reported previously as one step three electron transfer process [91-93].

Cyclic voltammetric measurements were also carried out for the reduction of LaCl_3 in equimolar NaCl-KCl melt. **Fig.5.6.** shows the comparison between the voltammograms obtained using NaCl-KCl electrolyte before and after addition of LaCl_3 over a potential range of 0 to -2.75V at a scan rate of 0.025V/s.

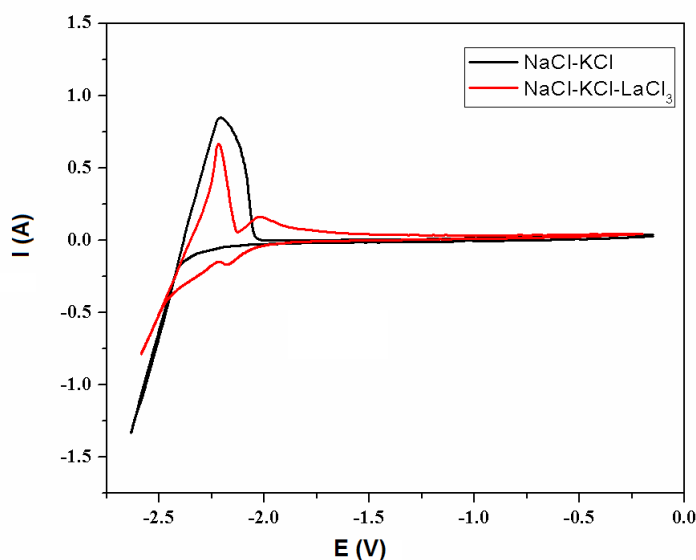


Fig.5.6 Comparison of the cyclic voltammogram for pure NaCl-KCl melt and LaCl_3 -NaCl-KCl melt in the potential range of 0 to -2.75V. Working electrode: Molybdenum, apparent electrode area: 0.30cm^2 , Temperature: 973K, scan rate: 0.025Vs^{-1} .

The black curve shows the spectra of the NaCl-KCl melt and the red curve represents the spectra after addition of LaCl_3 into the molten NaCl-KCl electrolyte at 973K. As seen from the figure on addition of LaCl_3 , a clear cathodic and corresponding sharp anodic peak due to the deposition and dissolution of lanthanum were appeared. The possibility of co-deposition of lanthanum and sodium to form La-Na intermetallics was verified by carrying the potentiostatic electrolysis at -

2.2 V for 10 minutes and the deposited product was analyzed by atomic absorption spectroscopy (AAS). AAS has revealed the presence of only lanthanum in the deposits, presence of Na was not observed from AAS measurements.

5.2.1.2 Reversibility of the electrode Process

Cyclic voltammetry was carried out in both the melts at various scan rates in the temperature range of 973K to 1053 K to investigate the dependence of peak potential and peak current on polarization rate. **Fig.5.7** represents the voltammograms recorded in molten LaCl_3 (2.5×10^{-4} mole/cc) in equimolar LiCl-KCl electrolyte at 973K at different scan rates. In order to obtain the contribution from the back ground current the cyclic voltammetry plot of La reduction in LiCl-KCl molten media were corrected with respect to the background plots at the corresponding scan rates. **Fig.5.8** shows the back ground curves i.e. the voltammetric curves obtained only in LiCl-KCl melt at 973K. Corresponding back ground corrected cyclic voltammetry plots are shown in **Fig.5.9**.

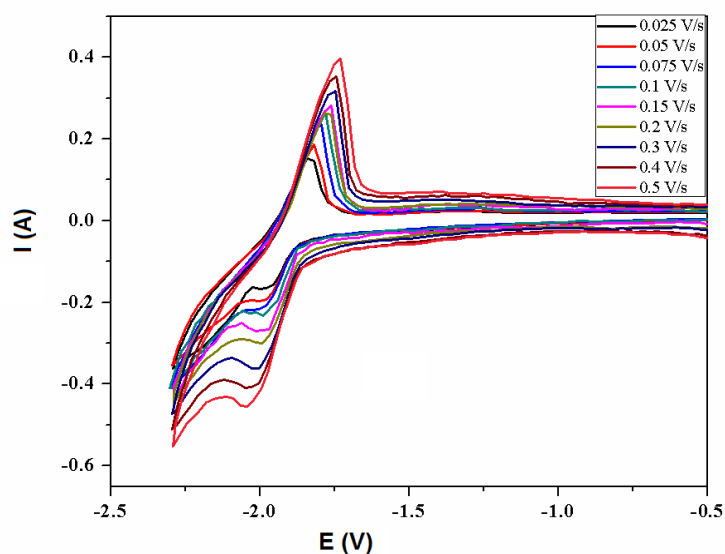


Fig.5.7 Cyclic voltammogram of $\text{LaCl}_3\text{-LiCl-KCl}$ melt on molybdenum electrode at various scan rates of 0.025 to 0.5Vs^{-1} . Concentration of La: 2.5×10^{-4} mole per cc, Electrode area: 0.53cm^2 , Temperature: 973K .

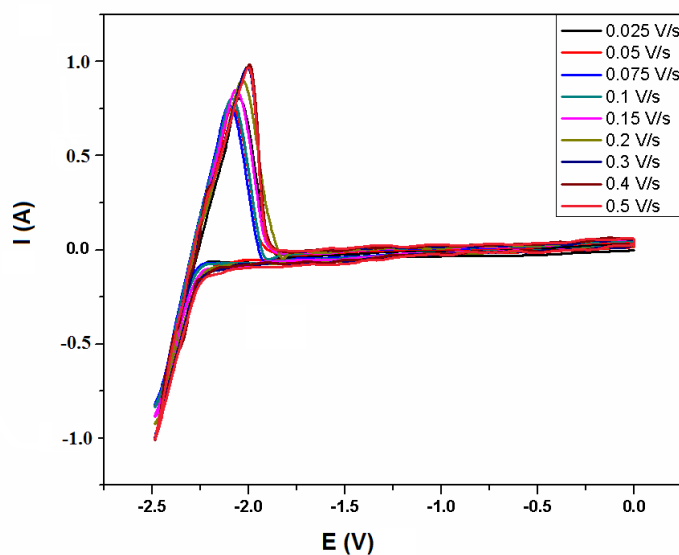


Fig.5.8 Cyclic voltammogram of LiCl-KCl melt on molybdenum electrode at various scan rates of 0.025 to 0.5Vs^{-1} . Electrode area: 0.53cm^2 , Temperature: 973K .

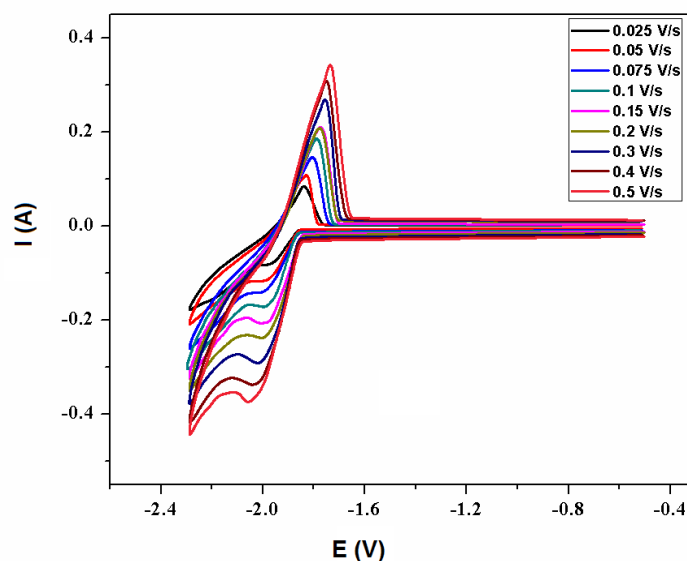


Fig.5.9 Back ground corrected cyclic voltammograms of $\text{LaCl}_3\text{-LiCl-KCl}$ melt on molybdenum electrode at various scan rates of 0.025 to 0.5Vs^{-1} . Electrode area: 0.53cm^2 , Temperature: 973K .

From **Fig.5.9**, it was observed that the separation between cathodic and anodic peak potentials ($\Delta E = E_a^P - E_c^P$) is constantly increasing with increase in the scan rate. Moreover, the value of ΔE was found to be larger than the value of $2.303RT/nF$ (0.064V at 973K considering 3 electron transfer of the electrode process) even at slowest scan rate (0.025V/s in the present case) which is unexpected for a reversible electrochemical process. At higher scan rates, the cathodic peak potential (E_c^P) shifted towards more negative side and anodic potential (E_a^P) shifted towards positive side. Such shifting of peaks indicated the irreversible nature of the electrochemical reaction. A discussion about the irreversibility of the electrochemical process was discussed in later sections.

The dependence of cathodic peak current (I_c) on square root of scan rate ($v^{1/2}$) was also studied and presented in **Fig.5.10**. Linear dependence of the peak current on square root of scan rate was

observed at higher scan rate. The linear relation between current and scan rate is the signature of fully reversible and fully irreversible electrode reactions. The nonlinear behavior in the scan range of 0.025 to 0.2 V/s could be due to quasi reversible nature of the electrode process.

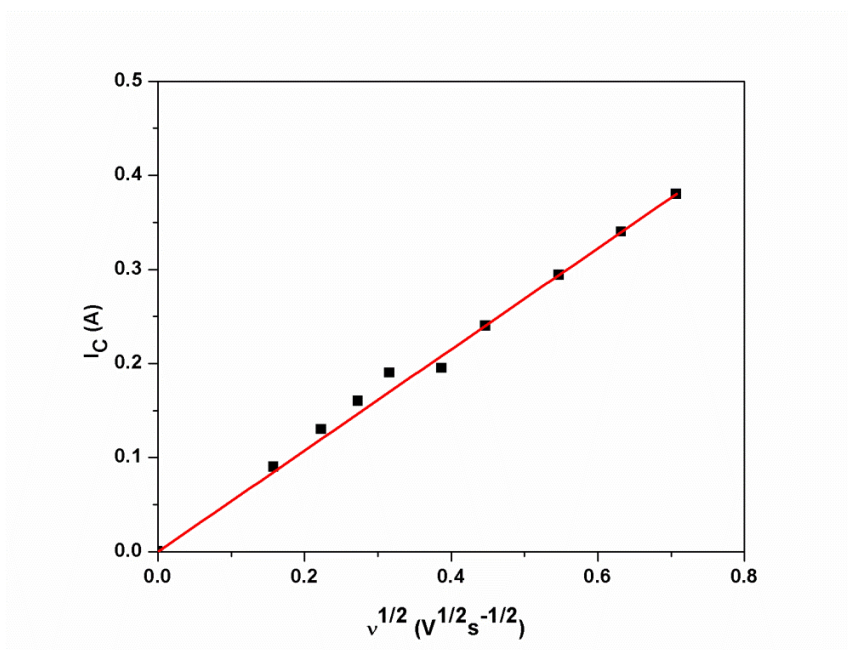


Fig.5.10 Variation of cathodic peak current vs. square root of scan rate in $LaCl_3$ -LiCl-KCl melt. Concentration of La: 2.5×10^{-4} mole per cc, Electrode area: 0.58 cm^2 , Temperature: 973K.

Similar to that in LiCl-KCl media cyclic voltammetry experiments were conducted in NaCl-KCl molten salt. Dependency of observed peak current with the square root of scan rate after background correction was shown in **Fig.5.11**. It was observed that the nature of electrochemical process (reduction of La (III) in NaCl-KCl melt) is similar to that of LiCl-KCl melt.

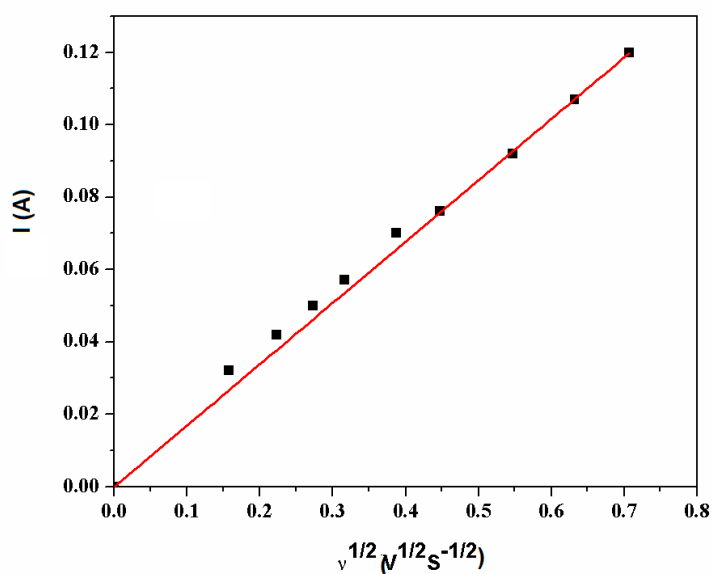


Fig.5.11 Variations of cathodic peak current vs. square root of scan rate for $LaCl_3-NaCl-KCl$ melt. Concentration of La: 1.5×10^{-4} mole per cc, Electrode area: 0.34 cm^2 , Temperature: 973K.

In order to investigate the effect of working electrode material on the electrochemical process, tungsten electrode was also used as the working electrode for the voltammetric measurements. Similar electrochemical response as that of molybdenum electrode was observed on tungsten electrode. The results of tungsten working electrode are not shown. A similar mechanism of the electrode process for the reduction of La (III) on both tungsten and molybdenum substrate was proposed.

5.2.1.3 Calculation of Diffusion coefficient and verification of the Arrhenius

law:

The linear dependence of cathodic peak current on square root of scan rate was observed at higher scan rates presented in **Fig.5.10** and **Fig.5.11** for the $LiCl-KCl$ and $NaCl-KCl$ melts

respectively. For an irreversible electrochemical process, the relation between the peak current and the diffusion coefficient was given by following equation [149]

$$I_p = 0.496nFCSD^{1/2} \left(\frac{\alpha n_\alpha F v}{RT} \right)^{1/2} \quad (5.1)$$

I_p is cathodic peak current (A), 'n' is the number of electrons involved in the reduction process which was taken as 3, 'F' is the Faraday constant, C is the bulk concentration of lanthanum ion (mol cm^{-3}), S is active surface area of working electrode (cm^2), D is the diffusion coefficient of lanthanum ion ($\text{cm}^2 \text{s}^{-1}$), 'R' is the universal gas constant ($8.314 \text{ J mol}^{-1} \text{ K}^{-1}$), 'T' is absolute temperature (K), v is the potential sweep rate (Vs^{-1}) and 'α' is the transfer co-efficient, n_α number of electrons involved in the reduction step.

To estimate the value of charge transfer co-efficient, cathodic peak potentials were plotted against logarithm of scan rate at various temperatures. **Fig.5.12** shows the relationship between cathodic peak potential (E_C^P) and logarithm of scan rate ($\log v$) at 973K for the reduction of La (III) in LiCl-KCl melt. The slope of this plot gives the charge transfer co-efficient value according to following equation

$$\frac{\Delta E_C^P}{\Delta \log v} = \frac{2.3 RT}{2\alpha n_\alpha F} \quad (5.2)$$

E_C^P is cathodic peak potential, v is the scan rate, R is the gas constant (8.314 J/(mol.K)), T is absolute temperature (K), F is Faraday constant (96500 C/mol), α is the charge transfer co-efficient and n_α is the number of electrons involved in the step. The value of 'α n_α ' obtained at three different temperatures for the reduction of La (III) in LiCl-KCl and NaCl-KCl melts were given in **Table-5.1**.

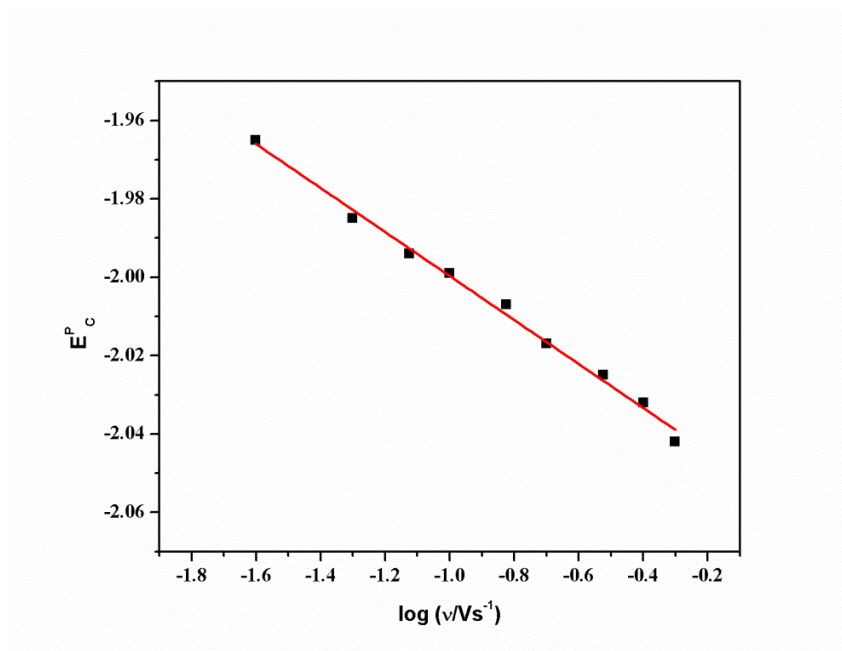


Fig.5.12 Variations of cathodic peak potentials with logarithm of sweep rate in LaCl₃-LiCl-KCl melt at 973K.

Temperature (K)	Value of αn_{α}	
	In LiCl-KCl medium	In NaCl-KCl medium
973	1.69	1.38
1023	1.77	1.45
1073	1.85	1.53

Table-5.1 The value of ' αn_{α} ' obtained at three different temperatures for the reduction of La (III) in LiCl-KCl and NaCl-KCl melts.

Diffusion coefficient values were estimated using the values of ' αn_{α} ' using the relation between peak current and scan rate mentioned in equation (5.1). The estimated values of diffusion coefficient with standard errors at 973K are presented in **Table-5.2**.

Temperature (K)	LiCl-KCl (10^5 D/cm ² s ⁻¹)		NaCl-KCl (10^5 D/cm ² s ⁻¹)	
	Mo	W	Mo	W
973	3.80 (± 0.03)	3.82 (± 0.03)	2.80 (± 0.02)	2.75 (± 0.04)
1023	4.60 (± 0.02)	4.56 (± 0.02)	3.56 (± 0.03)	3.55 (± 0.04)
1073	5.60 (± 0.05)	5.62 (± 0.05)	4.43 (± 0.05)	4.33 (± 0.02)

Table-5.2 Diffusion coefficient of La (III) evaluated in equimolar LiCl-KCl and NaCl-KCl melt at 973K.

The diffusion coefficients obtained at various temperatures in both the solvent (LiCl-KCl and NaCl-KCl) showed good linearity in the Arrhenius plots. **Fig.5.13** represents the logarithm of diffusion coefficient vs. $1/T$ which shows the validity of Arrhenius law. From the plot, empirical relation between diffusion coefficient and temperature were formulated. The diffusion coefficients with temperature dependence were shown as follows;

$$\log D_{La(III)} = -2.61(\pm 0.06) - 1.756(\pm 0.06) \times \frac{1000}{T} \quad \text{in LiCl-KCl system.}$$

$$\log D_{La(III)} = -2.45(\pm 0.07) - 2.047(\pm 0.07) \times \frac{1000}{T} \quad \text{in NaCl-KCl system.}$$

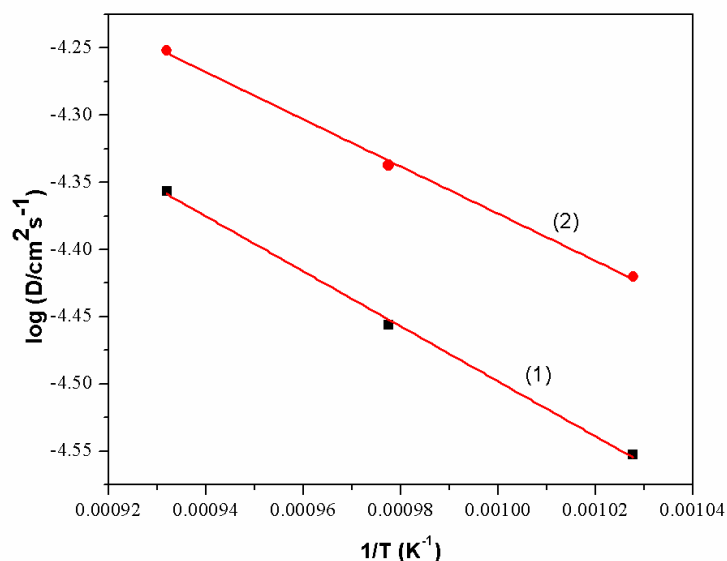


Fig.5.13 Verification of Arrhenius law. (1) LaCl₃ in equimolar LiCl-KCl melt. (2) LaCl₃ in equimolar NaCl-KCl melt.

The value of activation energy of the diffusion process (E_a) as obtained using the above mentioned empirical equation, were 33.6 (± 1.14) and 39.2 (± 1.5) kJ/mole for LiCl-KCl and NaCl-KCl system respectively. It was observed that the in the present case the activation energy is marginally higher compared to the literature reports. This could be due to the different composition of melt i.e. equimolar mixture of LiCl-KCl used in the present investigation compared of eutectic LiCl-KCl used in previous studies.

Present observation, thus indicated that, La (III) diffuses slowly in NaCl-KCl melt compared to LiCl-KCl melt. This slow diffusion of lanthanum ion in NaCl-KCl melt may be due to the higher viscosity of the melt. Lithium being the smaller ion compared to sodium ion, it gets heavily chlorinated leaving lanthanum ion less solvated which eventually helps in better diffusion.

5.2.1.4 Determination of standard rate constant

Nicholson treatment was applied to verify the reversibility of the electrochemical reduction process. The standard rate constant (K_s) of electrode reaction is correlated to a function ‘ Ψ ’ according to the following relation

$$\Psi = \frac{K_s}{(\pi D n F / RT)^{1/2} v^{1/2}} \quad (5.3)$$

K_s is standard rate constant (cm/s), Ψ is a function related to the difference between cathodic and anodic peak potentials (ΔE_p).

The dependence of ΔE_p on the Ψ function is given in the Nicholson table [150]. The value of Ψ in the Nicholson table represents the function for one electron transfer at room temperature (298K). The normalized Ψ function (Ψ_T) with respect to operating temperature and 3 electron transfer were calculated using following equations [151]

$$\Delta E_p^{298} = 3 \times \Delta E_p^T \left(\frac{298}{T} \right) \quad (5.4)$$

$$\Psi_T = \Psi_{298} \sqrt{\frac{T}{298}} \quad (5.5)$$

From the normalized Ψ function (Ψ_T) obtained from Eqns. (5.4) and (5.5), the values of standard rate constant (K_s) were estimated at various scan rates using Eq. (5.3). The values of normalized Ψ function (Ψ_T) and standard rate constant (K_s) for charge transfer on molybdenum electrode at various scan rates in both LiCl-KCl and NaCl-KCl melts are presented in **Table-5.3**.

It was observed from the table that within the scan range of 0.025 to 0.2 V/s, the standard rate constant for La (III)/La(0) in LiCl -KCl system estimated from Nicholson equation was (4.84 to 5.07) $\times 10^{-3}$ cm/s. The values of K_s obtained here are almost same and independent of scan rate. Similar results were obtained in NaCl-KCl system as presented in the table. The derived value of K_s in the scan range of 0.025 to 0.2V/s, located well within the region of quasi reversible domain

according to Matsuba-Ayabe method [152]. At higher scan rates, the normalized Ψ_T values fall beyond the reversible limit of the Nicholson table indicating irreversible nature of the electrode process. Based on the observation, the electrochemical reduction of La (III) is regarded as quasi reversible to irreversible reaction under present experimental conditions. Previously reported literatures have reported reversible to quasi reversible nature of the electrochemical reaction in the eutectic mixtures of LiCl-KCl molten salt media. Presently the electrochemical investigations were carried out in equimolar mixtures of LiCl-KCl and NaCl-KCl, such difference in molten salt composition might alter the electrochemical kinetics of the La (III) electrochemical deposition. Tungsten electrode was also used as the working electrode in place of molybdenum and similar electrochemical response and rate constants were obtained. Thus the electrochemical kinetics of the reduction of La (III) to La (0) remained unaltered upon changing the working electrode from molybdenum to tungsten.

Medium	$v/V.s^{-1}$	$\Delta E_P^T/V$	$\Delta E_P^{298}/V$	Ψ_{298}	Ψ_T	K_s
LiCl-KCl	0.025	0.146	0.134	0.269	0.486	4.84×10^{-3}
	0.05	0.152	0.140	0.248	0.447	6.29×10^{-3}
	0.075	0.172	0.158	0.185	0.334	5.76×10^{-3}
	0.1	0.187	0.172	0.162	0.292	5.81×10^{-3}
	0.15	0.206	0.190	0.13	0.234	5.70×10^{-3}
	0.2	0.228	0.209	0.1	0.18	5.07×10^{-3}
NaCl-KCl	0.025	0.157	0.145	0.229	0.413	3.59×10^{-3}
	0.05	0.165	0.152	0.212	0.382	4.69×10^{-3}
	0.075	0.179	0.165	0.185	0.334	5.03×10^{-3}
	0.1	0.188	0.173	0.162	0.292	5.07×10^{-3}
	0.15	0.212	0.195	0.13	0.234	4.98×10^{-3}
	0.2	0.233	0.213	0.1	0.18	4.58×10^{-3}

Table-5.3 Determination of rate constant (K_s) for the reduction of La (III) employing Nicholson method (in $LaCl_3$ -LiCl-KCl and $LaCl_3$ -NaCl-KCl melts).

5.2.1.5 Exchange current density:

The exchange current density is an important parameter to know the kinetics of electron transfer during electrochemical reaction. Exchange current (i) is the rate of reaction at reversible potential. Here the exchange current (i) was determined employing Tafel treatment shown in **Fig.5.14**. Linear sweep experiments were carried out at a scan rate of 0.025 V/s in the scan range of -1.7 to -2.2 V. Tafel treatments was applied and exchange current values were calculated at three different temperatures. Exchange current density (i_0) was calculated by dividing J with the area of electrode (A). The value of transfer coefficient (α) was also determined from the cathodic slope of the Tafel plot.

The results are shown in **Table-5.4**. From the table, it is concluded that the exchange current density is smaller on both tungsten and molybdenum electrodes, which could be due to the lattice mismatch effect as reported by Tang et.al. [98]. The exchange current density was increased marginally with the temperature indicating lower temperature coefficient of the process.

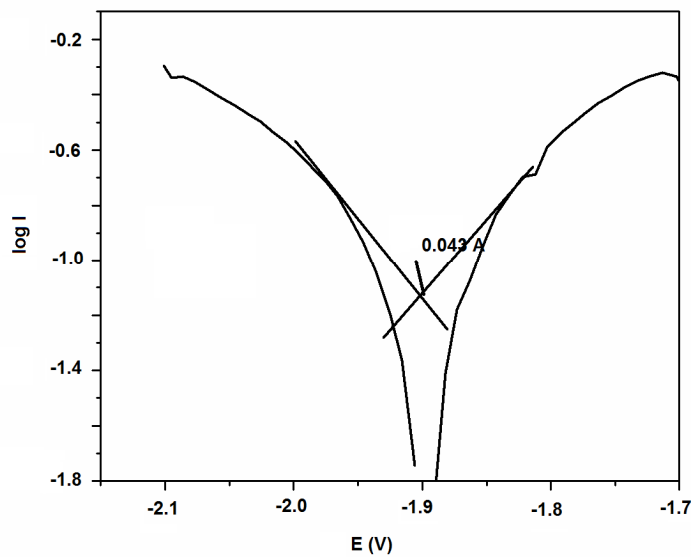


Fig.5.14 Tafel plot for LaCl_3 in equimolar mixture of LiCl-KCl melt on molybdenum electrode. Conc. $= 2.5 \times 10^{-5} \text{ mol cm}^{-3}$, area $= 0.77 \text{ cm}^2$, $T = 973 \text{ K}$, scan rate $= 0.025 \text{ V/s}$.

Media	Temperature	i_0 on Mo (Acm^{-2})	i_0 on W (Acm^{-2})	Value of α
LiCl-KCl	973	0.056	0.055	0.55
	1013	0.062	0.065	0.56
	1053	0.069	0.071	0.68
NaCl-KCl	973	0.053	0.052	0.46
	1013	0.059	0.061	0.58
	1053	0.068	0.066	0.62

Table-5.4 Values of exchange current density and transfer coefficients estimated at various temperatures. (For the reduction of La (III) in $\text{LaCl}_3\text{-LiCl-KCl}$ and $\text{LaCl}_3\text{-NaCl-KCl}$ melts).

5.2.2 Electrochemical behavior of CeCl₃ in alkali chloride melts

In this subsection the electrochemical characteristics of Ce (III) in molten salt electrolyte media was discussed.

5.2.2.1 Reduction behavior of Ce (III) in LiCl-KCl and NaCl-KCl systems characterized by cyclic voltammetry

The voltammograms obtained at 963 K with $2.1 \times 10^{-4} \text{ mol/cm}^3$ CeCl₃ at molybdenum electrode using LiCl-KCl electrolyte are shown in **Fig.5.15**. The dashed curve shows the voltammogram of the blank salt which has no additional peak except the reduction and the corresponding oxidation peak of lithium in the electrochemical window investigated. After the addition of CeCl₃, a cathodic peak at -2.0 V and corresponding anodic peak at -1.84 V were observed in the voltammogram. Energy dispersive X-ray Fluorescence Spectra (EDXRF) of the deposited product was carried out to obtain elemental information of the deposited product and the results are shown in **Fig.5.16**. These experiments were carried out using the deposits obtained after applying -2.05 V on the working electrode for 10 minutes. Analysis of the electrodeposited products by EDXRF spectra confirmed the formation of cerium metal on electrochemical deposition. This substantiates that the observed cathodic peak at -2.0 V was due to the reduction of cerium ion to metallic Ce. The peak obtained at -1.84 V during the reverse scan was due to the dissolution of cerium metal in the melt. Electrochemical deposition and dissolution of Ce might be through multistep process; however present cyclic voltammetric scans could not resolve all those elementary deposition and dissolution steps. Instead of that a broad voltammetric plot due to the anodic dissolution of Ce was obtained.

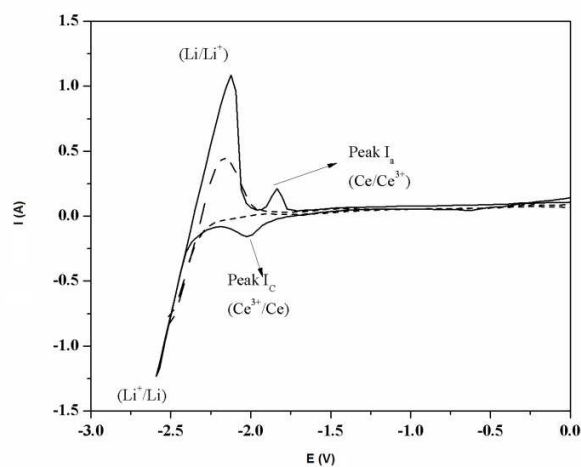


Fig.5.15 Comparison of the cyclic voltammogram for pure LiCl-KCl melt and CeCl₃-LiCl-KCl melt in the potential range of 0 to -2.6V. Working electrode: Mo, Conc: 2.1×10^{-4} mol cm⁻³, electrode area: 0.55cm², Temperature: 963 K, scan rate: 0.2 Vs⁻¹.

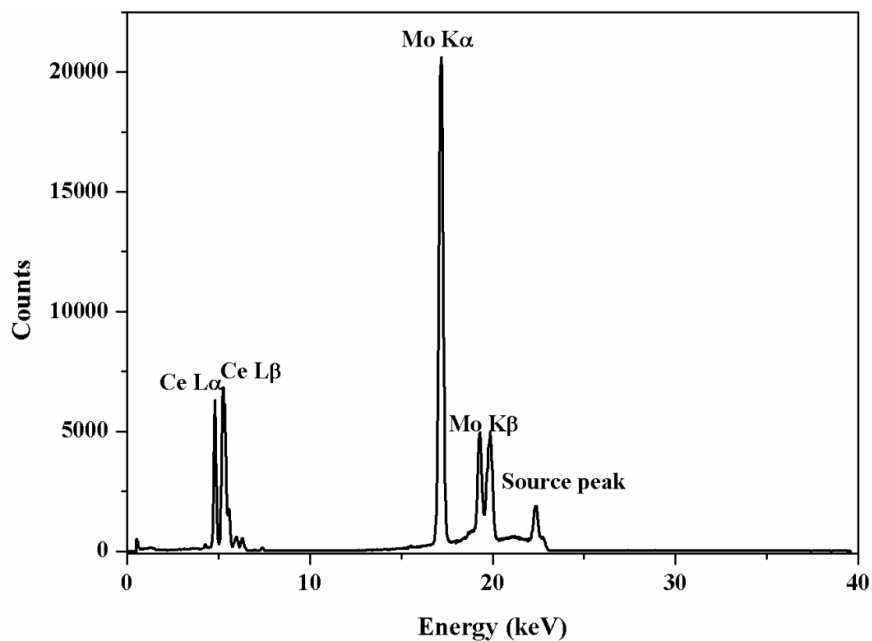


Fig.5.16 Energy dispersive X-ray fluorescence (EDXRF) spectra of the deposit (metallic cerium) obtained under potentiostatic condition in equimolar LiCl-KCl mixture at 963K (-2.05 V).

Cyclic voltammetric measurements were recorded for the reduction of Ce (III) in equimolar NaCl-KCl melt at 963K which is above the melting point of equimolar mixture of NaCl-KCl i.e. 918 K and the results are shown in **Fig.5.17**. Reduction peak of Ce (III) in this melt was not as sharp as that of LiCl-KCl. Electrochemical process was assumed as the three electron transfer process considering similar results reported earlier [27]. In the case of LiCl-KCl the Ce (III) reduction peak was well separated from the reduction of Li^+ whereas the Ce (III) reduction peak was almost merged with the reduction of Na^+ in the case of NaCl-KCl melt. To check the possibility of formation of Ce-Na intermetallics, atomic absorption spectroscopy (AAS) analysis was carried out of the deposited product obtained after potentiostatic electrolysis at -2.1V for 10 minutes in NaCl-KCl flux. Absence of any sodium ruled out the formation of Ce-Na intermetallics. The narrow difference in the Na^+ and Ce^{3+} reduction peaks is due to the small difference in their electrode potentials.

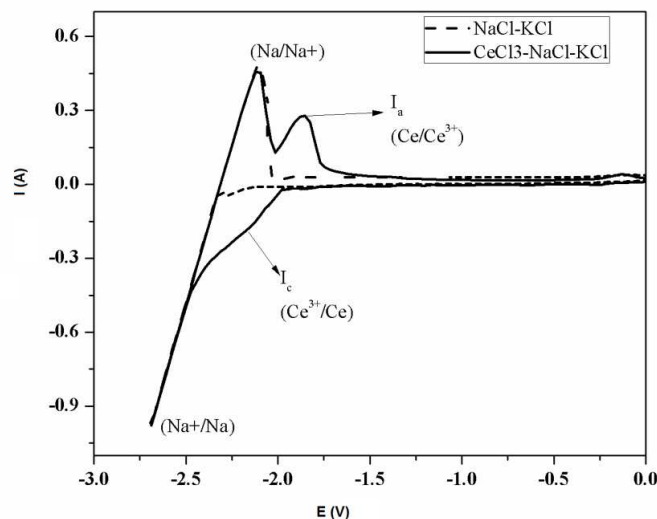


Fig.5.17 Comparison of the cyclic voltammogram for pure NaCl-KCl melt and CeCl_3 -NaCl-KCl melt in the potential range of 0 to -2.6V. Working electrode: Molybdenum, CeCl_3 : $2.05 \times 10^{-4} \text{ mol cm}^{-3}$, Electrode area: 0.38 cm^2 , Temperature: 963K, scan rate: 0.2 Vs^{-1} .

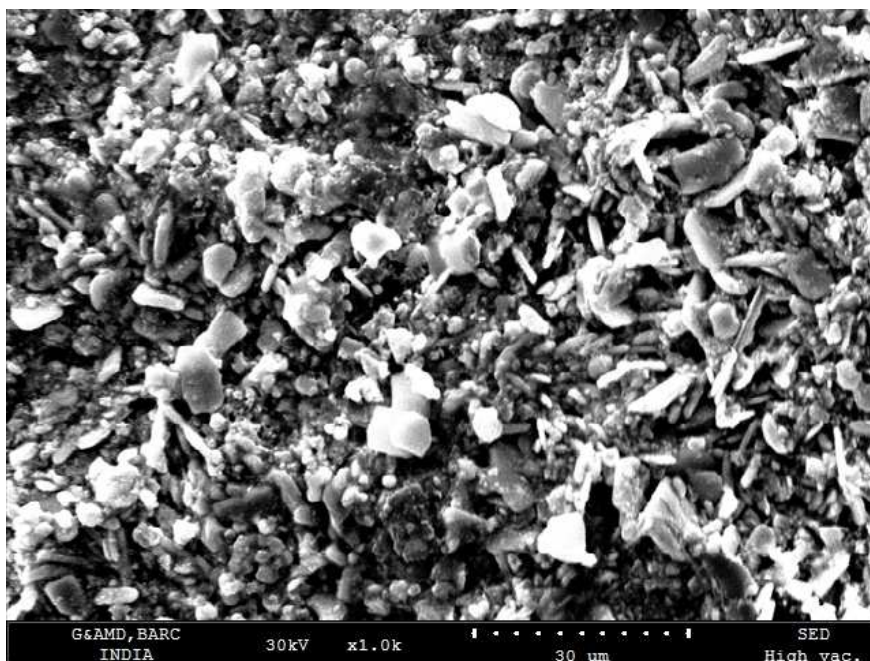


Fig.5.18 SEM micrograph of the deposit product (metallic cerium) obtained under potentiostatic condition in equimolar LiCl-KCl mixture at 96K (-2.05 V).

Morphology of the as deposited Ce metal was investigated from SEM measurements and the micrograph is shown in **Fig.5.18**. Uniform crystallite size was observed with the average crystallite diameter of 5 μm .

5.2.2.2 Kinetics of the electrode process

Cyclic voltammetry was carried out in both the melts at various scan rates in the temperature range of 963K to 1053K to investigate the dependence of peak potential and peak current on polarization rate. **Fig.5.19** represents the voltammogram recorded in molten CeCl_3 (2.1×10^{-4} mole/cc) in equimolar LiCl-KCl electrolyte at 963K at different scan rates. The dependency of the observed peak current with the scan rates is shown in **Fig.5.20**. The peak currents (I_c) varied linearly with the square root of scan rates ($v^{1/2}$) of the measurements at the scan rate range

investigated, which signify the diffusion controlled electrochemical process. Detailed analysis of voltammograms disclosed more about the kinetics of the electrochemical reduction process. From **Fig.5.19** it was observed that the cathodic peak potential (E^P_c) shifted slightly towards more negative side and anodic peak potential (E^P_a) shifted towards positive side with increase in scan rates. Moreover the separation between cathodic and anodic peak potentials (ΔE_p) was increasing with the scan rates. All these observations indicated that reduction of Ce (III) on molybdenum substrate was an irreversible electrochemical process. The cyclic voltammograms obtained at different scan rates in NaCl-KCl melt and the dependency of the peak current with the scan rates are shown in **Fig. 5.21 and Fig.5.22** respectively. It was observed that electrochemical characteristics of Ce (III) in NaCl-KCl melt were similar to that in LiCl-KCl melt.

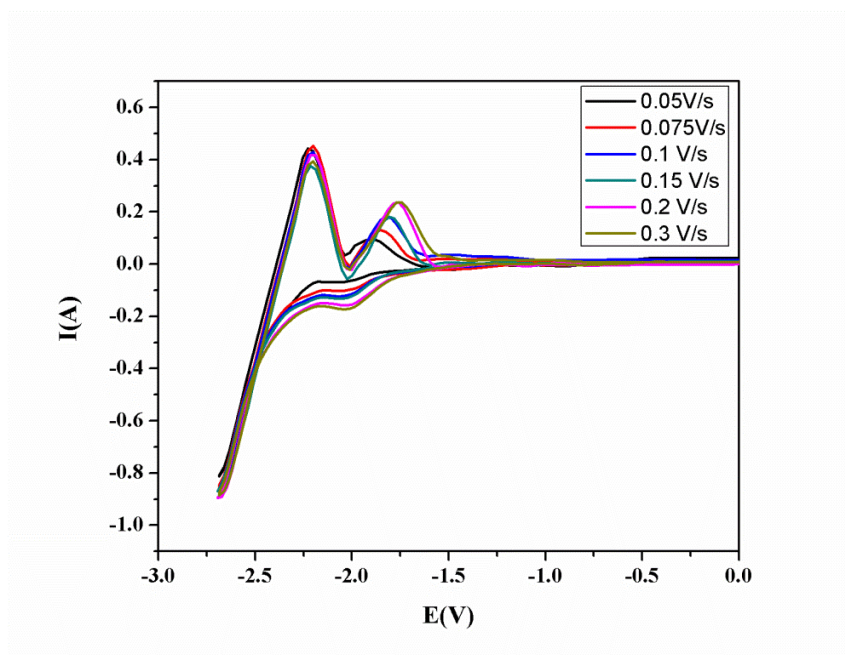


Fig.5.19 Cyclic voltammogram for $2.1 \times 10^{-4} \text{ mol cm}^{-3}$ of CeCl_3 in equimolar LiCl-KCl melt on molybdenum electrode at various scan rates. Electrode area: 0.53 cm^2 , Temperature: 963K.

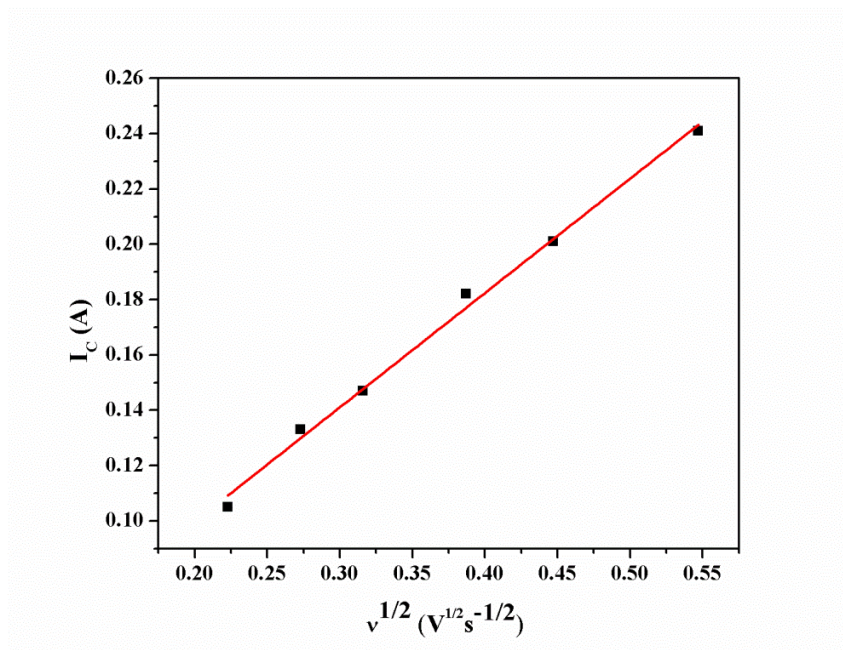


Fig.5.20 Plot between the square root of scan rate and cathodic peak current for $CeCl_3$ -LiCl-KCl melt. Concentration of $CeCl_3$: $2.1 \times 10^{-4} \text{ mol cm}^{-3}$, Electrode Area: 0.53 cm^2 , Temperature: 963K.

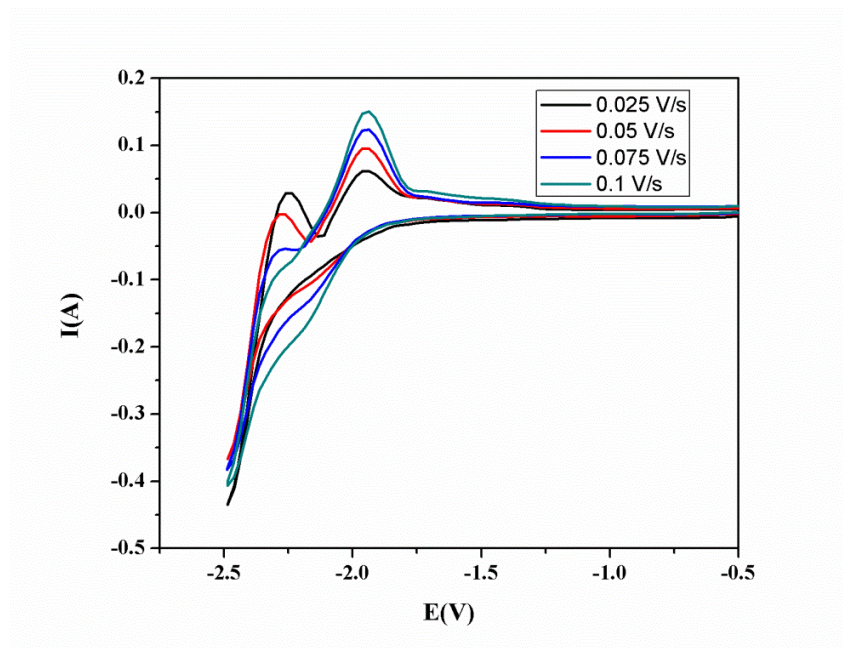


Fig.5.21 Cyclic voltammogram of $CeCl_3$ -NaCl-KCl melt on molybdenum electrode at various scan rates. Concentration of $CeCl_3$: $2.05 \times 10^{-4} \text{ mol cm}^{-3}$, Electrode area: 0.38 cm^2 , Temperature: 963K.

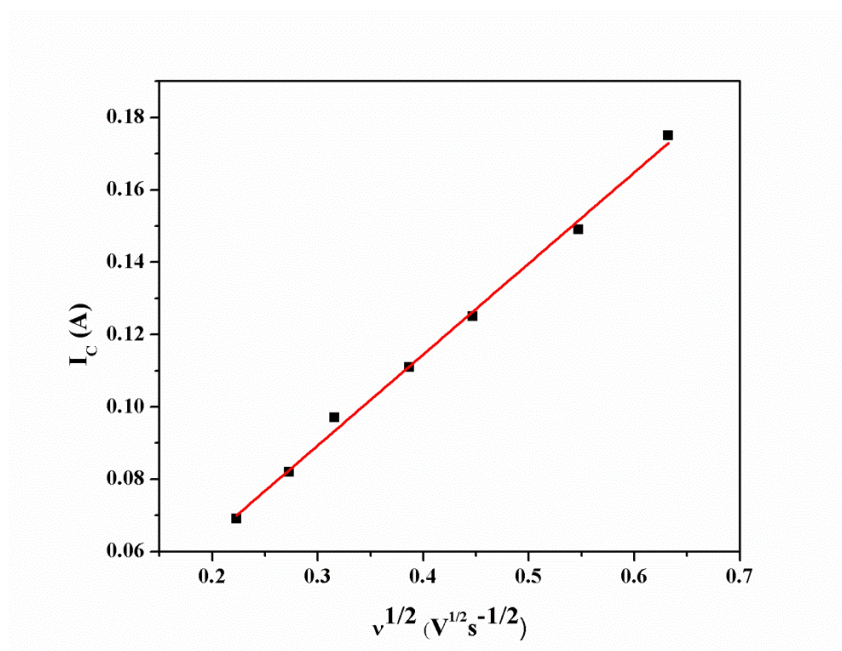


Fig.5.22 Plot between the square root of scan rate and cathodic peak current for $CeCl_3$ -NaCl-KCl melt. Concentration of $CeCl_3$: $2.05 \times 10^{-4} \text{ mol cm}^{-3}$, Electrode area: 0.38 cm^2 , Temperature: 963K.

Tungsten electrode was also used for the measurements and similar results were obtained for which the results are not shown, thus a similar electrochemical process on both tungsten and molybdenum substrates was proposed.

5.2.2.3 Calculation of standard rate constant:

Standard rate constant of electron transfer reaction was estimated applying Nicholson equation as described in section 5.2.1.4.

The values of normalized Ψ function (Ψ_T) and standard rate constant (K_s) for charge transfer on molybdenum electrode at various scan rates in both LiCl-KCl and NaCl-KCl melts are presented in **Table-5.5**. It was observed that the value of standard rate constant falls in the quasi reversible to irreversible range. At higher scan rates, the normalized Ψ_T values fall beyond the Nicholson table and could not be determined. Based on this study, the electrochemical reduction of Ce (III) is regarded as quasi reversible to irreversible reaction. Presently the values of Ψ_T falls

approximately in the range of 0.2 to 0.6 and α is supposed have influence in the cyclic voltammogram. However, α has strong influence on the shape of the cyclic voltammetric plot. With decrease in α cathodic peak shifts cathodically and the anodic peak also shifts cathodically thus the peak difference remained unaffected [153]. Therefore the influence of α assumed to be negligible in the present case and the reported standard rate constant values indicated the quasi reversible to irreversible nature of the electrochemical process. Similar results were also obtained for tungsten electrode. Therefore, it was concluded that electrochemical reduction of Ce (III) to Ce (0) is quasi reversible to irreversible in nature on both tungsten and molybdenum electrode in LiCl-KCl and NaCl-KCl melts.

Medium	$v/V.s^{-1}$	$\Delta E_p^T/V$	$\Delta E_p^{298}/V$	Ψ_{298}	Ψ_T	K_s
LiCl-KCl	0.05	0.132	0.12	0.356	0.639	9.0×10^{-3}
	0.1	0.165	0.15	0.212	0.380	7.56×10^{-3}
	0.15	0.216	0.18	0.15	0.269	6.56×10^{-3}
	0.2	0.231	0.21	0.1	0.179	5.04×10^{-3}
	0.3	0.243	0.225	-	-	-
	0.4	0.264	0.243	-	-	-
NaCl-KCl	0.05	0.198	0.183	0.15	0.328	4.03×10^{-3}
	0.075	0.210	0.194	0.125	0.224	3.37×10^{-3}
	0.1	0.225	0.208	0.1	0.179	3.11×10^{-3}
	0.15	0.280	0.259	-	-	-
	0.2	0.300	0.278	-	-	-
	0.3	0.320	0.296	-	-	-

Table-5.5 Rate constant (Ks) values obtained for the reduction of Ce (III) employing Nicholson method in CeCl₃-LiCl-KCl and CeCl₃-NaCl-KCl melts) using Nicholson method.

5.2.2.4 Square wave voltammetry:

Square wave voltammetric scans were recorded to investigate the deposition and stripping characteristics during Ce deposition and stripping. Results are shown in **Fig.5.23** and **Fig.5.24** for of 2.2×10^{-4} mole cm^{-3} of CeCl_3 in LiCl-KCl and of 2.0×10^{-4} mole cm^{-3} of CeCl_3 in NaCl-KCl melts at 963K at 5 kHz respectively. Only a single reduction peak was observed in the potential range studied which indicated that the electroreduction of cerium is a single step process in both the flux. It can also be observed that both the peaks are somewhat asymmetric in shape which may be due to the nucleation of rare earth metals as described by previous researchers. In this case the nucleation process was marginally slower compared to the stripping process.

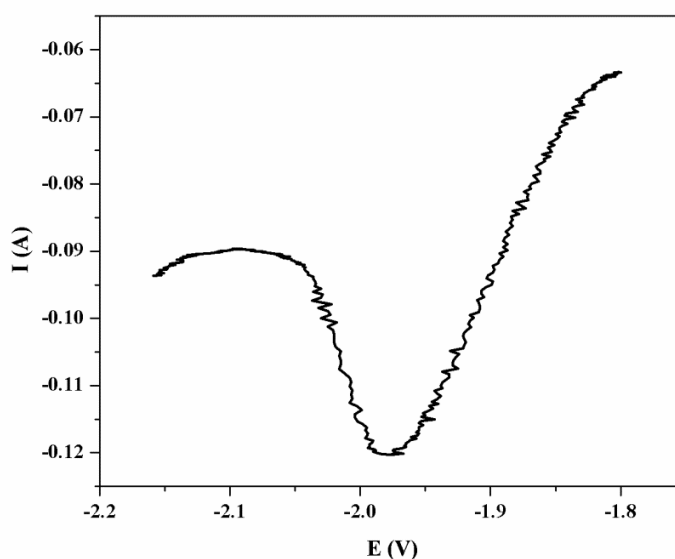


Fig.5.23 Square wave voltammogram for reduction of CeCl_3 at molybdenum electrode in LiCl-KCl melt. Experimental parameters are Pulse height=25mV, Potential step=1mV, Frequency=5 kHz, $\text{CeCl}_3=2.05 \times 10^{-4}$ mol cm^{-3} , T = 963K.

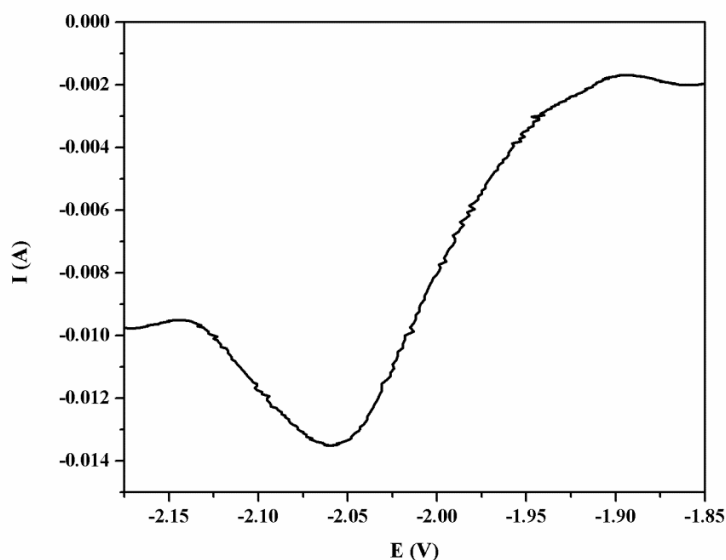


Fig.5.24 Net square wave voltammogram for reduction of CeCl_3 at molybdenum electrode in NaCl-KCl melt. Pulse height=25mv, Potential step=1mV, Frequency=5 kHz, $\text{CeCl}_3=2.0 \times 10^{-4} \text{ mol cm}^{-3}$, $T=963\text{K}$.

5.2.2.5 Calculation of diffusion coefficient:

The linear dependence of cathodic peak current with the square root of scan rate was presented in **Fig.20** and **Fig.22** respectively for LiCl-KCl and NaCl-KCl melts. For diffusion controlled irreversible electrochemical process, the relation between peak current and diffusion coefficient was given by the following relation [149]

$$i_p = 0.4958 \times n \times F^{3/2} \times A \times (RT)^{-1/2} \times D^{1/2} \times C \times \nu^{1/2} \times (an)^{1/2} \quad (5.6)$$

i_p is cathodic peak current (A), n is the number of electrons involved in the reduction process which was taken to be 3, ' F ' is the Faraday constant, ' R ' is the universal gas constant ($8.314 \text{ J mol}^{-1}\text{K}^{-1}$), ' T ' is absolute temperature (K), ' A ' is active surface area of working electrode (cm^2), $D_{\text{Ce(III)}}$ is the diffusion coefficient (cm^2s^{-1}), ' C ' is the bulk concentration of cerium ion (molcm^{-3}),

' ν ' is the potential sweep rate in (Vs^{-1}) and α is the transfer coefficient which was taken as 0.5. Diffusion coefficients values were calculated by applying the relation between the peak current with scan rate as per the above mentioned equation. The values of diffusion coefficients with standard error at are presented in **Table-5.6**.

Temperature	LiCl-KCl ($10^5 \text{ D/cm}^2\text{s}^{-1}$)		NaCl-KCl ($10^5 \text{ D/cm}^2\text{s}^{-1}$)	
	Mo	W	Mo	W
963	3.48 (± 0.02)	3.53 (± 0.05)	2.65 (± 0.03)	2.68 (± 0.01)
993	4.08 (± 0.04)	4.05 (± 0.03)	3.09 (± 0.01)	3.10 (± 0.01)
1023	4.49 (± 0.03)	4.45 (± 0.06)	3.56 (± 0.02)	3.54 (± 0.03)
1053	5.05 (± 0.05)	5.04 (± 0.03)	4.08 (± 0.02)	4.05 (± 0.02)

Table-5.6 Diffusion coefficient of Ce (III) evaluated from different cyclic voltammetry technique in equimolar LiCl-KCl and NaCl-KCl melt.

The diffusion coefficients obtained at various temperatures in both the solvents (LiCl-KCl and NaCl-KCl) are plotted with respect to the experimental temperatures and shown in Fig. 12. Diffusion coefficient values were correlated well with the experimental temperatures as suggested by the Arrhenius treatment

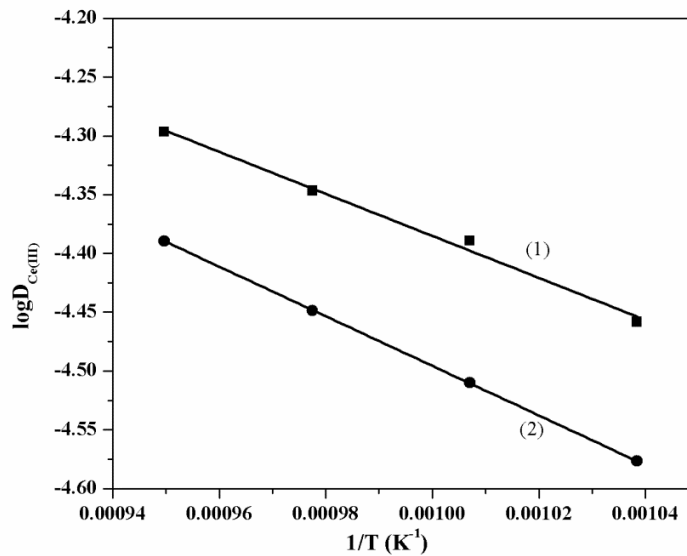


Fig.5.25 Logarithm of the diffusion coefficient of Ce (III) as a function of inverse of temperature in (1) Equimolar LiCl-KCl melts (2) Equimolar NaCl-KCl melt.

5.2.2.6 Estimation of activation energy for the diffusion process:

The diffusion co-efficient values were used to calculate activation energy for the diffusion process. Effect of temperature on the diffusion co-efficient obeys the Arrhenius law through the following equation:

$$D = D_0 \exp\left(\frac{-E_a}{RT}\right) \quad (5.7)$$

D (cm^2s^{-1}) is diffusion coefficient; E_a is the activation energy (kJ/mole). D_0 is the pre-exponential term (cm^2s^{-1}) in the Arrhenius eqn.

The logarithm of eqn. can be represented as follows

$$\log D = \log D_0 - \frac{E_a}{RT} \quad (5.8)$$

Fig.12 shows the relationship between $\log D$ and $1/T$ and the slope of the lines in were used to calculate the activation energy for diffusion of Ce (III) ions. Empirical relations between

diffusion coefficient and temperature as well as estimated activation energy for diffusion of Ce (III) ions in both the molten salt mixtures are presented in **Table-5.7**.

The activation energy for diffusion in the case of NaCl-KCl was higher than in LiCl-KCl. This was reflected in the observation of higher diffusion coefficients in LiCl-KCl melt compared to NaCl-KCl melt. This was possibly due to the comparatively higher viscosity of NaCl-KCl melt.

Medium	Equation		$-E_a$ (kJ mol ⁻¹)
	$\log D_{\text{Ce(III)}} = A + B/T$		
	A	B	
LiCl-KCl	-2.59	-1786	34.2
NaCl-KCl	-2.38	-2108	40.3

Table-5.7 Variation of diffusion coefficient of Ce (III) with the temperature and activation energy of the diffusion process in equimolar LiCl-KCl and NaCl-KCl melts.

5.2.2.7 Exchange current density:

Exchange current density was determined employing the Tafel treatment as shown in Fig.13 and Fig. 14 in two metals. Linear sweep experiments were carried out at a scan rate of 20 mV/s at the potential range of -2.10 V to -1.85 V. Tafel treatment was applied and the exchange current density was calculated and the values of exchange current densities at various temperatures on both molybdenum and tungsten electrodes are given in **Table.5.8**. As per the Butler-Volmer equation the Tafel region falls at the moderately higher over potentials. In the present case (cf. **Fig. 5.26 and Fig 5.27**) in the anodic region the diffusion limiting condition started early and there is limited scope of getting the extended linear Tafel region. In the cathodic

region there are some more quasi linear regions. However we choose a similar potential difference away from the equilibrium potential. The value of transfer coefficient (α) was also determined from the cathodic slope of Tafel plot.

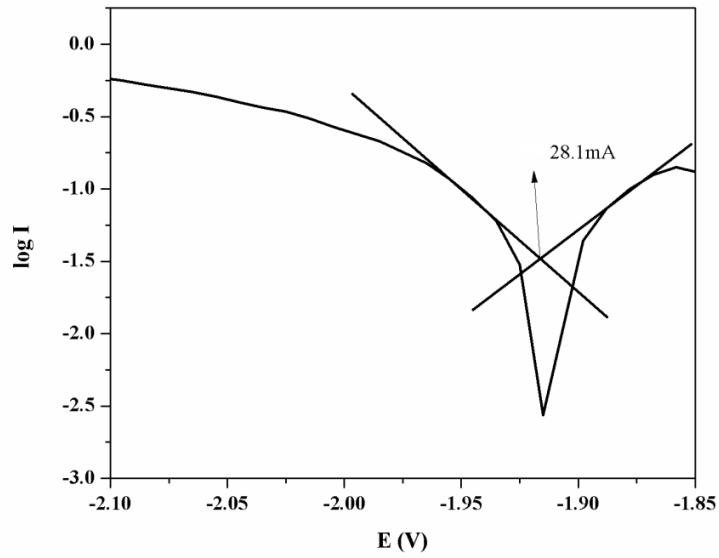


Fig.5.26Tafel for CeCl_3 in equimolar LiCl-KCl salt on Mo electrode $\text{CeCl}_3=2.1 \times 10^{-4} \text{ mol cm}^{-3}$, $T = 963\text{K}$ Area of Mo= 0.48cm^2 , scan rate = 20 mV/s.

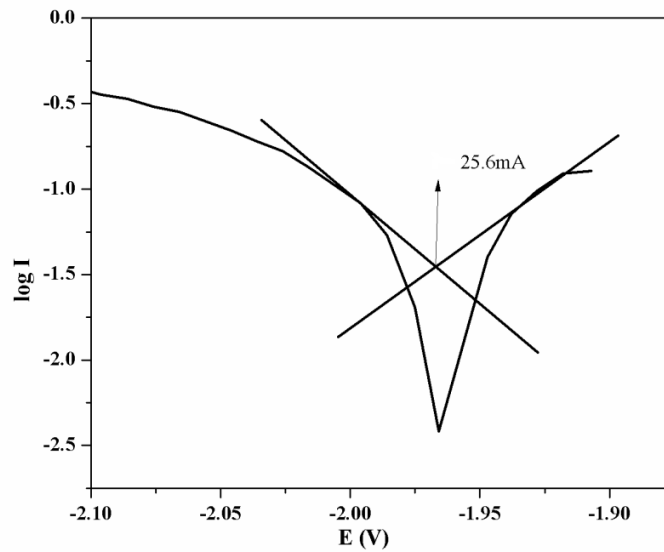


Fig.5.27Tafel for CeCl_3 in equimolar NaCl-KCl salt on Mo electrode $\text{CeCl}_3=2.0 \times 10^{-4} \text{ mol cm}^{-3}$, $T = 963\text{K}$ Area of Mo= 0.43cm^2 , scan rate = 20 mV/s .

The exchange current densities as reported previously [154] were in the range of 0.04 to 0.1 Acm^{-2} at 773K . In the present investigation, the exchange current densities were obtained in the range of 0.05 to 0.08 Acm^{-2} in the experimental temperature of 963 to 1053K . Thus the current densities at higher experimental temperatures in the present case were lower in comparison to previously reported values [154]. A lower value of exchange current density has been reported in the case of La deposition and explained to be due to the lattice mismatch effect between substrate and the deposits. However a generalized conclusion on the lowering of exchange current density could not be obtained based on the present findings and the previous reports.

Media	Temperature	i_0 on Mo (Acm^{-2})	i_0 on W (Acm^{-2})	Value of α
LiCl-KCl	963	0.058	0.056	0.48
	993	0.064	0.065	0.56
	1023	0.070	0.070	0.62
	1053	0.076	0.075	0.52
NaCl-KCl	963	0.059	0.060	0.50
	993	0.065	0.065	0.43
	1023	0.071	0.069	0.68
	1053	0.075	0.077	0.55

Table-5.8 Evaluation of exchange current density for the reduction of Ce (III) on Mo and W at various temperatures in CeCl_3 -LiCl-KCl and CeCl_3 -NaCl-KCl melts.

5.2.3 Electrochemical investigation of PrCl_3 in alkali chloride melts

In this subsection the electrochemical characteristics of Pr (III) in molten salt electrolyte media was discussed.

5.2.3.1 Reduction behavior of Pr (III) in LiCl-KCl and NaCl-KCl systems characterized by cyclic voltammetry

The reduction mechanism of praseodymium chloride on molybdenum and tungsten electrodes in LiCl-KCl and NaCl-KCl molten salt systems was studied by cyclic voltammetry technique. **Fig.5.28** shows the voltammograms obtained in LiCl-KCl electrolyte on molybdenum electrode at 973 K in the absence and presence of PrCl_3 . Clear reduction peak due to the reduction of Pr (III) distinctly different from the blank response was observed at -1.93 V, corresponding oxidation peak was obtained at -1.77 V. To substantiate the assumption, EDXRF analysis was carried out of the deposited product obtained after applying -2.0V on the working electrode for 10 minutes. **Fig.5.29** shows the Energy dispersive X-ray fluorescence (EDXRF) analysis of the deposited product which confirmed the formation of praseodymium metal on electrochemical deposition. Thus, the cathodic peak at -1.93 V and corresponding anodic peak at -1.77 were due to the deposition and dissolution of praseodymium ion at molybdenum electrode. Electrochemical deposition and dissolution of Pr might be thorough multistep process; however present cyclic voltammetric scans could not resolve all those elementary deposition and dissolution steps. Instead of that a broad voltammetric plot due to the anodic dissolution of Pr was obtained.

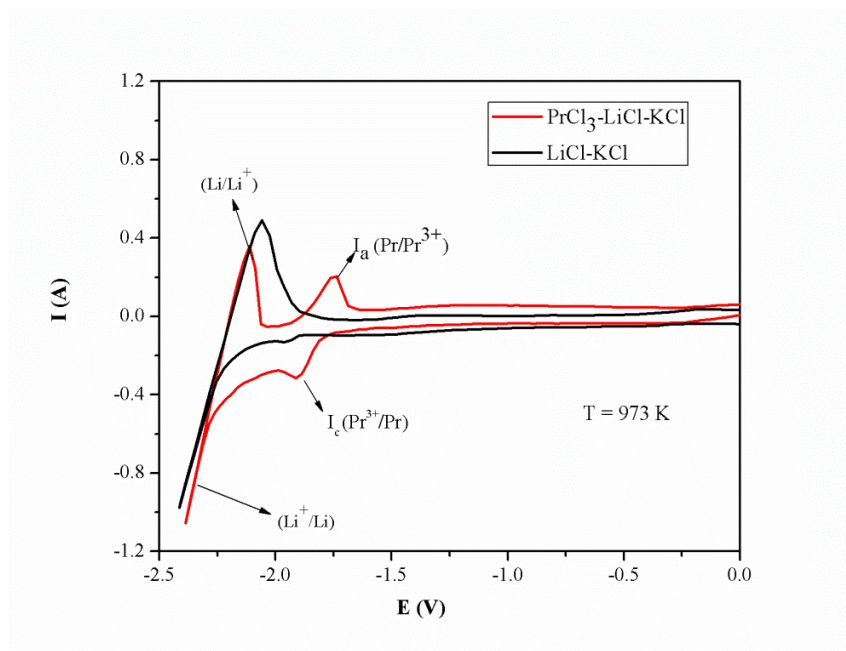


Fig.5.28 A Comparison of the cyclic voltammogram for pure LiCl-KCl melt and PrCl₃-LiCl-KCl melt in the potential range of 0 to -2.5V. Working electrode: molybdenum, apparent electrode area: 0.55cm², Temperature: 973K, Conc.: 2.5×10^{-4} mol/cc, scan rate: 0.1Vs⁻¹.

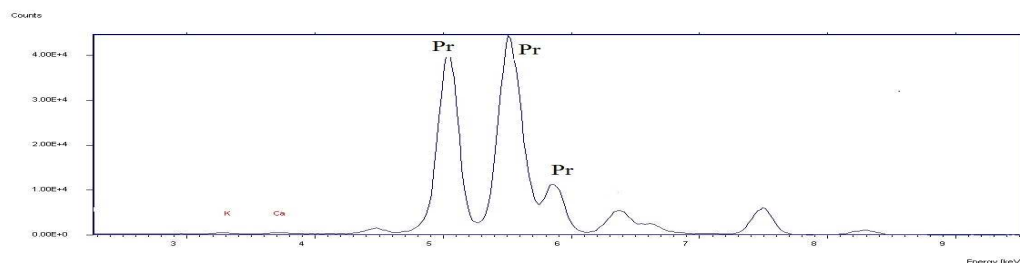


Fig.5.29 EDXRF spectra of the deposit (metallic Praseodymium) obtained under potentiostatic condition in equimolar LiCl-KCl mixture at 973K (-2.05 V).

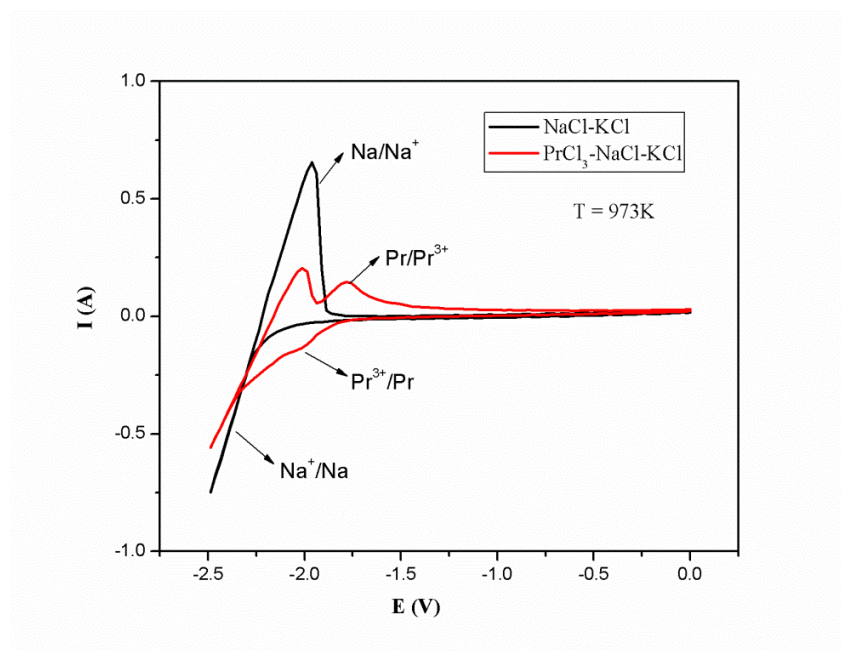


Fig.5.30 Comparison of the cyclic voltammogram for pure NaCl-KCl melt and PrCl₃-NaCl-KCl melt in the potential range of 0 to -2.5V. Working electrode: Molybdenum, apparent electrode area: 0.30cm², Temperature: 973K, scan rate: 0.025Vs⁻¹.

In case of equimolar NaCl-KCl, voltammograms recorded for the reduction of Pr (III) in at 973K on molybdenum electrode is shown in **Fig.5.30**. The black curve represents the voltammogram of the blank salt which has no additional peak except the reduction and oxidation peaks of sodium metal. After additions of PrCl₃, a small cathodic and corresponding sharp anodic peak were appeared in the figure (represented by red curve) expected for a metal deposition process. Therefore, the observed pair of peaks was attributed to the reductive deposition and oxidative dissolution of praseodymium metal in the melt. Reduction peak of Pr (III) in NaCl-KCl melt was not sharp as that of LiCl-KCl melt. In the case of LiCl-KCl, the Pr (III) reduction peak was well separated from the reduction of Li⁺ whereas the Pr (III) reduction peak was almost merged with the reduction of Na⁺ in the case of NaCl-KCl melt. Pr-Na intermetallic formation could not be expected as there was no extra peak observed except the dissolution of praseodymium metal in

the reverse scan. Atomic absorption spectroscopy (AAS) analysis confirmed the absence of Na in the electrodeposited Pr.

It was also noticed that intensities of the anodic signals due to the oxidation of Na on both W and Mo electrodes are much smaller than that of their corresponding reduction signals. This could be due to the high solubility of Na in NaCl melt [155]. It was observed that the reduction peak was more cathodically shifted in NaCl–KCl media compared to that in LiCl–KCl media. In such molten media two phenomena can affect the peak position; (1) the micro viscosity of the media and (2) the ion association effect of the molten salt [156].

5.2.3.2 Reversibility of the electrode Process

Cyclic voltammetry was carried out in both the melts at various scan rates in the temperature range of 973K to 1053 K to investigate the dependence of peak potential and peak current on polarization rate. **Fig.5.31** represents the voltammograms recorded in molten PrCl_3 (2.5×10^{-4} mole/cc) in equimolar LiCl-KCl electrolyte at 973K at different scan rates.

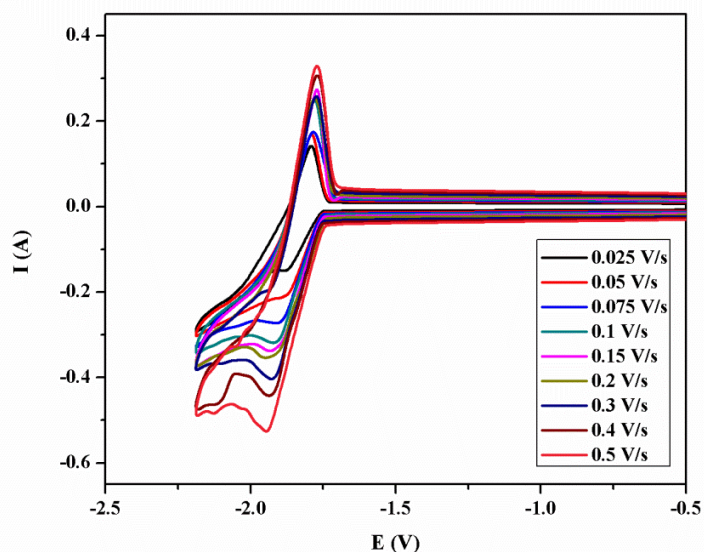


Fig.5.31 Cyclic voltammogram of $\text{PrCl}_3\text{-LiCl-KCl}$ melt on molybdenum electrode at various scan rates of 0.025 to 0.5Vs^{-1} . Concentration of Pr: 2.5×10^{-4} mole per cc, Electrode area: 0.53cm^2 , Temperature: 973K .

From **Fig.5.31**, It was observed that the separation between cathodic and anodic peak potentials ($\Delta E = E_{\text{pa}} - E_{\text{pc}}$) is constantly increasing with increase in the scan rate. This indicates the characteristics limit of an irreversible electrochemical reaction.

The dependence of cathodic peak current (I_c) on square root of scan rate ($v^{1/2}$) was also studied and presented in **Fig.5.32**. Linear dependence of the peak current on square root of scan rate was observed at higher scan rate. The linear relation between current and scan rate is the signature of fully reversible and fully irreversible electrode reactions. The nonlinear behavior in the scan range of 0.025 to 0.2 V/s could be due to quasi reversible nature of the electrode process.

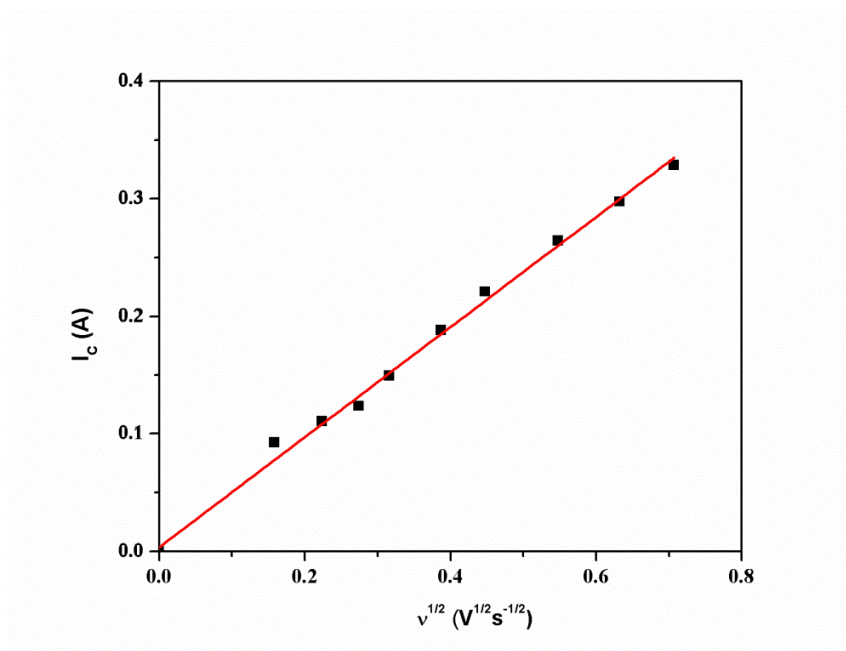


Fig.5.32 Variation of cathodic peak current vs. square root of scan rate in $\text{PrCl}_3\text{-LiCl-KCl}$ melt. Concentration of Pr: 2.5×10^{-4} mole per cc, Electrode area: 0.58 cm^2 , Temperature: 973K.

Similar experiments were conducted in NaCl-KCl molten salt. **Fig.5.33** represents the voltammograms recorded in molten PrCl_3 (2.5×10^{-4} mole/cc) in equimolar NaCl-KCl electrolyte at 973K at different scan rates. Dependency of observed peak current with the square root of scan rate after back ground correction was shown in **Fig 5.34**. It was observed that nature of electrochemical process (reduction of Pr (III) in NaCl-KCl melt) is similar to that of LiCl-KCl melt.

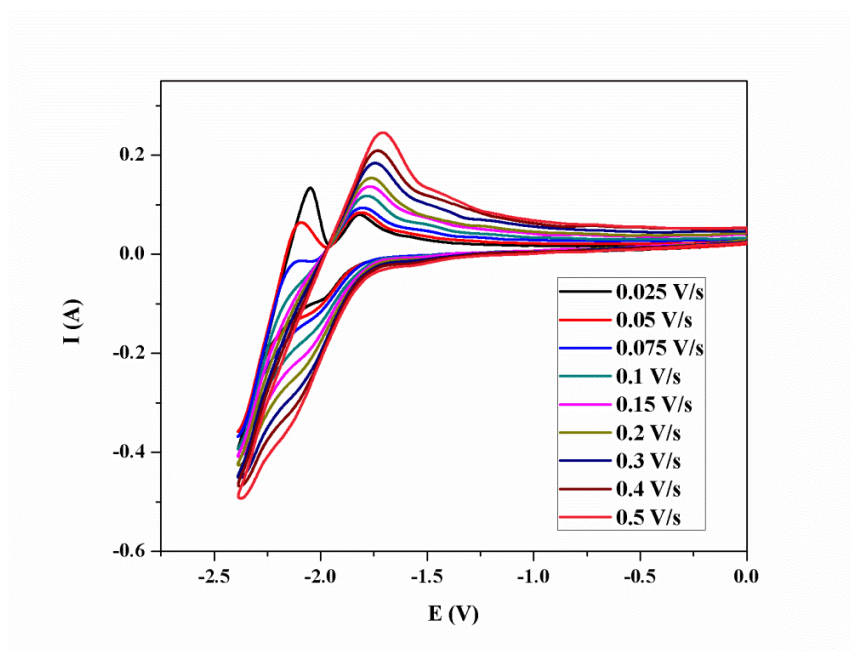


Fig.5.33 Cyclic voltammogram of $\text{PrCl}_3\text{-NaCl-KCl}$ melt on molybdenum electrode at various scan rates of 0.025 to 0.5Vs^{-1} . Concentration of Pr: 2.5×10^{-4} mole per cc, Electrode area: 0.53cm^2 , Temperature: 973K.

Tungsten electrode was also used as the working electrode for the voltammetric measurements and similar results were obtained. The results of tungsten working electrode are not shown. We propose a similar mechanism of the electrode process for the reduction of Pr (III) on both tungsten and molybdenum substrates.

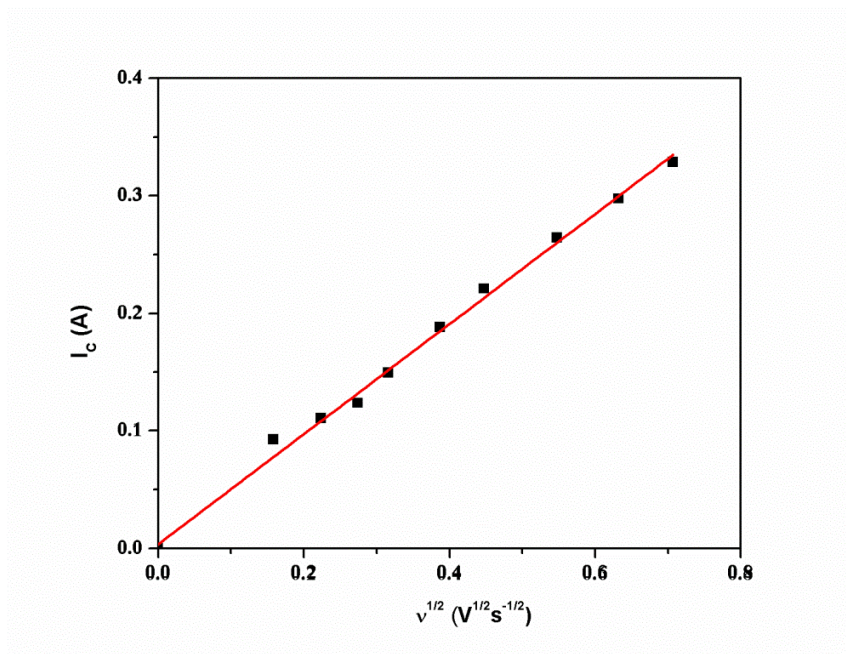


Fig.5.34 Variations of cathodic peak current vs. square root of scan rate for $PrCl_3$ -NaCl-KCl melt. Concentration of Pr: 1.5×10^{-4} mole per cc, Electrode area: 0.34 cm^2 , Temperature: 973K.

5.2.3.3 Calculation of Diffusion coefficient and verification of the Arrhenius law:

Diffusion coefficient of Pr (III) in LiCl-KCl and NaCl-KCl medium were calculated applying following equation as described in **section 5.2.1.3**.

The values of diffusion co-efficient estimated at three different temperature are presented in **Table-5.9**.

Temperature (K)	LiCl-KCl (10^5 D/cm 2 s $^{-1}$)		NaCl-KCl (10^5 D/cm 2 s $^{-1}$)	
	Mo	W	Mo	W
973	3.62 (± 0.04)	3.60 (± 0.03)	2.60 (± 0.02)	2.62 (± 0.03)
1023	4.38 (± 0.04)	4.38 (± 0.02)	3.26 (± 0.03)	3.25 (± 0.04)
1073	5.21 (± 0.05)	5.22 (± 0.05)	4.02 (± 0.05)	4.05 (± 0.05)

Table-5.9 Diffusion coefficient of Pr (III) evaluated in equimolar LiCl-KCl and NaCl-KCl melt at 973K.

The diffusion coefficients obtained at various temperatures in both the solvent (LiCl-KCl and NaCl-KCl) showed very good linearity in the Arrhenius plots. **Fig.5.35** represents the logarithm of diffusion coefficient vs. $1/T$ which shows the validity of Arrhenius law. From the plot, empirical relation between diffusion coefficient and temperature were formulated. The diffusion coefficients with temperature dependence were:

$$\log D_{La(III)} = -2.75(\pm 0.05) - 1.645(\pm 0.08) \times \frac{1000}{T} \quad \text{in LiCl-KCl system.}$$

$$\log D_{La(III)} = -2.55(\pm 0.06) - 1.980(\pm 0.07) \times \frac{1000}{T} \quad \text{in NaCl-KCl system.}$$

The value of activation energy of the diffusion process found out using the empirical equation, were 31.5 (± 1.5) and 37.9 (± 1.3) kJ/mole for LiCl-KCl and NaCl-KCl system respectively.

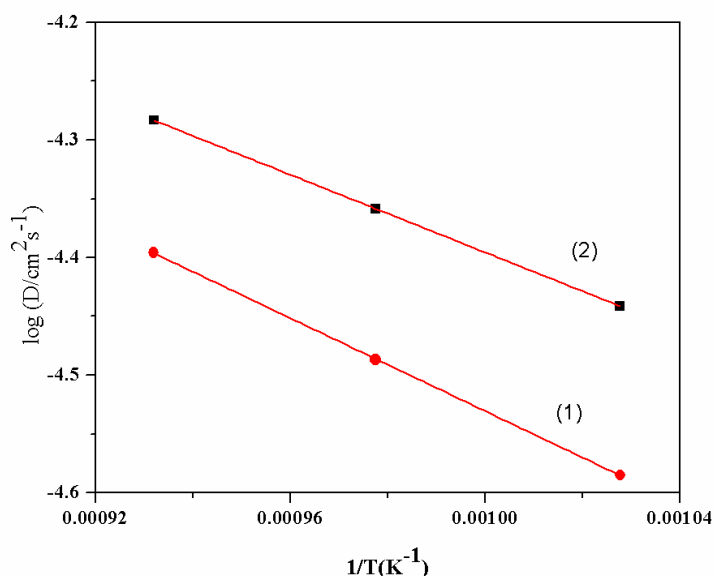


Fig.35 Verification of Arrhenius law. (1) PrCl_3 in equimolar LiCl-KCl melt. (2) PrCl_3 in equimolar NaCl-KCl melt.

Based on this present study, Pr (III) diffuses slowly in NaCl-KCl melt compared to LiCl-KCl melt. This slow diffusion of praseodymium ion in NaCl-KCl melt may be due to the higher viscosity of the melt. Lithium being the smaller ion compared to sodium ion, it gets heavily chlorinated leaving praseodymium ion less solvated which eventually helps in better diffusion.

5.2.3.4 Determination of standard rate constant

Standard rate constant for electron transfer reaction was calculated applying Nicholson equation as discussed in the **section 5.2.1.4**.

The values of normalized Ψ function (Ψ_T) and standard rate constant (K_s) for charge transfer on molybdenum electrode at various scan rates in both LiCl-KCl and NaCl-KCl melts calculated. It was observed that within the scan range of 0.025 to 0.2 V/s, the standard rate constant for Pr (III)/Pr (O) in LiCl-KCl system estimated from Nicholson equation was in the order of 10^{-3} cm/s. The values of K_s obtained here are almost same and independent of scan rate. Similar

results were obtained in NaCl-KCl system. The derived value of K_s in the scan range of 0.025 to 0.2V/s, located well within the region of quasi reversible domain according to Matsuba-Ayabe method [160]. At higher scan rates, the normalized Ψ_T values fall well beyond the reversible limit of the Nicholson table indicating irreversible nature of the electrode process. Based on this study, the electrochemical reduction of Pr (III) is regarded as quasi reversible to irreversible reaction under present experimental conditions. Similar results were obtained for tungsten electrode also. Therefore, it was concluded that electrochemical reduction of Pr (III) to Pr (0) is quasi reversible to irreversible in nature on both tungsten and molybdenum electrode in LiCl-KCl and NaCl-KCl melts. The table containing the values of rate is not shown in this case.

5.2.3.5 Exchange current density:

Exchange current density was determined employing Tafel treatment shown in **Fig.5.36**. Linear sweep experiments were carried out at a scan rate of 0.025 V/s in the scan range of -1.7 to -2.0 V. Tafel treatments was applied and exchange current density values were calculated at three different temperatures. The value of transfer coefficient (α) was also determined from the cathodic slope of the Tafel plot.

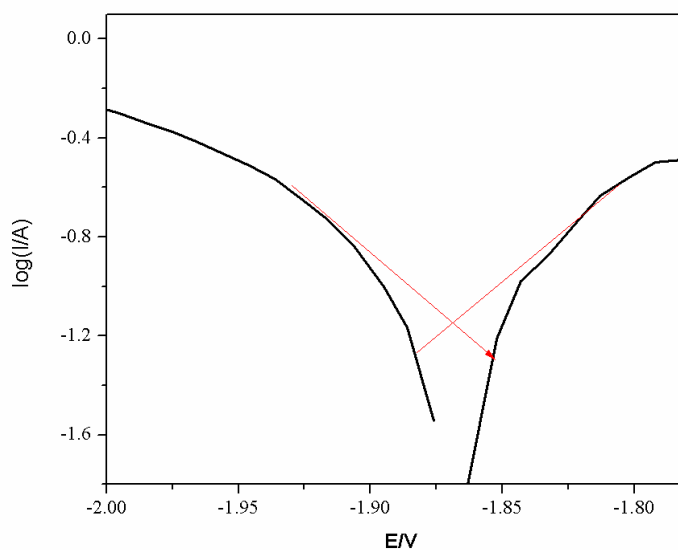


Fig.5.36Tafel plot for PrCl_3 in equimolar mixture of LiCl-KCl melt on molybdenum electrode .Conc. $=2.5 \times 10^{-5} \text{ mol cm}^{-3}$, $T = 973 \text{ K}$, scan rate $= 0.025 \text{ V/s}$.

The results are shown in **Table-5.10**.The exchange current density was increased marginally with the temperature indicating lower temperature coefficient of the process.

Media	Temperature	i_0 on Mo (Acm^{-2})	i_0 on W(Acm^{-2})	Value of α
LiCl-KCl	973	0.061	0.060	0.58
	1023	0.072	0.072	0.60
	1073	0.081	0.080	0.64
NaCl-KCl	973	0.059	0.058	0.46
	1023	0.070	0.069	0.50
	1073	0.078	0.078	0.58

Table-5.10 Values of exchange current density and transfer coefficients estimated at various temperatures (For the reduction of Pr (III) in PrCl_3 -LiCl-KCl and PrCl_3 -NaCl-KCl melts).

5.2.4 Electrochemical investigation of NdCl_3 in alkali chloride melts

5.2.4.1 Reduction behavior of Nd (III) in LiCl-KCl and NaCl-KCl systems characterized by cyclic voltammetry

The reduction mechanism of neodymium chloride on molybdenum and tungsten electrodes in LiCl-KCl and NaCl-KCl molten salt systems was studied by cyclic voltammetry technique. **Fig.5.37** Shows cyclic voltammograms obtained on molybdenum electrode in LiCl-KCl salt, at 973 K, before and after addition of NdCl_3 . For the blank salts, the cathodic peak observed at -2.4 V indicates the cathodic limit of the electrolyte. After addition of NdCl_3 in LiCl-KCl melt, two successive cathodic waves observed at about -1.78 and -2.01V, followed by their corresponding anodic waves at about -1.61 and -1.84 V were observed. Previous researchers [157-159] had concluded that the reduction of Nd (III) ion to Nd metal takes place in two steps with the formation of Nd (II) ion in the intermediate step. Therefore the observed pair of peaks was attributed to the reduction of Nd (III)/Nd (II) and then Nd (II)/Nd (0) respectively.

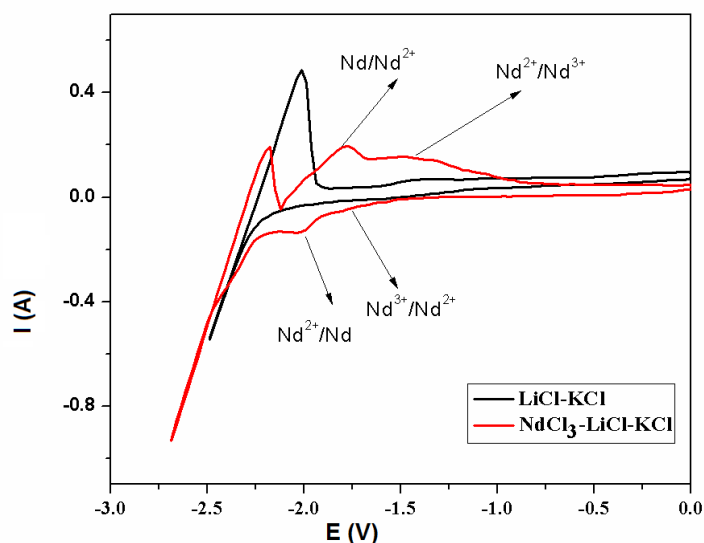


Fig.5.37 Comparison of the cyclic voltammogram for pure LiCl-KCl melt and NdCl₃-LiCl-KCl melt in the potential range of 1 to -2.5V. Working electrode: molybdenum, apparent electrode area: 0.77 cm², Temperature: 973K, Conc.: 2.5×10^{-4} mol/cc, scan rate: 0.1 Vs⁻¹.

Voltammograms recorded for the reduction of Nd (III) in NaCl-KCl melt at 973K on molybdenum electrode is shown in **Fig.5.38**. The electrochemical window of the blank molten salt system is limited by the reduction of sodium ion. After additions of NdCl₃, only one additional pair of signals (one cathodic and its corresponding anodic peak) was observed. The peak observed in the cathodic region was attributed to the reduction of Nd (III) through the process: $\text{Nd (III)} + 3e^- = \text{Nd}$ [155]. Therefore, the corresponding anodic peak was due to dissolution of neodymium metal in the melt. Unlike LiCl-KCl system, in NaCl-KCl system there is no intermediate formation of Nd (II) observed from the voltammogram.

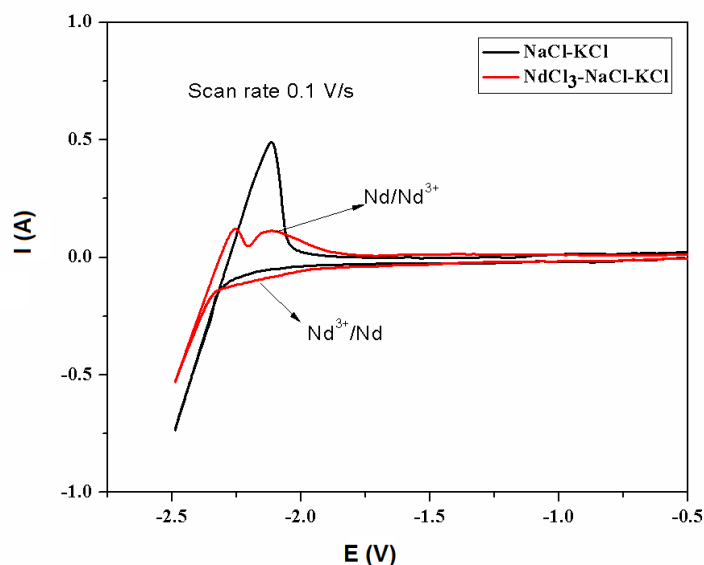


Fig.5.38 Comparison of the cyclic voltammogram for pure NaCl-KCl melt and NdCl₃-NaCl-KCl melt in the potential range of 0 to -2.75V. Working electrode: Molybdenum, apparent electrode area: 0.30cm², Temperature: 973K, scan rate: 0.025Vs⁻¹.

It was also noticed that intensities of the anodic signals due to the oxidation of Na on electrodes are much smaller than that of their corresponding reduction signals. This could be due to the high solubility of Na in NaCl melt. It was observed that the reduction peak was more cathodically shifted in NaCl-KCl media compared to that in LiCl-KCl media.

5.2.4.2 Reversibility of the electrode Process

Cyclic voltammetry was carried out in both the melts at various scan rates in the temperature range of 973K to 1053 K to investigate the dependence of peak potential and peak current on polarization rate. **Fig.5.39** represents the voltammograms recorded in molten NdCl₃ (2.5×10^{-4} mole/cc) in equimolar LiCl-KCl electrolyte at 973K at different scan rates.

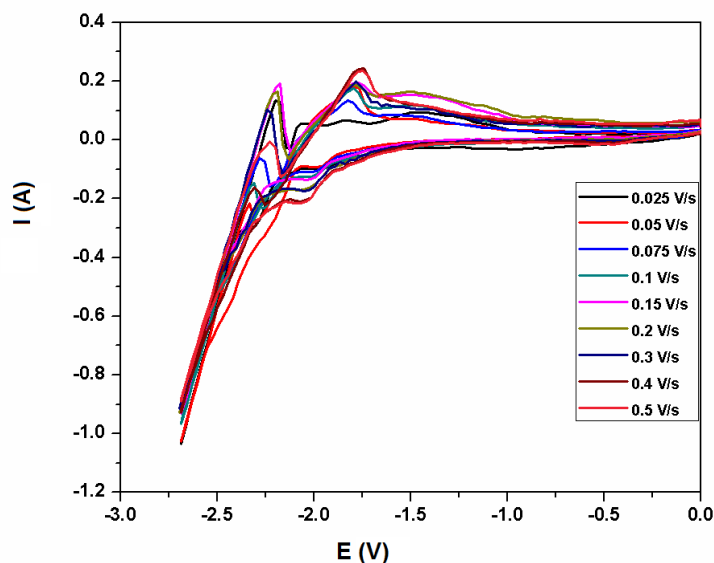


Fig.5.39 Cyclic voltammogram of $\text{NdCl}_3\text{-LiCl-KCl}$ melt on molybdenum electrode at various scan rates of 0.025 to 0.5Vs^{-1} . Concentration of Nd: 2.5×10^{-4} mole per cc, Electrode area: 0.53cm^2 , Temperature: 973K .

From **Fig.5.39**, It was observed that the separation between cathodic and anodic peak potentials ($\Delta E = E_{\text{pa}} - E_{\text{pc}}$) is constantly increasing with increase in the scan rate. At higher scan rates, the cathodic peak potential (E_{pc}) shifted clearly towards more negative side and anodic potential (E_{pa}) move towards positive side. This indicates the characteristics limit of an irreversible electrochemical reaction.

The dependence of cathodic peak current (I_c) on square root of scan rate ($v^{1/2}$) for both the reactions Nd(III)/Nd(II) and Nd(II)/Nd(0) were studied and presented in **Fig.5.40** and **5.41**. Linear dependence of the peak current on square root of scan rate was observed at higher scan rate. The nonlinear behavior in the scan range of 0.025 to 0.2 V/s could be due to quasi reversible nature of the electrode process.

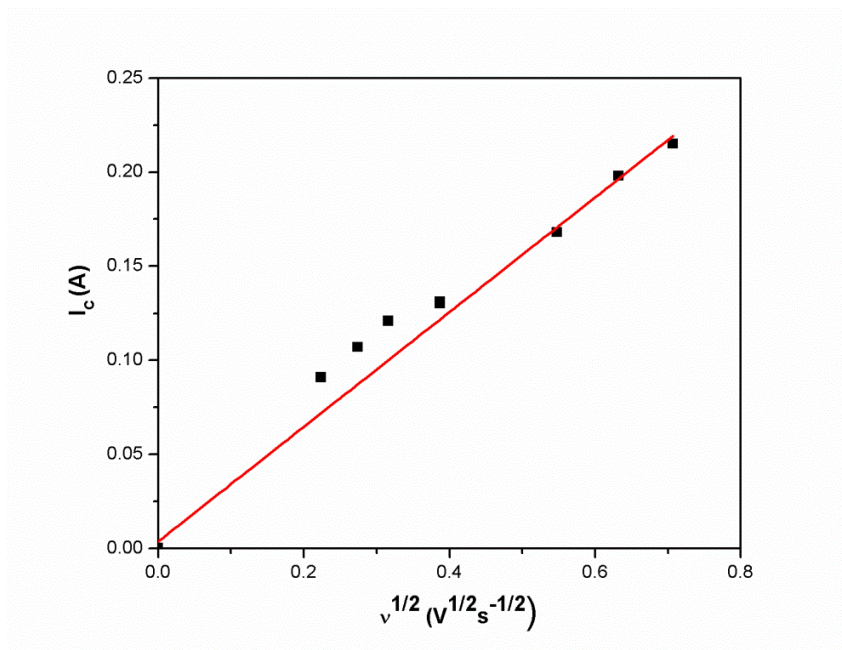


Fig.5.40 Variation of cathodic peak current vs. square root of scan rate for Nd (III)/Nd (II) in $NdCl_3$ -LiCl-KCl melt. Concentration of Nd: 2.5×10^{-4} mole per cc, Electrode area: 0.58 cm^2 , Temperature: 973K.

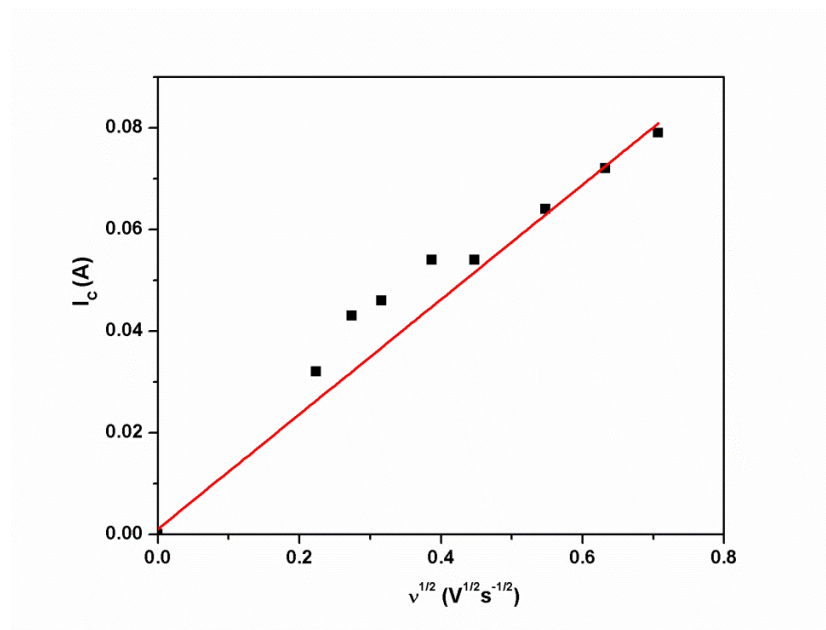


Fig.5.41 Variation of cathodic peak current vs. square root of scan rate for Nd (II)/Nd (0) in $NdCl_3$ -LiCl-KCl melt. Concentration of Nd: 2.5×10^{-4} mole per cc, Electrode area: 0.58 cm^2 , Temperature: 973K.

Similar experiments were conducted in NaCl-KCl molten salt. **Fig.5.42** represents the voltammograms recorded in molten NdCl_3 (2.5×10^{-4} mole/cc) in equimolar NaCl-KCl electrolyte at 973K at different scan rates. Dependency of observed peak current with the square root of scan rate after back ground correction was shown in **Fig 5.43**.

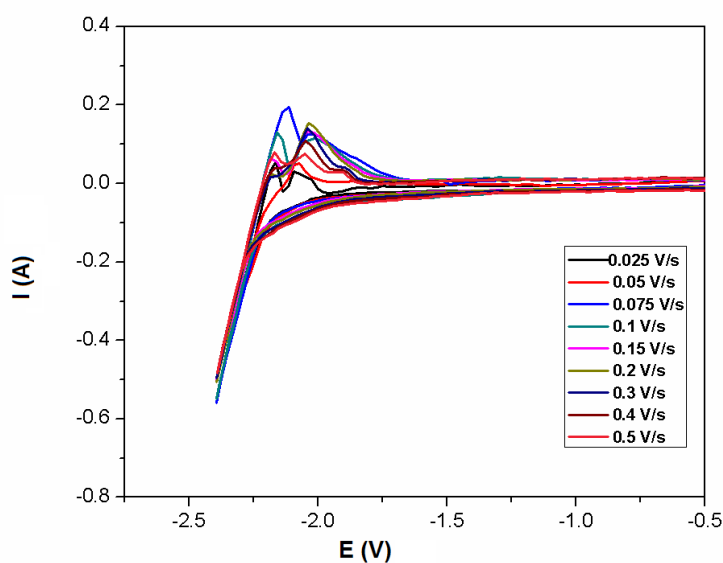


Fig.5.42 Cyclic voltammograms of NdCl_3 -NaCl-KCl melt on molybdenum electrode at various scan rates of 0.025 to 0.5Vs^{-1} . Electrode area: 0.53cm^2 , Temperature: 973K .

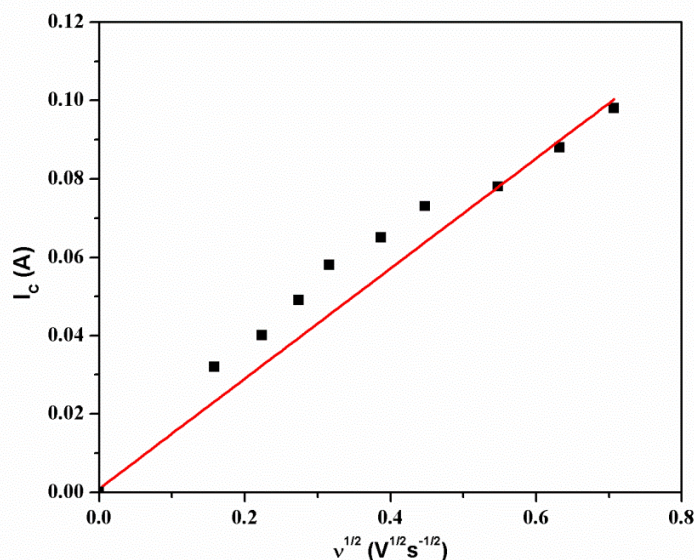


Fig.5.43 Variations of cathodic peak current vs. square root of scan rate for $NdCl_3$ -NaCl-KCl melt. Concentration of Nd: 1.5×10^{-4} mole per cc, Electrode area: 0.34 cm^2 , Temperature: 973K.

Tungsten electrode was also used as the working electrode for the voltammetric measurements and similar results were obtained. The results of tungsten working electrode are not shown. We propose a similar mechanism of the electrode process for the reduction of Nd (III) on both tungsten and molybdenum substrates.

5.2.4.3 Calculation of Diffusion coefficient and verification of the Arrhenius law:

Diffusion coefficient of Nd ions in LiCl-KCl and NaCl-KCl medium were calculated applying following equation as described in section 5.2.1.3. The diffusion coefficients obtained at various temperatures in both the solvent (LiCl-KCl and NaCl-KCl) showed in **Table-5.11**. Empirical relation between diffusion coefficient and temperature were formulated. The diffusion coefficients with temperature dependence were:

$$\log D_{Nd(III)} = -2.58(\pm 0.04) - 1.836(\pm 0.07) \times \frac{1000}{T} \quad \text{in LiCl-KCl system.}$$

$$\log D_{Nd(II)} = -2.55(\pm 0.04) - 1.530(\pm 0.07) \times \frac{1000}{T} \quad \text{in LiCl-KCl system.}$$

$$\log D_{Nd(III)} = -2.40(\pm 0.06) - 2.140(\pm 0.08) \times \frac{1000}{T} \quad \text{in NaCl-KCl system.}$$

The value of activation energy of the diffusion process of Nd(III) found out using the empirical equation, were 35.1 (± 1.3) and 40.9 (± 1.5) kJ/mole for LiCl-KCl and NaCl-KCl system respectively. Activation energy required for diffusion of Nd(II) in LiCl-KCl melt was 29.2 (± 1.3) kJ/mole.

Temperature (K)	D of Nd(III) in LiCl-KCl ($10^5/\text{cm}^2\text{s}^{-1}$)	D of Nd(II) in LiCl-KCl ($10^5/\text{cm}^2\text{s}^{-1}$)	D of Nd(III) in NaCl-KCl ($10^5/\text{cm}^2\text{s}^{-1}$)
973	3.41 (± 0.04)	7.54 (± 0.05)	2.50 (± 0.05)
1023	4.20 (± 0.07)	8.9 (± 0.06)	3.21 (± 0.06)
1073	5.12 (± 0.02)	10.1 (± 0.04)	4.02 (± 0.04)

Table-5.11 Diffusion coefficient of Nd ions evaluated in equimolar LiCl-KCl and NaCl-KCl melt at 973K.

Based on this present study, Nd (II) diffuses fast compared to Nd (III) because of its lower charge it gets less chlorinated compared to Nd (III). The slow diffusion of Nd (III) in NaCl-KCl melt compared to LiCl-KCl melt could be due to the higher viscosity of the melt.

5.2.4.4 Determination of standard rate constant

Standard rate constant of the electron transfer reaction was determined using Nicholson equation as discussed in **section 5.2.1.4**.

The values of normalized Ψ function (Ψ_T) and standard rate constant (K_s) for Nd (II)/Nd in LiCl-KCl medium and for Nd (III)/Nd in NaCl-KCl medium were estimated. It was observed that within the scan range of 0.025 to 0.2 V/s, the standard rate constant for Nd(III)/Nd(II) and Nd (II)/Nd(0) in LiCl -KCl system estimated from Nicholson equation was in the order of 10^{-2} to 10^{-1}

³ cm/s. Similarly the standard rate constant for Nd (III)/Nd (0) in NaCl -KCl system estimated from Nicholson equation was in the order of 10^{-3} cm/s. At higher scan rates, the normalized Ψ_T values fall well beyond the reversible limit of the Nicholson indicating irreversible nature of the electrode process. Based on this study, the electrochemical reduction of Nd (II)/Nd and Nd (III) to Nd in LiCl-KCl and NaCl-KCl systems respectively are regarded as quasi reversible to irreversible reaction under present experimental conditions.

5.2.4.5 Exchange current density:

Here the exchange current density was determined employing Tafel treatment shown in **Fig.5.14**. Exchange current density for Nd (II)/Nd (O) and Nd (III)/Nd (O) coupled reactions were estimated in LiCl-KCl and NaCl-KCl melt respectively.

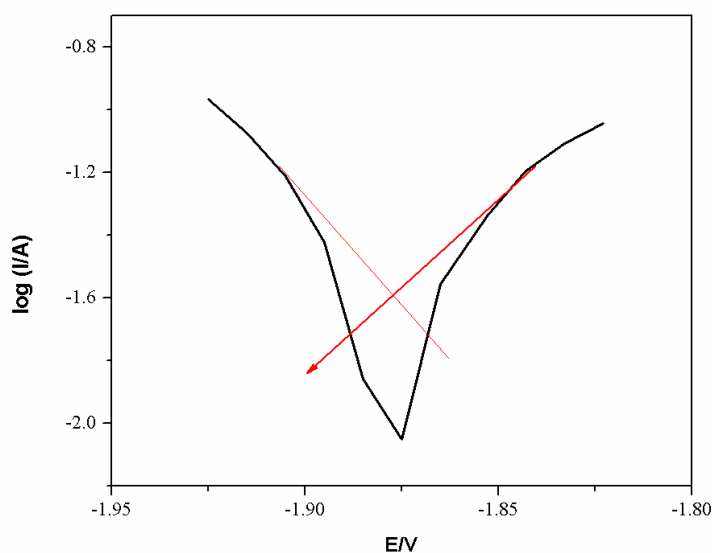


Fig.5.44 Tafel plot for NdCl_3 in equimolar mixture of LiCl-KCl melt on molybdenum electrode .Conc. $=2.5 \times 10^{-5} \text{ mol cm}^{-3}$, $T = 973 \text{ K}$, scan rate $= 0.025 \text{ V/s}$.

The results are shown in **Table-5.12**. The exchange current density was increased marginally with the temperature indicating lower temperature coefficient of the process. The exchange current of Nd (II)/Nd (0) was found to be higher to that of Nd (III) /Nd (0). This may be due to participation of two electrons in the Nd (II)/Nd (0) redox process compared to 3 electrons in Nd (III)/Nd (0) process.

Media	Reactions	Temperature	i_0 on Mo (Acm^{-2})	Value of α
LiCl-KCl	Nd(II)/Nd(0)	973	0.070	0.45
		1023	0.079	0.53
		1073	0.088	0.65
NaCl-KCl	Nd(III)/Nd(0)	973	0.060	0.49
		1023	0.070	0.58
		1073	0.079	0.68

Table-5.12 Values of exchange current density and transfer coefficients estimated at various temperatures (For the reduction of Nd ion in NdCl_3 -LiCl-KCl and NdCl_3 -NaCl-KCl melts).

5.3 Summary:

Under this chapter the electrochemical behavior of lanthanides (La, Ce, Pr and Nd) were investigated in two molten salts; LiCl-KCl and NaCl-KCl electrolyte media. Electrochemical kinetics of the reduction of rare earth metal ions to their corresponding metallic form and the dissolution characteristics of the reduced metal to the corresponding metal ions were investigated. Variation of the voltammetry with the change in the molten salt media and the variation across the different rare earth metal ions have been investigated. Mechanism of electrochemical reduction and diffusivity plays an important role in deciding the deposition condition during recovery by electrochemical deposition of rare earth metals from their molten states. Diffusion kinetics of rare earth metal ions have been investigated and discussed in length in all the four rare earth metal ions.

It was observed from the investigation that the reduction La (III), Ce (III) and Pr (III) undergo a 3 electron transfer process in both the molten salt media investigated. Whereas the reduction of Nd (III) in LiCl-KCl media has shown two step reduction process. In the first step Nd (III) was reduced to Nd (II) and in the second step Nd (II) was reduced to metallic Nd deposits. Interestingly it was observed that in the case of NaCl-KCl molten media Nd (III) undergoes electrochemical reduction through one step reduction process from Nd (III) to metallic Nd. This difference might be due to the better stability of Nd (II) by solvation in LiCl-KCl compared to that in NaCl-KCl media.

It has been observed that the diffusion co-efficient of lanthanide ions decreased with the decrease of their ionic radii among the lanthanides investigated presently. This is attributed to the greater degree of solvation of the smaller lanthanide ions, which resulted in effective bulkier solvated

cation. Thus the diffusion coefficient was observed to be less among the smaller lanthanide ions compared to the larger ions.

It was observed that the exchange current density values were marginally increased from lanthanum to neodymium. Increase in the exchange current density is related to the better electron transfer kinetics of the process. Therefore the enhanced exchange current density trend from lanthanum to neodymium is related to the increase in the electron transfer kinetics; though no significant difference in their electron transfer kinetics was observed under the present investigation by cyclic voltammetry measurements.

ELECTROCHEMICAL DEPOSITION OF RARE EARTH (RE) METALS

6.1 Introduction

Molten salt electrolysis is an attractive and effective method to produce light rare earth metals. Relatively low melting point of light rare earth metals facilitates the electrowinning of these metals in molten state. Due to narrow difference in electrode potential of RE metal and solvent ions (Li^+/Na^+), it is very difficult to separate the RE metal from the solvent. Therefore, a careful control of process parameters like temperature, concentration of electrolyte and current density are required for production of pure metal in the large scale operation. Information on the effect of temperature, bath composition and current densities on the yield and current efficiency in the production of rare earth production are limited in the literature. The objective of this study is to develop detail process parameters for the extraction of light rare earth metals by molten salt electrolysis process using LiCl-KCl and NaCl-KCl salt mixtures. In addition, the effect of using single carrier electrolysis using electrolytes like KCl, NaCl and LiCl, in the preparation of lanthanum and cerium metals have been carried out.

6.2 Experimental

6.2.1 Preparation of electrolyte

The starting materials such as rare earth oxides (Indian Rare Earths Ltd), potassium chloride, sodium chloride and lithium chloride with purity >99% (LR Grade) were used the present experiment.

The first step in the process was the conversion of RE oxides to their corresponding chlorides. The oxides were dissolved in hot hydrochloric acid (30% strength) at 353-373 K and the solution was stirred till the formation $RECl_3 \cdot XH_2O$ crystals [160]. The dehydration of samples was done by step wise heating up to 473 K for 24 hours in dynamic vacuum of 0.1mbar and the evolved water vapor was collected using a liquid nitrogen trap described in section 4.4. Mixture of LiCl-KCl (1:1 mole ratio) was also dehydrated at 473 K for 12hours to remove adsorbed moisture. The anhydrous $RECl_3$ and LiCl-KCl mixture, intimately mixed in the required proportion was used as electrolyte for extraction of metal. Similar Experimental procedure was followed for extraction of RE metal using NaCl-KCl (1:1mole ratio) electrolyte.

6.2.2 Electrolytic cell

The electrolytic mixture was charged into a graphite crucible which served the purpose of container material as well as anode. A molybdenum or tungsten rod with 6 mm diameter was used as cathode. The cathode rod was sheathed by a close fitting alumina tube stuffed with asbestos rope. The role of alumina tube was to prevent the rod from getting corroded with Cl_2 gas formed during electrolysis. A schematic diagram of the electrolytic cell assembly is shown in **Fig.6.1**. It consists of a vacuum tight inconel retort (100mm dia) fitted with a stainless steel flange system having provision for placing cathode rod, thermocouple, gas inlet and outlet tubes. The graphite crucible was placed inside the inconel retort which was kept in a tubular vertical resistance furnace as shown in Figure. The resistance furnace with temperature accuracy $\pm 2^{\circ}C$ was used to heat the cell up to the operating temperature. The electrolyte in the graphite crucible was melted under the protective argon gas. The temperature of the bath was measured with a protected K-type thermocouple. The negative terminal of DC power supply was connected to cathode rod and positive terminal to inconel retort that eventually made graphite as anode. After

equilibrating the bath for 1 hour at the operational temperature, pre-electrolysis was carried out to remove residual water followed by electrolysis applying potential from a DC power supply. Electrolysis was carried out at temperatures higher than the melting points of the metals to be extracted. To collect the metal deposited at cathode, an alumina crucible was placed below it inside the graphite crucible. The Alumina crucible and cathode rod were kept in such a manner that the tip of the cathode rod remained just above the alumina crucible. Electrolysis was continued for a specific period and after each electrolysis, the cell was allowed to cool to room temperature under the flow of argon gas. Cathode rod and thermocouple were taken above the electrolytic bath before allowing the furnace to cool to prevent them sticking inside the salt. The molten metal collected in the alumina crucible was recovered by washing the solidified molten salt with water. The alumina being non-conducting helped to protect the metal from anodic attack as well as from reaction with graphite crucible. The amount of metal collected in each experiment was found to be 200-300 gram in accordance with the amount of functional electrolyte ($RECl_3$) used. **Figs.6.2, 6.3, 6.4 and 6.5** give the picture of lanthanum, cerium, praseodymium and neodymium metals prepared by the above method.

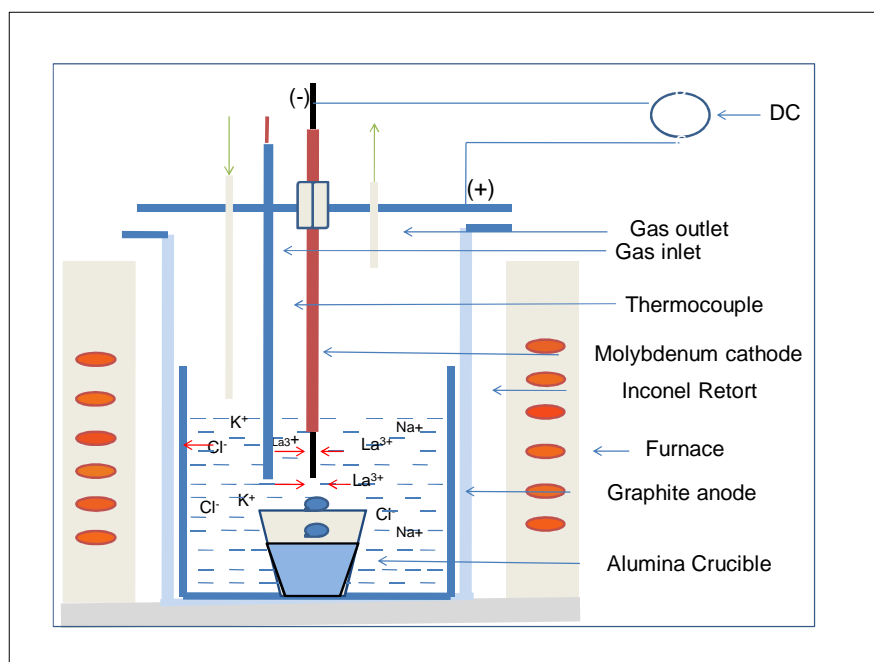


Fig.6.1. Schematic view of the molten salt electrochemical set-up



Fig.6.2 Electrodeposited product obtained from the electrolysis of LaCl_3 in LiCl-KCl flux.



Fig.6.3 Electrodeposited product obtained from the electrolysis of CeCl_3 in LiCl-KCl flux.



Fig.6.4 Electrodeposited product obtained from $\text{PrCl}_3\text{-LiCl-KCl}$ electrolyte.



Fig.6.5 Electrodeposited product obtained from $\text{NdCl}_3\text{-LiCl-KCl}$ electrolyte.

6.2.3 Instrumentation

The extracted metal ingots were characterized by X-ray diffraction (XRD) and Energy dispersive X-ray fluorescence (EDXRF) techniques. The chemical analysis of the metal was carried out employing Inductively Coupled Plasma-Atomic Emission Spectroscopic (ICP-AES) technique.

6.3 Results and discussion:

6.3.1 Analysis of the electrodeposited metals:

Fig.6.6, 6.7, 6.8 and 6.9 show the Energy dispersive X-ray Fluorescence Spectra (EDXRF) of La, Ce, Pr and Nd metals obtained by electrolysis process. The EDXRF spectra confirmed the presence of RE metal only. No peaks due to the impurity phases could be observed. Lanthanum and cerium metals were characterized by XRD using MoK α radiation. **Fig.6.10 and 6.11** show the XRD pattern of cerium and lanthanum metals. The observed XRD pattern for the Ce and La metals are found to match well with the reported pattern of the metal corresponding to the PCPDF file no 36-0815 and 78-0638, respectively.

The impurities present in the deposited metals analyzed by ICP-AES technique were found to be around 0.5 wt %. Impurity from cathode material was comparatively more when molybdenum was used as cathode rod compared to tungsten rod. This could be due to higher solubility of molybdenum in rare earth metal compared to tungsten at operating temperature. Carbon impurity in the metal was determined to be around 0.01 wt % by vacuum fusion method. Concentration of K, Na and Li were determined by Atomic Absorption Spectroscopy (AAS) analysis and found in ppm level. The gaseous impurities of hydrogen, nitrogen and oxygen were also found in ppm level.

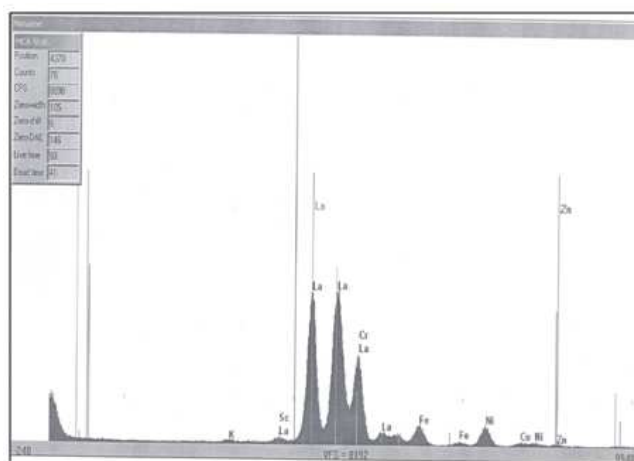


Fig.6.6 EDXRF spectra of the electrodeposited product from $\text{LaCl}_3\text{-LiCl-KCl}$ electrolyte

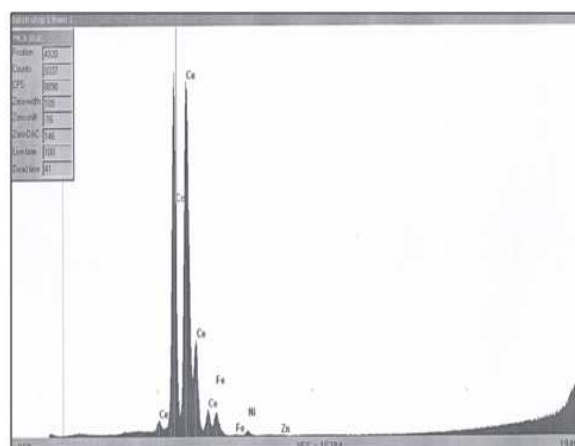


Fig.6.7 EDXRF spectra of the electrodeposited product obtained from $\text{CeCl}_3\text{-LiCl-KCl}$ electrolyte.

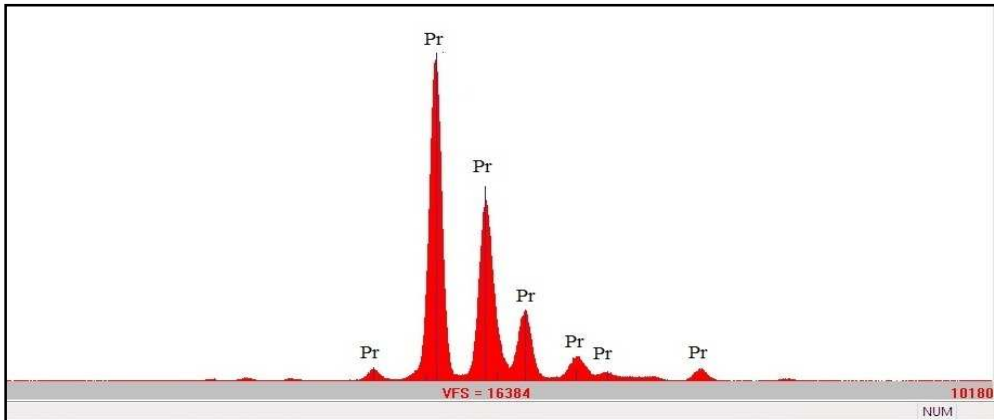


Fig.6.8 EDXRF spectra of the electrodeposited product obtained from $\text{PrCl}_3\text{-LiCl-KCl}$ electrolyte.

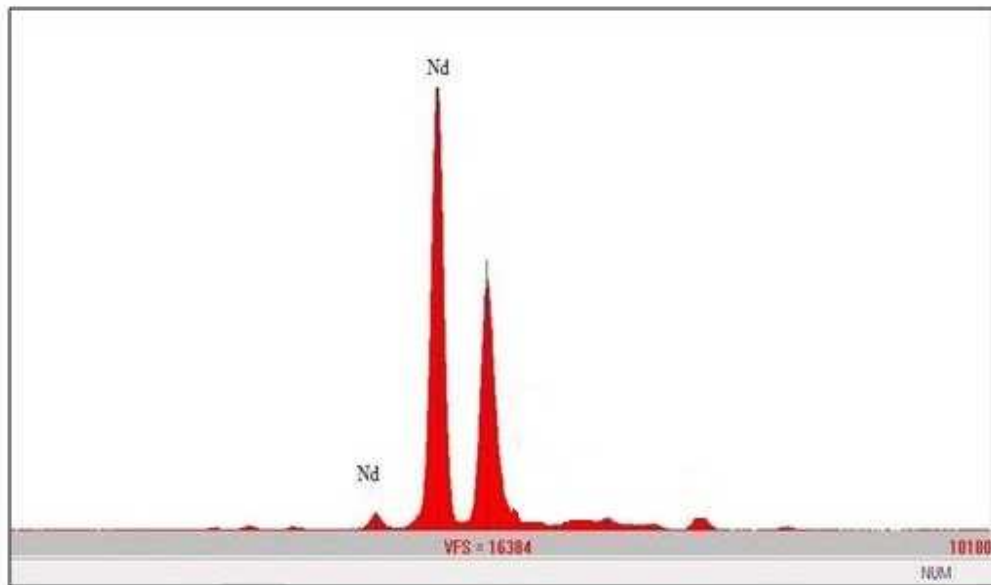


Fig.6.9 EDXRF spectra of the electrodeposited product obtained from $\text{NdCl}_3\text{-LiCl-KCl}$ electrolyte.

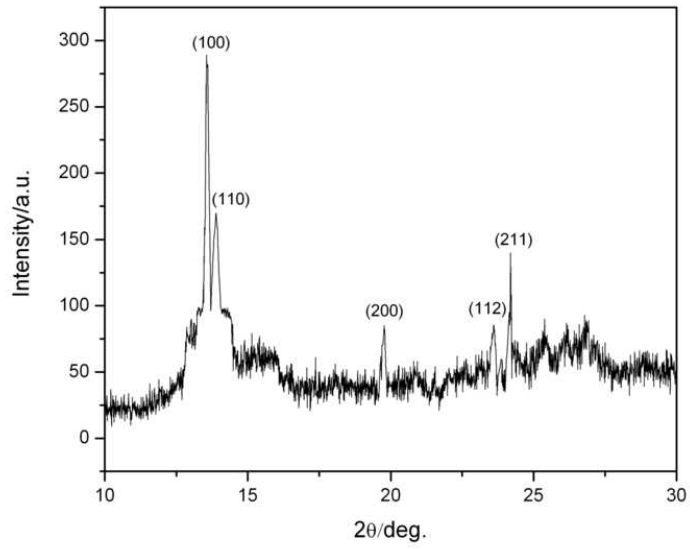


Fig.6.10 XRD plot of the electrodeposited product from $\text{LaCl}_3\text{-LiCl-KCl}$ electrolyte

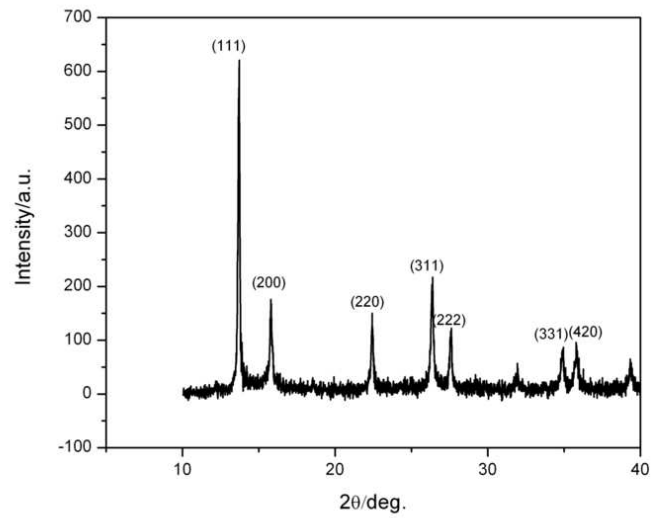
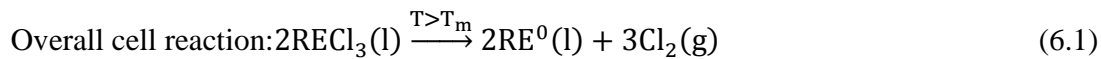


Fig.6.11 XRD plot of the electrodeposited product obtained from $\text{CeCl}_3\text{-LiCl-KCl}$ electrolyte.

6.3.2 Electrolytic reaction:

The cell reactions can be represented as follows.

C (graphite), Cl₂(g)|RECl₃ – LiCl – KCl|RE³⁺/RE, Mo (When molybdenum was used as cathode and LiCl-KCl was used as carrier electrolyte)



T is the temperature of operation and T_m = melting point of RE metal. During the electrolysis process, RE ions were reduced to RE metal and deposited on cathode surface in liquid form, which are then collected in an alumina crucible kept below the cathode rod. The difference in the density of RE metal and molten salt (6 gm/cc and 2gm/cc, respectively) helped the metal to settle at the bottom of the alumina crucible. At anode surface, chloride ions form chlorine gas by. The chlorine gas released during the process was effectively swept out from the electrolytic cell by bubbling high purity argon gas in the molten electrolyte. In order to prevent air pollution and toxicity of chlorine gas, the evolved Cl₂ gas was converted to NaOCl(aq) by dissolving in sodium hydroxide solution according to following reaction



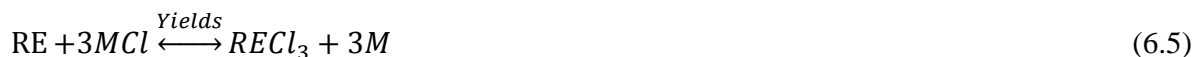
Current efficiency for the electrowinning process was calculated as per Faraday's 1st law by following expression:

$$\eta = \frac{W}{e} \times \frac{96500}{Q} \times 100 \quad (6.3)$$

η represents current efficiency (%), W = mass of metal deposited (gm), e is the electrochemical equivalent of the metal (g), Q is the quantity of charge passed through the electrolytic cell (Col).

6.3.3 Relation between electrolytic temperature and current efficiency

The effect of temperature on current efficiency in the electrowinning of all the four metals (i.e. La, Ce, Pr and Nd) was summarized in **Fig.6.12**. Experiments were carried out at a constant cathode current density in a bath containing 40 wt% RECl₃ in equimolar LiCl-KCl melt. Table-6.1 shows the typical operating data for electrowinning of RE metal from RECl₃-LiCl-KCl and RECl₃-NaCl-KCl electrolytes chosen for this study. The temperature of electrolysis was raised in 20 K intervals. From fig. 6.12, it could be observed that the temperature at which, cerium, lanthanum praseodymium and neodymium yielded maximum efficiency were 1173 K, 1223 K, 1233 K and 1323 K respectively. The optimum temperature obtained in the electrowinning of La, Pr and Nd metals were found to be 30-40 K above the melting point of these metals. The current efficiency obtained just above their melting temperatures is low because of the higher surface tension of the liquid metal formed which results in poor coalescence of metal droplets. At optimum temperature (30 to 40 K above melting point) the surface tension of metal droplet decreases which enhances the coalescence of metal droplets resulted in higher recovery. At much higher operational temperature current efficiency is low due to the increased solubility of the metal in the melt [75]. At high temperature, the RE metal formed at cathode redissolved in molten chloride according to following reaction [161].



Mass of supporting electrolyte (LiCl + KCl) or (NaCl + KCl)	600 g
Mass of functional electrolyte (RECl ₃)	400g
Applied current	31 A
Cathode current density	10 A cm ⁻²
Voltage measured	4.5 to 5.5
Duration of electrolysis	3 hours

Table-6.1 Typical operating data chosen to study the effect of temperature on current efficiency in electrowinning of RE metal from RECl₃-LiCl-KCl and RECl₃-NaCl-KCl electrolytes.

In case of cerium the optimum temperature of operation was found to be 100°C above its melting point. This is because cerium has a lower melting temperature where the viscosity and conductivity of the melt is poor which results in low efficiency.

It can also be observed keeping above mentioned temperature of the corresponding metal, the efficiency decreases from lanthanum to neodymium. The difference in the observed efficiency could be explained by the increase in the operational temperature. Except for Ce, the operational temperature increase from La to Nd. The evaporation loss of electrolyte at higher operational temperature resulted in low efficiency of the process. The lower efficiency in the case of Ce as compared to La can be attributed to cyclic oxidation and reduction of Ce³⁺/Ce⁴⁺ [58].

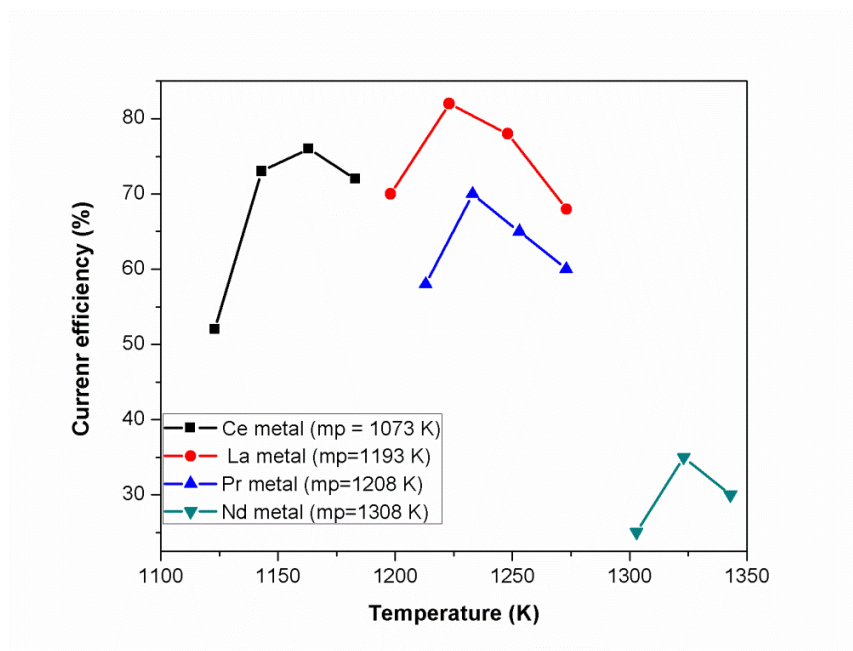


Fig.6.12 Relationship between current efficiency and operating temperature in the electrowinning of RE metals using RECl_3 (40wt%)-LiCl-KCl electrolytes. (RE = La, Ce, Pr and Nd).

6.3.4 Effect of concentration of functional electrolyte on current efficiency

The effect of electrolytic composition on current efficiency is illustrated in **Fig.6.13**. Here the wt% of RECl_3 was varied keeping the current density (cathodic and anodic) and the operating temperature constant. Table -6.2 shows the typical operating data for electrowinning of RE metal from RECl_3 -LiCl-KCl and RECl_3 -NaCl-KCl electrolytes chosen for this study. It was observed that there is an improvement in current efficiency with increase in concentration of functional electrolyte (RECl_3), which is the indication of mass transferred controlled phenomena. At higher concentration of RECl_3 , the electrolyte becomes more viscous which results into lower current efficiency [58]. The poor result at low concentration of RECl_3 may be due to the codeposition of solvent ions along with RE ions. The optimum concentration of RECl_3 for deposition of rare

earth metal was found to be 30-50 wt % in both LiCl-KCl and NaCl-KCl mixtures. **Fig.6.13** gives the plot of current efficiency as a function of concentration of RECl₃ at constant operating temperature. From the figure it could be observed that the optimum concentration of RECl₃ decreases from La to Nd, which could be due to the decrease in solubility of RECl₃ in molten chloride.

Mass of supporting electrolyte (LiCl + KCl) or (NaCl + KCl)	600 g
Mass of functional electrolyte (RECl ₃)	100-800 g
Applied current	31 A
Cathode current density	10 A cm ⁻²
Voltage measured	4.5 to 6
Duration of electrolysis	1 hour

Table -6.2 Typical operating data chosen to study the effect of composition of electrolyte on current efficiency in electrowinning of RE metal from RECl₃-LiCl-KCl and RECl₃-NaCl-KCl electrolytes.

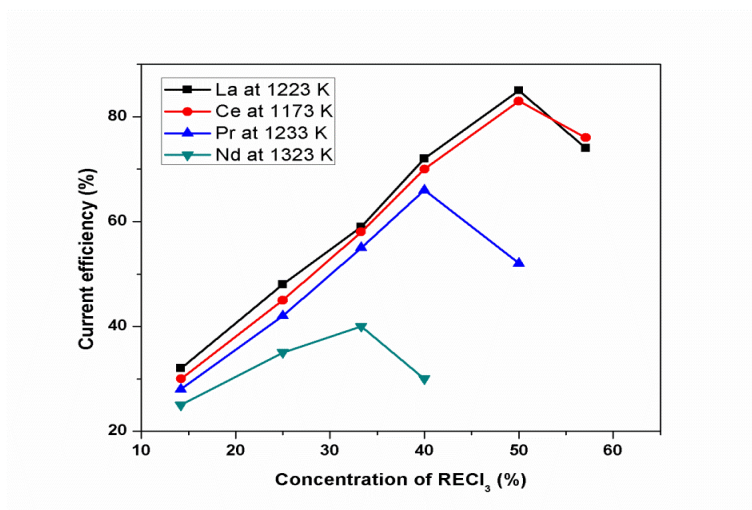


Fig.6.13 Relationship between current efficiency and electrolyte composition of LiCl-KCl-RECl₃ systems obtained on a molybdenum electrode at 10 A.cm⁻² at T=1223 K for La, T=1173 K for Ce, T=1233 K for Pr and T=1323 K for Nd.

6.3.5 Effect of cathode current density on current efficiency:

The effect of cathode current density (CCD) on current efficiency was studied in LiCl-KCl and NaCl-KCl melts. **Fig.6.14** shows the variation of current efficiency in the CCD in the range 5-18 A/cm² in the electrowinning of La, Ce, Pr and Nd in LiCl-KCl melt. Table-6.3 shows the typical operating data for electrowinning of RE metal from RECl₃-LiCl-KCl and RECl₃-NaCl-KCl electrolytes chosen for this study. From the figure, an improvement in the current efficiency could be observed with increase in CCD for all the metals. With higher CCD, the kinetics of migration of lanthanide ions towards cathode surface increases which help in depositing metals at a greater speed. However, at a very high current density, the codeposition of solvent ions resulted in high negative potential of cathode and hence there was fall in C.E. The optimum CCD for deposition of the RE metals under present investigation was found to be 12 A/cm² in LiCl-KCl and 14 A/cm² in NaCl-KCl melts. The higher current density required in NaCl-KCl melt was probably due to the higher viscosity of bath compared to LiCl-KCl melt.

Higher current efficiency was also observed in LiCl-KCl melt compared to NaCl-KCl melt. The range of stability and greater fluidity of LiCl-KCl over NaCl-KCl solvent could be the possible reason for this trend as described by some researchers [75].

Mass of supporting electrolyte (LiCl + KCl) or (NaCl + KCl)	600 g
Mass of functional electrolyte (RECl ₃)	400 g
Applied current	15.5 to 55.8A
Cathode current density	5 to 18 A cm ⁻²
Voltage measured	3.5 to 8
Duration of electrolysis	2 hour

Table-6.3 Typical operating data chosen to study the effect of CCD on current efficiency for electrowinning of RE metal from RECl₃-LiCl-KCl and RECl₃-NaCl-KCl electrolytes.

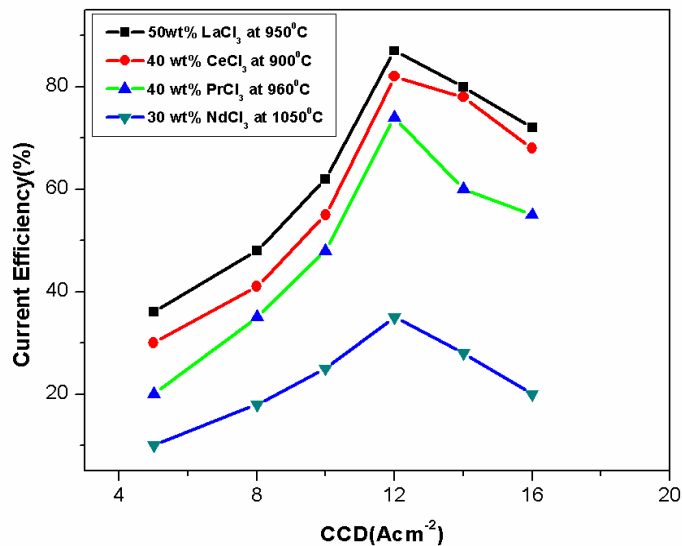


Fig.6.14 Relationship between CE and CCD obtained in the electrolysis of LiCl-KCl-RECl₃ systems on molybdenum at mentioned temperature and composition of electrolyte.

6.3.6 Effect of electrolysis duration on yield and current efficiency

Fig.6.15 shows the metal yield and current efficiency obtained with time in the electrowinning of lanthanum metal. Typical operating data for electrowinning of La metal from $\text{LaCl}_3\text{-LiCl-KCl}$ and $\text{LaCl}_3\text{-NaCl-KCl}$ electrolytes chosen for the present investigation is mentioned in table-6.4. It is evident from the figure that short duration of electrolysis resulted in higher current efficiency which steadily reduced with the increase in the electrolysis time. The decrease in current efficiency with time can be explained due to the increase solubility of metal deposit in the molten salt due to longer time of contact. It is also observed that metal yield increases with electrolysis time. However, after a certain time, yield increases marginally but current efficiency decreases drastically. This is due to the fact that after consumption of a certain concentration of functional electrolyte during the electrolysis process, the applied voltage reaches the over potential limiting of solvent deposition. Therefore after optimum duration (4 hours in this case), the deposition of solvent ion occurs with functional ion which reduces the current efficiency. In this case, it is observed that after 85% recovery of the metal, the maximum fraction of current used in the deposition of solvent ion. Therefore, current efficiency reduces. Maximum metal yield of 85% was obtained when 25% excess charge was passed over the theoretical charge required for complete decomposition of LaCl_3 . Similar behaviors were also observed in the electrowinning of cerium, praseodymium and neodymium metals.

Mass of supporting electrolyte (LiCl + KCl) or (NaCl + KCl)	600 g
Mass of functional electrolyte (RECl ₃)	400 g
Applied current	31 A
Cathode current density	10 A cm ⁻²
Voltage measured	4.5 to 5.5

Table-6.4 Typical operating data chosen to study the effect of electrolysis time on yield and current efficiency in the electrowinning of La metal from LaCl₃-LiCl-KCl and LaCl₃-NaCl-KCl electrolytes.

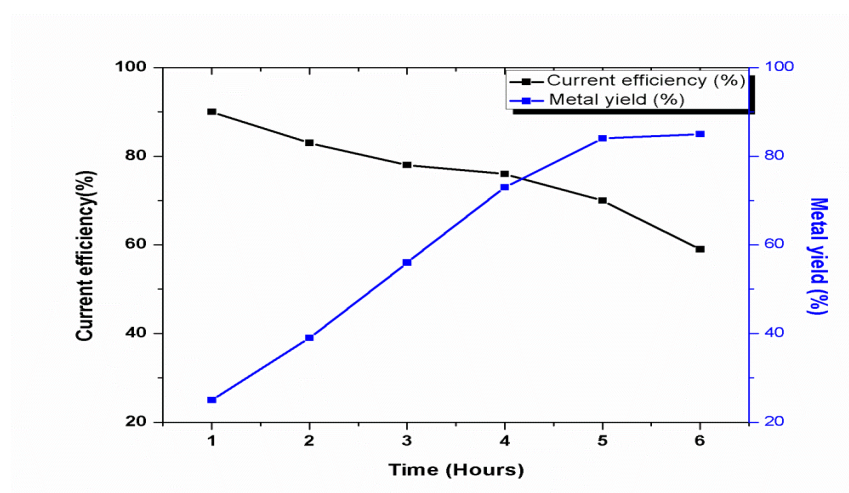


Fig.6.15 Metal yield and current efficiency obtained with time in the electrowinning of lanthanum metal.

6.3.7 Effect of single carrier electrolyte:

Extractions of lanthanum and cerium metals were studied using single carrier electrolyte such as KCl, NaCl and LiCl. Fig 6.16 showed the effect of CCD on CE in the electrowinning of lanthanum metal using single carrier electrolyte. Here, the applied voltage in the electrolysis was slightly higher compared to LiCl-KCl or NaCl-KCl electrolyte. The current efficiencies obtained in the single carrier electrolyte are found to be low to that obtained in mixture solvent. However, the

purity of metal was comparable to that mixed solvent. The current efficiency single carrier electrolyte was found to be in the order $\text{KCl} > \text{NaCl} > \text{LiCl}$. The lower current efficiency for NaCl and LiCl compared to KCl could be due to formation of higher order lanthanide complex in these solvent [162]. The bulkier complex formed in case of NaCl and LiCl resulted in slow mass transfer which eventually makes the current efficiency low. It may be related to the solubility of lanthanide chloride in the salt. However a detailed explanation and experimental evidence was not obtained so far by us.

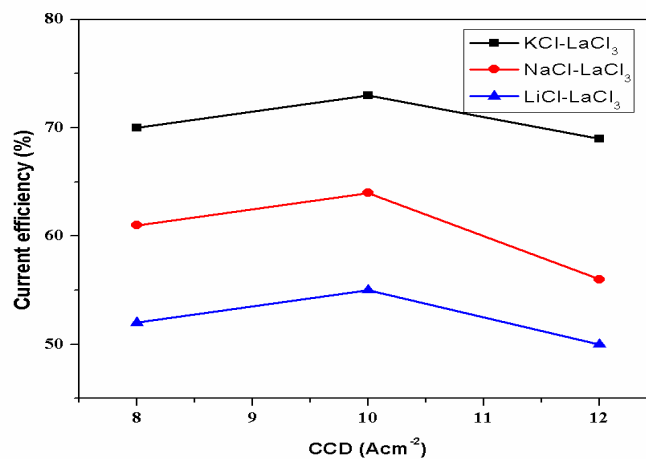


Fig.6.16 Relationship between CE and CCD obtained in the electrowinning of lanthanum from the electrolytic composition containing 40wt% of LaCl_3 in LiCl, KCl and NaCl respectively.

6.3.4 Conclusion:

Electrowinning process has been successfully developed to produce Lanthanum, Cerium, and Praseodymium and Neodymium metals with more than 99% purity from their corresponding chlorides. The process parameters for maximum current efficiency such as composition of electrolyte, operational temperature, and cathode current density have been standardized for the extraction of these metals in both LiCl-KCl and NaCl-KCl solvents. The standardized parameters

are summarized in **Table-6.5**. It is proposed to get higher current efficiency using these standardized parameters by operating the electrolytic cell in continuous or semi-continuous mode.

Metal	Optimum Temp	Optimum Conc.	Optimum CCD	
			LiCl-KCl	NaCl-KCl
La	1223 K	50 wt% LaCl ₃	12A/cm ²	14A/cm ²
Ce	1173 K	50 wt% CeCl ₃	12A/cm ²	14A/cm ²
Pr	1233 K	40 wt% PrCl ₃	12A/cm ²	14A/cm ²
Nd	1323 K	30 wt% NdCl ₃	12A/cm ²	14A/cm ²

Table-6.5 Standardized parameters in the electrowinning of La, Ce, Pr and Nd metals in LiCl-KCl and NaCl-KCl carrier electrolytes.

6.5- Verification of optimized parameters by Taguchi method:

Taguchi method [163] is a multi-parameter optimization procedure, which is very useful in identifying and optimizing dominant process parameters with a minimum number of experiments. Taguchi method has been adopted in the present work to select the most influential parameters and their effect on electrowinning process. The three key parameters in the electrowinning process i.e. temperature, concentration of electrolyte and cathode current density have been selected and varied in three different levels, which makes it a 3 factor three level system. The method [164] is based on an orthogonal array set of experiments with various combinations of parameter levels. Output of the orthogonal array, which indicates the relative influences of various parameters on the formation of the desired product, is used to optimize an objective function. There are three types of objective functions: larger- the-better, smaller-the-

better and nominal-the-best. The influences are commonly referred in terms of S/N (signal to noise) ratio.

For optimization of electrolysis parameters to get highest current efficiency, larger-the better type of objective function has been used. Here, the exact relation between S/N ratio and the signal is given by

$$\frac{S}{N} = -10 \log \left(\frac{1}{n} \right) \sum_i^n \frac{1}{y_i^2} \quad (6.6)$$

' y_i ' is the average measured current efficiency. The effect of a parameter level on the S/N ratio (m_i) and the relative effect of process parameters (sos) can be obtained computed using following relations

$$m_i = \left(\frac{1}{N_i} \right) \sum \frac{S}{N} \quad (6.7)$$

&

$$\text{Sum of squares (SOS)} = \sum_{i=1}^j N_i (m_i - \langle m_i \rangle)^2 \quad (6.8)$$

m_i represents the contribution of each parameter level to S/N ratio, $\langle m_i \rangle$ is the average of m_i 's for a given parameter and the coefficient and N_i represents the number of times the experiment is conducted with the same factor level in the entire experimental region. SOS is obtained by using Eqn (10). This term is divided by corresponding degrees of freedom (DoF = number of parameter level minus 1) to derive relative importance of various experimental parameters by following equation

$$\text{Factor effect} = \frac{SOS}{\{DOF \times \sum(SOS/DOF)\}} \quad (6.9)$$

Several researchers [165-166] have extensively used this technique in optimization of parameters in various processes. Here optimum conditions for the electrowinning of praseodymium metal in LiCl-KCl melt were determined employing Taguchi method.

6.5.1 Selection of parameters for Taguchi optimization:

The objective is to verify the optimum operating condition in the electrowinning of praseodymium metal. Three parameters in three different levels have been identified for optimization. These are Temperature (1213 K, 1233 K and 1253 K), wt% of PrCl_3 (20%, 40%, 60%) and cathode current density ($8\text{A}/\text{cm}^2$, $12\text{A}/\text{cm}^2$, $16\text{A}/\text{cm}^2$). **Table-6.6** shows the parameters and their levels. This is a three-parameter-three-level design. Therefore, L-9 orthogonal array has been chosen as per design and same has been presented in **Table-6.7**.

Parameters	Level1	Level2	Level3
Temperature(K)	1213	1233	1253
Wt% of PrCl_3	20	40	60
CCD(A/cm^2)	8	12	16

Table-6.6 Taguchi parameters and their levels

.No. experiments	Temp	Cd	Conc	efficiency	S/N
1	1213	8	20	46	33.26
2	1213	12	40	63	35.99
3	1213	16	60	45	33.06
4	1233	12	60	65	36.26
5	1233	8	40	60	35.56
6	1233	16	20	40	32.04
7	1253	8	60	38	31.60
8	1253	12	40	55	34.81
9	1253	16	20	52	34.32

Table-6.7 L9 Orthogonal array according to Taguchi method

Parameters	Level	mi	<mi>	SoS	%effect
Temp(K)	1213	34.10	34.10	0.55	9.54
	1233	34.62			
	1253	33.57			
CCD(A/cm ²)	8	33.47	34.10	3.82	66.62
	12	35.68			
	16	33.14			
	20	34.38			
Conc. (wt %)	40	35.29	34.44	1.37	23.82
	60	33.64			

Table-6.8 Effect of each parameter on current efficiency

The results of the experiments as per the L-9 array and the corresponding S/N ratios are given in **Table 6.6**. The effect of each parameter on the current efficiency is shown in **Table-6.7**. It can be observed from **Table 6.8**, that cathode current density has the maximum effect (66.62%) and

the temperature and concentration of electrolyte have less effect. The effect of concentration of functional electrolyte is more than effect of temperature. Column 3 in **Table-6.8** represents the effect of different parameters on S/N ratio in the electrowinning of praseodymium metal .It predicts that the best conditions (corresponding to highest S/N) to get maximum current efficiency in the electrowinning of praseodymium metal are Temp=1233 K, Conc. = 40wt% of PrCl_3 and CCD= $12\text{A}/\text{cm}^2$.

Conclusion: The results obtained from Taguchi calculation are in well agreement with the results obtained in our study. This model was also applied to validate the optimized process parameters obtained in the electrowinning of lanthanum and cerium metals. The dominant factor which greatly affects the current efficiency was found to be CCD.

6.4 Determination of solubility of RECl_3 in molten alkali chloride

melts:

Solubility of RECl_3 in molten salt media i.e. in LiCl-KCl or NaCl-KCl medium is an important parameter in determining the current efficiency and yield in the electrowinning of RE metals. The data on solubility of individual rare earth chloride in molten alkali chloride melts are not available in the literature. To understand the trend in current efficiency in the electrowinning of RE metals, solubility of individual RECl_3 both in LiCl-KCl and NaCl-KCl medium were carried out in the present investigation.

The molten salt mixture LaCl_3 -LiCl-KCl was vacuum sealed in 8mm diameter Pyrex tube and 1173 K. The salt mixture was equilibrated at that temperature for more than 2 hours and then it was quenched to room temperature immediately. Some of the un-dissolved rare earth chloride in the bottom of the Pyrex tube was clearly observed. The upper portion of the tube was colorless showing complete solubility. Lanthanide ion solubility in the molten salt mixture was measured

by quantitative measurement of lanthanide concentration from upper solidified portion of the melt by ICP-AES analysis. In case of La and Ce, dissolved La (III) and Ce (III) in LiCl-KCl are colorless but the undissolved chloride is white which is clearly visible to the naked eye. Similarly in case of Pr and Nd, dissolved Pr (III) and Nd (III) were colorless, whereas undissolved chlorides were green and pink in color for Pr and Nd respectively.

To verify the results obtained in the above mentioned process, solubility test was conducted in another way. The salt mixtures i.e. LiCl-KCl (1:1) was first melted in an alumina crucible under an argon atmosphere at 1173 K. Calculated amount of anhydrous RECl₃ was put into the treated LiCl-KCl melts and the molten mixture was allowed to equilibrate there for sufficient time. Very small sample was pipetted out from the mixture in the molten state itself. The total concentrations of lanthanide ions in prepared salts were measured by inductive coupled plasma-atomic emission spectroscopy (ICP-AES) analysis. To verify the vaporization loss of the RECl₃ from the molten salt mixture was also studied by collecting the sample at various interval. It was observed that vaporization behavior of RECl₃ is almost negligible in the alkali chloride melt in the experimental temperature. It was observed that the results obtained from both the experiments were consistent with each other. Similar experiments were carried out for the solubility of RECl₃ in NaCl-KCl melts also. The results obtained are shown in Table-6.9 and 6.10.

Solute	Solubility in wt% (from EXPT-I)	Solubility (from EXPT-II)
LaCl ₃	40.3	40.1
CeCl ₃	35.8	34.6
PrCl ₃	26.9	26.8
NdCl ₃	20.5	19.8

Table-6.9 Solubility of RECl₃ in LiCl-KCl electrolyte measured at 1173 K.

Solute	Solubility in wt% (from EXPT-I)	Solubility (from EXPT-II)
LaCl ₃	39.5	40
CeCl ₃	36.2	35.8
PrCl ₃	25.7	25.2
NdCl ₃	17.5	18.2

Table-6.10 Solubility of RECl₃ in NaCl-KCl electrolyte measured at 1173 K.

From the results it is clear that, RECl₃ is more soluble in molten LiCl-KCl media compared to NaCl-KCl media. The solubility of LaCl₃ was found to be highest and NdCl₃ was lowest in both the media.

6.6 Summary:

In this chapter, the effects of process parameters on current efficiency in the electrowinning of RE (La, Ce, Pr & Nd) metals were studied in two molten salts; LiCl-KCl and NaCl-KCl. The three important process parameters i.e. temperature, composition of electrolyte and cathode current density were optimized to get highest current efficiency for each of these four rare earth metal. Variation of current efficiency with the change in the molten salt media and the variation across the different rare earth metal ions have been investigated. Current efficiency for the electrowinning of La, Ce, and Pr metal using molten chloride electrolytes was to be in the range of 70-90% which definitely more than the value reported in the literature which is 50%. The current efficiency obtained in the present investigation with chloride medium has been compared with the current efficiency obtained in oxide-fluoride media in Table 6.11.

Metal	Molten salt media	Current efficiency (%)
La	Oxide-Fluoride	75-90 (59)
	Chloride(present study)	88
Ce	Oxide-Fluoride	75-90 (60)
	Chloride(present study)	85
Pr	Oxide-Fluoride	80 (61)
	Chloride(present study)	75
Nd	Oxide-Fluoride	70 (62)
	Chloride(present study)	40

Table-6.11 Comparison of current efficiency value in chloride (present study) and oxide-fluoride media (literature).

It is evident from the table that the current efficiency obtained in the electrowinning of lanthanum; cerium and praseodymium in chloride media are comparable with that of oxide-fluoride media. It can be noted that the current efficiency was determined in continuous mode operation in case of oxide-fluoride media as compared to batch mode operation in the present investigation. The current efficiency obtained in this case can be substantially improved with the continuous mode operation.

Neodymium electrowinning from the chloride electrolytes is perhaps not the best method for the production of neodymium metal. The low current efficiency observed in the electrowinning of neodymium metal in molten chloride electrolysis could be due to low solubility of NdCl_3 in LiCl-KCl or NaCl-KCl melt. Slow diffusion co-efficient of Nd ion, existence of divalent ion in the molten chloride salt (evident from chapter-V) and excessive vaporization of electrolyte due to higher operational temperature could be responsible for low current efficiency in the electrowinning of Nd metal. The optimized parameters derived in each case were verified using Taguchi method.

Although a slightly higher current efficiency was observed in the electrowinning of metals from molten LiCl-KCl electrolyte compared to NaCl-KCl electrolyte, from industrial production point of view NaCl-KCl has the advantage over LiCl-KCl due to its low cost. Regarding the use of only one carrier electrolyte, some more investigations are definitely required to make any meaningful conclusion. In the study, a method for the efficient neutralization of chlorine gas has been established, where the evolved chlorine gas is passed through sodium hydroxide solution to form sodium hypochlorite which is a commonly used bleaching agent in many households. Containment of chlorine is a critical factor which may find wide spread acceptance in the electrowinning process.

ELECTROCHEMICAL DEPOSITION OF RARE EARTH (RE) ALLOYS

7.1 Introduction:

Electrochemical synthesis of alloys and compounds is a very efficient tool to produce materials and coatings [167-169]. It is performed most often from aqueous solutions. However, due to the limiting factor of hydrogen evolution and small potential window, alloys consisting of more electronegative metals cannot be electrodeposited in aqueous electrolysis process. Therefore, Alloys [170] and compounds [171] having more electronegative metals are usually produced from molten salts. Molten salt electrochemical process is a powerful method to develop rare earth alloys. This process has some advantages in terms of batch size, homogeneity of alloy composition and ease of operation which facilitates inexpensive mass production. Electrochemical technique is useful in significantly reducing the production cost of rare earth alloys. There are two methods employed in the molten salt electrolysis process to produce alloys.

- 1) Electrochemical co-deposition technique
- 2) Consumable cathode technique

Choice of either of these two methods depends on the electrochemical nature and reactivity of the alloying elements. The electrolytic codeposition method involves simultaneous deposition of two metal ions from the electrolyte on the cathode. Preparation of La-Mg alloys by electrochemical co deposition of Mg (II) and La (III) ions on a molybdenum cathode from molten chloride electrolyte has been studied here. The electro reduction of rare earth on a

reactive cathode to yield the alloy directly is called as consumable cathode technique. The preparation of neodymium-iron alloys from molten salt electrolysis in a chloride bath using a consumable iron cathode has been studied here.

7.2 Electrochemical codeposition technique:

In co-deposition technique, the electrolyte (molten salt) consists of two electrochemically active cations, with their known concentrations. The cations are considered to co-deposit on the surface of the same inert cathode in their metallic states forming different possible phases under the influence of the outer electric source. Production of La-Mg alloy was studied by this technique.

La-Mg alloys:

Rare earth-magnesium intermetallic have attracted interest in the recent past due to technological important properties such as high temperature ductility, corrosion resistance and low temperature superconductivity etc. [172-173]. The high hydrogen storage capability of lanthanum-magnesium intermetallic is relevant for hydrogen storage and for Ni-MH batteries [174-176]. Some La-Mg compounds have enhanced effect on hydrogen absorption and desorption kinetics in various materials [177-179].

The traditional method for producing the La-Mg alloy is pyro-metallurgical, which involves the metal mixing and thermal reduction processes. Both these processes have their limitations like micro-segregation and small batch size [180]. These problems can be circumvented by employing molten salt electrolysis process.

7.2.1 Basic electrochemical study:

In this work, the electrochemical co-reduction of Mg (II) and La (III) ions was investigated employing transient electrochemical techniques on a molybdenum electrode in LiCl-KCl-MgCl₂-LaCl₃ melt.

7.2.1.1 Cyclic voltammetry:

Fig.7.1 illustrates the cyclic voltammograms obtained on a molybdenum electrode in the LiCl-KCl-MgCl₂ (2 wt%) melt before and after addition of LaCl₃ at 773K. The black line in the figure corresponds to the cyclic voltammogram without LaCl₃ and red line correspond to the spectra after addition of LaCl₃ (5wt%). The cathodic peak A at -1.70 V in the red curve was attributed to the deposition of Mg (evident from the black curve) and anodic peak A1 correspond to the dissolution of Mg metal. After addition of LaCl₃, there was substantial increase in the cathodic current at an potential of around -1.8 V which could be due to the under potential deposition of La(III) on deposited Mg layer or due to the co-deposition of La(III) and Mg(II) to form La-Mg alloy. The cathodic signal C at -2.1 V was ascribed to the deposition of La (III) and corresponding anodic peak C1 corresponds to the dissolution of La metal.

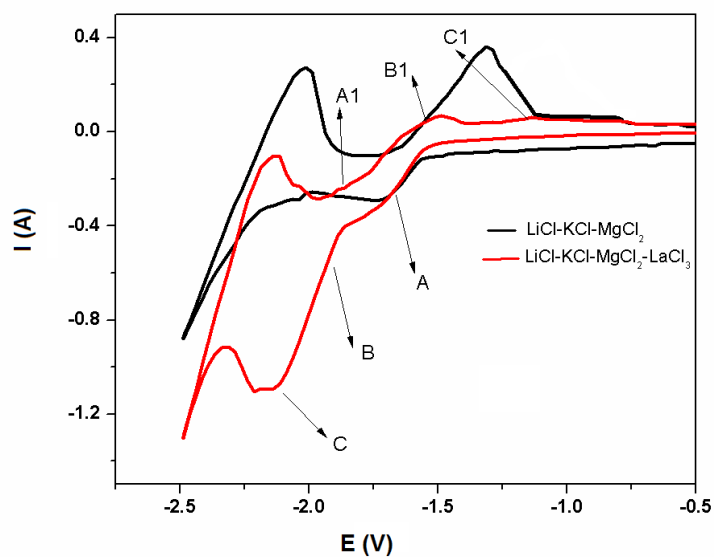


Fig.7.1 Cyclic voltammograms obtained on molybdenum electrode in LiCl-KCl-MgCl₂ In the presence and absence of LaCl₃.

7.2.1.2 Open circuit potentiometry:

OCP is an suitable electrochemical technique to study the possible formation of an alloy at the working electrode. **Fig.7.2** corresponds to the OCP of the electrode versus time obtained after potentiostatic electrolysis at -2.4 V for 10 minutes. The first plateau corresponds to the -1.99 V was related to the equilibrium potential of La (III)/La system. The second plateau corresponds to the -1.70 V was attributed to the formation of La-Mg alloys. The third and last plateau at -1.66 V was related to the Mg²⁺/Mg redox couple.

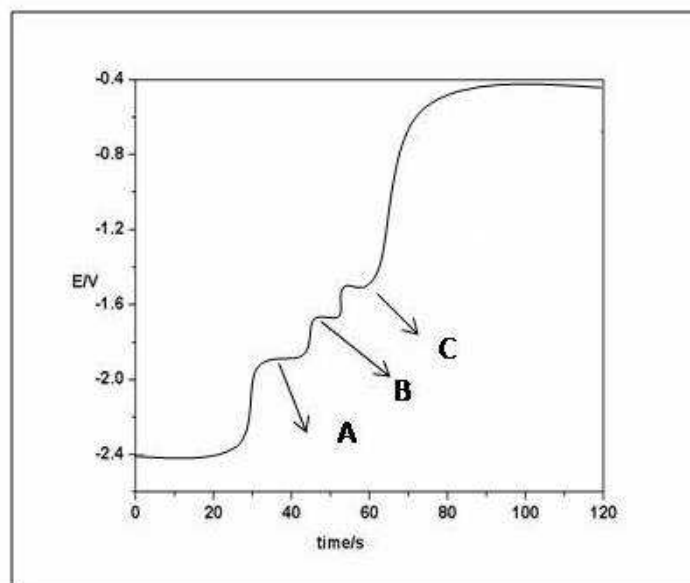


Fig.7.2 Open circuit potentiogram of $\text{LaCl}_3\text{-MgCl}_2\text{-LiCl-KCl}$ system at molybdenum electrode at 773K, $E_{\text{applied}}=-2.4$ V.

7.2.1.3 Potentiostatic electrolysis and characterization of La-Mg alloys:

Based on the results of CV and OCP studies, potentiostatic electrolysis was carried out at -1.80 V for 30 minutes on molybdenum electrode in LiCl-KCl melt with 5.0 wt% of MgCl_2 and 2 wt% LaCl_3 . The XRD characterization of the product shows the formation of LaMg and LaMg_2 alloys. **Fig.7.3** shows the XRD pattern of La-Mg alloys obtained by potentiostatic electrolysis at -1.80 V for 30 minutes from LiCl-KCl- LaCl_3 (2wt%)- MgCl_2 (5wt%) electrolyte. Similar experiments were carried out with different composition of electrolyte and ICP-AES analysis of the obtained products are shown in **Table-7.1**. It was evident from the study that with varying concentration of LaCl_3 and MgCl_2 in the electrolyte the alloy composition can be controlled.

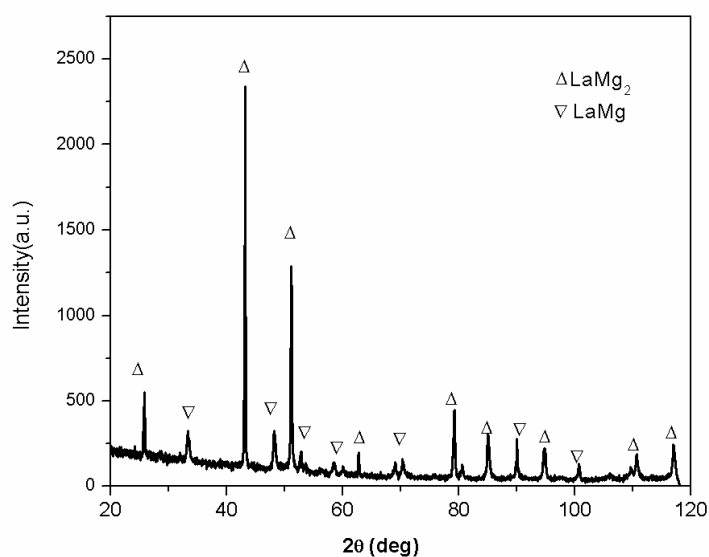


Fig.7.3 XRD pattern of La-Mg alloys obtained by potentiostatic electrolysis at -1.80 V for 30 minutes from LiCl-KCl-LaCl₃ (2wt%)-MgCl₂ (5wt %) electrolyte

Sample No	MgCl ₂ conc. (Wt %)	LaCl ₃ conc. (Wt %)	La content (Wt %)	Mg content (Wt %)
1	2	6	84.2	Bal.
2	2	5	77.8	Bal.
3	3	5	74.3	Bal.
4	3	3	39.7	Bal.

Table-7.1 ICP-AES analysis of the obtained products with varying concentration of LaCl₃ and MgCl₂.

7.2.1.4 Conclusion:

Electrochemical co reduction behavior of Mg (II) and La (III) ions was investigated in LiCl-KCl-LaCl₃-MgCl₂ electrolyte on molybdenum electrode employing cyclic voltammetry and open

circuit potentiometry studies. It was concluded that direct electrodeposition using MgCl_2 and LaCl_3 in molten chloride electrolyte has the potential for the industrial production of La-Mg alloys.

7.2.2 Bulk preparation of La-Mg alloy:

With this background, we studied the preparation of La-Mg alloys by electrochemical co-deposition of Mg and La on a molybdenum cathode from LaCl_3 - MgCl_2 -KCl melt. Here KCl was only used as carrier electrolyte instead of LiCl-KCl (used in the CV study) to increase the potential window of the solvent and thereby suppress the possible co-deposition of Li (I) ion. The main aim was to see the feasibility in obtaining the intermetallic compounds of La-Mg alloys particularly in molten state. So, the electrolytic cell was operated above 1073 K in order to obtain the intermetallic compounds in molten state. In this study, the preparation of different phases of La-Mg alloys in LaCl_3 - MgCl_2 -KCl melt was investigated. The phase control of La-Mg alloys with variation in LaCl_3 and MgCl_2 concentration in the electrolyte was studied. The effect of experimental parameters like temperature, cathode current density (CCD) on current efficiency was also investigated.

Description regarding electrolytic cell is given in the **section 6.1.3**. The schematic of the cell is given in the **Fig.7.4**

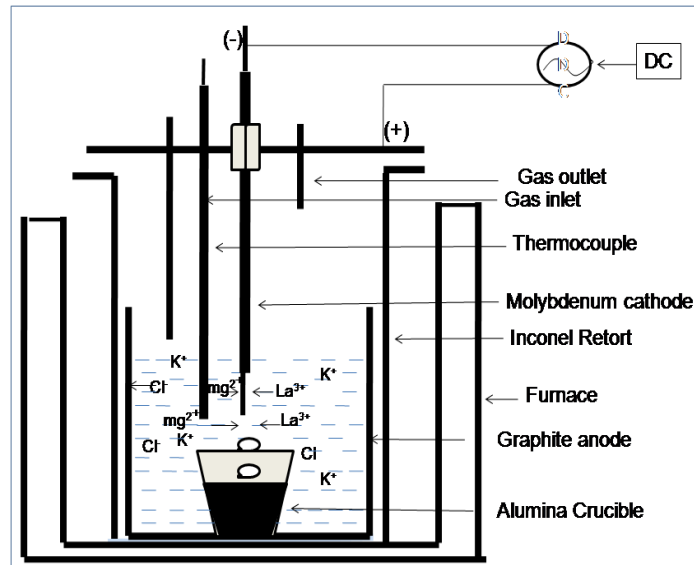


Fig.7.4 Schematic of the molten salt electrolytic set-up used in our study for La-Mg alloy production.

7.2.2.1 Results and Discussion:

7.2.2.1.1 Effect of electrolyte composition

The molten salt bath used in this study consisted of LaCl_3 , MgCl_2 and KCl where LaCl_3 and MgCl_2 acted as functional electrolyte and KCl as carrier electrolyte. The function of KCl is to increase the electrical conductivity and reduce the viscosity of bath. **Table 7.2** shows the current efficiency with the change in composition of carrier electrolyte. The results show rate of deposition is slow in the composition where $(\text{LaCl}_3+\text{MgCl}_2)$: KCl ratio is 60:40. Current efficiency starts increasing and reaches maximum where wt% of KCl is 60. when wt% KCl becomes more than 60 wt% current efficiency starts decreasing due to co-deposition of potassium ions. Thus an electrolyte bath of $(\text{LaCl}_3+\text{MgCl}_2)$: $\text{KCl}=40:60$ was selected for the study.

Wt% LaCl ₃	Wt% MgCl ₂	Wt % KCl	Current Efficiency
45	15	40	42
37.5	12.5	50	64
30	10	60	76
22.5	7.5	70	60

Table-7.2 Current efficiency obtained with change in composition of electrolyte in the electrodeposition of La-Mg alloys.

7.2.2.1.2 Formation of alloys

Electrolysis was carried out at a constant current density of 10A/cm² in LaCl₃-MgCl₂-KCl melt for 3 hours using molybdenum electrode at 1123 K. **Table-7.3** gives the composition of alloy obtained with varying concentration of electrolyte. **Fig.7.5** shows typical XRD pattern with LaMg, LaMg+LaMg₂, LaMg₂ and La₂Mg₁₇ alloy phases. In the sample 'a', the peaks of only LaMg phase were obtained where the concentration of MgCl₂ was 10%. The presence of strong LaMg₂ and LaMg phase was observed in sample 'b' obtained from the melt having 12% MgCl₂ in the electrolyte. The pure LaMg₂ phase appears in the pattern where MgCl₂ concentration in the melt increased further to 15 weight %. Similarly increasing concentration of MgCl₂ to 20 weight % resulted in forming a new La₂Mg₁₇ phase. From the XRD pattern a-d, magnesium content in the alloy increases with increasing concentration of MgCl₂ in the electrolyte.

XRD study which shows the existence of LaMg₂ phase at room temperature is an interesting observation. According to phase diagram, LaMg₂ phase is only stable above 998 K temperature. The existence of LaMg₂ phase could be due to the slow decomposition kinetics in presence with

molten salt. In the sample 'C', there may be presence of other phase in very low concentration which is beyond the detection limit of XRD.

The ICP results are shown in **Table-7.4** which confirms the elemental composition of the alloys are consistent with the phase revealed by XRD. Increasing concentration of magnesium ion enhances the Mg^{2+} deposition rate leading to formation of alloys having higher magnesium content. Experiments were also carried out to study the effect of electrolysis time on the phase pattern of the alloys. **Table-7.5** gives the phase structure of La-Mg alloys with varying duration of electrolytic process. It is evident from the table that the duration of electrolysis process doesn't have any effect on the phase structure of the alloy. It therefore appears that phase composition of the alloy can be controlled by varying concentration of $LaCl_3$ and $MgCl_2$ in the electrolyte.

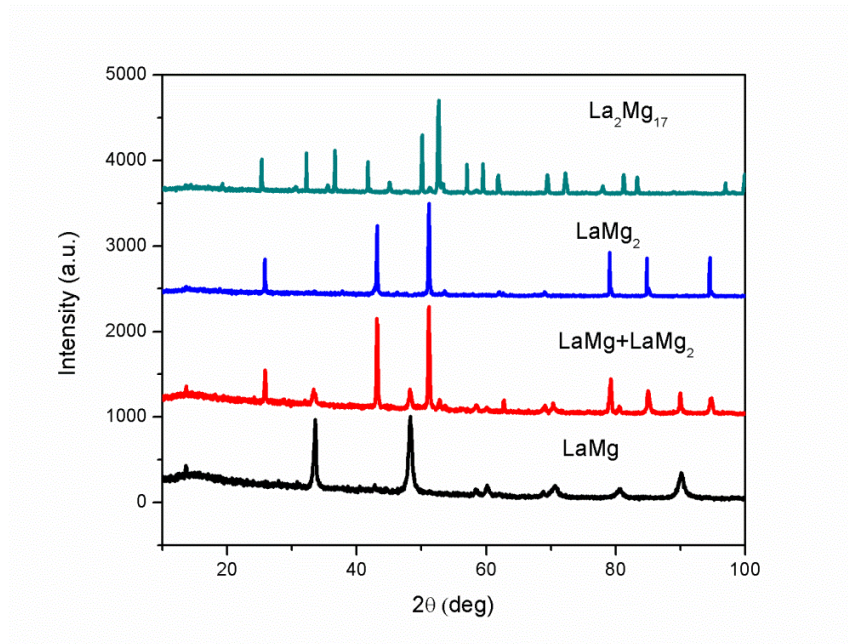


Fig.7.5 X-ray diffraction pattern of the products obtained by electrolysis in $LaCl_3$ - $MgCl_2$ -KCl (60wt %) melt containing a-10wt%, b-12.5wt%, c-15wt% and d-20wt% of $MgCl_2$.

Sample No.	Weight% LaCl ₃	Weight% of MgCl ₂	Weight% of KCl	Phase Products obtained after cooling
1	30	10	60	LaMg
2	27.5	12.5	60	LaMg+LaMg ₂
3	25	15	60	LaMg ₂
4	20	20	60	La ₂ Mg ₁₇

Table-7.3 Phases of products obtained in the electrolysis of LaCl₃-MgCl₂-LiCl-KCl electrolyte at 850⁰C temperature at cathode current density (CCD) of 10A/cm² for 3 hours duration

Sample No	Phase	La Content (wt %)	Mg content (wt %)
1	LaMg	84.5	Bal.
2	LaMg+LaMg ₂	78	Bal.
3	LaMg ₂	74.3	Bal.
4	La ₂ Mg ₁₇	40.1	Bal.

Table-7.4 ICP-AES analysis of the samples obtained in the electrolysis of LaCl₃-MgCl₂-LiCl-KCl electrolyte at 1123 K temperature at cathode current density (CCD) of 10A/cm² for 3 hours duration.

Duration of electrolysis(hours)	Phase obtained
2	LaMg ₂
3	LaMg ₂
4	LaMg ₂

Table-7.5 Effect of electrolysis duration on composition of the alloy obtained in the melt containing 25wt% of LaCl₃ and 15wt% MgCl₂ at 1123 K temperature at CCD of 10A/cm².

7.2.2.1.3 Microstructure Evolution

The SEM images of the identified products are shown in the **Fig.7.6**. The product shows uniform distribution of particles in the alloy powder. The average grain size of the alloys is around 30 μ m indicating the absence of grain growth. The mapping analysis shows that magnesium and lanthanum distribute homogeneously throughout the alloys.

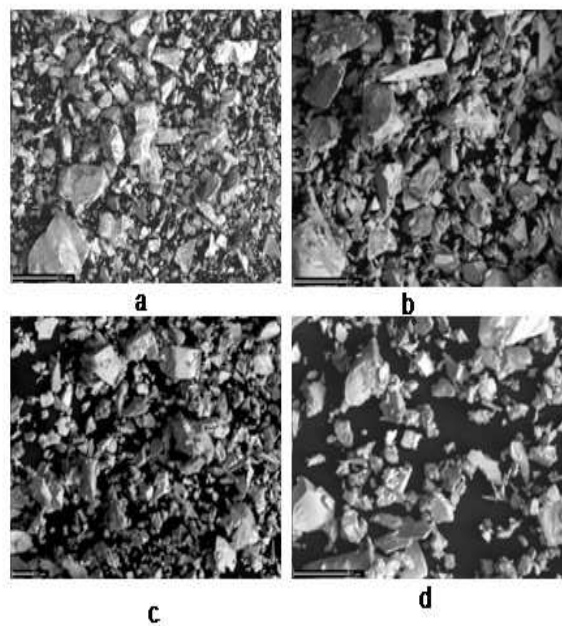


Fig.7.6 SEM images of samples a-LaMg, b-LaMg+LaMg₂, c-LaMg₂ and d-La₂Mg₁₇ obtained by electrolysis in LaCl₃-MgCl₂-KCl electrolyte at 850⁰C temperature at current density of 10A/cm² for 3 hours duration. Electrolytic Composition a-30 wt% LaCl₃+10 wt% MgCl₂ + 60wt% KCl b-27.5 wt% LaCl₃+12.5 wt% MgCl₂ + 60wt% KCl c-25 wt% LaCl₃+15 wt% MgCl₂ + 60wt% KCl d-20 wt% LaCl₃+20 wt% MgCl₂ + 60wt% KCl

7.2.2.1.4 Current efficiency:

Current efficiency is the ratio between the actual weights of the material obtained upon the theoretical weight calculated as per Faraday's 1st law. Mathematical equation for current efficiency (η) used in the present study has given below [181].

$$\eta = \frac{W}{e_{\text{alloy}}} \times \frac{96500}{Q} \times 100$$

W-is the mass of the alloy deposit in (gm).

e_{alloy} -is the electrochemical equivalent of the alloy

Q-is the quantity of electricity passed (Col)

Electrochemical equivalent of the alloy was calculated as

$$e_{\text{alloy}} = \frac{e_{\text{La}} \times e_{\text{Mg}}}{e_{\text{La}} \times f_{\text{Mg}} + e_{\text{Mg}} \times f_{\text{La}}}$$

f_{Mg} and f_{La} are the fractions in the deposit which were found out from ICP-AES analysis of the alloys. e_{La} and e_{Mg} are the electrochemical equivalents of lanthanum and magnesium respectively.

The point to note here is the current efficiency mentioned here has not been calculated for liquid alloy. This has been calculated by taking into consideration the total mass of the alloy and fraction of individual elements of the solid mass obtained after electrolysis.

7.2.2.1.5 Effect electrolysis temperature on current efficiency

Fig.7.7 shows the relationship between current efficiency and electrolysis temperature. The alloys were obtained by electrolysis in the electrolytic bath containing 60 wt % of KCl, 30wt %

of LaCl_3 and 10 wt % of MgCl_2 . All these experiments were carried out at a constant current density of $10\text{A}/\text{cm}^2$ for 3 hours in the temperature range of 1073 to 1173 K. The products obtained after each experiment were consisting of only La-Mg phase having lanthanum content of 84wt%. This shows the composition of products does not change within the temperature range studied here. From **Fig.7.7** it is clearly seen that with increase in electrolysis temperature, current efficiency increased and reaching maximum of 85% and thereafter started falling. The explanation here remains same as that in section 6.2.3.

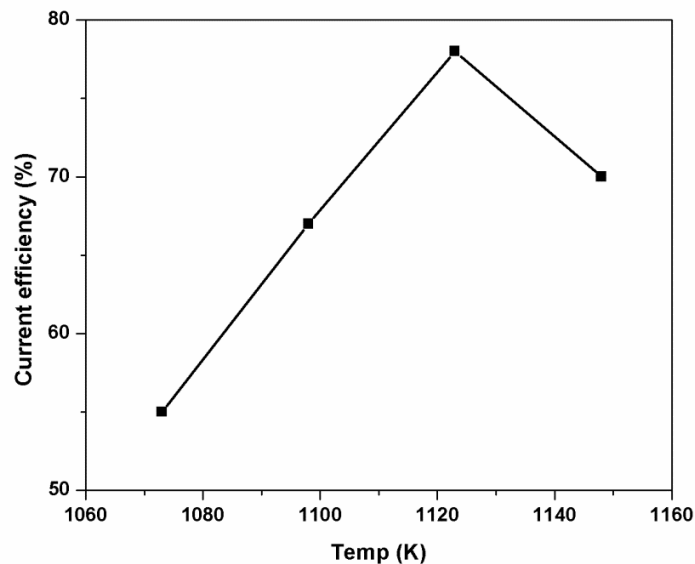


Fig.7.7 Effect of electrolysis temperature on current efficiency (CE) in the electrolytic bath containing 60wt % KCl, 30wt % LaCl_3 and 10 wt % MgCl_2 .

7.2.2.1.6 Effect of cathode current density on current efficiency:

The relationship between cathode current density (CCD) and current efficiency is shown in **Fig. 7.8**. The effect of cathode current density (CCD) on current efficiency were studied for CCD from $5\text{-}15\text{A}/\text{cm}^2$ in the electrolyte consisting of 60 wt % of KCl, 10wt % of MgCl_2 and 30 wt % of

LaCl₃.La-Mg alloys were prepared by electrolysis at 1123 K for duration of 3 hours at different CCD. Here also the product composition does not change with current density. The current efficiency increases with increase in CCD from 5-12.5A/cm² and thereafter decreases. The explanation remains same as in section 6.2.5.

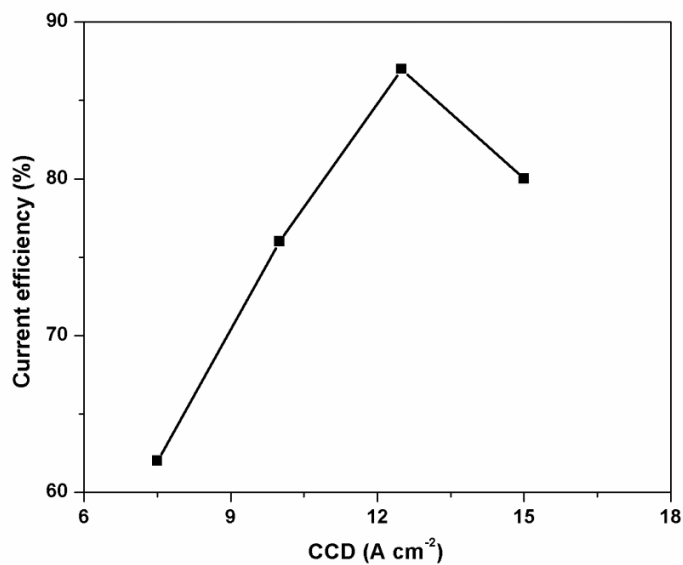


Fig.7.8 Effect of cathode current density (CCD) on current efficiency (CE) in the electrolytic bath containing 60 wt % KCl, 30 wt% LaCl₃ and 10 wt% MgCl₂.

7.2.2.2 Conclusion:

La-Mg alloys were successfully prepared in the molten state in 150-200g scale by electrochemical codeposition of lanthanum and magnesium ions in LaCl₃-MgCl₂-KCl electrolyte. Different phases of La-Mg alloys were prepared by varying LaCl₃ and MgCl₂ concentration in the electrolyte. The optimum conditions were established to have high current efficiency in the process.

7.3 Consumable cathode technique:

In this technique, one component of the alloy is taken as cathode. The other component/s of the alloy is taken as functional electrolyte. Metal ion from the functional electrolyte is deposited on the reactive cathode during the electrolysis process and forms alloy. In this process, the cathode is consumed and hence this is called as consumable cathode technique. Nd-Fe alloy production in this technique has been studied here.

Nd-Fe alloy:

The Nd-Fe alloys have attracted a lot of interest because it is used in the development of high-performance magnetic materials based on the hard magnetic compound $\text{Nd}_2\text{Fe}_{14}\text{B}$. To have large scale preparation of Nd-Fe-B alloy, it is necessary to reduce the production cost of metallic neodymium. The neodymium metal can be prepared by calciothermic reduction or molten salt electrolysis. It is known that continuous production of the molten salt electrolysis process offers great advantage in reducing the cost of the preparation compared to batch mode of metallothermic reduction process. But the current efficiency obtained in the electrolysis of Nd is low as discussed in the chapter-V. This problem could be alleviated by direct production of Nd-Fe alloy by reducing the electrolytic temperature, using consumable cathode (Fe) in molten chloride electrolytes.

7.3.1 Analysis of cyclic voltammograms:

Electrochemical reduction of Nd (III) on iron electrode was investigated employing cyclic voltammetry technique. The comparison of electrochemical domain of NaCl-KCl electrolyte on Fe electrode with that of molybdenum electrode is shown in **Fig.7.9**. It is apparent from the figure that the electrochemical window of the NaCl-KCl melt is significantly smaller than that on the molybdenum electrode although the cathodic limit remains same for both the

cases. **Fig.7.10** shows the comparison of the voltammogram obtained in NaCl-KCl molten media before and after addition of NdCl_3 on iron electrode at 973K. The black curve represents the spectra obtained in NaCl-KCl electrolyte and red curve represents the spectra of NdCl_3 -NaCl-KCl system. The peak correspond to the extreme end of the cathodic side is definitely due to deposition of Na(I) ion which is the cathodic limit of the melt. After addition of NdCl_3 in NaCl-KCl melt two extra pair of cathodic/anodic signals (B/B1, A/A1) appeared in the voltammogram. This corresponds to the participation of two phenomena. The first reaction step A/A1, is associated with the electrochemical formation and dissolution of Nd-Fe alloy and the Nd (III)/Nd (O) redox reaction was responsible for the B/B1 wave [182]. The formation of Nd-Fe alloy occurs at less cathodic potential because activity of neodymium (a_{Nd}) in Nd-Fe alloy is less compared to pure neodymium metal. Energy dispersive X-ray Fluorescence (ED-XRF) analysis was employed to characterize the deposited product obtained after potentiostatic electrolysis at -2.0 V for 10 minutes. **Fig.7.11** shows the EDXRF analysis of the deposited product which confirmed the formation of Nd-Fe alloy on electrochemical deposition.

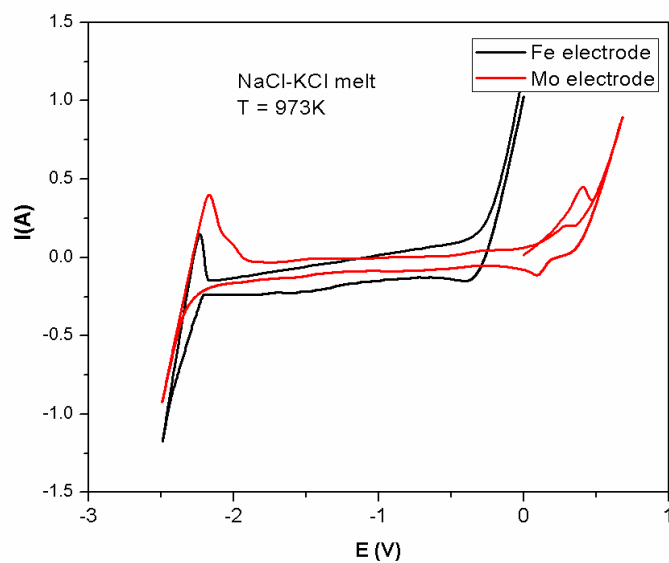


Fig.7.9 The comparison of electrochemical domain of NaCl-KCl electrolyte on Fe electrode with that of molybdenum electrode

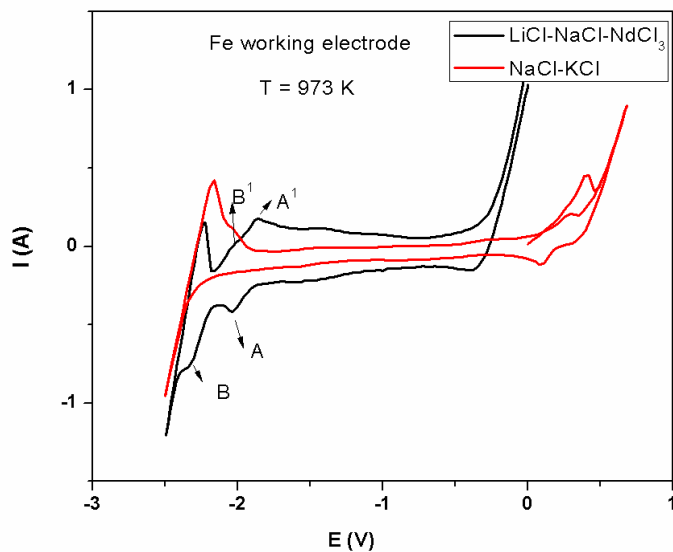


Fig.7.10 Comparison of the voltammogram obtained in NaCl-KCl molten media before and after addition of NdCl₃ on iron electrode at 973K.

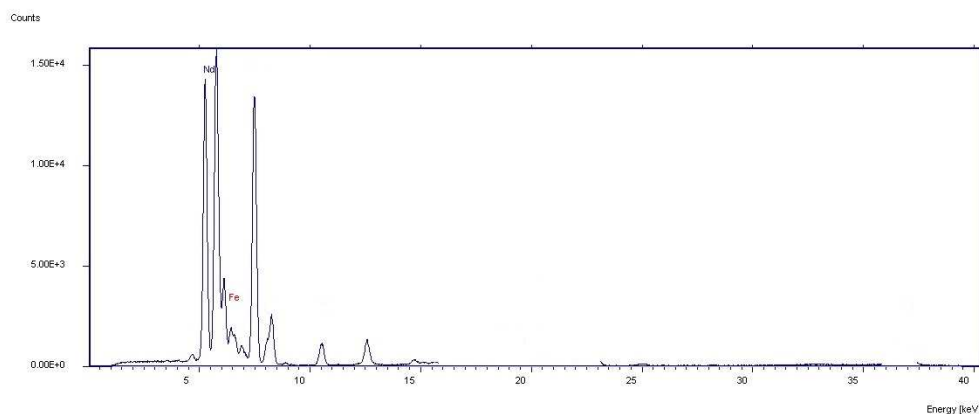


Fig.7.11 Fluorescence (ED-XRF) analysis of the deposited product obtained after potentiostatic electrolysis at -2.0 V for 10 minutes.

7.3.2 Bulk Preparation of Nd-Fe alloy:

The description regarding electrolytic cell remains same as given in the **section-6.1.3**. The only difference here is the cathode used in the La-Mg preparation is an inert electrode (molybdenum) where as consumable cathode iron (mild steel) was used in this case. The schematic of the electrolysis set-up is shown in **Fig.7.12**.

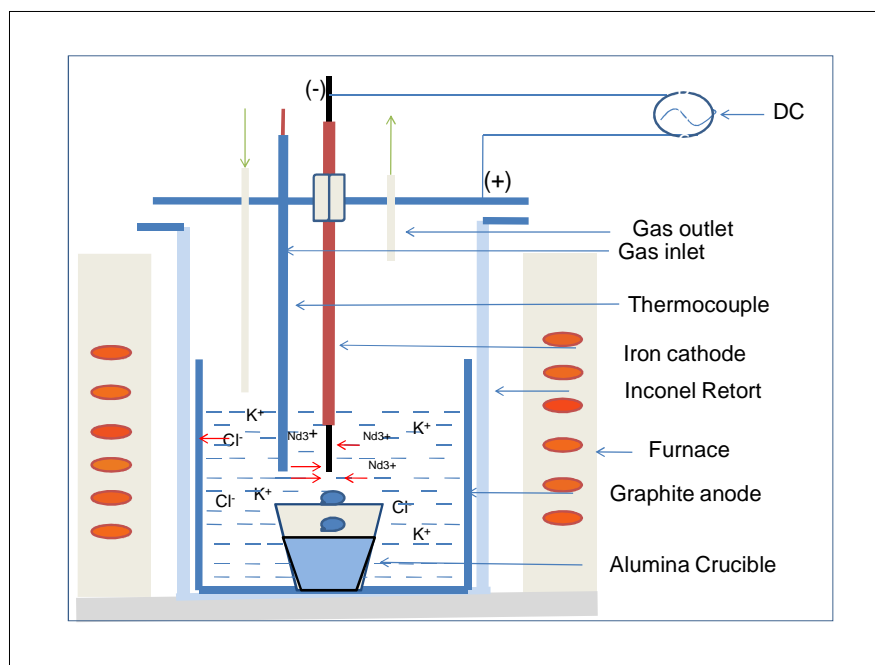
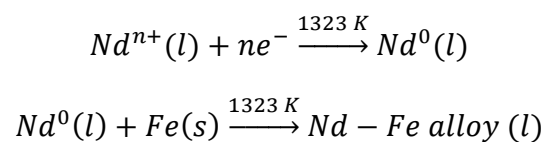


Fig.7.12 Schematic of the electrolytic set-up used in the Nd-Fe alloy preparation

Here the electrolysis temperature was kept 1323 K to ensure that Nd metal forms in the liquid state at cathode and that neodymium reacts with the iron cathode to form Nd-Fe alloy. The electrodeposited neodymium on cathode surface reacted with Fe to produce molten alloy according to following reaction:



The liquid alloy dripped into an alumina crucible placed just below the tip of cathode rod. Typical product obtained in the experiment was shown in **Fig.7.13** and the EDXRF spectrum of the product is shown in **Fig.7.14**. Characterization of the product by EDXRF technique confirmed

the formation of Nd-Fe alloy. Typical alloy product contains 85 mass % of Nd and 15 mass % Fe.



Fig.7.13 Photograph of the Nd-Fe product obtained in our experiment.

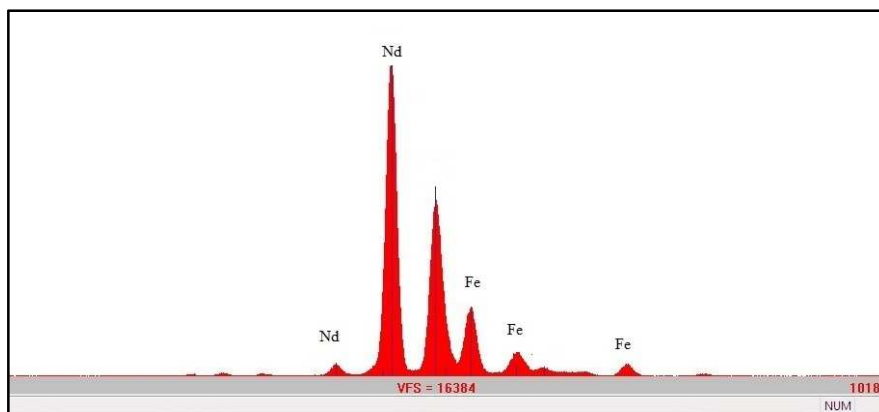


Fig.7.14 EDXRF spectra of the obtained Nd-Fe product

7.3.2.1 Results and discussion

7.3.2.1.1 Effect of concentration of electrolyte:

The effect of variation of concentration of NdCl_3 in the electrolyte on the current efficiency (CE) was studied and the results are presented in **Table-7.6**. The CE was found to increase from

12 to 45% as the concentration of the electrolyte increases from 10 to 35 wt% .Further increase in concentration decreases the current efficiency which could be due to increase in the viscosity of the bath.

Conc. Of NdCl ₃	Current efficiency (%)
10	12
20	23
30	34
35	45
40	38
45	33

Table-7.6 Current efficiency obtained with varying conc. of NdCl₃ in the electrodeposition of Nd-Fe alloy using NdCl₃-NaCl-KCl electrolyte and Fe cathode.

7.3.2.1.2 Effect of cathode current density:

The relationship between cathode current density (CCD) and current efficiency is shown in **Fig. 7.15**.The effect of cathode current density (CCD) on current efficiency were studied for CCD from 2-10A/cm² in the electrolyte consisting of 35 wt % NdCl₃.The applied voltage in this case was in between 4-7V.The current efficiency increases with increase in CCD from 2-7A/cm² and thereafter decreases. The explanation remains same as described in **section 6.2.5**.

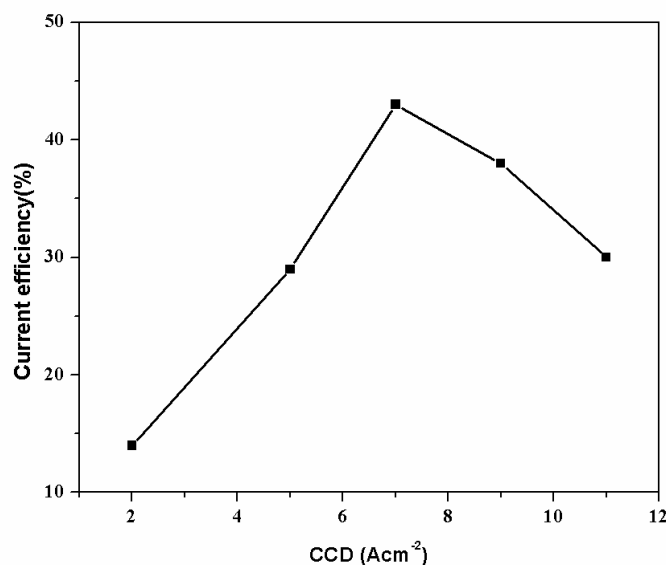


Fig.7.15 Current efficiency obtained in the electrowinning of Nd-Fe alloy with varying CCD.

7.3.2.2 Conclusion:

Nd-Fe alloy was successfully prepared in the molten state deposition of neodymium on iron cathode using NdCl₃-KCl electrolyte. Typical composition of obtained products contains 85% Nd and 15% Fe. The electrolytic process has been studied at 1323 K at varying amount of NdCl₃ and with different CCD. The optimum conditions were established to have high current efficiency in the present electrochemical set-up. The current efficiency in this process was found to be low.

7.4 Summary:

Under this chapter, synthesis of two alloys namely La-Mg and Nd-Fe were studied by electrochemical codeposition and consumable cathode technique respectively. Basic information of deposition in both the cases was evaluated using transient electrochemical techniques like cyclic voltammetry and open circuit potentiometry.

Bulk deposition of La-Mg alloy was carried out using $\text{LaCl}_3\text{-MgCl}_2\text{-KCl}$ electrolyte. Different phases of La-Mg alloys could be prepared with varying concentration of electrolyte. The operational parameters like composition of electrolyte, bath temperature and cathode current density were varied to get maximum current efficiency. Similarly bulk deposition of Nd-Fe alloy was carried out in $\text{NdCl}_3\text{-KCl}$ electrolyte using iron cathode. Here also process conditions were varied to get maximum efficiency. It was observed that good current efficiency and yield was obtained in La-Mg preparation where as in Nd-Fe case efficiency was poor. Three reasons could be attributed for the poor efficiency in preparation of Nd-Fe alloy (i) slow diffusion of Nd (III) in the melt (ii) slow diffusion of Nd and Fe atom to form alloy (iii) higher operational temperature.

CONCLUSION

In this work, the mechanism for the thermal dehydration of $RECl_3 \cdot XH_2O$ ($X = 7, 6$) viz., $LaCl_3 \cdot 7H_2O$, $CeCl_3 \cdot 7H_2O$, $PrCl_3 \cdot 7H_2O$ and $NdCl_3 \cdot 6H_2O$ was established and the onset temperatures of each dehydration step have been determined from equilibrium thermogravimetric experiments. The vapor pressure of water over $RECl_3 \cdot XH_2O$ and the decomposition products have been measured employing dynamic transpiration technique. From the measured vapor pressure data, thermodynamic parameters for $RECl_3 \cdot XH_2O$ and the decomposition products such as standard molar Gibbs energy of formation, standard molar enthalpy of formation and standard molar entropy of have been derived. The derived thermodynamic data have been used to predict condition for complete removal of water of crystallization from $RECl_3 \cdot XH_2O$, require for maximum yield of RE metal in the electrolysis process. From this study it is concluded that $RECl_3 \cdot XH_2O$ can be completely dehydrated by heating the hydrated chlorides up to $200^\circ C$ under a dynamic vacuum of $\sim 10^{-2}$ mbar. With this procedure, 500 gm per batch of anhydrous $RECl_3$ (RE – La, Ce, Pr and Nd) have been prepared by dehydration in our laboratory.

Electrochemical behavior of lanthanides i.e. La, Ce, Pr and Nd in molten LiCl-KCl and NaCl-KCl salts have been studied using transient electrochemical technique. The reduction mechanism and diffusion co-efficient of lanthanide ions in molten chloride mixtures have been investigated by cyclic voltammetry. The diffusion co-efficient (D) of RE (III) ions in molten salt mixture was found to decrease with decrease in ionic radius, which has been attributed to the higher solvation

of smaller ions forming bulkier complex. Similarly diffusion co-efficient D of RE (III) in LiCl-KCl electrolyte was found to be higher than that of NaCl-KCl electrolyte. The slow diffusion of RE ions in NaCl-KCl electrolyte could be due to the higher viscosity of the melt. Reversibility of the reduction reactions were also studied by analyzing cyclic voltammograms obtained at different scan rates. The nature of reduction of RE (III) ions to corresponding metal could be described as quasi-reversible to irreversible.

Process parameters for the extraction of light rare earth metals by molten salt electrolysis process using LiCl-KCl and NaCl-KCl salt mixtures have been standardized. Lanthanum, cerium, praseodymium and neodymium metals were electroplated with good current efficiency and yield from their corresponding chlorides salts. The optimum operating conditions have been established for highest current efficiency in the electroplating process. Electrolysis of molten chloride is found to be an efficient process for the extraction of La, Ce and Pr metals, whereas, production of Nd metal by this process is found to be less efficient.

Electrochemical techniques such as electrochemical codeposition technique and consumable cathode technique have been explored in the preparation of rare earth alloys. La-Mg alloys have been prepared following co-deposition technique. Reliable information on reduction mechanism has been generated from cyclic voltammetric and open circuit potentiometric studies. La-Mg alloys of different compositions in 150-200 gm scale have also been synthesized following co-deposition technique. Operational parameters were standardized to get maximum current efficiency and yield in the process. Synthesis of La-Mg alloy by this is found to be attractive and the method is suggested for its large scale production.

Consumable cathode technique has been adopted for the synthesis of Nd-Fe alloy, where Nd metal was electrodeposited on iron cathode to form Nd-Fe alloy in NaCl-KCl-NdCl₃ electrolyte.

In this case, the mechanism of formation of alloy was also established from cyclic voltammetry study. The bulk production of Nd-Fe alloy has been successfully carried out using this method and the operational parameters for maximum current efficiency has been determined

Future scope of work

The data on the solubility of rare earth chlorides in molten LiCl, KCl and NaCl media which is limited and needs to be generated in order to further improve the metal yield. Similarly; vapor pressure data of $RECl_3$ -LiCl-KCl and $RECl_3$ -NaCl-KCl are required to minimize the loss precious RE metal. These data will also helpful in understanding the current efficiency trend among the lanthanides. These studies are planned for the future course of work.

References

1. Jones, A.P., Wall, F., Williams, C.T., 1996. Rare Earth Minerals: Chemistry, Origin and Ore Deposits. Chapman & Hall, London.
2. A. Chakhmouradian, F. Wall, 2012, Rare earth elements: minerals, mines, agents (and more), Elements 8,333-340.
3. M. Bau, 2014. Interview with author. 7th February and 14th October.
4. C. K. Gupta, N. Krishnamurthy, 2005, Extractive metallurgy of Rare earths. CRC Press.
5. D.N Trifonov, 1963. The Rare-Earth Elements. Macmillan, New York.
6. C.K .Gupta, N. Krishnamurthy, International Materials Reviews **37**, 5(1992) 197.
7. Yufeng Wu, Xiaofei Yin, Qijun Zhang, Wei Wang, XianzhongMu, Resources, Conservation and Recycling **88** (2014) 21.
8. K. A. Gschneidner, V. K. Pecharsky, Journal of Rare Earths **24** (2006) 641.
9. C.R Ronda, T Jüstel, H Nikol, Journal of Alloys and Compounds, **275–277**, 24 (1998)669.
10. Nazarov, M., Noh, D.Y., Journal of Rare Earths **28** (2010) 1.
11. S .Ye, F. Xiao, Y.X Pan, Y.Y. Ma, Q. YZhang, Materials Science and Engineering R **71**(2011) 1.

12. G. Liu, X. Chen, 2007. Spectroscopic properties of lanthanides in nonmaterial, Handbook on the Physics and Chemistry of Rare Earths, Vol 37, pp. 99–169.
13. E. C. Karsu, E. J. Popovici, A. Ege, M. Morar, E. Indrea, T. Karali, N. Can, Journal of Luminescence **131** (2011) 1052.
14. I.R. Harris and G.W. Jewell, 19 - Rare-earth magnets: properties, processing and applications, In Woodhead Publishing Series in Energy, edited by John A. Kilner, Stephen J. Skinner, Stuart J.C. Irvine and Peter P. Edwards, Woodhead Publishing, 2012, Pages 600-639, Functional Materials for Sustainable Energy Applications.
15. Jacques Lucas, Pierre Lucas, Thierry Le Mercier, Alain Rollat and William Davenport, Chapter 10 - Rare Earths in Rechargeable Batteries, In Rare Earths, edited by Jacques Lucas Pierre, Lucas Thierry, Le Mercier, Alain Rollat, William Davenport, Elsevier, Amsterdam, 2015, Pages 167-180.
16. H.F. Song, M. Hong, 2010a. The analysis and prediction of rare earth industry in China (I), Rare Earth, Information, No.2, 6–8 (in Chinese).
17. Song, H.F., Hong, M., 2010b. The analysis and prediction of rare earth industry.
18. W. S. Lee, T. H. Chen, Materials Transactions, **49**, 6(2008) 1284.
19. Z. S. Yu, M. B. Chen, 1995. Rare Earth Elements and Their Applications. Metallurgical Industry Press, Beijing (P.R. China).
20. Buchert, M., 2010. Life cycle assessment (LCA) of nickel metal hydride batteries for HEV application. In: Presentation at IARC, Basel (Switzerland), 4th March 2010.
21. A.R. Wu, C.Q. Xia, Materials & Design. **28** (2007) 1963.

22. Chao-Chi Jain and Chun-Hao Koo, *Mater. Trans.* **48** (2007) 265.
23. H. Oesterreicher, F.T. Parker, *J. Appl. Phys.* **55** (1984) 4334.
24. D. Brown, B.M. Ma, Z. Chen, *Journal of Magnetism and Magnetic Materials* **248** (2002) 432.
25. Long, K.R., Van Gosen, B.S., Foley, N.K., Cordier, D., 2010. *The Principal Rare Earth Elements Deposits of the United States - A Summary of Domestic Deposits and Global Perspective – U.S. Geological Survey Scientific Investigations Report 2010–5220*, Reston, VA, USA, pp. 1–104.
26. C. V. Sundaram and C. K Gupta, *Bull. Mater. Sci.* **6**, 5 (1984) 901.
27. T.K.S. Murthy and C.K. Gupta, *Rare earth resources, their extraction and application*, In *The Science and Technology of Rare Earth Materials*, edited by E.C. Subbarao, W. E. Wallace, Academic Press, 1980, pp. 3-23.
28. E. Stefanidaki, C. Hasiotis, C. Kontoyannis, *Electrochim. Acta*, **46** (2001) 2665.
29. P. N. Mohan Das, A. D. Damodaran, M. Subhash, *Materials Science Forum*, **30** (1988) 61.
30. L. Yujiu, H. Feng, "The development of pyrometallurgical processing of rare earths and its problems, In *New Frontiers in Rare Earth Science and Applications*", edited by Xu Guangxian and Xiao Jimei, Academic Press, 1985, pp. 1107-1116.
31. Y.W. Miao, J.S. Horng and Y.C. Hoh, *The preparation of Nd metal from Taiwan black monazite*, In *Proceedings of Metallurgical Society of Canadian Institute of Mining and Metallurgy*, edited by Bernard Closset, Pergamon, Oxford, 1989, pp. 271-278, *Production and Electrolysis of Light Metals*.

32. E.C. Subbarao and W.E Wallace, Science and Technology of rare earth materials, Academic press INC.
33. R. A. Sharma, J.Met. **39**, 2 (1987) 33.
34. T S Krishnan, Bull. Mater. Sci., **2**, 3 (1980) 161.
35. P. Pramanik, M. Akhtar, Materials Science Forum **30** (1988) 173.
36. M. Ohtsuka, D. Y. Kim and K. Itagaki, Journal of Alloys and Compounds, **230**, 1, (1995) 46.
37. A. H. Daane, D. H. Dennison, F. H. Spedding, J. Amer. Chem. Soc., **75**(1953) 2272.
38. F. H. Spedding, S. Iegvold, A. H. Daane and L. D. Jennings: progress in low temperature physics, Vol-11(ed. C. J. Garter), 368-394; Amsterdam, North Holland.
39. F. M. Lever and J. B. Payne: in 'Advance in extractive metallurgy'789- 817; 1968. London. The institute of mining and metallurgy.
40. O. N. Carlson, T. A. Haefling, F. A. Schmidt and F. H. Spedding, J. Electrochem. Soc., **107**(1960)540.
41. F. A. Schmidt and O. N. Carlson (1974) Method for preparing scandium metal, U. S. Patent 3, 846, 121.
42. W. Hillenbrand and T. Norton, Ann. Phys. U. Chem. **155** (1895) 633.
43. W. Muthann, W. Hofer and L. Weiss, Ann.**320** (1902)131.
44. W. Muthann, W. Hofer and L. Weiss, Ann.**331** (1904)1.

45. A. Hirsh, Trans. Am. Electrochem. Soc. **20**(1912) 57.
46. H. Kremers and R. Stevens, J. A. C. S. **45**(1923)614.
47. E. Schuemaker and J. Harris, J.A.C.S. **48**(1926) 3108.
48. M. Billy and F. Trombe, Compt .rend. **193**(1931)421.
49. H. Kremers, Trans. Am .Electrochem, Soc. **47**(1925)365.
50. A. Thompson, H. Kremers, Trans. Am. Chem. Electrochem. Soc. **47**(1925)345.
51. H. Kremers, H. Beuker, Trans. Am. Chem. Electrochem. Soc. **47**(1925) 353.
52. A. Thompson, W. Holten and H. Kremers, Trans. Am. Chem. Electrochem. Soc. **48**(1926) 3108.
53. T. Kuroda (1957) "The preparation of lanthanum by fused salt electrolysis and its application", Denki Shinkenjo, Kenkyu Hokoku, 561,103.
54. F. Seon, G. Barthole: Pat. EP 188 515, 1986.
55. S. Singh, A. L. Pappachan and H. S. Gadiyar, Journal of less common Metals, **120** (1986) 307.
56. W. Muthann, J. Scheidemandel, Ann. **355**(1907)116.
57. P. M. J. Grey Trans. Inst. Min.Met. **61**(1951)141.

58. E. Morrice, J. Darrah, E. Brown, C. Wyche, W. Hedrich, R. Williams, R. G. Knickerbocker (1960) Metallurgical laboratory data of reduction refining of ceric oxide and cerous fluoride to cerium ingot, R1 5549, U.S. Department of interior, Washington D.C.
59. E. Morrice, C. Wyche, T. A. Henrie (1962) "Electro-winning of molten lanthanum from lanthanum oxide, Bureau of Mines Report of Investigations 6075", U. S. Department of interior, Washington D.C.
60. E. S. Shedd, J. D. Marchant and T. A. Henrie (1964) Continuous electro-winning of cerium metal from cerium oxides, Bureau of Mines Report of Investigations 6362, U. S. Department of interior, Washington D.C.
61. E. S. Shedd, J. D. Marchant and T. A. Henrie (1966) Electro-winning and tapping of lanthanum metal, Bureau of Mines Report of Investigations 6882, U. S. Department of interior, Washington D.C.
62. E. Morrice, C. Wyche, T. A. Henrie (1967) Electro-winning of high purity neodymium, praseodymium and didymium metal from their oxide, Bureau of Mines Report of Investigations 6957, U. S. Department of interior, Washington D.C.
63. D. Bratland, K. A. Gschneidner, J. Electrochim. Acta **25**(1980)145.
64. Z. Zhao, H. Jia, B. Yan (2005) Science and Technology of Baotou Corporation, Vol. 31, Supplement Nov. 2005.
65. G.J.Janz, R.P.T.Topkins, C.B.Allen, J.R.Downey, G.L.Gardner, U.Krebs, and S.K.Singer, Journal of phy.chem.ref.data vol 4, No-4, 1975.
66. C. Bale, Facility for the Analysis of Chemical Thermodynamics. 2012 (2012).

67. D.S. Coleman, P.D.A. Lacy, *Mat. Res. Bull.* Vol. 2, pp. 935-938, 1967. Pergamon Press, Inc. Printed.
68. M. V. Bosco, G. G. Fouga and A. E. Bohe, *Thermochimica Acta*, **540**(2012) 98.
69. Z. Darzens and F. Bourion, *Compt. rend.*, **153**, (1911) 270.
70. E. Demarcay, *Compt. rend.*, **104**(1887)111.
71. E. Chauvenet, *Compt. rend.*, **152**(1911)87.
72. B. S. Hopkins, D. H. West, *J. Am. Chem. Soc.*, **57**(1935)1159.
73. Nolting, *J. Inorg. Nucl. Chem.***14** (1960) 208.
74. S. Singh and A. L. Pappachan, *Bulletin of Electrochemistry* **6(1)** (1990) 97.
75. J. Sundstrom, O. Wijk, *Journal of alloys and compounds* **249**(1997) 224.
76. J. H. Kleinheksel and H. C. Kremers, *J. Am. Chem., Soc.* **109** (1962) 247.
77. T. Kuruda and O. Matsumoto, *J. Electrochem .Soc. Jpn.*, **30** (1962) E149.
78. M. D. Taylor, *Chem. Rev.*, **62**(1962) 503.
79. R. Didchenko and L. M. Litz, *Journal of electrochemical soc.*, **109** (1962) 247.
80. W.W. Wendlandt, *J.Inorg.Nucl.Chem.*, **5** (1957) 118.
81. W.W. Wendlandt, *J.Inorg.Nucl.Chem.*, **9** (1959) 136.

82. J.E. Powell, H.R. Burkholder, *J. Inorg. Nucl. Chem.*, **14** (1960) 65-70.
83. S.J. Ashcroft, C.T. Mortimer, *J. Less Common Metals*, **14** (1968) 403.
84. V. Van Hong, J. Sundström, *Thermochim. Acta*, **307** (1997) 37.
85. G. Ren, X. Chen, Y. Pei, H. Li, H. Xu, *J. Alloys Compd.*, **467** (2009) 120.
86. G. J. Kipouros, R. A. Sharma, *Journal of Less Common Metals*, **160** (1990) 85.
87. G. Haeseler, F. Matthes, *Journal of Less Common Metals*, **9** (1965) 133.
88. G. Zheng, C. Peiheng, G. Zhizhen, M. Jinhua, C. Yunsheng, *Acta Chim. Sin.*, **41** (1983) 463.
89. F. Lantelme, T. Cartailier, Y. Berghoute, M. Hamdani, *J. Electrochem. Soc.* **148** (2001) C604.
90. P. Masset, R. J. M. Konings, R. Malmbeck, J. Serp, J.-P. Glatz, *J. Nucl. Mater.* **344** (2005) 173.
91. S. P. Fusselman, J. J. Roy, D. L. Grimmer, L. F. Grantham, C. L. Krueger, C. R. Nabelek, T.S. Storvick, T. Inoue, T. Hijikata, K. Kinoshita, Y. Sakamura, K. Uozumi, T. Kawai, N. Takahashi, *J. Electrochem. Soc.* **146** (1999) 2573.
92. F. Gao, C. Wang, L. Liu, J. Guo, S. Chang, L. Chang, R. Li, Y. Ouyang, *Journal of Rare Earths* **27** (2009) 986.
93. S. Vandarkuzhali, N. Gogoi, S. Ghosh, B. Prabhakara Reddy, *Electrochim. Acta* **59** (2012) 245.

94. H. Tang, B. Pesic, *Electrochim. Acta* **119** (2014) 120.
95. Y. Castrillejo, M.R. Bermejo, R. Pardo, A.M. Martínez, *J. Electroanal. Chem.*, **522** (2002) 124.
96. S. P. Fusselman, J. J. Roy, D. L. Grimmitt, L. F. Grantham, C. L. Krueger, C. R. Nabelek, T. S. Storvick, T. Inoue, T. Hijikata, K. Kinoshita, Y. Sakamura, K. Uozumi, T. Kawai, N. Takahashi, *J. Electrochem. Soc.*, **146** (1999) 2573.
97. F. Lantelme, T. Cartailier, Y. Berghoute, M. Hamdani, *J. Electrochem. Soc.*, 2001, **148**, C604.
98. M. Iizuka, *J. Electrochem. Soc.*, **145** (1998) 84.
99. K. C. Marsden, B. Pesic, *J. Electrochem. Soc.*, **158**(2011) F111.
100. C. Wang, Y. Liu, H. Hi, F. Gao, L. Liu, S. Chang, J. Guo, L. Chang, Y. Ouyang, *Journal of Rare Earths*, **31**, (2013) 405.
101. H. Tabg, B. Pesic, *Journal of Nuclear Materials* **458** (2015) 37.
102. S. Vandrakuzhali et al., *Electrochimica Acta* **145** (2014) 86.
103. E. Morrice and M. M. Wong, *Min. Sci. Engg.* **11**, 3(1979) 125.
104. H. Groult, H. El Ghallali, H., A. Barhoun, E. Briot, L. Perrigaud, S. Hernandorena and F. Lantelme, *Electrochim. Acta*, **55** (2010) 1926.
105. Takahisalida, Toshiyuki Nohira. and Yasuhiko Ito, *Electrochim. Acta.* **48** (2003) 2517.

106. Sen-Lin Wang, Ji-Bei Lin, Qiu-Yan Cai, Yan Zhang, *J. Alloys Compounds.* **450** (2008)142.
107. V. Soare, M. Burada, T. Ostvold, C. Kontoyannis and E. Stefanidaki, *J. Min. Met. B.* **39** (2003) 209.
108. P. Cao, M. L. Zhang, W. Han, Y. D. Yan and L. J. Chen, *Trans. Inst. Min. Metall. C.* **12** (2012) 12.
109. M. L. Zhang, P. Cao. W. Han, Y. D. Yan, L. J. Chen. *Trans. Nonferrous. Met. Soc. China.* **22** (2012) 16.
110. E. Morrice, E. S. Shedd and T. A. Henrie (1968) Direct electrolysis rare earth oxide to metals and alloys in fluoride melts, Bureau of Mines Report of Investigations 7146, US Department of the Interior, Washington D.C.
111. E. Morrice, E. S. Shedd, M. M. Wong and T. A. Henrie *J. Metals*, **21**, 1(1969)34.
112. *Journal of Applied Electrochemistry* **25** (1995) 1139.
113. H.G. J. Moseley, *Phil. Mag.*, **26** (1913) 1024.
114. Boron in glass determination using WDXRF, Alexander Seyfarth, JCPDS-International. Centre for Diffraction Data 2008 ISSN 1097-0002 269.
115. K. Baur, S. Brennan, B. Burrow, D. Werho, P. Pianetta, *Spectrochim. Acta, Part B*, **56** (2001) 2049.
116. Minemasa Hida, Toshiyuki Mitsui, Yukio Minami, *Forensic Sci. Int.*, **89** (1997) 21.
117. J.T. Hutton, S.M. Elliott, *Chem. Geol.*, **29**(1980) 1.

118. Dennis J. Kalnicky, Raj Singhvi, J. Hazard. Mater., **83** (2001) 93.
119. S. Canepari, C. Perrino, M.L. Astolfi, M. Catrambone, D. Perret, Talanta, **77** (2009)1821.
120. Liqiang Luo David R. Chettle, Huiling Nie, Fiona E. McNeill, Marija Popovic, Theeffect of filters and collimators on Compton scatter and Pb K-series peaks in XRF bonelead analysis, Nucl. Instrum. Methods Phys. Res., Sect. B, **263** (2007) 258.
121. D. Cullity, "Elements of X-ray diffraction", *Addison-Wilson Publishing Comp. Inc.*, USA (1959).304
122. H. P. Klug and L. E. Alexander, "X-ray diffraction procedures", *Wiley-Interscience Publication*, New York (1974).
123. L. V. Azaroff and M. J. Buerger, "The Powder Method in X-ray Crystallography"*McGraw-Hill Book Comp.*, New York (1958).
124. R. W. Cahn, P. Haasen, E. J. Kramer, "Material Science and Engineering: Characterisation of Materials", VCH Publisher Inc., 1991, New York.
125. W. Zhou, Z. L. Wang, "Scanning microscopy for nanotechnology: Techniques andapplications", Springer science and business media, 2006, New York.
126. P. W. Atkins, "Physical Chemistry", 5th ed. *W. H. Freeman*, New York (1994).
127. P. J. Haines, and F. W. Wilburn, "Differential thermal analysis and differentials scanningcalorimetry. In Thermal Methods of Analysis", (P. J. Haines, ed.). pp. 63–*Blackie Academic and Professional, London*. (1995).

128. L. Pengyu, Journal of Rare Earths, **25**, 3 (2007) 377.
129. M. Aryanov, Journal of Rare Earths, **27**, 1 (2009) 123.
130. S. Gu, H. Wing, Spectrochimica Acta B, **52**, 11 (1997) 1567.
131. A. J. Bard, L. R. Faulkner, "Electrochemical Methods: Fundamentals and Applications", Wiley, New York (1980).
132. R. G. Compton, C. E. Banks, "*Understanding Voltammetry* p. 74", World Scientific Publishing Co. Pte. Ltd. (2009).
133. H. Matsuda, Y. Ayabe, Z. Electrochem. **59**(1955) 494.
134. V. A. Golovin, G. A. Dobrenkov, Trans. Kazan. Khim.-Tekhnol. Inst. **34**(1965) 202.
135. L. Ramaley and M. S. Krause, Jr., Anal. Chem., **41** (1969)1362.
136. L. Ramalay, M. S. Krause, Anal. Chem. 41: (1969)1362.
137. T Yamamura, M Mehmood, H. Maekawa, Y. Sato, Chem.for Sustainable Dev. **12** (2004) 105.
138. L. Feng, C. Guo, D. Tang, J. Alloys Compd., **234** (1996) 183.
139. S. R. Dharwadkar, A. S. Kerkar, M. S. Samant, Thermochem. Acta, **217** (1993) 175.
140. F. H. Spedding, J. A. Rard, A. Habenschuss, J. phys. Chem. **81**, 11 (1977) 1069.

141. E. H. P Cordfunke, R. J. M. Konings, *Thermochim. Acta* **375** (2001) 51.
142. R. J. Roy, G. J. Kipouros, *Thermochim. Acta* **178**(1991) 169.
143. W. Judge, G. J. Kipouros, *Can Metall. Q.* **52**, 3 (2013) 303.
144. I. Barin, O. Knacke, "Thermochemical Properties of Inorganic Substances", Springer-Verlag, Berlin; New York, 1973.
145. O. G. Polyachenok, A. A. Iorbalidi, E. N. Dudkina, L. D. Polyachenok, "Thermal Stability and Thermodynamics of LaCl₃ lowest hydrate", XVIII International Conference on Chemical thermodynamics in Russia Samara, Russian Federation, October 3-7, 2011.
146. R. C. Weast, "CRC Handbook of Chemistry and Physics", 69th Ed., CRC Press, Florida, 1988.
147. F. H. Spedding, C. W. Dekock, G. W. Pepple, A. Habenschuss, *J. Chem. Eng. Data* **22** (1) (1977) 58.
148. R. J. Roy, G. J. Kipouros, *Thermochim. Acta*, **178** (1991) 169.
149. C. Wang, Y. Liu, H. Hi, F. Gao, L. Liu, S. Chang, J. Guo, L. Chang, Y. Ouyang, *Journal of Rare Earths*, **31**(2013) 405.
150. R.S.Nicholson, *Analytical Chemistry* **37** (1965) 1351.
151. S.A.Kuznetsov, S.V.Kuznetsova, P.T.Strangrit, *Soviet Electrochem.* **26** (1990) 55.
152. H.Matsuda, Y.Z.Ayabe, *Z. Electrochem.*, **59** (1955) 494.

153. R. S. Nicholson, I. Shain, *Anal. Chem.* **26** (1964) 706.
154. K.C.Marsden and B.Pesic, *Journal of Electrochem.Soc.*158 (2011) F111.
155. X.Li, Y.Yan, M.Zhang, Y.Xuo, H.Tang, DeJi, Z.Zhang, *RSC Adv.*, 2014, 4, 40352–40358.
156. D. K.Sahoo, A. Satpati, N .Krishnamurthy, *RSC Adv.*, 2015, 5, 33163–33170.
157. Y. Castrillejo, M. R. Bermejo, E. Barrado, A.M. Martneza, P. Diaz Arocas, *J. Electroanal. Chem* 545 (2003) 141.
158. P. Masset, R. J. M. Konings, R. Malmbeck, J. Serp, J.P. Glatz, *J. Nucl. Mater* **344** (2005) 173.
159. K. Fukasawa, A. Uehara, T. Nagai, T. Fujii, H. Yamana, *J. Alloys Compd***509** (2011)5112.
160. M. Gaune-Escard, A. Bogacz, L. Rycerz, W. Szczepaniak, *J. Alloys Compd*, **235** (1996) 176 .
161. Ruren Xu and Qiang Su, Chapter 2 - High-temperature Synthesis, In *Modern Inorganic Synthetic Chemistry*, edited by RurenXu, Wenqin Pang and QishengHuo, Elsevier, Amsterdam, 2011, pp. 9-38
162. Y. Okamoto, T.Tsuruoka, T. Yaita, P. A. Madden, *JAEA-Research*, 2007,005.
163. G. Taguchi, *Introduction to Quality Engineering: Designing Quality into Products and Processes*, Asian Productivity Organization, 1986.

164. G. Taguchi, S. Konishi, *Orthogonal Arrays and Linear Graphs*, ASI Press, Dearborn, MI, 1987.
165. K. Dasgupta, D. Sen, S. Mazumder, C.B. Basak, J.B. Joshi, S. Banerjee, J. *Nanosci.Nanotechnol.* **10** (2010) 4030.
166. M.E. Nasab, A. Sam, S.A. Milani, *Hydrometallurgy* **106** (2011) 141.
167. D. Landolt, *J. Electrochem. Soc.* **149** (2002) 9.
168. V. V. Malyshev, K. B. Kushkhov, *Russ. J. Gen. Chem.* **74** (2004) 1139.
169. I. Bakonyi, L. Péter, *Progr. Mater. Sci.* **55** (2010) 107.
170. R. A. Sharma, R. N. Seefurth, *Metall. Trans. B* **20** (1989) 805.
171. K.H. Stern, D.R. Rolison, *J. Electrochem. Soc.* **137** (1990) 178.
172. B. Mayer, H. Anton, E. Bott, M. Methfessel, J. Sticht, J. Harris, P.C. Schmidt, *Intermetallics.* **11** (2003) 23.
173. T. F. Smith, H. L. Luo, *J. Phys. Chem. Solids.* **28** (1967) 569.
174. Xiaoping Dong, Fanxiu Lu, Yanghuan Zhang, Liying Yang, Xinlin Wang, *Mater. Chem. Phys.* **108** (2008) 251.
175. Yi Wang, Weiqiao Deng, Xuwei Liu, Shuangyin Wang, Xin Wang, *Int. J. Hyd. Energy.* **34** (2009) 1444.
176. Xuezhong Xiao, Guangcheng Liu, ShukePeng, Kairong Yu, ShouquanLi, Changpin Chen, Lixin Chen, *Int. J. Hyd.Energy.* **35** (2010) 2786.

177. B. Darriet, M. Pezat, A. Hbika, P. Hagenmuller, *Int. J. Hyd. Energy*. **5** (1980) 173
178. M. Khrussanova, M. Terzieva, P. Peshev, *J. Less-Common Met.* **125**(1986) 117.
179. M. Pezat, B. Darriet, P. Hagenmuller, *J. LessCommon Met.* **74** (1980) 427.
180. J.Mengetal.US Patent 7 744 814B2 (2010).
181. A.Subramania, A R S Priya, V S Muralidharan,Portugaliae ElectrochimicaActa**25** (2007) 481.
182. Christophe A. Zing1Mingzong Su, Senlin Du, Dinxiang Tang, *Journal of Electroanalytical Chemistry and Interfacial Electrochemistry*, **263**, 2 (1989), 399.